Autonomous Landing of a Fixed-Wing Unmanned Aerial Vehicle onto a Moving Platform

by

Cornelus Tjaart Le Roux

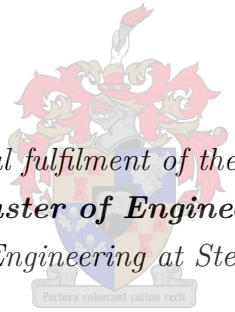

Thesis presented in partial fulfilment of the requirements for the degree
Master of Engineering
in the Faculty of Engineering at Stellenbosch University.

Supervisor:
J.A.A. Engelbrecht

Department of Electrical and Electronic Engineering

December 2016

Acknowledgements

For their assistance in completing this project, I would like to thank the following people:

- Japie Engelbrecht for his excellent insight, guidance and support.
- Johan Treurnicht and Corné Van Daalen for their advice during research group meetings.
- Michael Basson for his flying skills as the safety pilot.
- Chris Fourie for his insights and support during flight tests.
- My friends in the ESL for creating an enjoyable working environment.
- My family for their support throughout my studies.

Declaration

By submitting this thesis electronically, I declare that the entirety of the work contained herein is my own, original work, that I am the sole author thereof (save to the extent explicitly otherwise stated), that reproduction and publication thereof by Stellenbosch University will not infringe any third party rights and that I have not previously in its entirety or in part submitted it for obtaining any qualification.

December 2016

Abstract

This thesis presents the analysis, design, simulation, implementation and partial practical flight testing of a flight control system to achieve accurate autonomous landing of a fixed-wing unmanned aerial vehicle onto a moving platform.

A landing strategy is proposed that is based on real aircraft scenarios and scaled down to be representative of a remotely controlled off-the-shelf model vehicle, outfitted with a custom computer controlling unit. To create a more representative environmental simulation, the existing wind model was expanded to conform to military standards.

The Total Energy Control System (TECS) was studied and used as the main longitudinal controller. The inner loop of the traditional TECS architecture was replaced with a normal specific acceleration controller. The specific energy and energy distribution controllers were developed based on this modified architecture using a simplified design loop. The outer altitude and airspeed loops were designed using a heuristic method.

Conventional classical control designs were used for the lateral controllers. A Dutch roll damper was used to reduce yaw rate oscillations and improve lateral stability. A roll angle controller was used to regulate the bank angle and allow steering of the aircraft. An aggressive cross-track controller was developed to improve steady state tracking performance. Due to inherent problems in this design, an additional heading and guidance control system was designed and included. A switching scheme was proposed and implemented to provide a safe transition from one controller to the other.

The integrated system was verified in hardware-in-the-loop simulations using a Monte-Carlo style approach for both stationary landing point and moving platform landings. It was able to achieve good accuracy in the longitudinal axis and exceptional accuracy in the lateral axis under various environmental disturbances. Overall, the system was able to hit the moving target with an 86% success rate.

Limited flight testing showed that the energy-based longitudinal controllers performed more poorly in practice than in simulation, likely due to insufficient structural vibration damping and subsequent poor acceleration measurements. This is problematic because the energy controllers are very reliant on good acceleration control. The lateral controllers that were tested performed as designed and were therefore practically verified.

It is concluded that this project can be used as a foundation for an energy-based landing system. Improvements are proposed that can aid future projects to enhance the system performance.

Uittreksel

Hierdie tesis handel oor die analise, ontwerp, simulasie, implementasie en gedeeltelike praktiese vlugtoetsing van 'n vlugbeheerstelsel vir die akkurate landing van 'n vastevlerk onbemande vliegtuig op 'n bewegende platform.

'n Landingstrategie wat gebaseer is op werklike vliegtuig scenarios en afgeskaleer is om verteenwoordigend te wees van 'n afstandbeheerde, "van die rak af" voertuig, uitgerus met 'n doelgemaakte aanboordrekenaar, is voorgestel. Om 'n meer verteenwoordigende omgewingsimulasie op te stel, is die bestaande windmodel uitgebrei om te voldoen aan militêre standaarde.

Die Totale Energie Beheerstelsel is bestudeer en gebruik as die hoof longitudinale beheerder. Die binnelus van die tradisionele argitektuur is vervang met 'n normale spesifieke versnellingsbeheerder. Die spesifieke energie- en energieverspreidingbeheerder is ontwikkel gebaseer op hierdie aangepaste argitektuur deur gebruik te maak van 'n vereenvoudigde ontwerpslus. Die buitelus hoogte- en lugspoedbeheerder is ontwerp deur gebruik te maak van 'n heuristiese metode.

Konvensionele klassieke beheerontwerpe is gebruik vir die laterale beheerders. 'n "Dutch roll" demper is gebruik om ossillasies in die rigtingkoerstempo te verminder en laterale stabiliteit te verbeter. 'n Rolhoekbeheerder is gebruik om die rolhoek te reguleer en die vliegtuig mee te stuur. 'n Aggressiewe kruisbaanbeheerder is ontwikkel om die bestendige toestand volgfout te verbeter. As gevolg van die inherente probleme in die ontwerp is 'n addisionele rigting- en leidingsbeheerstelsel ontwerp en bygevoeg. 'n Skakelskema is voorgestel en geïmplementeer om veilige skakeling van een beheerder na die ander te verseker.

Die geïntegreede stelsel is geverifieer in hardeware-in-die-lus simulasies vir beide 'n stasionêre landingsteiken en bewegende platform landings deur van 'n Monte-Carlo benadering gebruik te maak. Goeie akkuraatheid is bereik in die longitudinale as en uitsonderlike akkuraatheid in die laterale as onder 'n verskeidenheid van omgewingstoestande. In die geheel was die stelsel in staat om 'n bewegende platform te tref met 86% sukses.

Beperkte vlugtoetsing het gewys dat die energie-gebaseerde longitudinale beheerders heelwat swakker in praktyk as in simulasie vertoon het, waarskynlik as gevolg van onvoldoende demping van strukturele vibrasies wat gelei het tot swak versnellingsmetings. Dit is problematies aangesien die energiebeheerders baie afhanklik van goeie versnellingsbeheer is. Die laterale beheerders wat getoets is, het presteer soos ontwerp en was dus prakties geverifieer.

Daar is tot die slotsom gekom dat hierdie projek as 'n fondasie vir 'n energie-gebaseerde landingsisteem gebruik kan word. Voorstelle is gemaak wat toekomstige projekte kan help om die stelsel se prestasie te verbeter.

Table of Contents

List of Figures

List of Tables

Nomenclature

Notation

$\dot{x}$	First derivative
$\ddot{x}$	Second derivative
$\boldsymbol{X}$	Vector or matrix
Δ	Difference between two coordinates
j	Imaginary component of a non-real number
s	Laplace frequency variable
t	Time
τ	Time constant
σ	Statistical standard deviation
$\overline{x}$	Statistical mean

Coordinate Vectors

ϕ, θ, ψ	Roll, pitch and yaw angles
l, m, n	Rolling, pitching and yawing moments
p, q, r	Roll, pitch and yaw rates
u, v, w	Axial, lateral and normal velocities
x, y, z	Axial, lateral and normal forces
p_N, p_E, p_D	North, East, and Down positions coordinates

Control System Dynamics

ω_n	Natural frequency
ζ	Damping ratio
p	Pole coordinate
z	Zero coordinate

Modelling Symbols

A	Wing aspect ratio
b	Wingspan
$\overline{c}$	Mean aerodynamic chord

C_η	Aerodynamic coefficient
S	Wing area
α	Angle of attack
β	Angle of sideslip
γ	Flight path angle
h	Altitude
$\delta_a, \delta_e, \delta_f, \delta_r$	Aileron, elevator, flaps and rudder deflection angles
δ_t	Thrust setting
$I_{\eta_1\eta_2}$	Moment of inertia about the $\eta_1\eta_2$-axis
m	Mass
$\overline{v}$	Velocity
e	Oswald efficiency factor
g	Gravitational constant
ρ	Air density
q_p	Dynamic pressure

Subscripts and Superscripts

B, I	Body and inertial axes coordinates
c	Command signal
e	Error signal
T	Trim value
lon, lat	Longitudinal and lateral components
A, G, T	Aerodynamic, gravitational and thrust components

Acronyms

3D	Three dimensional
ATOL	Autonomous take-off and landing
AVL	Athena vortex lattice
CAN	Controller Area Network
CG	Centre of gravity
CoX	Centre of Expertise
DC	Direct current
DCM	Direction cosine matrix
DE&EE	Department of Electrical and Electronic Engineering
DFCS	Digital flight control system
DGPS	Differential global positioning system
EKF	Extended Kalman filter
ENU	East-North-Up
ESC	Electronic speed controller

ESL	Electronic Systems Laboratory
GCS	Ground control station
GPS	Global Positioning System
HIL	Hardware-in-the-loop
HPF	High-pass filter
IDE	Integrated development environment
IMU	Inertial measurement unit
IR	Infrared
LiPo	Lithium polymer
MCU	Micro controller unit
MLC	Multi-layer cell
NEM	Nonlinear energy-based control method
NMP	Non-minimum phase
OBC	On-board computer
PBC	Passivity-based control
PCB	Printed circuit board
PD	Proportional-derivative
PID	Proportional-integral-derivative
PWM	Pulse-width modulation
QFT	Quantitative feedback theory
RC	Remotely controlled
RMS	Root mean square
RPM	Revolutions per minute
RTK	Real-Time Kinematic
SIL	Software-in-the-loop
SLC	Single layer cell
TECS	Total Energy Control System
UART	Universal asynchronous receiver / transmitter
UAV	Unmanned aerial vehicle

§ 1

Introduction

This chapter gives an overview of the current state of unmanned aerial vehicle (UAV) development by presenting research from both internal and external sources. An overview of the project objectives and the testing platform is given.

Section 1.1 discusses the background of UAVs in general as well as in the context of this project, the research environment where most of the work towards this project is undertaken, and the state of UAV development in South Africa at the time of writing. Section 1.2 presents the specific objectives set for this project. Section 1.3 discusses previous research done in the relevant field of study, both in the local research environment and globally in the aeronautical field. Section 1.4 gives an overview of the project by providing high-level explanations of how the subsystems are integrated. Section 1.5 details the layout and presentation of this thesis. Section 1.6 provides a summary of the chapter.

1.1 Background

In the aeronautical field, UAVs are currently a widely researched topic due to their advantages over traditional piloted aircraft. They can be operated for long periods of time without the consequence of pilot fatigue as computers do not suffer from mental or physical exhaustion, at very high altitudes without pressure-suit requirements of a pilot since they do need oxygen to breathe, and in areas of low visibility as they can incorporate more types of sensing equipment than just visible-spectrum eyes. UAVs will however not become fully autonomous in the near future because ethical behaviour and decision-making are very complex concepts, especially to program into a computer. Therefore, the design and development around UAVs usually attempt to exploit the physical advantages that they provide, while mission-control, judgement and responsibility are usually left to an operator, controlled at a high-level in a computerised fly-by-wire fashion.

The work presented in this thesis was performed as a master's degree project at Stellenbosch University in South Africa. The research was performed at the Electronic Systems Laboratory (ESL), a postgraduate research laboratory in the Department of Electrical and Electronic Engineering (DE&EE). The aim of this laboratory is to provide opportunities to students and

industries to become involved in joint research developments to advance skills in computers, control, data communications, imaging and system simulation through demonstrator development. The development of systems include mostly satellites and unmanned aeronautical, terrestrial and underwater vehicles [8].

The ESL forms a major part of the Centre of Expertise (CoX) in autonomous flight at the university. The CoX specialises in the development and implementation of complex embedded control, automation and information systems and can be considered an academic research environment. Staff are incorporated not only from the DE&EE, but also from the mechanical department to enhance knowledge diversity. The ESL takes part in support activities where related studies are undertaken to advance the state of aeronautical technology in general, which includes vehicle certification, system identification and collision avoidance systems [8].

The various research projects undertaken are not all standalone projects. One project generally forms the foundation of a follow-up project to increase diversity in the projects undertaken and to promote technological development while reducing duplicated effort. This resembles the industrial environment where projects are not always new, but rather an expansion or improvement of a previous one. This project builds on the previous autonomous navigation and landing projects completed by other students to form a more complete autonomous flight system.

UAVs have been used for various intelligence, surveillance and reconnaissance missions around the world since the 1960s. In South Africa, two large companies are developing UAVs at the time of writing — Denel Dynamics and ATE (now Paramount Group). Denel Dynamics currently has, amongst others, the Hungwe UAV capable of piloted and autonomous flight, as well as the Seeker II+ UAV, capable of autonomous take-off and landing (ATOL) [9]. ATE currently has, amongst others, the Kiwit UAV capable of fully autonomous flight and ATOL [10]. The DE&EE was motivated by this fast growing field of research and started their own research group in 2001. The first project was completed after two years, resulting in a UAV based on the Reliance 0.46 trainer aircraft. For that project, a simple waypoint navigation autopilot was developed by using low-cost off-the-shelf components. A nonlinear simulation model was developed in order to accurately simulate aircraft behaviour. Test flights were performed to verify the system in practice to success [11]. Since the first UAV project was very analytical and complete, it is considered as a good foundation for other similar projects. Therefore, most UAV projects in the ESL, including this one, use it as a starting point.

1.2 Research Objectives

The goal of this project is to develop the control system for a UAV to enable it to land autonomously onto a moving platform. This is similar to the real world scenario where a pilot has to land an aircraft onto the deck of an aircraft carrier, usually done with the assistance from the Fresnel Lens Optical Landing System, nicknamed the “meatball”, which visually guides the pilot in from afar [12]. Problems could arise when vision is impaired by conditions such as reflective sunlight or fog, or by physical hindrances such as severe wind or rough seas. The aim

of a computer-aided landing system would allow for faster, more accurate responses to these types of scenarios and reduce the risk of an error in judgement by a human pilot. A real naval vessel will not be available for testing during this project, so the deck will be emulated with a suitable alternative as discussed in Chapters 2 and 3.

An additional goal of this project is to investigate the use of a total energy control architecture for the flight control system as an alternative to the acceleration based control architecture that has been used in most of the previous projects. The system will be evaluated on its ability to perform general flight manoeuvring as well as keeping the aircraft on the correct glide slope, or trajectory of descent, during the landing phase. The lateral control system will also be refined to increase the aggressiveness for tight waypoint and landing path tracking to compensate for disturbances discovered in previous projects, such as a roll angle bias and the effects of wind flow on the aircraft. These potential improvements should allow for a more safe, consistently accurate and complete landing system for a UAV.

At the end of the project, the author should have much understanding about flight dynamics and the control algorithms applied to aircraft in practice. Also, practical experience will be obtained through research, design, implementation and debugging of such systems, as well as physical flight tests and the procedures around it.

1.3 Previous Research

Before any new project is initiated, research should be undertaken into previous work in the particular field of interest. Not only does this give the researcher an overview of the technological position of the work and more knowledge about the particular field of study, it also indicates where the field needs development or where potential pitfalls are. Knowing this, the project can be directed into a desired and viable direction without duplicating work or replicating previous unfavourable results.

Research was done by looking at both what was achieved inside the ESL by previous postgraduate students, as well as work done globally by other professionals in the aeronautical and control design industry. An overview of previous research relevant to this project is provided in the following sections, grouped into subsections according to the different aspects of this project that they address.

1.3.1 Internal Research

Peddle [4] developed a conventional flight autopilot for a UAV where all aspects from system modelling to flight tests were considered. Off-the-shelf components were used to develop a cheap avionics system. The system was successfully flight tested, with the rapid success attributed to the extensive nonlinear simulations beforehand.

Roos [13] presented a breakdown of the take-off and landing sequences of a UAV in flight, as well as the transition between them as a continuation of the project in [4]. When all phases

are in place, the UAV simply needs to be guided from one phase to the next. In summation, the conventional landing sequence was divided into three main phases:

1. approach, where the aircraft is aligned with the runway and airspeed is reduced while the altitude is gradually decreased;

2. flare, where the sink rate of the aircraft is decreased to allow for a gentle touchdown just above stall speed; and

3. ground roll, where the aircraft translates over the runway until it comes to a halt.

It was found that altitude control is very important during the landing sequence, therefore the system relies on different types of sensors in each phase to ensure accuracy. The system was successfully flight tested, but significant cross-track errors could occur, therefore a large runway was required for a safe landing.

Visser [14] designed a vision-based accurate landing controller for a fixed-wing UAV. By using markers on the runway to aid the position estimation of the vehicle, the goal was to ensure that arrestor cables hooked onto the landing aircraft. An infrared (IR) camera with monovision techniques were used to detect and recognise IR LEDs on the runway to determine the position and orientation of the aircraft. Practical tests showed acceptable lateral tracking, but altitude tracking with the NSA controller was unsatisfactory.

Smit [15] developed a UAV system to land with more precision using a Differential Global Positioning System (DGPS) on a stationary platform. Since a new aircraft was used, the stability derivatives were calculated using Athena Vortex Lattice (AVL) and the inertia using the double pendulum method. The performance was tested in software-in-the-loop (SIL) and hardware-in-the-loop (HIL) simulations and evaluated using Monte Carlo analysis. Five practical landings were achieved, but longitudinal accuracy was not as well as expected due to a bias on the climb rate estimate and the shallow glide slope used for the landing.

Alberts [16] also worked on precision landing of a UAV, but implemented the concept of direct-lift control which uses the flaps to control lift directly, instead of the conventional method where the pitching moment produced by the elevator changes the angle of attack to indirectly control the lift. This concept improved the control of the aircraft altitude and climb rate. Two controllers were designed, where the first was a conventional moment-based controller, and the second a direct-lift-augmented controller. The project demonstrated successful autonomous landings in the presence of both normal and gusty wind conditions. The flight tests also showed that the new direct-lift controller achieved better results in the presence of disturbances.

Various other UAV research projects were also completed at the ESL, but are not of immediate interest for this project as they either used very different approaches, other types of vehicles, or had different end goals. This project uses the same vehicle as the one used by [16], and therefore his project will be considered the immediate predecessor of this one. Similar techniques and strategies will be followed, but with a completely new avionics stack.

1.3.2 External Research

This section provides an overview of previous research relevant to this project performed by other researchers outside of the ESL.

1.3.2.1 Autonomous Landing / Navigation

Cho et al. [17] developed a system for fixed-wing UAVs which could automatically take off, land and taxi on a runway by using only a single-antenna Global Positioning System (GPS) receiver. They implemented DPGS for increased accuracy in position information when performing these manoeuvres. Additionally, the only extra sensor used was the pitot tube to measure airspeed, as accurate airspeed measurements are very important during the landing phase. Linearised equations of motion around the steady state were used to develop linear quadratic regulator controllers for the take-off and landing. Flight tests confirmed that a single-antenna GPS can be used as a main sensor for a backup or for use in low-cost UAVs.

Liu et al. [18] worked on the landing of UAVs on a predefined trajectory with strong robustness under windy conditions. Traditionally, in a longitudinal landing trajectory, the altitude or sink rate is adjusted through the pitch motion controlled by the elevator and the airspeed is stabilised by the throttle. In the lateral, the roll angle is regulated by the aileron, and the yaw motion is controlled by the rudder. To increase performance under wind disturbances, introduction of a fuzzy gain scheduled controller and an adaptive neural network to the automated landing system was used.

López et al. [19] presented a paper on the design of an autonomous landing controller that should be robust against wind disturbances and control the altitude accurately for autonomous landing. They studied and compared the differences between H_∞ and quantitative feedback theory (QFT) techniques during the landing phase. For their landing approach, they used the sideslip technique for their comparisons. They found that controllers designed by both techniques guaranteed robust stability and attenuated high frequency noise due to sensors supplying suitable control signals. The QFT design gave a smoother performance and reduced control effort, but had slightly worse trajectory tracking than the H_∞ design, which indicated the latter as the preferred approach to use during landing.

Masuko et al. [20] opted to use visual feedback in a controller to recognise the landing site for ATOL using a small Linux ARM computer running OpenCV. The main problem with this solution was that the vehicle moved too fast with respect to a stationary landing area, resulting in blurred images taken by the camera which could not be processed fast enough to ensure a safe landing. For a future target, they proposed that a faster image processing method be used to land the UAV safely.

Wang et al. [21] presented a design for a robust longitudinal landing controller for a fixed-wing UAV to track a given trajectory under disturbances. It was based on a mixed H_2/H_∞ method — the H_2 part for excellent dynamic response and the H_∞ part to minimise the effect of disturbances, while the feedback control gain was derived by a linear matrix inequality approach. They also took into account the ground effect and various atmospheric disturbances.

The results showed that the robust controller meets the requirements better than the classical proportional-integral-derivative (PID) controller, but this was only tested in simulation and not in practical flight.

Salfi et al. [22] proposed and implemented control laws for longitudinal and lateral guidance for UAVs up to the touchdown point based on a linearised dynamic model of the aircraft. Glide slope control consisted of speed control and off-glide slope distance control in the pitch axis. They devised a new nonlinear control law in the pitch axis so that the glide slope is maintained during the flare manoeuvre. The ground effect was modelled by an increase in the lift coefficient and a decrease in the induced drag for altitudes less than half the wing span above ground. The controllers were designed for stability margins to show robustness against modelling deficiencies and disturbances. The system was successfully tested in a nonlinear simulation environment, giving nearly zero cross-track error even in the presence of lateral winds with a magnitude of 20% of flight speed.

Singh and Padhi [23] used the nonlinear approach of dynamic inversion for the design of an autonomous landing UAV. This techniques relies on the philosophy of feedback linearisation, where the feedback control structure cancels nonlinearities in the plant in such a way that the closed-loop plant behaves like a stable linear system. The benefit of this technique is that the control structure is simple and easy to implement, however it requires accurate knowledge of the plant dynamics and true estimates of the states, although these problems can be addressed by augmenting the dynamic inversion design with a neuro-adaptive technique and using an extended Kalman filter (EKF) for state estimation. Careful selection of landing trajectory parameters are required since the glide slope and flare path are calculate online, i.e. it is not fixed beforehand. The controller was tested in simulation and showed promising results, but the simulation did not include wind shear and gust effects.

Park et al. [24] presented a new nonlinear guidance logic for trajectory tracking which approximates a proportional-derivative (PD) controller when following a straight line path, but contains anticipatory elements that enable tight tracking on curved paths. This method uses inertial speed in the computation of commanded lateral acceleration and adds adaptive capability to changes in vehicle speed caused by disturbances. Flight tests showed UAVs being controlled within 1.6m root mean square (RMS) cross-track error following circular paths, which was much better compared to traditional linear techniques.

1.3.2.2 Total Energy Control System (TECS)

Bruce [25] compiled a report of the NASA test flight of a heavily modified Boeing B737. In this system, the total kinetic and potential energy were controlled by the throttles, while the energy distribution was controlled by the elevator as in the traditional TECS architecture. During a series of flight tests, the system did not show any instabilities or design problems that required gain adjustments during flight. The performance in all modes was comparable to the simulation results, although a speed tracking error was noted on large altitude changes.

Bruzzini [26] developed a lateral TECS controller for the F-15 Eagle. High order techniques

such as linear quadratic Gaussian, loop transfer recovery and H_2 are not cost effective, and classical procedures on a multi-loop system based on root locus design and single-loop closure methods could lower performance and lead to poor robustness against uncertainties. Bruzzini had access to a numerical optimisation program called SANDY, which was used to calculate optimum controller gains for the control laws. The foundation of the lateral TECS controller is the energy balance between the roll and yaw motions, controlled by the ailerons and rudder respectively, to perform a coordinated turn. The system was tested in simulation and was found to be effective in controlling the lateral motion.

Chudý and Rzucidlo [27] compared designs between a classical "best practice" design and a TECS controller for a Digital Flight Control System (DFCS) based on simulations. In general aviation, the aircraft is primarily flown by a single pilot, so a well-developed DFCS could serve as a virtual co-pilot. Advantages of TECS were excellent performance for a moderate complexity controller and showed to be an ideal candidate for implementation on a general aviation aircraft, although the response is slightly slower than that of the "classical" controller, but with little to no overshoot. It was suggested that further investigation into the nonlinearities and corrupted control data should be conducted.

Dutton [28] developed a longitudinal TECS controller for the F-15 Eagle. Dutton also had access to a numerical optimisation program called SANDY, which was used to calculate optimum controller gains for the control laws. For the linearised dynamics, the closed-loop characteristics were satisfactory for stability, robustness, turbulence rejection and control bandwidth. In the nonlinear model, several differences were observed when compared to the linear model. These included high-frequency elevator-response characteristics, steady state altitude errors, irregular throttle-response characteristics and high steady state throttle values. Despite these issues, the controller was deemed successful with respect to achieving stable command responses in simulation similar to the linear model.

Ji et al. [29] developed a lateral controller utilising bias control and total energy decoupling, where rolling and yawing modes are decoupled and a zero steady state error is achieved. In flight, the roll and yaw motions of the aircraft are closely linked to each other. Therefore, in a coordinated turn, the pilot needs to add rudder to counter the adverse yaw due to aileron deflection and induced drag. Using this principle, the lateral controller was successfully implemented in simulation.

Qingzhen et al. [30] found that it is difficult to match the dynamics of the total energy and energy distribution paths, as recommended for the design of TECS, because the thrust model is much slower than that of the elevator model. If the dynamics are set to be equal, the usually fast elevator response slows down to that of the engine. They proposed improvements to the core TECS algorithm which diminishes the response oscillations caused by the cooperation between aircraft total energy and its distribution. The key to this was a feedback loop based on an energy cooperation error to enhance decoupling performance for the airspeed and flight path angle. Simulations indicated that this proposition can reduce system response oscillations and deliver superior performance.

1.3.2.3 Autonomous Landing using TECS

Akmeliawati and Mareels [31] presented a nonlinear energy-based control method (NEM) based on passivity-based control (PBC) techniques similar to TECS for a twin-engine civil aircraft. The resulting controller was relatively simple and guaranteed the stability and performance robustness. The difference between their technique and TECS was that the nonlinearity of the system dynamics were directly taken into account, where the aircraft dynamics are expressed in Euler-Lagrange equations of motion, derived from the energy equations. The PBC methods consist of the energy shaping stage, where the energy of the system is modified and translated into control forces to achieve the desired trajectory, and the damping injection stage, which ensures that asymptotic stabilisation is achieved. Additional integral control was added to ensure tracking in the presence of disturbances and plant errors. Separation of the short-period and phugoid dynamics were accomplished by using ideas from singular perturbation theory. Disturbance rejection and robustness analysis were performed using Monte Carlo simulations, where the proposed control laws behaved well even under extreme flight conditions.

Akmeliawati and Mareels [32] extended the NEM technique used in [31] by further exploiting the inherent time scales of the dynamics using a singular perturbation technique to simplify the overall design. The aircraft is treated as a single point mass while disregarding the fast pitch and elevator dynamics. In the sense of minimum energy, the best trajectories are found using energy ideas. The resulting controller still does not depend on linearisation or cancellation of system nonlinearities and conforms to the Lyapunov stability criteria. Good stability and performance were achieved during Monte Carlo simulations.

Looye and Joos [33] used multi-objective optimisation to design an autonomous landing controller consisting of stability and command augmentation, speed and flight path tracking, glide slope guidance, and flare functions. The purpose of the multi-objective optimisation is to synthesise the free parameters (gains, filter time constants) in these controller functions by using parameter weighting. An optimisation problem set-up was defined for each controller function and synthesis was sequentially expanded from the inner loops to the simultaneous optimisation of all these functions, accounting for the dynamic interactions between the controller components. The dynamic inversion technique was used in the inner loops of the system, but was found to be very sensitive to modelling errors. The performance criteria was computed from linear and nonlinear analysis, while the robustness was computed from gain and phase margins as well as Monte Carlo simulations. The system was successfully flight tested, however the glide slope and disturbance rejection criteria did not work to full satisfaction.

1.3.2.4 Moving Platforms

Lee et al. [34] described a vision based algorithm for a vertical take-off and landing UAV while tracking and landing on a moving platform. Image-based visual servoing, which is computationally cheaper than other vision-based control algorithms due to less sensitivity to depth estimation, was used to track the platform in two-dimensional image space. The use of image-based landing techniques are proposed since the low resolution of general GPS units are not

sufficient for precision landing. In this method, the vehicle searches for pre-defined features on the landing platform to determine the position and to decide when to reduce throttle to start the landing sequence. An adaptive rule was applied to compensate for the ground effect when nearing the platform. The system was validated with an experimental quad-rotor setup.

Xu et al. [35] proposed an imaged-based scheme to autonomously and precisely land a UAV on a ship in all weather situations by using IR computer vision techniques. It was also stated that landing schemes dependant on GPS and satellites are easily interfered with in a warlike scenario, so a visual solution is preferred. The system uses an IR transmitter on the ship, which is tracked by the aircraft to locate the landing platform. By flying in an Archimedes spiral and using a camera with a large enough field of view, the ship is eventually detected without using a GPS. Experiments showed that the spiral search strategy can make the UAV find the ship reliably under navigation errors.

1.4 Project Integration Overview

As previously stated, the main objective of this project is to successfully and safely land a fixed-wing aircraft onto a moving platform using an automated pilot, specifically using energy principles for the longitudinal controllers and more aggressive lateral controllers. It is therefore evident that many subsystems will need to be designed to achieve this complex goal. This section provides a high-level overview of the system to give a mental picture of what subsystems are involved in the project. A more in-depth discussion of each subsystem will be presented in Chapter 2.

The hardware used in this project consists of several subsystems, each initially developed for separately and then integrated afterwards and reconfigured to work together as a whole over several projects. This simplifies the development of each subsystem so that each one works optimally before merging them to create a complex integrated system. The different subsystems are discussed below, with a diagrammatic overview shown in Figure 1.1.

1.4.1 Vehicle

The airframe used for this project is an off-the-shelf remotely controlled hobbyist Phoenix Trainer 60 model aircraft. It has been modified by engineers in the ESL to better suit the needs of the projects undertaken at the laboratory. The modifications include replacing the main engine to provide more powerful and efficient thrust to energy consumption ratios, as well as replacing the landing gear to withstand more aggressive forces during landing procedures. The main on-board computer (OBC) has also been replaced with equipment and parts more commonly used in the ESL to speed up development and increase familiarity and support for continuing projects, as well as being redesigned over time to be more compact. A photograph of the airframe is shown in Figure 1.2.

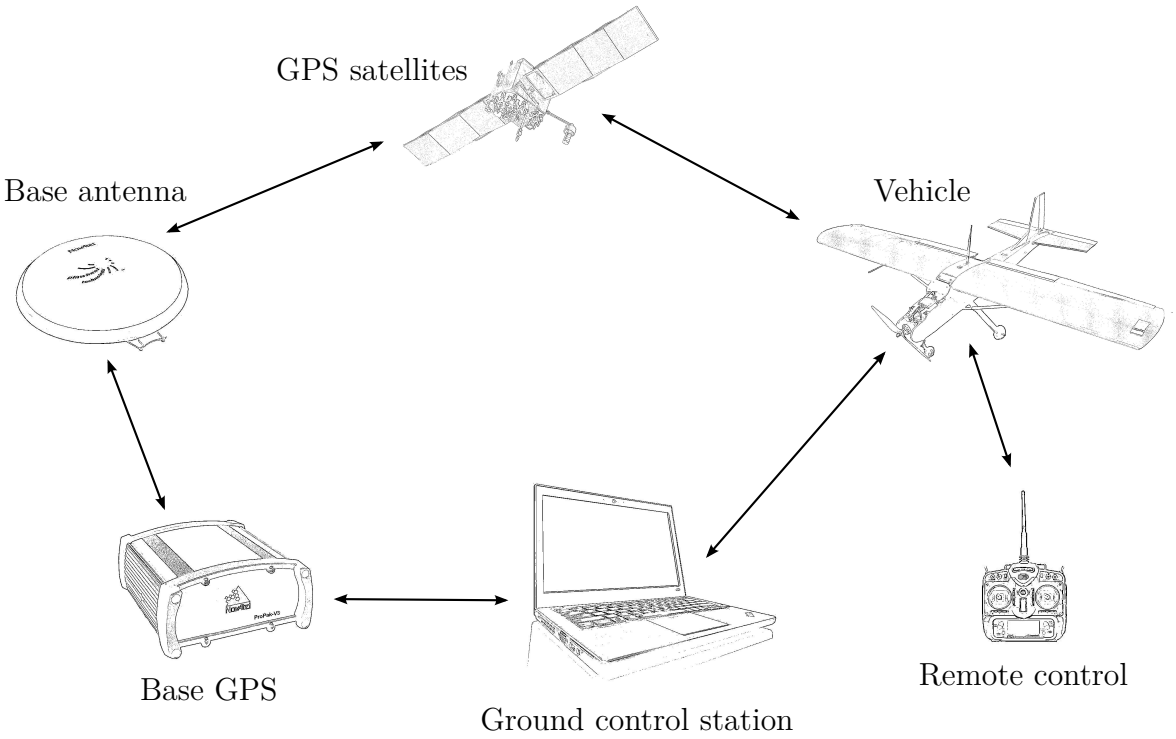

Figure 1.1: System block diagram showing the interactions between the aircraft, GCS, RC, GPS and GPS satellites.

Figure 1.2: The modified Phoenix Trainer 60 airframe used throughout this project.

1.4.2 Ground Control Station

The ground control station (GCS) consists of a regular consumer laptop computer, running custom software designed during previous projects specifically for the hardware used on the various UAV predecessor projects. The GCS connects directly to the DGPS and wireless radio systems to allow for position updates and wireless communication between the GCS and the aircraft. Not only does the ground station receive flight data, it can also be used to dynamically upload new flight paths and commands to the aircraft. This makes the flight test execution more versatile in the sense that if in-flight changes need to be made, they can be done without the need to land the aircraft and reprogram the OBC first.

1.4.3 Moving Platform

Ideally, the intended moving platform for a project such as this would be a full-sized ship out at sea with the real effects of waves and currents acting upon it. Unfortunately, the research environment does not have access to such a platform or anything of similar size that could be used or modified to emulate a real ship deck. However, a real ship is not required for research purposes as a custom platform can be built to serve the same purpose.

The ESL already has such a platform, designed and built in a previous project for emulating the motion of a ship deck for use in rotary-wing autonomous landing projects. In the sense of a fixed-wing landing, this platform is very small and not of the expected rectangular landing shape, nor does it have hydraulic cylinder tethered-arresting equipment required for limited-runway landings as found on a real aircraft carrier. The aircraft will therefore be designed to perform a touch-and-go manoeuvre on the platform during practical flights. The base station of the DGPS will be attached to the platform and set up to provide relative position and velocity information. A photo of the intended platform is shown in Figure 1.3.

1.4.4 Global Positioning System

The GPS can be considered the main sensor used in the project. It can be separated into three components, namely

1. the base station;
2. the rover; and
3. the satellite constellations.

The base station is usually stationary on the ground and the rover is usually attached to the vehicle, both receiving position data directly from the GPS satellite constellations. The two GPS units communicate through the laptop and RF link to compare satellite, positional and velocity information in time. This set-up is called DGPS, and is a significant enhancement over conventional GPS in terms of positional accuracy. For accurate landings, the integrity of position data is critical, which stresses the significance of the reliance on accurate GPS

Figure 1.3: The platform intended for use in this project as a moving landing target.

measurements. In this project, the DGPS is configured into a mode that permits a moving base station as per the objectives stated in Section 1.2. This is a special feature of the hardware used, as DGPS modes normally require the base station to remain stationary.

1.4.5 Remote Control

The remote control (RC) transmitter is a regular off-the-shelf unit that is bound to the specific receiver inside the aircraft. It is used by the safety pilot to perform manual take-off and landing during initial testing, as well as to assume complete control of the vehicle in any failure event. The signals from the remote are read by the OBC to switch between manual and autopilot as required, but the remote will always receive priority over autopilot mode due to safety considerations.

1.4.6 Project Execution

This project is divided into several phases. The first phase consists primarily of research on previous projects to gather information on the different approaches and techniques used, which strategies were successful and which were not, and to familiarise the student with the research field. This is followed by a mathematical modelling phase in which the system is defined in mathematical terms in order to apply control theory to it and to obtain a measure of the physical limits of the system. After mathematical modelling is complete, a design phase follows in which control or mechanical systems are developed and implemented in software. These are then tested in a software simulated environment to ensure that initial expected results are obtained. If this is successful, the software is loaded onto the target hardware and tested

with HIL simulations using the real hardware to ensure correct functioning and to tune the controllers for optimal results. This testing phase is usually very extensive and comprehensive to ensure maximum confidence in the system before practical tests are performed. Finally, when it is fairly certain that the project will succeed in practice, flight tests are scheduled and performed. This implementation-and-test phase resembles the Agile philosophy as the phase progresses, as rapid implementation and testing becomes more feasible with short-term goals and results. These test are then analysed and the project evaluated for its success.

1.5 Thesis Outline

This section explains the layout of this thesis to give a roadmap of how the material will be presented while trying to keep it chronological as the project progressed. This thesis is divided into the following chapters:

- Chapter 1: Gives background on the current UAV developments, both locally and globally. Research objectives are set and an overview of previous research is given, followed by a short project overview. An outline of the thesis is also provided.
- Chapter 2: Gives an overview and explanation of the physical systems that were used for the project. This includes both mechanical and electronic components, computer systems, the moving platform and the airfield.
- Chapter 3: Presents the possible landing scenarios, as well as the landing procedures and state machine that is implemented in this project.
- Chapter 4: Explains the mathematical conventions used to develop the models for the aircraft motion, platform motion and wind disturbances. The detailed mathematics and assumptions are explained.
- Chapter 5: Presents the linearisation of the aircraft dynamic model and provides an analysis of the open-loop dynamics and selected trim conditions.
- Chapter 6: Presents the control architecture and the development of the controllers used, both longitudinal and lateral.
- Chapter 7: Describes the simulation setup and provides the simulation results and the evaluation thereof. Tuning of the system is also presented to give acceptable results.
- Chapter 8: Describes the physical flight setup, assumptions made for virtual landings, and interprets the flight data from the practical tests.
- Chapter 9: Provides a summary of the work done, stating both where the project succeeded and where there is room for improvement. Recommendations are given for future projects using this one as a foundation.

Each section is also accompanied by a chapter breakdown for quick reference, as well as a short summary in conclusion to highlight the most important developments during that phase.

1.6 Summary

This chapter briefly discussed the background of UAVs in South Africa with the scene set for this project inside the ESL, a postgraduate research facility inside Stellenbosch University. Objectives for this project were set in the light of ongoing and completed research, both locally and globally, while this research history was summarily presented. A high-level overview of the system and design phases required for such a project was stated, and the content structure of this thesis was given.

§ 2

System Overview

This chapter provides detail on the different subsystems that comprises the integrated autonomous landing system.

Section 2.1 discusses the physical characteristics of the aircraft used during this project. Section 2.2 details the electronic components installed on the aircraft. Section 2.3 discusses the computer used to communicate with the OBC. Section 2.4 presents the platform intended for use as a landing surface. Section 2.5 describes the airfield where most flight tests are conducted. Section 2.6 provides a summary of the chapter.

2.1 Airframe

The airframe used in this project is an off-the-shelf hobbyist aircraft used specifically for training RC pilots — a Phoenix Trainer 60. Trainer aircraft generally have qualities that make them easier to fly, including [36]:

1. a high wing design where the fuselage hangs below the wings, making the aircraft less likely to topple over after slight perturbations;
2. dihedral wing design where the wings are swept slightly upwards, producing self-correcting behaviour towards straight and level flight after roll angle perturbations;
3. high lift wing foil design where the shape of the wing produces more lift and therefore reduces the stall speed, allowing the aircraft to fly at a lower and safer velocity;
4. tricycle landing gear where the steering is controlled by the nose wheel instead of wheels attached to the rudder, increasing the ease of steering on the runway as the aircraft is less sensitive to remote inputs; and
5. multi-blade propellers to reduce the effective thrust, thereby narrowing the throttle command range which leads to reduced sensitivity to RC inputs.

The original airframe had all of these properties with the exception of the propeller, which was paired with the engine by the choice of the pilot to increase thrust efficiency. Additionally, it

is desirable to use such a vehicle as a testbed because of its balsa and plywood construction, making it sturdy and easy to modify, and its large wing and stabiliser areas, which makes it easy to fly and even more stable in flight. However, the original 3° dihedral wings were replaced with a flat horizontal design so that the OBC could be fit inside the fuselage as close to the centre of gravity (CG) as possible where it would have the minimum effect on the inertia of the aircraft. Any additions made attempted to place the accompanying weight in front of the CG as to not reduce static stability [37]. Due to the additional weight of the various electronic systems added to the aircraft, a more effective two-blade propeller was used so that the maximum control authority was available. These modifications were made during the foundation project with some additional finishing work, resulting in the aircraft as shown in Figure 1.2, standing 375mm high at its canopy, 1400mm in length and 1970mm wide in wingspan, with the CG approximately 255mm high above the ground.

The aircraft is forward-propelled by a Hyperion ZA4025-10 brushless DC electric engine. Use of an electric engine is favoured to a liquid fuel engine mostly due to the fact that it requires less maintenance, produces less vibration, is more efficient, and is generally easier to work with. However, both engine types have a detrimental effect on control if the duration of the flight is extended:

- The electric engine KV-rating, or its RPM/V and therefore thrust potential, is influenced by the voltage of the main battery. During extended duration flight, the voltage of the battery drops, thereby reducing the thrust output for an equivalent driving signal. This is further discussed in Chapter 9.

- The liquid fuel engine consumes its fuel source over the course of the flight which gradually reduces the total mass of the aircraft. This causes the dynamics of the aircraft to change which may have a negative impact on the behaviour of controllers since they are typically designed around a fixed nominal working point if controller gain scheduling is not applied.

The engine is fitted with an APC Electric 15/8e propeller and driven by a Hyperion 90A Opto Programmable BL electronic speed controller (ESC) unit using a Hyperion CXG^3 LiPo 5S / 18.5V 25C 5000mAh battery. The combination of these propulsion components is capable of delivering up to 33N of thrust as tested on a motor test jig.

Manual control of the aircraft is accomplished via a RC transmitter, which for this project is a Spektrum DX-7 bound to an on-board receiver unit. Communication between the receiver and transmitter is in the form of wireless signals around the 2.4GHz frequency band, which is common for modern RC aircraft systems. Instead of passing the received signals directly to the servo motors as in traditional RC systems, it is passed to a custom servo board as discussed in Section 2.2.

The control surfaces are driven by JR Eagle Eservo 381 analogue servo motors, capable of 4.1kg/cm torque and 0.22sec/60° turn rates. A single elevator controls pitching motion, two ailerons with inverted mixing are used to control rolling motion, and a single rudder controls yawing motion. Two flaps are also available, which can be used to directly increase lift or drag,

but are not used in the controller implementations in this project and are instead kept level with the wing airfoil. Finally, a nose wheel, mixed inversely with rudder, controls steering on the ground. The undercarriage and nose wheel were replaced with more durable components since the foundation project due to slight damage caused by excessive use.

2.2 Electronics

The electronic systems used in this project are comprised of many smaller subsystems. Each subsystem will be discussed in the separate sections below, with an illustration of the full system shown in Figure 2.1.

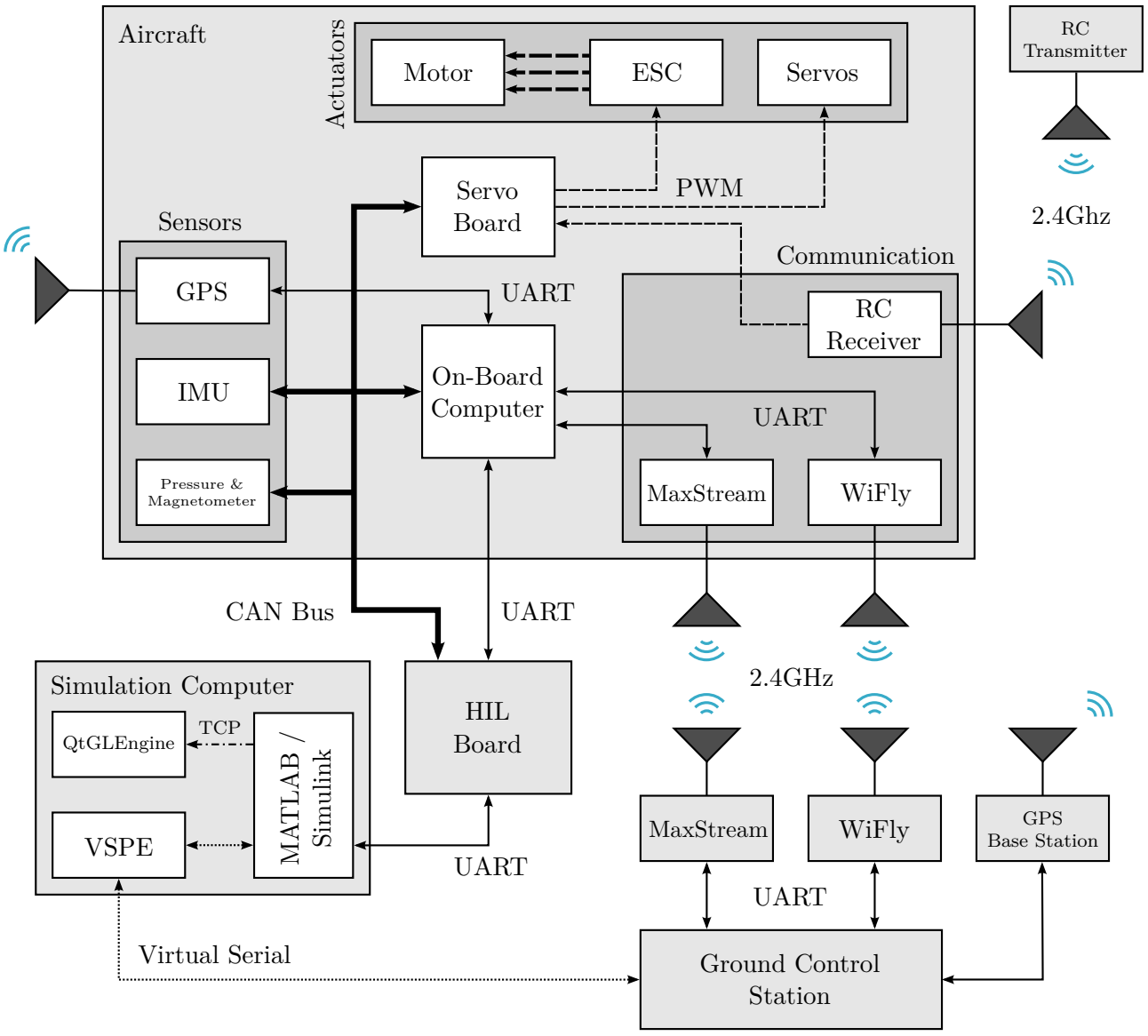

Figure 2.1: Diagrammatic overview of the electronic systems showing the communication between subsystems.

2.2.1 OBC Stack

The OBC is the main computing unit on the aircraft, responsible for all telemetry communication, data logging, control, and decision-making. It consists of many separate printed circuit boards (PCBs), grouped into a single stack, enclosed in a transparent box and placed inside the aircraft fuselage as close to the CG as possible. In previous projects, it was powered by a Hyperion VXG^3 3 cell 11.1V 1100mAh LiPo, but this was replaced by a Gens Ace B-45-2600-3S1P 3 cell 11.1V 2600mAh LiPo for this project. The reason for this upgrade is twofold:

1. Increased battery capacity means that the system could run for a longer period of time without a full restart; and

2. dead weight, which was used to move mass in front of the CG for static stability [37], was replaced by beneficial weight.

Currently at the 3rd revision, the main board consists of two Microchip dsPIC33EP512GP806 micro controller units (MCUs) — one which handles all the telemetry, controller and logging functions and the other which handles communication with the GPS and parsing of GPS packets with the main cycle, and therefore the control cycle, running at 50Hz. The two MCUs can communicate with each other through a universal asynchronous receiver / transmitter (UART) interface. The system continuously logs all relevant data to a SD card, which was upgraded from a Transcend 2GB multi-layer cell (MLC) to an Innodisk 1GB single layer cell (SLC). The advantages of this upgrade were that SLC cards [38]:

1. are about three times as fast as MLC cards;

2. offers up to 10 times the endurance; and

3. has reduced power consumption due to simpler technology.

For the purposes of this project, the primary concern was the rate at which data could be logged. This upgrade showed a significant improvement in logging performance, meaning less occurrences of the control cycle being delayed due to the logging of data.

An Analog Devices ADIS16350AMLZ six-axis inertial measurement unit (IMU) senses all rotational and acceleration rates experienced by the aircraft and is processed by a Microchip dsPIC30F4013 which transmits the data to the main computer by means of a Controller Area Network (CAN) bus interface at a rate of 50Hz. The IMU is mounted to be as close to the CG of the aircraft as possible so that sensor measurements do not require significant further processing to fit the point-mass approximation made in Chapter 4.

Telemetry communication is achieved through a MaxStream 24XStream 2.4GHz 19200 baud wireless module, which is paired with an identical unit connected to the GCS computer and communicates at a rate of 9600 baud. This unit also facilitates the transmission of measurement correction packets between the NovAtel GPS units when operated in Real-Time Kinematic (RTK) mode. Additionally, a Microchip Roving WiFly 2.21RN-131G 802.11 b/g wireless LAN module acts as a wireless serial link and also communicates with a paired unit connected to

the GCS computer. This unit facilitates the transmission of measurement correction packets between the NovAtel GPS units when operated in ALIGN mode. The antennae for the 24XStream and WiFly units were placed on the canopy and between the landing gear, respectively. This is to prevent sections of the aircraft body from obstructing the signal path between the receiver and transmitter, called "shadowing", which can have a negative impact on the range and coverage of the antennae [39].

A Novatel OEMV-1G GPS unit with a GPS-532 Active L1 GPS/GLONASS L-Band antenna acts as the main sensor to feed an EKF to estimate the position of the aircraft at a rate of 10Hz. This unit is capable of running in a DGPS mode, where the main unit receives corrections from a different receiver to increase overall accuracy in positional information. However, this enhancement comes at the cost of more complexity in integration and significantly more data that needs to be transmitted between the two units. The modes to be used, in increasing accuracy, are [40]:

1. single point — a non-differential mode which does not require a base station receiver and provides a RMS accuracy of 1.8m;
2. RTK — which requires a stationary base station receiver for measurement correction and provides a RMS accuracy of 0.45m (pseudo-range differential), 0.20m (L1 Float) or 0.02m (L1 Int); and
3. ALIGN — which does not require the base station to remain stationary to perform measurement corrections and provides the same relative accuracy as RTK mode, although the absolute accuracy remains the same as that of single point mode.

This unit has a special daughter board on the main PCB in order to maintain the required operating voltage as the GPS unit pulls a significant in-rush current during its own start-up sequence.

2.2.2 CANsense Board

The CANsense board is a PCB housed inside the starboard wing and contains a magnetometer, an absolute pressure sensor and a dynamic pressure sensor. It receives power from and communicates through the CAN bus interface. The Honeywell HMC2003T magnetometer is used to sense magnetic fields for attitude estimates. The Motorola MPXA4115A measures absolute air pressure and the Freescale Semiconductor MPXV5004DP measures dynamic air pressure. The absolute pressure sensor can be used to calculate the barometric altitude of the aircraft, and both sensors are used to calculate the airspeed. Since both sensors output analogue data, a Microchip PIC18F458 is used to read the values and transmit them to the OBC for further processing at a rate of 50Hz. The board is purposely placed as far away from the other electrical and mechanical components as possible to reduce electromagnetic interference, which could influence the magnetic fields close to the sensor and cause invalid measurements. This mounting causes the CG to be shifted off the longitudinal centre line of the aircraft, therefore counterweights are attached to the port-side wing to maintain a balanced airframe.

2.2.3 Servo Board

The servo board is used to switch control of the aircraft servo actuators between manual control by the safety pilot and automatic control by the OBC. Like the CANsense board, it also receives power from and communicates through the CAN bus interface. A Microchip dsPIC30F5011 reads the wireless signals from the paired RC transmitter and receiver as well as the controller signals from the OBC, then reroute and mix the signals as outputs to the different servo channels, each driving a different servo motor. The MCU is set up to always allow the RC to override the OBC controller signals, which allows a safety pilot to assume control of the aircraft in the event of failure from the OBC, controller code, or other unforeseen events that could result in damage to the system. Since this board is so critical to the safety of the aircraft, an additional JR Sport 1500mAh 4.8V NiMH battery is connected as a backup.

2.2.4 HIL Board

The HIL board is a separate PCB that facilitates HIL simulations using the real OBC. It is only connected to the system during HIL simulations where its purpose is to relay simulated sensor data from Matlab/Simulink to the OBC and actuator commands from the OBC back to Matlab/Simulink. This is performed in such a fashion that the data values from the physical sensors are substituted by the simulated values, thereby letting the system react in simulation as it would in practice if receiving the same data values from all sources. Data is transmitted from the computer to a Microchip dsPIC30F6014 through a USB/UART connection, which then transmits sensor data to the OBC via the CAN bus and GPS readings to the OBC via a UART connection. Actuator commands are returned to the computer through the same channels and used as inputs to the simulation models in Matlab/Simulink.

This HIL simulation approach largely contributes to the success of flight tests as many software and hardware issues can be identified and resolved before the aircraft even takes off. However, the results are only as reliable as the simulation models and parameters, therefore it remains critical to model the systems as accurately as possible.

2.3 Ground Control Station

The GCS is used to send commands and receive telemetry from the UAV during HIL simulations and flight tests. It also configures and facilitates communication between the DGPS base unit on the ground and the DGPS rover unit on the aircraft. For this project, the GCS is a Lenovo ThinkPad X240 consumer laptop. The GCS software is an in-house developed application based on the Qt4 framework. It receives telemetry information and sends commands via a MaxStream 24XStream 2.4GHz 19200 baud wireless module which is paired with the unit on the aircraft. Communication with the DGPS base station is accomplished via a USB cable as a communications port connection. The majority of the software code base was written in previous projects and was merely updated to suit the requirements of the current project, such

as new references and flag values to the newly implemented controllers.

The NovAtel Propak-V3-L1L2-G with GPS-702-GG antenna were used as the DGPS base station. During set-up, the base station is allowed time to survey where it takes multiple readings over a set period of time and averages them according to their accuracy to obtain a best estimate of the current GPS coordinates for its position. When running in RTK mode, these coordinates are subsequently fixed, and measurement corrections are transmitted to the vehicle to obtain very accurate absolute position information. When running in ALIGN mode, the base station can be moved, and measurement corrections are transmitted to the vehicle to obtain very accurate position information relative to the base station, although absolute position accuracy is reduced to that of single point mode. This trade-off is acceptable for a moving platform landing, as the base station will be attached to the platform, thereby guiding the aircraft according to its relative position.

2.4 Moving Platform

Since a real naval vessel will not be available as a test platform, the practical test platform will be a rigid wire-mesh structure mounted on a trailer, which will be towed with another motor vehicle. The platform is 3000mm in length and 3000mm in width, mounted at a position higher than the towing vehicle to reduce the effect of the following air wake, which could cause increased turbulence and unmodelled effects near landing. The wire-mesh surface also diminishes the ground effect, discussed further in Section 4.3. The DGPS base station is attached to the trailer as the relative distance between the base station and the aircraft is used by the landing controller. A photo of the complete platform is shown in Figure 1.3.

The system has the additional capability of heaving, rolling, and pitching the platform using pneumatic pistons driven by multiple compressors. These features will however not be used as discussed in Section 3.2. Since this project is the first fixed-wing moving platform landing project in the ESL, it aims to be as complete as possible to form a foundation for future projects.

2.5 Airfield

For initial testing of the controllers and virtual platform landings, the system will be flight tested at the Helderberg Radio Flyers Club airfield near Stellenbosch. The field is relatively open, although some obstacles did hinder flight paths and specifically landing trajectories during preceding projects. An autonomous landing is only feasible in a single orientation along the runway, so the landing sequence was adjusted to take these obstacles into account. The real moving platform landing can not take place here as driving a vehicle on the runway is prohibited by the club rules. An aerial view of the airfield is shown in Figure 2.2.

This field is ideal for initial testing as it is located fairly close to development environment. For the final moving platform landing, this airfield will not suffice as the runway is too short, being approximately 150m in length. It was recommended that a larger airfield capable of

Figure 2.2: Satellite view of the Helderberg Radio Flyers Club showing the flyable zone [1].

handling full-size aircraft and motor vehicles be used during the final testing phases of the project. This would not only ensure enough distance for the touch-and-go manoeuvre, but also enough surrounding area in which to perform a go-around if required.

2.6 Summary

This chapter gave an overview of the unmanned aerial system that was used for this project and discussed the details of its different subsystems. The system components included the airframe, the electronic components, GCS, the platform to be used as a landing surface, and the airfield where test flights were conducted. A clear overview of how the different components of the system fit together was presented.

§ 3

Landing Strategy

This chapter gives an overview of the landing strategy that will be used in this project and discusses some key aspects of the landing that must be considered.

Section 3.1 draws comparisons between a real aircraft carrier and the landing attempted in this project to form target specifications. Section 3.2 discusses the various landing scenarios considered. Section 3.3 discusses the landing strategies used by real pilots and how they are adapted to fit the purposes of this project. Section 3.4 provides a summary of the chapter.

3.1 Landing Specifications

This section compares a real aircraft and aircraft carrier to the model aircraft and platform with respect to landing target size and accuracy, travel velocity, and landing conditions to derive a set of specifications for this project.

3.1.1 Accuracy

A typical carrier-based aircraft, such as the McDonnell Douglas F/A-18 Hornet, has a length of 18.5m and a wingspan of 13.68m [41]. On an aircraft carrier flight deck surface, there are four arresting wires spaced 15m apart, with the pilot usually aiming for the third wire. This target reduces the risk of premature contact at the back of the hull or a late landing which increases the chance of an arrest failure [12]. The scaling down of these values to the model aircraft is detailed below, with graphical representations shown in Figures 3.1 and 3.2 for the ship and platform, respectively.

If it is assumed that an acceptable landing would be between the first and fourth wire, therefore one wire-distance before and after the ideal zone, then the scaled down acceptable longitudinal target zone length, normalised to wingspan, can be calculated with

$$\overline{l_f} = \frac{l_f}{b_f} \tag{3.1}$$

where $\overline{l_f}$ and l_f are, respectively, the normalised and the non-normalised longitudinal target zone distances between four arresting cables, and b_f is the full aircraft wingspan. Substituting

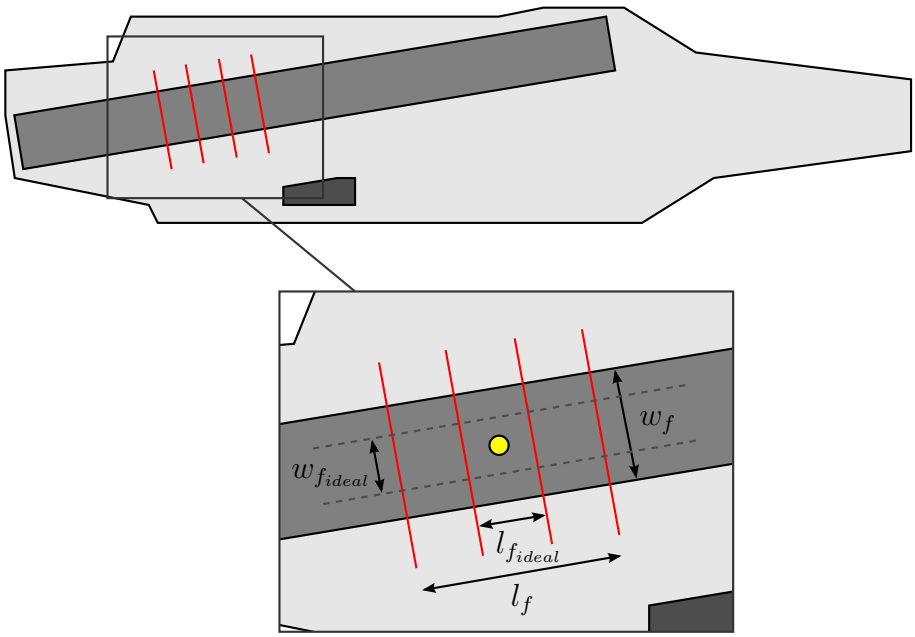

Figure 3.1: Aircraft carrier landing zone dimensions used for scaling to the platform landing zone dimensions.

the values into Equation 3.1 yields

$$\begin{aligned}\overline{l_f} &= \frac{(45.00)}{(13.68)} \\ &= 3.29\end{aligned}$$

If it is assumed that an ideal landing would be between the second and third wire, then the scaled down ideal longitudinal target zone length, normalised to wingspan, can be calculated with

$$\overline{l_{f_{ideal}}} = \frac{l_{f_{ideal}}}{b_f} \tag{3.2}$$

where $\overline{l_{f_{ideal}}}$ and $l_{f_{ideal}}$ are, respectively, the normalised and the non-normalised longitudinal target zone distances between two arresting cables. Substituting the values into Equation 3.2 yields

$$\begin{aligned}\overline{l_{f_{ideal}}} &= \frac{(15.00)}{(13.68)} \\ &= 1.10\end{aligned}$$

The lateral target length should be fairly small to avoid collisions with structures on a real deck, which has a landing width of approximately 80ft, or 24.38m. The maximum acceptable lateral distance can be calculated with

$$w_{f_{ideal}} = w_f - b_f \tag{3.3}$$

where $w_{f_{ideal}}$ is the maximum acceptable lateral distance and w_f is the width of the runway on the flight deck. Substituting the values into Equation 3.3 yields

$$\begin{aligned} w_{f_{ideal}} &= (24.38) - (13.68) \\ &= 10.70 \text{ m} \end{aligned}$$

This can be normalised to wingspan to give

$$\overline{w_{f_{ideal}}} = \frac{w_{f_{ideal}}}{b_f} \tag{3.4}$$

where $\overline{w_{f_{ideal}}}$ and $w_{f_{ideal}}$ are, respectively, the normalised and the non-normalised lateral target zone width. Substituting the values into Equation 3.4 yields

$$\begin{aligned} \overline{w_{f_{ideal}}} &= \frac{(10.70)}{(13.68)} \\ &= 0.78 \end{aligned}$$

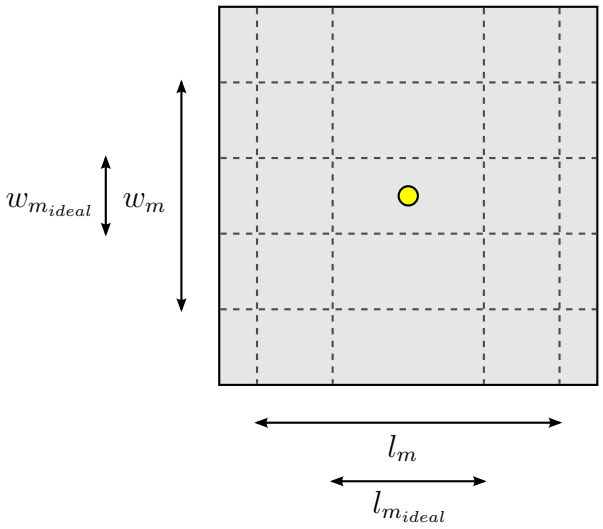

Figure 3.2: Platform landing zone dimensions.

If the normalised values are used as scaling coefficients for the model aircraft, the target lengths become

$$l_m = b_m \overline{l_f} \tag{3.5}$$

$$l_{m_{ideal}} = b_m \overline{l_{f_{ideal}}} \tag{3.6}$$

$$w_m = b_m \overline{w_{f_{ideal}}} \tag{3.7}$$

Substituting the values into Equations 3.5 through 3.7 yield

$$\begin{aligned} l_m &= (1.97)(3.29) \\ &= 6.48 \text{ m} \end{aligned}$$

$$\begin{aligned} l_{m_{ideal}} &= (1.97)(1.10) \\ &= 2.17 \text{ m} \\ w_m &= (1.97)(0.78) \\ &= 1.54 \text{ m} \end{aligned}$$

Because the project goal is to perform an accurate landing, these values are chosen to be further restricted by 50%, which yield target values of

$$\begin{aligned} l_m &= 3.24 \text{ m} \\ l_{m_{ideal}} &= 1.09 \text{ m} \\ w_m &= 0.77 \text{ m} \end{aligned}$$

Furthermore, the platform used in this project is only 3.00m in length and in width. Since the aircraft position as calculated by the estimator is really the position of the OBC, it is important to take the actual contact points of the undercarriage into account so that none of the wheels miss the platform on touchdown. As a safety precaution, the maximum longitudinal and ideal lateral landing distances are reduced to

$$\begin{aligned} l_m &\approx 2.50 \text{ m} \\ w_{m_{ideal}} &\approx 0.39 \text{ m} \end{aligned}$$

where $w_{m_{ideal}}$ is the ideal width for the landing area. The final specifications are summarised as allowable distances from the optimal landing point in Table 3.1. The values are also scaled back to the size of the full aircraft for clearer comparisons of the accuracy that this project attempts to achieve.

Table 3.1: Summary of specifications for the landing accuracy.

Parameter	Allowed Deviation [m]	Normalised by Wingspan	Scaled to Full Aircraft [m]
$l_m/2$	1.25	0.63	8.62
$l_{m_{ideal}}/2$	0.55	0.28	3.83
$w_m/2$	0.39	0.20	2.74
$w_{m_{ideal}}/2$	0.19	0.10	1.37

These values can now be treated as standard deviations to be used for statistical analysis of the landing point accuracy. For an ideal landing, the aircraft longitudinal and lateral touchdown points should, respectively, be within the following deviations

$$\sigma_{lon} = 0.55 \text{ m} \tag{3.8}$$

$$\sigma_{lat} = 0.19 \text{ m} \tag{3.9}$$

3.1.2 Touchdown Velocity

The velocity of the aircraft at the time of touchdown is important to determine the possible impact on the undercarriage. When ignoring effects like damping, this impact is influenced mainly by the sink rate of the aircraft at the moment it makes contact with the platform. In turn, the sink rate is affected by the velocity of the aircraft and its angle of descent, or glide path. This relationship is shown in Figure 3.3. The sink rate can be calculated using simple

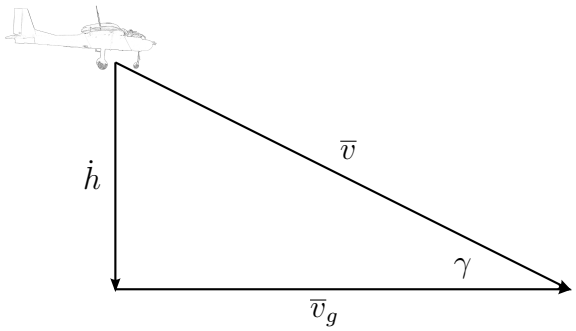

Figure 3.3: Aircraft sink rate for a given velocity and glide path.

trigonometry as

$$\dot{h} = \overline{v}\sin(\gamma) \tag{3.10}$$

where $\dot{h}$ is the climb rate, $\overline{v}$ is the velocity and γ is the glide path angle. Aircraft generally follow a glide path of between 2° and 4° when approaching for landing. For this project, the glide path was chosen to be $\gamma = 3.5°$ and the landing velocity as $\overline{v} = 18$ m/s. Substituting the values into Equation 3.10 yields

$$\begin{aligned}\dot{h} &= (18)\sin(-3.5°)\\ &= -1.0989 \ \text{ m/s}\end{aligned}$$

When determining if this is a safe sink rate for the model aircraft to land at, it can simply be dropped from an altitude that would cause it to impact the ground at the desired velocity. This can be calculated in two ways. Using the conservation of energy method, it can be shown that

$$mgh - \frac{1}{2}m\overline{v}^2 = 0 \tag{3.11}$$

where m is the mass of the aircraft, g is the gravitational constant, h is the altitude that the aircraft will be released from, and $\overline{v}$ is the aircraft velocity on impact. Substituting the values into Equation 3.11 yields

$$\begin{aligned}(6.11)(9.81)h - \frac{1}{2}(6.11)(-1.0989)^2 &= 0\\ h &= 0.0615 \text{ m}\end{aligned}$$

This can also be shown with the equations of motion and integration over time as

$$\ddot{h} = -g \tag{3.12}$$

$$\dot{h} = \overline{v}_0 - gt \tag{3.13}$$

$$h = h_0 - \overline{v}_0 t - \frac{1}{2}gt^2 \tag{3.14}$$

where $\ddot{h}$ is the acceleration in altitude, $\overline{v}_0$ is the initial velocity, h_0 is the initial altitude and t is the time. Substituting the values into Equations 3.13 and 3.14 yield

$$\begin{aligned} -1.0989 &= (0) - (9.81)t \\ t &= 0.112 \text{ s} \\ (0) &= h_0 - (0)(0.112) - \frac{1}{2}(9.81)(0.112)^2 \\ h_0 &= 0.0615 \text{ m} \end{aligned} \tag{3.15}$$

Both methods calculate that the aircraft can be released from an altitude of 6.15cm to reach a velocity of 1.0989m/s upon impact with the ground. This test was performed and regarded as safe for the model aircraft.

Aircraft carriers, such as the Nimitz class USS Theodore Roosevelt (CVN 71), can cruise at speeds of 56km/h [42] with an aircraft landing at 241km/h [12]. The trim airspeed of the model aircraft is set to be 18m/s, or 65km/h, which is significantly above stall speed, but preserves enough control authority to reject wind disturbances. However, at this speed, it will take a significant amount of time, and therefore distance, for the aircraft to reach the platform when both are travelling with the same heading direction. Since an aircraft travels at a much faster velocity than the ship that it is landing on, the platform speed will be reduced to 10m/s, or 36km/h, which would allow the aircraft to reach the platform over a distance short enough to be feasible for practical testing. This speed remains fast enough for the GPS to give reliable velocity and heading updates, as a slow movement speed causes measurement noise to become significant in the calculation of numerical derivatives, resulting in random spikes.

The ratio of aircraft speed over the speed of the intended landing surface can be calculated by the equations

$$\overline{v}_{rf} = \frac{\overline{v}_{acf}}{\overline{v}_{ship}} \tag{3.16}$$

$$\overline{v}_{rm} = \frac{\overline{v}_{acm}}{\overline{v}_{platform}} \tag{3.17}$$

where $\overline{v}_{rf}$ and $\overline{v}_{rm}$ are, respectively, the landing velocity ratios of the full and model aircraft, $\overline{v}_{acf}$ and $\overline{v}_{acm}$ are, respectively, the landing velocities of the full and model aircraft, and $\overline{v}_{ship}$ and $\overline{v}_{platform}$ are, respectively, the velocities of an aircraft carrier and the moving platform used

in this project. Substituting the values into Equations 3.16 and 3.17 yield

$$\begin{aligned} \overline{v}_{rf} &= \frac{(241)}{(56)} \\ &= 4.30 \\ \overline{v}_{rm} &= \frac{(65)}{(36)} \\ &= 1.81 \end{aligned} \tag{3.18}$$

From these ratios, it can be seen that the aircraft in this project attempts to land onto a platform moving at a significantly faster velocity in comparison with a fighter jet and aircraft carrier scenario. A faster aircraft landing speed is however not achievable with the current model aircraft. Additionally, landing at faster velocities can cause damage to the undercarriage. For the purposes of this project, the platform speed of 36km/h is deemed challenging enough for proof of concept.

3.1.3 Environmental Conditions

Whenever possible, real aircraft take off and land into a headwind. This incoming airflow increases the lift generated which allows the aircraft to take off earlier, as well as reducing the distance required to come to a halt when landing. For carrier-based operations, the reduced landing distance is not important as the aircraft is stopped by the arresting system. However, the additional lift it provides is critical to allow for a quicker take off, and also provides a safety margin in the event that the arresting system fails to capture the aircraft and it needs to take off again to do a go-around for another attempt.

In the real-life scenario, the environmental conditions cannot be controlled and a landing in unfavourable conditions is inevitable. Therefore, the aircraft in this project will be subjected to several wind conditions in simulations to increase confidence in the system and to evaluate its ability to reject such disturbances. The following scenarios will be simulated:

1. no wind;
2. headwinds;
3. tailwinds;
4. port side winds; and
5. starboard side winds.

Additionally, whenever winds are simulated, the following effects will be added:

1. turbulence, the chaotic flow of air, simulated under “light” severity; and

2. shear, the increase of wind magnitude as the aircraft gains altitude, at 3.6m/s for trim flight and 2.7m/s for landings at an altitude of 6m.

The wind models will be discussed in more detail in Section 4.4. These wind speed values are chosen to provide the maximum tolerable disturbance while not exceeding the acceptable risk levels for the safety pilot and therefore the project. The ratio of maximum wind disturbance to landing flight speed can be calculated by

$$\overline{\overline{v}_{wm}} = \frac{\overline{v}_{wm}}{\overline{v}_{acm}} \tag{3.19}$$

where $\overline{\overline{v}_{wm}}$ is the ratio of landing flight to wind speed and $\overline{v}_{wm}$ is the maximum wind speed that the model aircraft will be subjected to as measured at an altitude of 6m. Substituting the values into Equation 3.19 yields

$$\begin{aligned}\overline{\overline{v}_{wm}} &= \frac{(2.7)}{(18)} \\ &= 0.15\end{aligned}$$

showing that the wind is 15% of landing flight speed. Using this as a scaling coefficient, the wind on the full aircraft can be calculated by

$$\overline{v}_{wf} = \overline{\overline{v}_{wf}}\overline{v}_{acf} \tag{3.20}$$

where $\overline{v}_{wf}$ is the maximum wind speed that the full aircraft will be subjected to as measured at an altitude of 6m and $\overline{v}_{acf}$ is the landing speed of the full aircraft. Substituting the values into Equation 3.20 yields

$$\begin{aligned}\overline{v}_{wf} &= (0.15)(241) \\ &= 36.15 \text{ km/h}\end{aligned}$$

This wind speed is representative of what could be expected for a full scale aircraft. However, when moving further off-shore, this value may under-represent the actual severity. For the purposes of this project, a maximum wind disturbance of 2.7m/s measured at an altitude of 6m is deemed acceptable for proof of concept.

3.2 Landing Scenarios

This section discuss the various scenarios of platform movement which the aircraft may need to compensate for when performing a landing on the flight deck of a ship. Each type of movement considered will be explained and its applicability to this project discussed. Inertial directions and attitudes referred to in this section conforms to the mathematical model described in Chapter 4.

3.2.1 Stationary

This occurs when the platform is completely stationary, therefore not moving in any direction or changing its attitude, which is exactly as landing on a regular runway. This scenario is included for consideration not only for the sake of completeness, but also since the platform may be very close to being stationary. Additionally, it is good practice to first test the control and navigation systems in a simpler scenario to verify correct behaviour. For this project, this was the first type of landing considered, and also aimed to be performed practically.

3.2.2 Translation

Linear horizontal movement, called translation, is the most simple and dominant motion of the platform, occurring when the ship is sailing under its own power and/or when driven by ocean currents. When subjected to this type of motion, the whole landing platform moves in any one or a combination of compass directions, but does not change its altitude or attitude, thereby changing only the GPS longitude and latitude touchdown coordinates. A positive longitudinal translation is defined as movement in the North direction, while positive lateral translation is defined as movement in the East direction. For this project, this was the primary type of motion considered, and also aimed to be performed practically.

3.2.3 Heaving

Linear vertical movement, called heaving, is mathematically similar to translation, but instead the platform moves in an upwards and downwards fashion, thereby changing only the altitude of the touchdown coordinates. Positive heaving motion is defined as movement in a downwards direction, while upwards is negative. Landing on such a platform would require more complicated estimation techniques, which would greatly broaden the scope of the project. It was therefore decided to not look into this type of platform motion so that the focus could be on controller design instead of rigorous estimation.

3.2.4 Pitching & Rolling

Pitching occurs when two ends in the line of motion of the platform are at different altitudes. When the closest end of the platform to the aircraft approach point is lower than the distant point, it is defined as a positive pitch angle. Rolling occurs when two ends across the line of motion of the platform are at different altitudes. When the starboard edge of the platform is lower than the port edge, it is defined as a positive roll angle. Landing on such a platform would require more complicated estimation techniques, which would greatly broaden the scope of the project. It was therefore decided to not look into this type of platform motion so that the focus could be on controller design instead of rigorous estimation.

3.2.5 Yawing

Yawing motion occurs when the platform sways in such a fashion that all ends remain at the same altitude, but the orientation revolves around the centre of the platform, therefore changing compass direction. This motion affects the entry point of the landing leg of the aircraft as it must land in the same heading orientation as the platform to be correctly aligned with the runway. For this project, it is assumed that this effect will be small and approximately in line with the velocity heading of the platform. The aircraft should however be able to compensate for it as it is unavoidable during practical flight tests. The GPS heading will be continuously uploaded from the ground station when the platform is moving above a minimum velocity to allow the aircraft to update its heading during landings.

3.3 Landing Procedure

This section describes the conventional strategies for landing an aircraft, as well as how they are modified to fit the requirements of this project. The circuitry flown prior to landing is explained, after which the actual landing trajectory is examined and modified to be practically feasible. Finally, the state machine design is presented to illustrate how the aircraft will be guided onto the runway.

3.3.1 Landing Circuit & Trajectory

During development of a landing strategy for an autonomous vehicle, it is useful to look at the procedures that the pilot of a real, full-sized aircraft would perform for such a manoeuvre. The following sections discuss the real procedure as well as the modified procedures investigated for this project.

3.3.1.1 Standard Aircraft Landing Procedure

A standard landing procedure is presented in [43], which consists of several phases followed successively from flight until standstill. This strategy is for a normal situation, defined as conditions where engine power is available, a light headwind acts on the aircraft, the final path is unobstructed from obstacles, and the landing surface is of sufficient length to bring the aircraft to a gradual stop. An illustration of this is shown in Figures 3.4 and 3.5 where the phases are broken up as follow:

Base leg As the last perpendicular leg to the centre line extension of the runway, it must be chosen with sufficient altitude and distance from the touchdown point to allow for a gradual descent, taking into account the effects of wind and usage of flaps. Velocity should be reduced to about 1.4 times that of stall speed. As a normal landing is performed with a headwind, the aircraft will likely experience a crosswind during this phase which should be compensated for by flying at an angle to prevent drifting. This leg should be continued up to a point

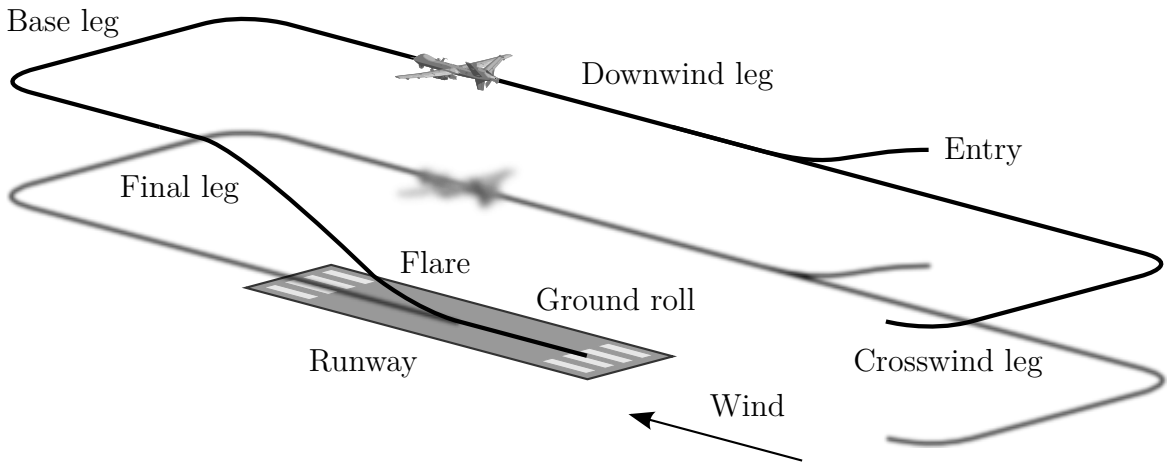

Figure 3.4: Standard landing flight circuit.

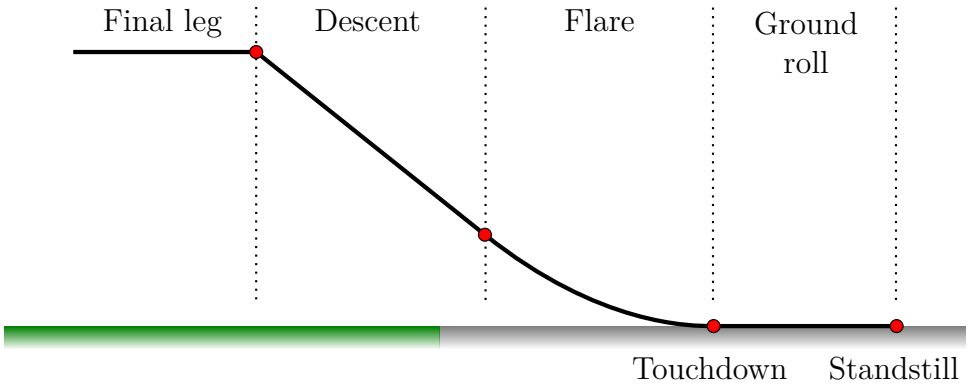

Figure 3.5: Standard landing profile.

where a shallow banked turn could be performed to align the aircraft with the runway, holding sufficient altitude to stay clear of any obstructions along the ground track. Shallow banking is recommended, as the stall speed increases with high roll angles.

Final approach As the leg aligned with the runway, the aircraft trajectory should continuously be kept in line with the centre line extension of the runway. The final flap settings should be applied and angle of pitch adjusted as required for the desired rate of descent, while slight adjustments may be required to keep the desired descent attitude. A velocity of 1.3 times that of stall speed is recommended and the aircraft should be retrimmed to relieve pressure held on the controls. The angle of descent should be controlled as to guide the aircraft to land at the point one third into the runway. The objective of the final approach is to descend at such a rate that the aircraft is in a near-stall state just before touchdown, which requires accurate control of descent angle and airspeed.

Flare The flare manoeuvre allows for a smooth transition of the aircraft from descending at a shallow glide slope above the runway during its final stages to a gentle touchdown. During this phase, the nose of the aircraft is lifted slightly to increase the angle of attack and therefore the lift, which decreases the rate of descent. Normally, power is reduced to idle which gradually

lowers the airspeed and subsequently reduces lift. This balance should be controlled to achieve a proper landing attitude and airspeed upon touchdown.

Touchdown A gentle settling on the landing surface is the core of the touchdown phase. The engine power should be at idle and the aircraft at the minimum controllable speed with the landing gear making contact with the surface at approximately stall speed. The aircraft should never be forced into the ground as this results in erroneous or even dangerous landing attitude. A positive angle of attack should be maintained for aerodynamic braking and holding the nose wheel off the ground to allow it to gently settle onto the runway. Important is precise longitudinal alignment of the aircraft with its velocity vector to negate any side loads on the landing gear.

Ground roll While the aircraft is still moving on the runway, the pilot must stay vigilant and control the aircraft. Directional control difficulties are common due to friction forces on the wheels by the landing surface. Centrifugal forces during large ground turns could cause the aircraft to tip over or even collapse the landing gear. If the aircraft is at high speed, the rudder can be used to steer while the speed slows down, after which a steerable nose wheel provides better directional control. Brakes can also be applied to increase the rate of reduction in speed while the ailerons are used to keep the wings level. If the runway length permits, the aircraft should be allowed to stop naturally due to friction on the wheels, body and control surfaces.

Go-arounds If at any time during the landing sequence abnormal attitude, speeds or other conditions are experienced, the landing should be aborted and the aircraft flown back into the circuit around the runway for another attempt.

3.3.1.2 Modified Aircraft Landing Procedure

The aircraft used for this project was not a full scale and highly advanced aircraft, but rather a small cost-effective model aircraft equipped with the necessary electronics to convert it into a functional UAV. Furthermore, the goal is to land on a moving platform rather than a stationary runway. In light of this, some modifications to the landing scheme are required to increase touchdown point accuracy and to create a landing scenario more representative of a moving deck of a naval vessel. An initial modified approach was implemented to compensate for possible obstructions during the final stages of landing by using two sequential glide slopes. This approach is presented below, with illustrative Figures 3.6 and 3.7 for clarity. It was designed according to slightly modified specifications of the previous project, with the aircraft flying at 16m/s and an obstacle located 200m before the runway, standing approximately 20m high.

The values of the landing parameters are calculated based on the touchdown point. The relationship between the altitude, longitudinal distance and glide slope for the first descent and

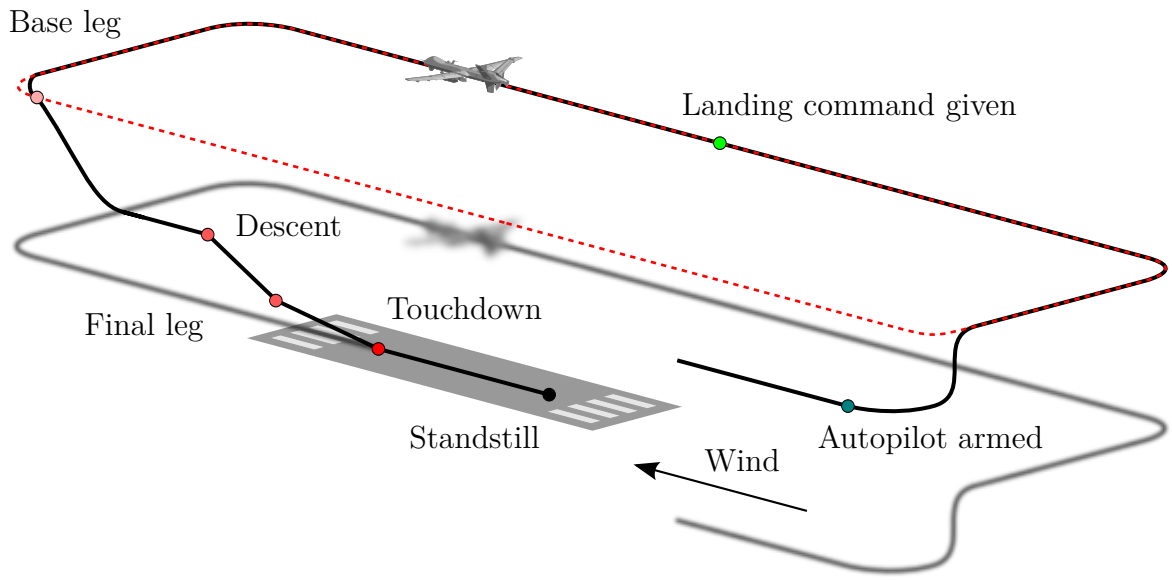

Figure 3.6: Modified landing flight circuit.

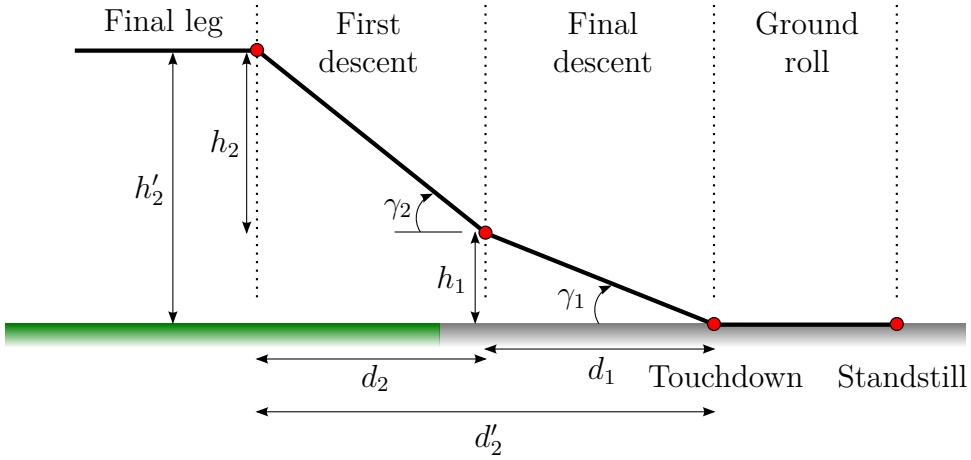

Figure 3.7: Modified landing profile with two sequential glide slopes.

final descent phases are calculated as

$$\tan(\gamma_1) = \frac{h_1}{d_1} \tag{3.21}$$

$$\tan(\gamma_2) = \frac{h_2}{d_2} \tag{3.22}$$

where γ_η is the glide path angle, h_η is the altitude and d_η is the longitudinal distance for each phase. The total altitude and distance are simply calculated as

$$h_2' = h_1 + h_2 \tag{3.23}$$

$$d_2' = d_1 + d_2 \tag{3.24}$$

where h_2' and d_2' are the total altitude and longitudinal distances, respectively. The real piloted scenario landing angle of 3° can be considered as the ideal angle. The aircraft should be given enough time to settle on this glide slope, chosen as about 6s assuming a shallow angle.

Substituting these values into the rearranged equations yield the following:

$$
\begin{aligned}
d_1 &= \overline{v}t \qquad (3.25)\\
&= (16)(6)\\
&= 96 \text{ m}\\
h_1 &= d_1 \tan(\gamma_1)\\
&= (96)\tan(3^\circ)\\
&= 5.031 \text{ m}\\
h_2 &= h_2' - h_1\\
&= (20) - (5.031)\\
&= 14.969 \text{ m}\\
d_2 &= d_2' - d_1\\
&= (200) - (96)\\
&= 104 \text{ m}\\
\gamma_2 &= \arctan\left(\frac{h_2}{d_2}\right)\\
&= \arctan\left(\frac{(14.969)}{(104)}\right)\\
&= 8.191^\circ
\end{aligned}
$$

The phases can now be broken up as follow:

Base leg The base leg is chosen at a distance of 300m from the touchdown point and at an altitude of 20m, which was confirmed in simulation to be safe for the landing of this specific aircraft. Because of obstructions between the runway approach point and base leg, the aircraft altitude must be kept at 20m until 200 m before the touchdown point. The landing speed was chosen as 16m/s, which is sufficiently higher than the stall speed of the aircraft as experimentally determined in manual flight. Aggressive but limited lateral control will be applied to control the aircraft onto the ground track. The base leg of the circuit is fixed to one side of the runway, as the other side is too hazardous due to physical obstructions.

First descent During this phase, a high negative flight path angle will be followed to rapidly reduce the altitude after clearing the obstruction before the runway. The aircraft will be kept aligned with the runway while still using aggressive lateral control to ensure fast regulation of cross-track errors. Unlike the standard landing procedure presented in [43], the airspeed will be kept constant during the entire approach.

Final descent When the aircraft is 96m from the touchdown point, its flight path angle is corrected to ensure the proper sink rate for a safe landing. Lateral control is relaxed to ensure no aggressive banking that might cause the wings to strike the runway. The rapid change in flight path angle causes the nose to lift, having effects similar to the standard landing procedure. Airspeed and attitude must be maintained during this phase. For aircraft carrier landings, the flare manoeuvre is omitted to increase touchdown point accuracy, referred to as a "controlled crash". This project will also omit the flare manoeuvre to keep the landing procedure for the subscale aircraft similar to the standard landing procedure for the full scale aircraft.

Touchdown Since the flare manoeuvre is omitted, the sink rate must be controlled well while airspeed is maintained until the aircraft touches down onto the runway. The wings are kept level to minimise the chance of one of the wings striking the runway.

Ground roll When a touchdown is detected, the autonomous landing is considered complete and control will be given back to the manual pilot, who will bring the aircraft to a halt. For a real carrier deck scenario, an arresting system will force the aircraft to stop.

Go-arounds If at any time during the landing sequence abnormal attitude, speeds or other conditions are experienced, the landing is to be aborted and the aircraft flown back in the circuit around the runway for renewed attempt. The relevant states are continuously evaluated against predetermined safe values during the landing phase, which causes an error to be raised when an unsafe state is entered.

In simulation, it was found that the longitudinal control system was unable to maintain the airspeed of 16m/s and flight path angle of -8.2° commanded for the first steep glide slope. The behaviour under these commands is discussed in more detail in Section 5.3. The control system settled to an undesired steady state, which saturated as the glide slope became steeper. Additionally, the second glide slope proved to negatively affect the settling time of the controllers, thereby reducing the landing accuracy. At this point, the approach of using a steep glide slope followed by a shallower glide slope was reconsidered. It was also practically observed that the runway obstruction for stationary landings could be avoided and that flying at an increased airspeed will improve the natural stability of the aircraft by it aligning its velocity vector into incoming airflow. It was therefore decided to merge the two sequential glide slopes into a single glide slope which more closely resembles the standard landing procedure. The aircraft could now also be put on this glide slope at an earlier point, allowing more time for it to reach a trim settling value. The single glide slope approach is shown in Figure 3.8. The glide slope angle is calculated with

$$\tan(\gamma_1) = \frac{h_1}{d_1} \tag{3.26}$$

The landing controller was also modified to adapt the starting point of the glide slope based on

the altitude command during flight which increases the versatility of the system. The distance from the touchdown point where the glide slope should start is calculated with

$$d_1 = \frac{h_1}{\tan(\gamma_1)} \tag{3.27}$$

The ideal steady state values for the landing was chosen and substituted into Equation 3.27, with the glide slope chosen slightly higher as 3.5° to increase landing accuracy [15]. The starting point of the glide slope can now be calculated as

$$\begin{aligned} d_1 &= \frac{(20)}{\tan(3.5°)} \\ &= 327.00 \text{ m} \end{aligned}$$

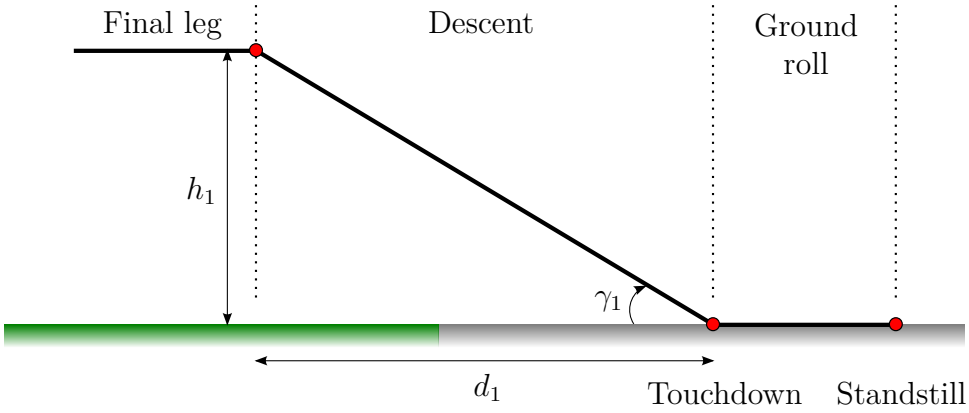

Figure 3.8: Modified landing profile with a single glide slope.

3.3.2 Landing State Machine

The autonomous landing sequence is executed by a state machine, a set of rules and conditions that guides the aircraft from one phase to the next. This section presents the state machine parameters and sequence used to guide the aircraft from the air onto the ground safely. The state machine, diagrammatically illustrated in Figure 3.9, is broken up into phases representing the landing circuit shown in Section 3.3.1.2. The states are implemented as follow:

State X: Although not truly a state within the state machine, a global override is available at any moment to deactivate any and all autonomous behaviour of the aircraft. This is a safety setting to allow the aircraft to be flown by only the safety pilot in a failure event.

State 0: Manual pilot This state, considered as the initial state, allows the safety pilot to give commands to the aircraft without the control system interfering, even though controller code may execute. This is useful to do testing of flight parameters, verifying flight conditions, or even backing out of a hazardous situation with increased versatility. This state evaluates the

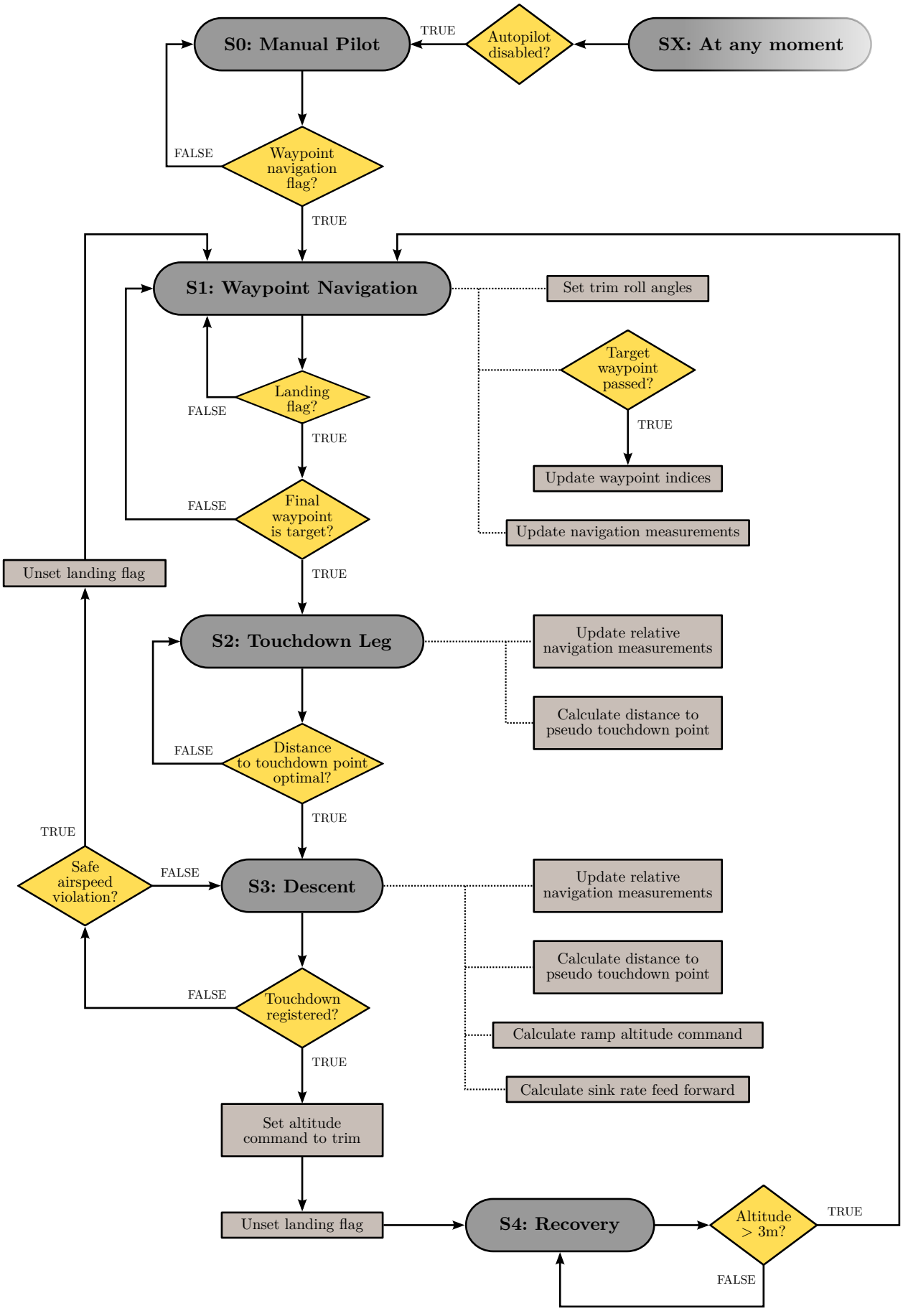

Figure 3.9: Landing state machine showing the transitions between the navigation and landing phases.

status of the waypoint navigation flag to see if the system has been requested to be navigated by the autopilot.

State 1: Waypoint Navigation This state lets the aircraft follow a set circuit of dynamically editable waypoints around the airfield. During this state, the roll angle controller limits are set to allow greater bank angles to be used during general flight. The position of the aircraft is continuously evaluated against the position of the target waypoint to check if the waypoint has been reached. If the target waypoint has been reached, it is changed to the next waypoint in the navigation list. The cross-track error and cross-track error rate are also continuously updated to be used as feedback variables by the lateral control laws. The status of the landing flag is also continuously polled to check whether an autonomous landing has been requested. If an autonomous landing has been requested, the state machine continuously checks whether the previous and next waypoints are those located over the runway. When this is the case, the landing controllers are activated.

State 2: Touchdown Leg In this state, the aircraft aligns itself with the platform to ensure a landing from the rear end of the platform, called the stern side, is attempted. This is achieved by generating a pair of waypoints 1000m before and 1000m beyond the current coordinates of the platform, using the current heading of the platform as the heading angle of the ground track between the two waypoints. This creates the ground track that the aircraft should follow until touchdown. The heading angle of the platform is continuously uploaded from the GCS to the OBC, but is filtered to reduce the variations in the positions of the waypoints generated based on the varying heading angle. A first-order low-pass filter with a time constant of 0.25s was implemented. The filter cut-off frequency was chosen to be high enough to allow the actual platform heading rate to pass through and low enough to suppress the heading measurement noise. The filter performance was verified in a simple simulation. Additionally, the platform heading angle is only uploaded when the platform moves faster than 10km/h due to the fact that the GPS heading angle becomes undefined when the platform is stationary, and becomes very noisy when the platform moves too slowly.

To accommodate a moving platform landing, the stationary landing system uses a simple projected touchdown point technique as complex estimation techniques are outside the scope of this project. The pseudo-landing point approach is shown in Figure 3.10. If it is assumed that a shallow glide path is used for the landing and that the flight path angle is therefore close to zero, the horizontal component of the aircraft speed is approximately equal to the magnitude of the aircraft speed. For the aircraft and the platform the reach the same point, they both need to cover the same distance as described by

$$d_{ap} + \overline{v}_p \Delta t = \overline{v}_a \Delta t \tag{3.28}$$

where d_{ap} is the distance between the aircraft and the platform at a given time instant, $\overline{v}_p$ is the velocity of the platform, $\overline{v}_a$ is the velocity of the aircraft, and Δt is the time until the touchdown

point is reached from the current time instant. The relative distance and velocity between the aircraft and the platform is provided by the DGPS base station relative East-North-Up (ENU) vector in ALIGN mode. Since both the aircraft and the platform need to cover this distance

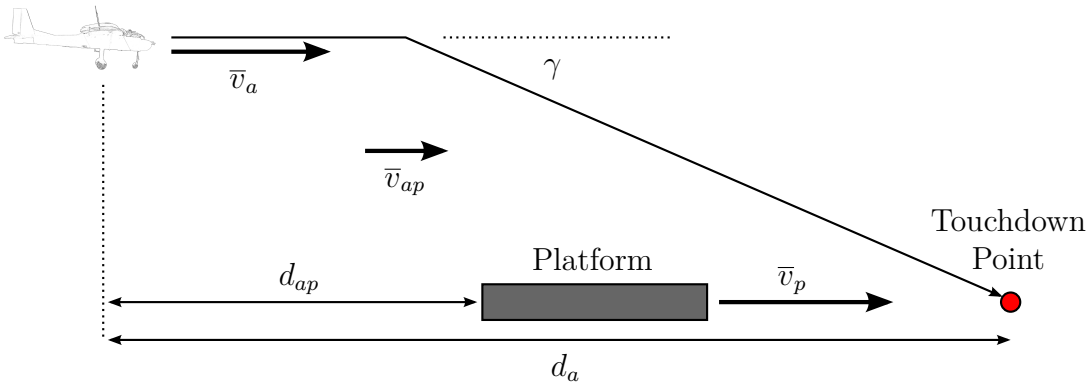

Figure 3.10: Estimation of the platform position at the time of touchdown.

in the same amount of time, Equation 3.28 can be rearranged to make Δt the subject of the equation

$$\Delta t = \frac{d_{ap}}{\overline{v}_a - \overline{v}_p} \tag{3.29}$$

The remaining distance that the aircraft has to cover to reach the landing point can now be calculated by

$$d_a = \overline{v}_a \Delta t \tag{3.30}$$

In the touchdown leg state, the value of d_a is continuously calculated and compared to the distance from the touchdown point at which the descent should commence based on the current altitude and desired glide slope for the descent. When the distance to the projected touchdown point is equal to the distance at which the descent should commence, the state machine advances to the descent state. The aircraft is assumed to immediately transition onto the desired glide slope without any transients. The online calculation of the distance to the projected touchdown point and the distance at which to commence the descent based on the current altitude and the desired landing glide slope angle makes the system more flexible and safer to test.

State 3: Descent When the distance to the projected touchdown point at which the descent should commence is reached, the aircraft transitions onto the glide slope while maintaining a constant airspeed of 18m/s. As in the previous state, the aircraft follows the ground track segment between the generated waypoint pair, allowing for yaw compensation as the platform changes in heading. The distance to the projected touchdown point at the current time instant is used to calculate the altitude reference at the same time instant. As the aircraft approaches

the projected touchdown point, the altitude reference is continuously reduced, thereby creating a negative ramp reference signal. The absolute distance to the projected touchdown point is used, which assumes that the cross-track error has been regulated to zero by the time that the aircraft touches down. This assumption also provides a safety factor as a zero altitude reference will not be commanded while the cross-track error is large.

To ensure that the aircraft touches down at the correct sink rate, a feed-forward climb rate command is superimposed onto the climb rate commanded by the altitude controller. This mimics the behaviour of a real pilot when landing on a ship, as the aircraft is gently forced down onto the deck, thereby performing a "controlled crash", ensuring that the aircraft touches down and does not "coast" parallel to the deck.

The airspeed is continuously polled and verified to be within a safety factor to prevent landing at a speed that is too high which could damage the undercarriage, and to prevent the aircraft from landing at a speed that is too close to the stall speed which would be unsafe in the event that the safety pilot must assume control. These speed deviations will be caused primarily due to wind effects, but may also be caused due to abnormal attitude behaviour. In such an event, the system disables the landing flag and returns to waypoint navigation mode.

Finally, the normal specific acceleration measurement is continuously polled to check for a large negative acceleration spike which would indicate that the aircraft has touched down. For this project, the threshold for the acceleration spike was determined experimentally from flight data and set to $-2g$. The threshold was chosen to be higher than the maximum acceleration magnitude experienced by the aircraft in normal flight due to turbulence, and lower than the minimum acceleration magnitude experienced by the aircraft on touchdown.

After a touchdown is detected, the state machine would normally advance to the ground roll state. However, for this project, the aircraft will perform a touch-and-go landing and will therefore advance to the recovery state instead. The landing flag is disabled to prevent the system from returning to the touchdown leg state.

State 4: Recovery When a touchdown is detected, the aircraft would normally enter a ground control state, but this is considered outside the scope of this project due to the short platform length and the absence of arresting wires. Instead, a touch-and-go manoeuvre will be performed, meaning that the aircraft will climb back to a minimum altitude after touching the platform using its regular longitudinal controllers. When the aircraft has gained sufficient altitude, set to 3m for this project, the touch-and-go is considered complete. Ideally, the aircraft should return to the original waypoint track. However, this would have reduced the ability to repeatedly test the system as the original waypoint track would now be very far away from the current location which could cause the aircraft to perform dangerous roll angles close to the ground. Although it does return to the waypoint navigation state, the source and destination waypoint are not overwritten and the waypoint pair generated relative to the moving platform will continue to be flown until the safety pilot assumes control, which is sufficient for the purposes of this project.

3.4 Summary

This chapter discussed the details of the landing specifications set for this project in the light of a real world scenario with respect to accuracy, velocity and environmental conditions. The different platform movements were discussed in terms of the feasibility of practically demonstrating them within the scope of this project. It was decided that the goals of this project would be to land on a stationary as well as a horizontally translating platform, but with no heaving, rolling or pitching motion of the platform. Slight yawing is permitted and will be compensated for. The initial landing procedure based on previous projects were discussed, with a simplified version presented that is more applicable to this project. The final landing system and state machine which were implemented and simulated in embedded software on the model aircraft were presented.

§ 4

Mathematical Model

This chapter presents the mathematical models used to analyse the aircraft, platform and environment in order to simulate their behaviour and develop a control system for the autonomous landing system. The aircraft model presented in this chapter is primarily based on [4, 2, 44].

Section 4.1 defines the different reference frames, notations and conventions used throughout this project. Section 4.2 describes the mathematical model of the aircraft consisting of the six degrees of freedom equations of motion and the aerodynamic, thrust, and gravitational forces and moments. Section 4.3 describes the model and simplification of the moving platform. Section 4.4 discusses the wind model implemented for simulation purposes. Section 4.5 provides a summary of the chapter.

4.1 Reference Frames and Conventions

To describe the motion of the aircraft, different sets of reference axes need to be defined. For this project, these axes are the inertial, body and wind axes systems, which will be discussed in the sections below.

4.1.1 Inertial Axes

To apply Newton's laws of motion, an inertial axis is required. Typical short-range UAV applications commonly use the North-East-Down axis system which assumes that the earth is a non-rotating flat surface. This is a useful approximation for short-range UAVs, as the Coriolis effect and curvature of the earth can be neglected. The origin is chosen to be a convenient point, such as the starting point on the runway. Using an orthogonal right-handed axis system as illustrated in Figure 4.1, the X-axis is chosen to face North from the initialisation point. The Y-axis is chosen East, perpendicular to the X-axis. The Z-axis is chosen down towards the Earth, perpendicular to the XY-plane.

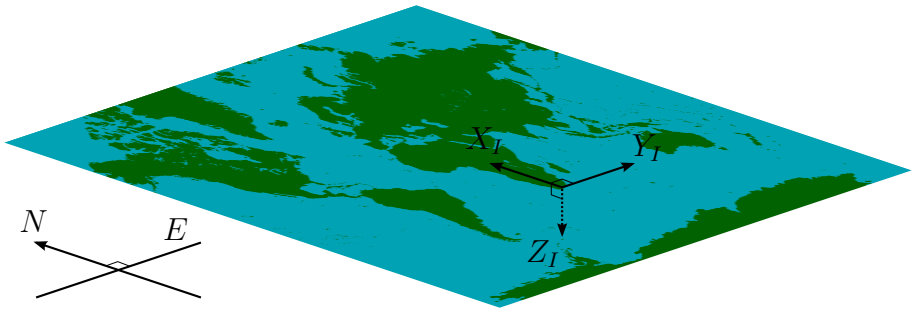

Figure 4.1: North-East-Down inertial axis system on a flat Earth.

4.1.2 Body Axes

This axes system is fixed to the body of the aircraft, moving along and rotating with the aircraft as it moves through inertial space. Its origin is chosen to coincide with the centre of mass of the aircraft. Using an orthogonal right-handed axis system, the X-axis is chosen to be in the plane of symmetry such as the zero angle of attack line. The Y-axis is chosen to be perpendicular to the symmetry plane pointing out through the right wing, or starboard wing. The Z-axis is chosen to complete the right-handed, orthogonal axis system, usually pointing downwards relative to the cockpit. A graphical representation is shown in Figure 4.2 with the notation discussed in Section 4.1.4.

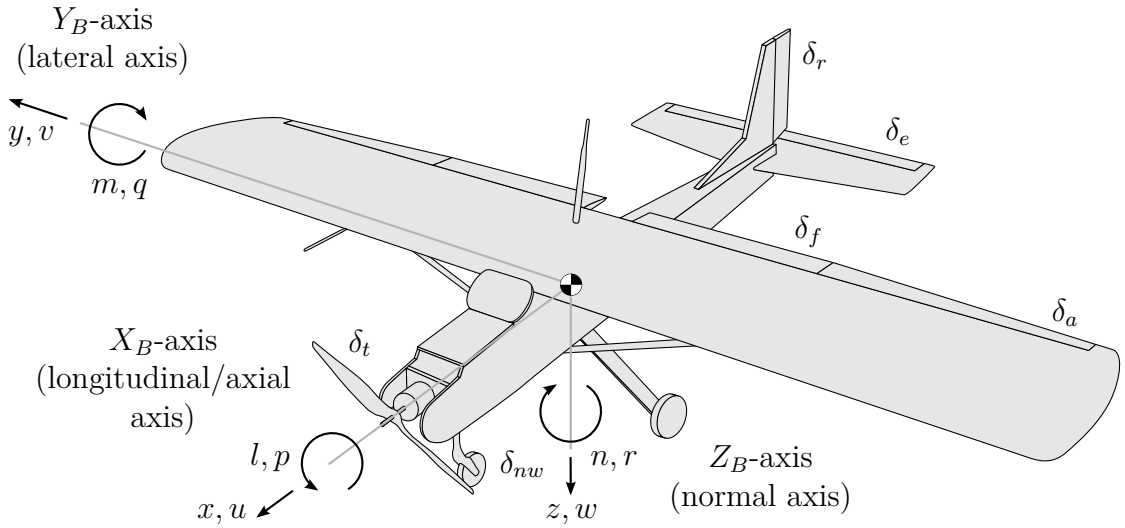

Figure 4.2: Body axes system and conventions including the forces, moments, velocities and angular rates. Adapted from [2].

4.1.3 Wind Axes

The wind axes also has its origin chosen at the centre of mass of the aircraft. Using an orthogonal right-handed axis system, the X-axis is chosen to align with the velocity vector of the aircraft. The Z-axis is chosen perpendicular downwards in the plane of symmetry, therefore as a vertical cross-section through the fuselage. The Y-axis is chosen to complete the right-handed, orthogonal axis system.

4.1.4 Notation

The symbols used to represent the forces, moments, velocities and angular rates in the aircraft model, as illustrated in Figure 4.2, are summarised as follow:

- x, y, z: coordinates of the force vector in the body axes as the axial, lateral and normal forces, respectively;
- l, m, n: coordinates of the moment vector in the body axes as the rolling, pitching and yawing moments, respectively;
- u, v, w: coordinates of the linear velocity in the body axes as the axial, lateral and normal velocity, respectively;
- p, q, r: coordinates of the angular rate vector in the body axes as the roll, pitch and yaw rates, respectively; and
- δ_a, δ_e, δ_f, δ_r: the control surface deflections for the aileron, elevator, flaps and rudder, respectively. A positive deflection is defined as one that produces a negative moment. For this project, the flaps will not be used and will always be commanded to zero deflection angles to follow the profile of the wing. This setting maintains a single lift and drag configuration which simplifies the control design.

For convenience, the velocity coordinates are often expressed in spherical coordinate form. As shown in Figure 4.3, the notation for these parameters are $\overline{v}$ as the velocity magnitude, α as the angle of attack and β as the angle of sideslip. The following equations relate the Cartesian velocity coordinates to the spherical coordinates:

$$\overline{v} = \sqrt{u^2 + v^2 + w^2} \tag{4.1}$$

$$\alpha = \tan^{-1}\left(\frac{w}{u}\right) \tag{4.2}$$

$$\beta = \sin^{-1}\left(\frac{v}{\overline{v}}\right) \tag{4.3}$$

The inverse relationship is given by

$$u = \overline{v}\cos\alpha\cos\beta \tag{4.4}$$

$$v = \overline{v}\sin\beta \tag{4.5}$$

$$w = \overline{v}\sin\alpha\cos\beta \tag{4.6}$$

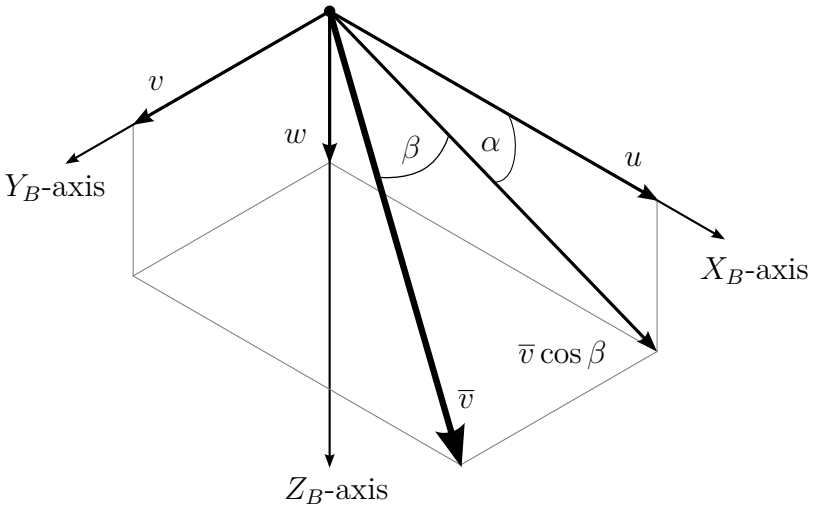

Figure 4.3: Spherical velocity coordinates often used in aircraft dynamics. Adapted from [2].

4.2 Aircraft Motion

To describe the motion of the aircraft, the different forces, moments, velocities, and angular rates must be related to one another to form a representative dynamic model. This section will describe the equations of motion for the aircraft as well as the force and moment models for the aerodynamics, thrust and gravity. Sections 4.2.1 through 4.2.4 will present the full nonlinear models, which are used for representative simulations in software. For the development of control systems, the models are linearised in Section 5.1 and the resulting dynamics analysed in Section 5.2.

4.2.1 Six Degrees of Freedom

The aircraft will be modelled as a rigid body with six degrees of freedom for its motion. The six degrees of freedom are the three translational motions (axial, lateral, normal) as well as the three rotational motions (rolling, pitching, yawing) that the aircraft can physically perform during flight. The implication of the aircraft being modelled as a rigid body is that each mass element remains fixed to the body of the aircraft at all times, irrespective of its current motion. Most large aircraft do display some structural flexibility, but since these modes are usually outside of the bandwidth of conventional controllers, they are not taken into account in the mathematical model. For the small aircraft used in this project, the structural flexibility may be neglected.

This section will present the six degrees of freedom equations of motion for a rigid body with the forces and moments presented in subsequent sections. A block diagram overview of the different models is shown in Figure 4.4.

4.2.1.1 Kinetics

Kinetics is the branch of mechanics relating the forces and moments acting on a body to its translational and rotational motion. To model these relationships, Newton's laws of motion for

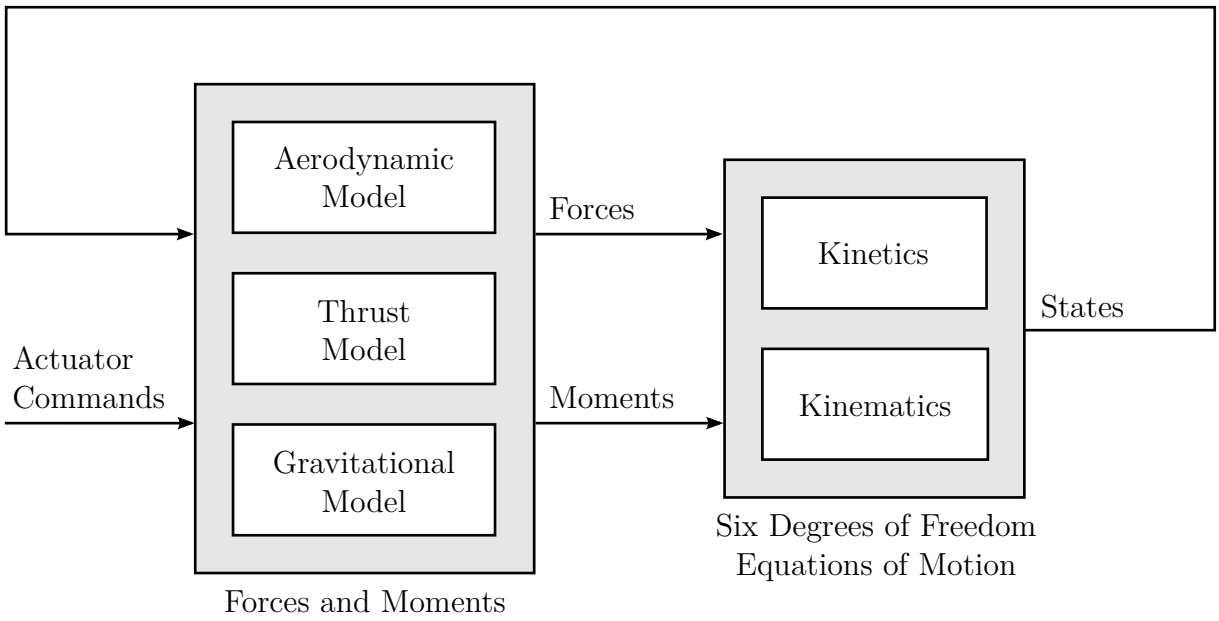

Figure 4.4: Aircraft model block diagram showing the models for forces, moments and six degrees of freedom equations of motion.

rigid bodies with six degrees of freedom can be used. The equations of motion in their classic forms, with vectors coordinated in the body axes, can be represented as

$$x = m(\dot{u} - vr + wq) \tag{4.7}$$

$$y = m(\dot{v} + ur - wp) \tag{4.8}$$

$$z = m(\dot{w} - uq + vp) \tag{4.9}$$

$$l = \dot{p}I_{xx} + qr(I_{zz} - I_{yy}) \tag{4.10}$$

$$m = \dot{q}I_{yy} + pr(I_{xx} - I_{zz}) \tag{4.11}$$

$$n = \dot{r}I_{zz} + pq(I_{yy} - I_{xx}) \tag{4.12}$$

where m is the aircraft mass and I_{xx}, I_{yy} and I_{zz} are the principle moments of inertia about each of their respective axes. To obtain these equations, the following assumptions are made to simplify the model:

1. the aircraft is symmetrical about the XZ-plane, which implies that the cross products of inertia I_{xy} and I_{yz} are exactly zero – an accurate assumption for all conventional aircraft; and

2. the cross product of inertia I_{xz} is negligibly small – most often the case for conventional aircraft.

Newton's second law is used to relate the forces and moments acting on the rigid body to the time rate of change of its velocity and angular rate coordinates, reflected in Equations 4.7 through 4.12. The cross product terms appearing in the equations stem from the coordination with respect to the body axes instead of the inertial axes.

For usage in control system design, equations are usually written in state-space form. Rearrangement of the above mentioned equations yield

$$\dot{u} = -wq + vr + \frac{1}{m}x \tag{4.13}$$
$$\dot{v} = wp - ur + \frac{1}{m}y \tag{4.14}$$
$$\dot{w} = -vp + uq + \frac{1}{m}z \tag{4.15}$$
$$\dot{p} = -\frac{1}{I_{xx}}qr(I_{zz} - I_{yy}) + \frac{1}{I_{xx}}l \tag{4.16}$$
$$\dot{q} = -\frac{1}{I_{yy}}pr(I_{xx} - I_{zz}) + \frac{1}{I_{yy}}m \tag{4.17}$$
$$\dot{r} = -\frac{1}{I_{zz}}pq(I_{yy} - I_{xx}) + \frac{1}{I_{zz}}n \tag{4.18}$$

as the rate of change of the system states in terms of the current states and inputs. The total forces and moments acting on the aircraft are the sum of the forces and moments from the aerodynamics, thrust and gravity. These sums are given by

$$x = x^A + x^T + x^G \tag{4.19}$$
$$y = y^A + y^T + y^G \tag{4.20}$$
$$z = z^A + z^T + z^G \tag{4.21}$$
$$l = l^A + l^T + l^G \tag{4.22}$$
$$m = m^A + m^T + m^G \tag{4.23}$$
$$n = n^A + n^T + n^G \tag{4.24}$$

where the superscripts A, T, and G denote the forces and moments originating from the aerodynamics, thrust and gravity, respectively. The models for these forces and moments will be more thoroughly discussed in Sections 4.2.2, 4.2.3 and 4.2.4.

4.2.1.2 Kinematics

Kinematics is the branch of mechanics relating the motion variables such as linear velocity, angular rate, position and attitude to one another over time. The following variables are used to represent the position and attitude of the aircraft:

- p_N, p_E, p_D: coordinates of the position vector in inertial space; and
- ϕ, θ, ψ: Euler 3-2-1 attitude parameters of the body axes system in inertial space.

The position coordinate origin is usually chosen to coincide with a convenient point, such as the starting point on the runway. The parameter definitions are p_N as north, p_E as east and p_D as down, meaning that an increase in altitude will result in a negative p_D coordinate.

Because of their simplicity and intuitiveness, Euler angles are commonly used to parameterise aircraft attitude for nonaerobatic flight. The disadvantage of the Euler angle repre-

sentation is that it contains a singularity in the attitude dynamics, while alternative attitude representations such as quaternions avoid these singularities but are more mathematically complex and significantly less intuitive to work with. The Euler 3-2-1 singularity at $\theta = \pm 90°$ should not be encountered in this project since such high pitch angles are not expected during normal flight and landing operations, therefore using Euler angles are deemed appropriate. Euler angles uses three rotation angles to relate the orientation of the body axes system relative to the inertial axes. The Euler 3-2-1 sequence moves the body axes through the following ordered set of rotations:

1. yaw the body axes system positively through the heading angle ψ;
2. pitch the body axes system positively through the pitch angle θ; and
3. roll the body axes system positively through the roll angle ϕ.

A graphical representation of these angles are shown in Figure 4.5. Note that the roll angle representation does not necessarily align with the horizon as it is defined relative to the pitch angle plane. The orientation of the aircraft body with respect to the inertial axes system is fully described by Euler angles and is therefore appropriate for use in this project.

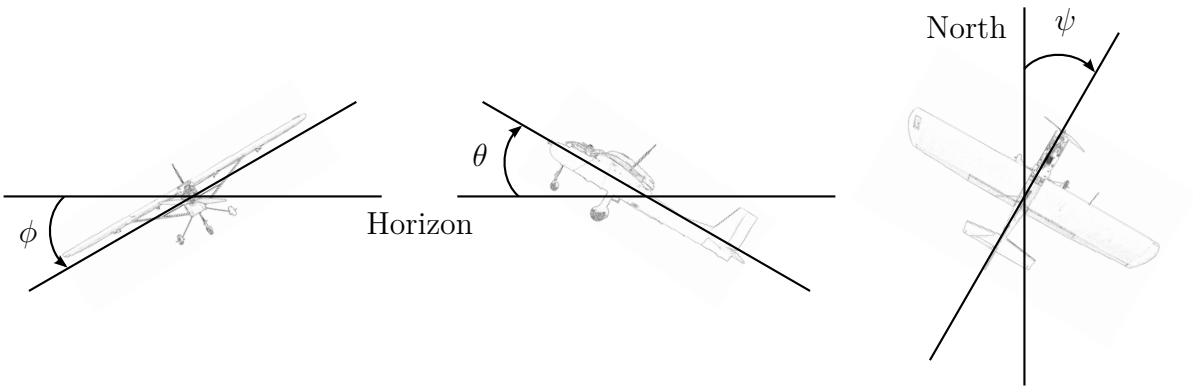

Figure 4.5: Euler angle attitude representation showing roll, pitch and yaw rotation angles. Adapted from [3].

Given the Euler angle attitude parameters, it can now be used to determine the time rate of change of these parameters and their relation to the other kinematic states. The rate of change in roll, pitch and yaw angles and their relations to rate of roll, pitch and yaw is described by

$$\begin{bmatrix} \dot{\phi} \\ \dot{\theta} \\ \dot{\psi} \end{bmatrix} = \begin{bmatrix} 1 & \sin\phi\tan\theta & \cos\phi\tan\theta \\ 0 & \cos\phi & -\sin\phi \\ 0 & \sin\phi\sec\theta & \cos\phi\sec\theta \end{bmatrix} \begin{bmatrix} p \\ q \\ r \end{bmatrix} \qquad |\theta| \neq \frac{\pi}{2} \tag{4.25}$$

Note the mathematical singularity occurring at $\theta = \pm 90°$ when an ambiguity exists between the roll and pitch angles. For the conventional flight performed in this project, this situation should never occur, allowing the singularity to be ignored.

With both vectors coordinated into the inertial axes, the relationship between position and velocity is represented by

$$\begin{bmatrix} \dot{p}_N \\ \dot{p}_E \\ \dot{p}_D \end{bmatrix} = \begin{bmatrix} v_N \\ v_E \\ v_D \end{bmatrix} \tag{4.26}$$

where v_N, v_E, and v_D are the north, east and down velocities respectively. To rotate the body axes parameters to inertial axes parameters, a transformation matrix is used. To illustrate this, consider the vectors in Figure 4.6.

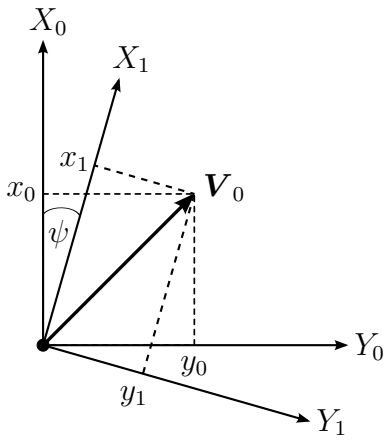

Figure 4.6: Single yaw axis rotation of $\boldsymbol{V}$ from vector components x_0 and y_0 to x_1 and y_1. Adapted from [4].

Let the coordinates of $\boldsymbol{V}_0$ in the original axes system be

$$\boldsymbol{V}_0 = \begin{bmatrix} x_0 \\ y_0 \\ z_0 \end{bmatrix} \tag{4.27}$$

Using simple trigonometry, it can be shown that the coordinates in the new axes system can be obtained using the transformation matrix

$$\begin{bmatrix} x_1 \\ y_1 \\ z_1 \end{bmatrix} = \begin{bmatrix} \cos\psi & \sin\psi & 0 \\ -\sin\psi & \cos\psi & 0 \\ 0 & 0 & 1 \end{bmatrix} \begin{bmatrix} x_0 \\ y_0 \\ z_0 \end{bmatrix} \tag{4.28}$$

Similarly, the new coordinates can subsequently be rotated through pitch with the matrix

$$\begin{bmatrix} x_2 \\ y_2 \\ z_2 \end{bmatrix} = \begin{bmatrix} \cos\theta & 0 & -\sin\theta \\ 0 & 1 & 0 \\ \sin\theta & 0 & \cos\theta \end{bmatrix} \begin{bmatrix} x_1 \\ y_1 \\ z_1 \end{bmatrix} \tag{4.29}$$

Finally, these coordinates can subsequently be rotated through roll with the transformation matrix

$$\begin{bmatrix} x_3 \\ y_3 \\ z_3 \end{bmatrix} = \begin{bmatrix} 1 & 0 & 0 \\ 0 & \cos\phi & \sin\phi \\ 0 & -\sin\phi & \cos\phi \end{bmatrix} \begin{bmatrix} x_2 \\ y_2 \\ z_2 \end{bmatrix} \tag{4.30}$$

Multiplying all the transformation matrices together yield the Direction Cosine Matrix (DCM), which can be used to convert coordinates from the inertial axes to the body axes. This can be summarised as

$$\begin{bmatrix} x_B \\ y_B \\ z_B \end{bmatrix} = \begin{bmatrix} C_\psi C_\theta & S_\psi C_\theta & -S_\theta \\ C_\psi S_\theta S_\phi - S_\psi C_\phi & S_\psi S_\theta S_\phi + C_\psi C_\phi & C_\theta S_\phi \\ C_\psi S_\theta C_\phi + S_\psi S_\phi & S_\psi S_\theta C_\phi - C_\psi S_\phi & C_\theta C_\phi \end{bmatrix} \begin{bmatrix} x_I \\ y_I \\ z_I \end{bmatrix} \quad C_\eta{=}\cos(\eta),\ S_n{=}\sin(\eta) \tag{4.31}$$

As it is required to convert the body coordinates of the velocity vector to the inertial coordinates, the inverse of the DCM is required. It can be shown that the DCM is an orthogonal matrix, thus its inverse is simply equal to its transpose. The final form of the transformation matrix now becomes

$$\begin{bmatrix} \dot{p}_N \\ \dot{p}_E \\ \dot{p}_D \end{bmatrix} = \begin{bmatrix} C_\psi C_\theta & C_\psi S_\theta S_\phi - S_\psi C_\phi & C_\psi S_\theta C_\phi + S_\psi S_\phi \\ S_\psi C_\theta & S_\psi S_\theta S_\phi + C_\psi C_\phi & S_\psi S_\theta C_\phi - C_\psi S_\phi \\ -S_\theta & C_\theta S_\phi & C_\theta C_\phi \end{bmatrix} \begin{bmatrix} u \\ v \\ w \end{bmatrix} \quad C_\eta{=}\cos(\eta),\ S_n{=}\sin(\eta) \tag{4.32}$$

A summarised block diagram of the six degrees of freedom equations of motion is shown in Figure 4.7. The forces and moments are used as inputs to drive the dynamics, with the kinetic equations relating these terms to rates of change in linear velocities and angular rates. The kinematic equations subsequently relate these linear velocities and angular rates to rates of change in inertial positions and attitude.

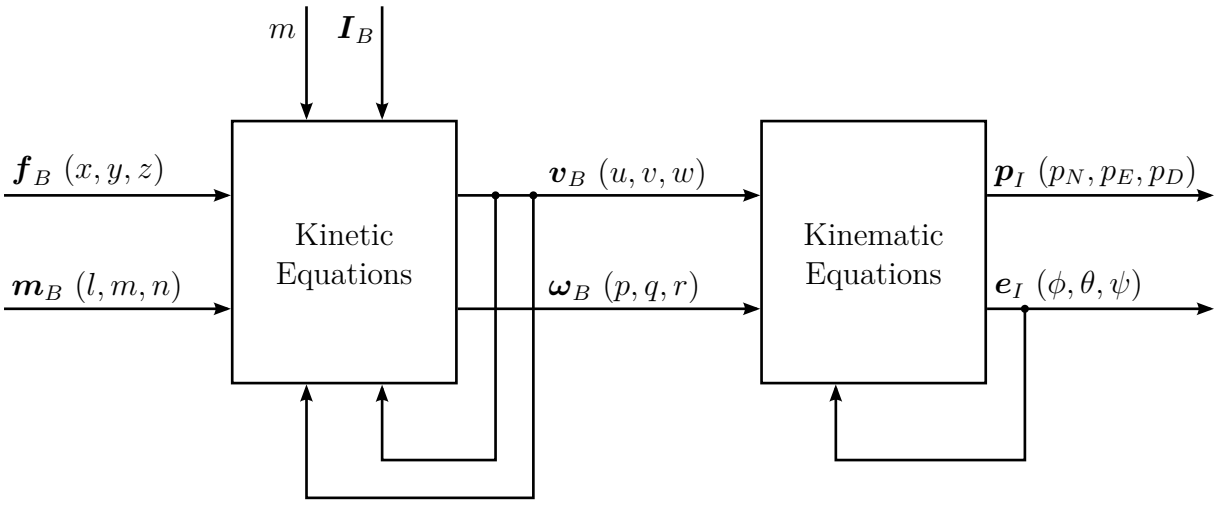

Figure 4.7: Block diagram overview of the six degrees of freedom equations of motion. Adapted from [5].

4.2.2 Aerodynamic Model

Aerodynamic forces and moments are very complex to model and therefore introduce the most uncertainty into the aircraft model. The Bernoulli equation and Continuity principle for incompressible fluids can be used to show that the forces and moments experienced by the aircraft during subsonic flight are proportional to the dynamic pressure. This pressure is defined as

$$q_p = \frac{1}{2}\rho\overline{v}^2 \tag{4.33}$$

where q_p is the dynamic pressure, ρ is the air density and $\overline{v}$ is the total airspeed magnitude. The different aerodynamic forces and moments can be written as

$$x^A = q_p S C_x \tag{4.34}$$
$$y^A = q_p S C_y \tag{4.35}$$
$$z^A = q_p S C_z \tag{4.36}$$
$$l^A = q_p S b C_l \tag{4.37}$$
$$m^A = q_p S \overline{c} C_m \tag{4.38}$$
$$n^A = q_p S b C_n \tag{4.39}$$

where S is the area of the aircraft wing, b is the wingspan, $\overline{c}$ is the mean aerodynamic chord, and C_η are the various nondimensional aerodynamic force and moment coefficients. These coefficients are specific to the airframe and mostly independent of the scale and flight speed of the aircraft, as these aspects are taken into account by the dynamic pressure and the various scaling factors. These coefficients are usually modelled with respect to the wind axes with an angle of sideslip assumed to be zero. The axial and normal force coefficients can be expanded to

$$C_x = -C_D \cos\alpha + C_L \sin\alpha \tag{4.40}$$
$$C_z = -C_L \cos\alpha - C_D \sin\alpha \tag{4.41}$$

where C_L and C_D are lift and drag coefficients respectively. Since the body and wind axes are assumed to coincide for small angles, the remaining coefficients are generally not transformed for simplification. Expanding the coefficients for typical subsonic, nonstall flight yield

$$C_y = C_{y_\beta}\beta + \frac{b}{2\overline{v}} C_{y_p} p + \frac{b}{2\overline{v}} C_{y_r} r + C_{y_{\delta_a}}\delta_a + C_{y_{\delta_r}}\delta_r \tag{4.42}$$
$$C_D = C_{D_0} + \frac{C_L^2}{\pi A e} \tag{4.43}$$
$$C_L = C_{L_0} + C_{L_\alpha}\alpha + \frac{\overline{c}}{2\overline{v}} C_{L_q} q + C_{L_{\delta_e}}\delta_e \tag{4.44}$$
$$C_l = C_{l_\beta}\beta + \frac{b}{2\overline{v}} C_{L_p} p + \frac{b}{2\overline{v}} C_{l_r} r + C_{l_{\delta_a}}\delta_a + C_{l_{\delta_r}}\delta_r \tag{4.45}$$
$$C_m = C_{m_0} + C_{m_\alpha}\alpha + \frac{\overline{c}}{2\overline{v}} C_{m_q} q + C_{m_{\delta_e}}\delta_e \tag{4.46}$$

$$C_n = C_{n_\beta}\beta + \frac{b}{2\overline{v}}C_{n_p}p + \frac{b}{2\overline{v}}C_{n_r}r + C_{n_{\delta_a}}\delta_a + C_{n_{\delta_r}}\delta_r \tag{4.47}$$

where C_{D_0} is the parasitic drag coefficient, C_{L_0} is the static lift coefficient, C_{m_0} is the static pitching moment coefficient, A is the wing aspect ratio (ratio of length to breadth), and e is the Oswald efficiency factor. The coefficients of the form

$$C_{\eta_\mu} \equiv \frac{\partial C_\eta}{\partial \mu'} \qquad (\mu'{=}n\mu, \text{ where } n \text{ is the appropriate normalising coefficient of } \mu) \tag{4.48}$$

are nondimensional stability and control derivatives, with the normalising coefficient as 1 for the incidence and control deflection angles, $\frac{\bar{c}}{2\overline{v}}$ for the pitch rate, and $\frac{b}{2\overline{v}}$ for the roll and yaw rates. These derivatives define the aerodynamic properties of a specific airframe. Several techniques exist to obtain the values of these derivatives, varying both in accuracy and complexity.

In this project, the values for the stability and control derivatives determined by [16] with the AVL software were used as the basis and were further refined with practical flight test data. The origins and interpretations of the various coefficients are detailed in C.6.

4.2.3 Thrust Model

The propulsion system used by the aircraft for this project is a single electric motor attached to the nose of the fuselage. Due to the simplicity of this setup, a complex propulsion model is not required, although such models exist. A first-order lag model would suffice to capture the band-limited nature of the propulsion source. If it is assumed that the spin-up and spin-down time constants are equal, the state-space representation of such a system can be written as

$$\dot{\delta}_t = -\frac{1}{\tau}\delta_t + \frac{1}{\tau}\delta_{t_c} \tag{4.49}$$

where δ_t is the thrust magnitude, δ_{t_c} is the thrust command and τ is the engine lag time constant. Furthermore, if the assumption is made that the thrust vector is aligned along the X-axis of the body axes system, the engine thrust does not produce any lateral or normal forces, nor any moments. It can then be stated that

$$x^T = \delta_t \tag{4.50}$$
$$y^T = z^T = 0 \tag{4.51}$$
$$l^T = m^T = n^T = 0 \tag{4.52}$$

or in vector form as

$$\boldsymbol{f}_B^T = \begin{bmatrix} \delta_t \\ 0 \\ 0 \end{bmatrix} \tag{4.53}$$

$$\boldsymbol{m}_B^T = \begin{bmatrix} 0 \\ 0 \\ 0 \end{bmatrix} \tag{4.54}$$

On single motor aircraft, the propeller produces the phenomenon known as the "corkscrew effect", where the helical shape of airflow from the propeller around the aircraft fuselage causes pressure against the vertical stabiliser and wings. This pressure results in a negative yawing moment, as well as a positive rolling moment. The magnitude of these moments depends on the angular rotation rate of the propeller and the forward velocity of the aircraft, which causes the helix shaped airflow to compress or elongate [45]. To combat this effect, many trainer aircraft mount the engine at a slight angle. For this project however, it is assumed that these moments are negligible.

4.2.4 Gravitational Model

If the assumption is made that the earth has a flat surface, the gravitational acceleration vector is adequately modelled as a downwards force equal to the weight of the aircraft and can be written in inertial coordinates as

$$\boldsymbol{f}_I^G = \begin{bmatrix} 0 \\ 0 \\ mg \end{bmatrix} \tag{4.55}$$

Using the inverse DCM, the gravitational force can be coordinated in the body axes as

$$\begin{bmatrix} x^G \\ y^G \\ z^G \end{bmatrix} = \begin{bmatrix} C_\psi C_\theta & S_\psi C_\theta & -S_\theta \\ C_\psi S_\theta S_\phi - S_\psi C_\phi & S_\psi S_\theta S_\phi + C_\psi C_\phi & C_\theta S_\phi \\ C_\psi S_\theta C_\phi + S_\psi S_\phi & S_\psi S_\theta C_\phi - C_\psi S_\phi & C_\theta C_\phi \end{bmatrix} \begin{bmatrix} 0 \\ 0 \\ mg \end{bmatrix} \qquad C_\eta = \cos(\eta),\ S_n = \sin(\eta) \tag{4.56}$$

which can be simplified to

$$\begin{bmatrix} x^G \\ y^G \\ z^G \end{bmatrix} = \begin{bmatrix} -\sin\theta \\ \cos\theta \sin\phi \\ \cos\theta \cos\phi \end{bmatrix} mg \tag{4.57}$$

Since the gravitational force is uniform and thus the force produced coincides with the centre of mass, no moments are produced. It can therefore be stated that

$$l^G = m^G = n^G = 0 \tag{4.58}$$

The gravitational forces and moments can be written in vector form as

$$\boldsymbol{f}_B^G = \begin{bmatrix} -\sin\theta \\ \cos\theta\sin\phi \\ \cos\theta\cos\phi \end{bmatrix} mg \tag{4.59}$$

$$\boldsymbol{m}_B^G = \begin{bmatrix} 0 \\ 0 \\ 0 \end{bmatrix} \tag{4.60}$$

4.3 Landing Platform

The autonomous landing system will be tested in a scenario similar to that of an aircraft landing on an aircraft carrier out at sea. The motion of such a ship is very complex as ocean waves are of varying amplitude, frequencies and direction, and the presence of currents can cause behaviour that is difficult to accurately and reliably predict. To keep the project practically testable and to focus on the control system rather than the deck prediction, it is decided to simplify the platform model to only have translational motion with minimal yawing.

4.3.1 Platform Motion

The platform is regarded as a simple point mass, while the target landing area is constrained by the physical size of the platform as discussed in Section 3.1. No control system will be designed for the platform as it will be towed by a motor vehicle. It is therefore suitable to discuss its motion in terms of time-varying equations in spherical coordinates and Euler angles, using the same notation as that of the aircraft model presented in Section 4.1.4. These equations can be stated as

$$\dot{\bar{v}} = f_{\dot{\bar{v}}}(t) \tag{4.61}$$
$$\dot{\alpha} = f_{\dot{\alpha}}(t) \tag{4.62}$$
$$\dot{\beta} = f_{\dot{\beta}}(t) \tag{4.63}$$
$$\dot{\phi} = f_{\dot{\phi}}(t) \tag{4.64}$$
$$\dot{\theta} = f_{\dot{\theta}}(t) \tag{4.65}$$
$$\dot{\psi} = f_{\dot{\psi}}(t) \tag{4.66}$$

where every state has its own value in time. If it is assumed that the platform will not be subjected to any roll or pitch rates, it can be stated that

$$f_{\dot{\phi}}(t) = 0 \tag{4.67}$$
$$f_{\dot{\theta}}(t) = 0 \tag{4.68}$$

The platform is also modelled as having no heaving motion. Furthermore, it is assumed that the velocity vector remains aligned with the heading vector for small heading changes and that the platform does not sideslip. These assumptions are expressed mathematically as

$$f_{\dot{\alpha}}(t) = 0 \tag{4.69}$$

$$f_{\dot{\beta}}(t) \approx 0 \tag{4.70}$$

When the platform reaches a predetermined speed, the velocity will be regulated to maintain a constant reference speed. The full platform motion is therefore governed by the following equations:

$$\overline{v}(t) = \overline{v}_T \tag{4.71}$$

$$\alpha(t) = 0 \tag{4.72}$$

$$\beta(t) = 0 \tag{4.73}$$

$$\phi(t) = 0 \tag{4.74}$$

$$\theta(t) = 0 \tag{4.75}$$

$$\psi(t) = f_{\psi}(t) \tag{4.76}$$

These equations imply that the platform motion will be constrained to only horizontal translational motion in the direction of the platform heading. Minor heading changes of a low angular rate of less than $4°/s$, as experimentally determined, will be considered. This is because the motion of the platform cannot be guaranteed to be perfectly straight during practical tests, therefore the aircraft should be able to compensate for this to ensure the safety of the vehicle. The heading angle is sensed on the platform-mounted DGPS module, typically calculated from velocity measurements. Since the heading is obtained from the DGPS velocity vector, it becomes undefined when the platform is stationary and is noisy at low platform speeds. The heading measurement from the DGPS will therefore only be trusted when the platform velocity exceeds 10km/h. The heading measurement is also filtered on the GCS to prevent spikes in measurements which would cause large steps in lateral reference values. Figure 4.8 shows an example of how this filter reacts to the maximum considered heading rate of change.

Rolling, pitching and heaving motion of the platform would require attitude matching between the aircraft and the platform, resulting in the project goal shifting more towards that of prediction of platform attitude than on controlling the landing impact. Interactive forces between the aircraft undercarriage and the platform are not modelled in this project as the aim is merely to hit the target area accurately and not to control the aircraft on the platform. In practice, only the heading of the aircraft needs to be controlled after touchdown as a tethered arrest system would prevent the aircraft from moving further. A safety procedure is usually in place to ensure that the aircraft can take off again in the event that it was not captured in this fashion.

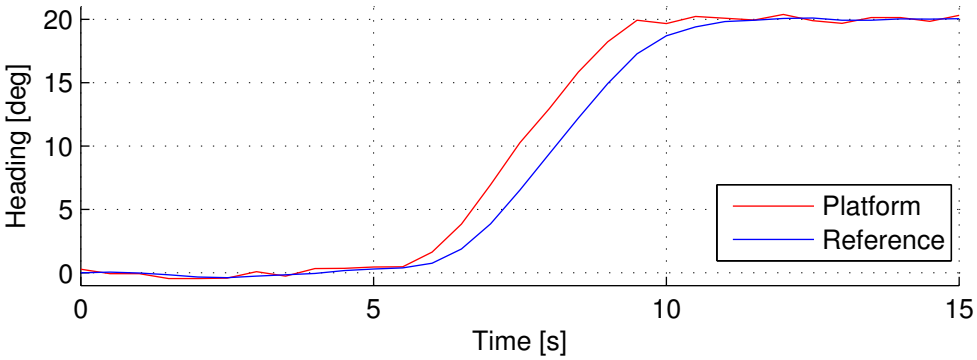

Figure 4.8: Example of the maximum heading rate of change of the platform and the filtered GPS heading transmitted to the OBC to be used for heading corrections.

4.3.2 Ground Effect

The ground effect is a phenomenon that occurs when a physical boundary, such as the earth or water, is present under the surface of the wing. This boundary causes a change in the upwash, downwash, and tip vortices as the air cannot expand against this plane as it normally would during free flight. For a given angle of attack, this effectively increases the angle of incidence which causes an increase in lift, a reduction in induced drag and an increase in pitching moment. Typically, this effect begins to manifest when the distance between the wing and the boundary is one wingspan in length [46].

The following points are important for an aircraft descending into the ground effect, and therefore of interest for this project [46]:

1. The reduced induced angle of attack and change in lift distribution will require a smaller wing angle of attack to produce the same lift coefficient, therefore the pitch angle should be reduced to maintain the same lift.

2. The reduced induced air flow causes a significant reduction in induced drag, but not a direct effect on parasitic drag, therefore a lower thrust setting will be required.

3. The reduced downwash produces a change in longitudinal stability and trim, and an additional negative pitching moment in conventional aircraft, therefore an increase in elevator setting is required.

4. The changes in upwash, downwash and tip vortices may cause errors in the airspeed sensor systems due to increased pressure at the static source.

5. The ground effect will be delayed in the scenario of a carrier-based operation until the aircraft passes the stern of the deck. Therefore, the same reduction in applied thrust should not be required as for normal runway landings.

These effects are significant for the real scenario of a carrier-based landing. In this project, the landing platform is constructed from a steel mesh, which should significantly reduce the air flow obstruction due to a boundary plane. Additionally, the longitudinal control system should

react to perform a "controlled crash" on the touchdown point rather than a gentle landing. The ground effect will therefore be considered negligible for the purposes of this project.

4.4 Wind Model

To build confidence in the flight control system, it is necessary to verify it against various disturbances that the aircraft may experience. This section describes the models used in simulation to replicate the environmental effects that act upon the aircraft during flight. As the effect of the wind can range from minor to major, it is important to verify the system against the worst conditions in which the aircraft remains operable. The wind effects considered are gusts, turbulence and shear, each discussed in their respective sections below.

Previous wind models used in the ESL consisted of only a wind gust generated by passing band-limited white noise through a first-order low-pass shaping filter, approximating translational turbulence. Although this model can be considered sufficient for the purposes of demonstration, it was decided to investigate and implement a more sophisticated model which can also be used in future projects. To this end, a new Simulink simulation block was developed to improve the model by adding additional features and effects to obtain a more realistic environmental representation for given wind scenarios. All models in this section are based on the specifications given in [47, 48].

4.4.1 Discrete Gusts

A discrete wind gust is defined as the gradual increase of speed in air flow until a certain maximum magnitude is reached. For the purposes of the simulation block that was developed, the gust is modelled as remaining at the maximum magnitude for a certain amount of time, and then gradually subsiding back to zero. No random components are included as the turbulence model will incorporate random effects.

The gust takes the "1–cosine" profile when building up. An additional inverted "1–cosine" profile was added when the gust is fading away. The expanded model is therefore represented by

$$\overline{v}_{wind} = \begin{cases} 0 & t < t_s \\ \frac{\overline{V}_m}{2}\left(1 - \cos\left(\frac{\pi x}{d_m}\right)\right) & 0 \leq x \leq d_m \\ \overline{V}_m & x > d_m,\ x < (d_m + d_s) \\ \frac{\overline{V}_m}{2}\left(1 + \cos\left(\frac{\pi x}{d_m}\right)\right) & (d_m + d_s) \leq x \leq (2d_m + d_s) \\ 0 & x > (2d_m + d_s) \end{cases} \tag{4.77}$$

where $\overline{v}_{wind}$ is the resultant magnitude of the gust, t is the elapsed simulation time, t_s is the gust start time, $\overline{V}_m$ is the maximum gust amplitude, x is the distance travelled by the aircraft, d_m is the gust build up and fade out distance, and d_s is the distance that the gust should stay

at its maximum strength before fading. The simulation block that was implemented allows for the setting of each parameter as well as an inertial direction component. An example of the gust profile is illustrated in Figure 4.9.

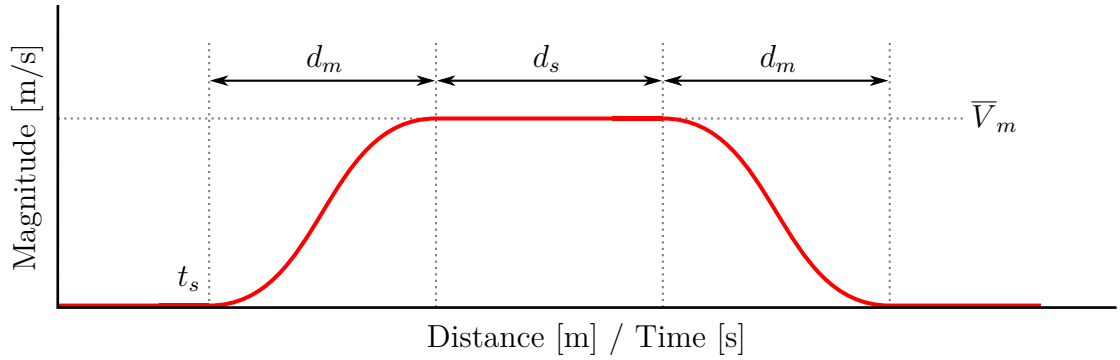

Figure 4.9: Illustration of the discrete wind gust as implemented in the simulation model.

4.4.2 Turbulence

Turbulence can be considered as random forces and moments acting on the aircraft during flight due to changes in wind, air pressure, air density and air temperature conditions. It is described as being a stochastic process defined by a velocity spectrum. This disturbance is realised by passing white noise through the appropriate shaping filters. For this project, the filters are implemented to achieve either the Dryden or Von Kármán spectral forms to mimic the Simulink simulation blocks from the Aerospace Toolbox [6, 49]. This model assumes clean air turbulence and does not incorporate conditions such as terrain roughness or wind shear.

For an aircraft flying at a velocity V through a turbulence field with an intensity that is small compared to the aircraft ground speed and a spatial frequency of Ω radians per meter, the circular frequency can be calculated by $\omega = V \times \Omega$. Table 4.1 displays the spectra forms used for implementation. In this table, b is the wingspan of the aircraft, σ_η are the turbulence intensities and L_η are the turbulence scale lengths dependant on the aircraft altitude. Three variations in the angular rates are defined by the military specifications, shown in Table 4.2, only affecting the vertical (q_g) and lateral (r_g) angular rates. The longitudinal angular rate spectrum $\Phi_{p_g}(\omega)$ is a rational function derived from curve-fitting of a complex algebraic function multiplied by a scaling factor and not of the vertical turbulence velocity spectrum $\Phi_w(\omega)$. It is suspected that, due to the angular rate spectra contributing less than the velocity spectra to the aircraft gust response, it may explain the variation in definition [6, 49]. This leads to the variations in angular rate spectra as shown in Table 4.3. Generation of a signal with the correct characteristics requires a unit variance band-limited white noise signal that is passed through an appropriate shaping filter. These shaping filters are derived from the spectral square roots of the spectrum equations. The filter forms implemented are shown in Table 4.4. Due to the effect that altitude has on the shaping filter scale length and intensities, the models are divided into three regions, each discussed in their respective section below.

Table 4.1: Wind turbulence model spectral forms.

Direction	Dryden	Von Kármán
Longitudinal		
$\Phi_u(\omega)$	$\frac{2\sigma_u^2 L_u}{\pi V} \cdot \frac{1}{1+\left(L_u \frac{\omega}{V}\right)^2}$	$\frac{2\sigma_u^2 L_u}{\pi V} \cdot \frac{1}{\left(1+\left(1.339 L_u \frac{\omega}{V}\right)^2\right)^{\frac{5}{6}}}$
$\Phi_p(\omega)$	$\frac{\sigma_w^2}{2VL_w} \cdot \frac{0.8\left(\frac{2\pi L_w}{4b}\right)^{\frac{1}{3}}}{1+\left(\frac{4b\omega}{\pi V}\right)^2}$	$\frac{\sigma_w^2}{2VL_w} \cdot \frac{0.8\left(\frac{2\pi L_w}{4b}\right)^{\frac{1}{3}}}{1+\left(\frac{4b\omega}{\pi V}\right)^2}$
Lateral		
$\Phi_v(\omega)$	$\frac{2\sigma_v^2 L_v}{\pi V} \cdot \frac{1+12\left(L_v \frac{\omega}{V}\right)^2}{\left(1+\left(4L_v \frac{\omega}{V}\right)^2\right)^2}$	$\frac{2\sigma_v^2 L_v}{\pi V} \cdot \frac{1+\frac{8}{3}\left(2.678 L_v \frac{\omega}{V}\right)^2}{\left(1+\left(2.678 L_v \frac{\omega}{V}\right)^2\right)^{\frac{11}{6}}}$
$\Phi_r(\omega)$	$\frac{\mp\left(\frac{\omega}{V}\right)^2}{1+\left(\frac{3b\omega}{\pi V}\right)^2} \cdot \Phi_v(\omega)$	$\frac{\mp\left(\frac{\omega}{V}\right)^2}{1+\left(\frac{3b\omega}{\pi V}\right)^2} \cdot \Phi_v(\omega)$
Vertical		
$\Phi_w(\omega)$	$\frac{2\sigma_w^2 L_w}{\pi V} \cdot \frac{1+12\left(L_w \frac{\omega}{V}\right)^2}{\left(1+4\left(L_w \frac{\omega}{V}\right)^2\right)^2}$	$\frac{2\sigma_w^2 L_w}{\pi V} \cdot \frac{1+\frac{8}{3}\left(2.678 L_w \frac{\omega}{V}\right)^2}{\left(1+\left(2.678 L_w \frac{\omega}{V}\right)^2\right)^{\frac{11}{8}}}$
$\Phi_q(\omega)$	$\frac{\pm\left(\frac{\omega}{V}\right)^2}{1+\left(\frac{4b\omega}{\pi V}\right)^2} \cdot \Phi_w(\omega)$	$\frac{\pm\left(\frac{\omega}{V}\right)^2}{1+\left(\frac{4b\omega}{\pi V}\right)^2} \cdot \Phi_w(\omega)$

Table 4.2: Wind turbulence model spectral derivative combinations.

$p_g = \frac{\partial w_g}{\partial y}$	$q_g = \frac{\partial w_g}{\partial x}$	$r_g = -\frac{\partial v_g}{\partial x}$
$p_g = \frac{\partial w_g}{\partial y}$	$q_g = \frac{\partial w_g}{\partial x}$	$r_g = \frac{\partial v_g}{\partial x}$
$p_g = -\frac{\partial w_g}{\partial y}$	$q_g = -\frac{\partial w_g}{\partial x}$	$r_g = -\frac{\partial v_g}{\partial x}$

Table 4.3: Wind turbulence model spectral variations.

Vertical	**Lateral**
$\Phi_q(\omega)$	$-\Phi_r(\omega)$
$\Phi_q(\omega)$	$\Phi_r(\omega)$
$-\Phi_q(\omega)$	$\Phi_r(\omega)$

Table 4.4: Wind turbulence model filter forms.

Direction	**Dryden**	**Von Kármán**
	Longitudinal	
$H_u(s)$	$\sigma_u\sqrt{\frac{2L_u}{\pi V}}\cdot\frac{1}{1+\frac{L_u}{V}s}$	$\frac{\sigma_u\sqrt{\frac{2}{\pi}\frac{L_u}{V}}\left(1+0.25\frac{L_u}{V}s\right)}{1+1.357\frac{L_u}{V}s+0.1987\left(\frac{L_u}{V}\right)^2s^2}$
$H_p(s)$	$\sigma_w\sqrt{\frac{0.8}{V}}\cdot\frac{\left(\frac{\pi}{4b}\right)^{\frac{1}{6}}}{(2L_w)^{\frac{1}{3}}\left(1+\left(\frac{4b}{\pi V}\right)s\right)}$	$\sigma_w\sqrt{\frac{0.8}{V}}\cdot\frac{\left(\frac{\pi}{4b}\right)^{\frac{1}{6}}}{(2L_w)^{\frac{1}{3}}\left(1+\left(\frac{4b}{\pi V}\right)s\right)}$
	Lateral	
$H_v(s)$	$\sigma_v\sqrt{\frac{2L_v}{\pi V}}\cdot\frac{1+\frac{2\sqrt{3}L_v}{V}s}{\left(1+\frac{2L_v}{V}s\right)^2}$	$\frac{\sigma_v\sqrt{\frac{1}{\pi}\frac{2L_v}{V}}\left(1+2.7478\frac{2L_v}{V}s+0.3398\left(\frac{2L_v}{V}\right)^2s^2\right)}{1+2.9958\frac{2L_v}{V}s+1.9754\left(\frac{2L_v}{V}\right)^2s^2+0.1539\left(\frac{2L_v}{V}\right)^3s^3}$
$H_r(s)$	$\frac{\mp\frac{s}{V}}{\left(1+\left(\frac{3b}{\pi V}\right)s\right)}\cdot H_v(s)$	$\frac{\mp\frac{s}{V}}{\left(1+\left(\frac{3b}{\pi V}\right)s\right)}\cdot H_v(s)$
	Vertical	
$H_w(s)$	$\sigma_w\sqrt{\frac{2L_w}{\pi V}}\cdot\frac{1+\frac{2\sqrt{3}L_w}{V}s}{\left(1+\frac{2L_w}{V}s\right)^2}$	$\frac{\sigma_w\sqrt{\frac{1}{\pi}\frac{2L_w}{V}}\left(1+2.7478\frac{2L_w}{V}s+0.3398\left(\frac{2L_w}{V}\right)^2s^2\right)}{1+2.9958\frac{2L_w}{V}s+1.9754\left(\frac{2L_w}{V}\right)^2s^2+0.1539\left(\frac{2L_w}{V}\right)^3s^3}$
$H_q(s)$	$\frac{\pm\frac{s}{V}}{\left(1+\left(\frac{4b}{\pi V}\right)s\right)}\cdot H_w(s)$	$\frac{\pm\frac{s}{V}}{\left(1+\left(\frac{4b}{\pi V}\right)s\right)}\cdot H_w(s)$

4.4.2.1 Altitudes Below 1000 Feet

For low altitudes beneath 1000ft, the scale lengths are defined as

$$2L_w = h \tag{4.78}$$

$$L_u = 2L_v = \frac{h}{(0.177 + 0.000823h)^{1.2}} \tag{4.79}$$

and the turbulence intensities as

$$\sigma_w = 0.1V_{20} \tag{4.80}$$

$$\frac{\sigma_u}{\sigma_w} = \frac{\sigma_v}{\sigma_w} = \frac{1}{(0.177 + 0.000823h)^{0.4}} \tag{4.81}$$

where V_{20} is the wind magnitude measured at an altitude of 20ft. The altitude is also lower-limit saturated to 20ft to avoid overaggressive nonlinear scaling.

4.4.2.2 Altitudes Above 2000 Feet

For high altitudes above 2000ft, the scale lengths are defined as

$$L_u = 2L_v = 2L_w = 2500 \text{ ft} \tag{4.82}$$

and the turbulence intensities are obtained from a lookup table. The lookup table severities are defined Table 4.5. The value sets for each severity were approximated and are defined in Table 4.6. The set contours are shown graphically in Figure 4.10.

Table 4.5: Wind turbulence model severities.

Turbulence Severity	**Contour**
Light	2×10^{-1} 10^{-1} 10^{-2}
Moderate	10^{-3} 10^{-4}
Severe	10^{-5} 10^{-6}

4.4.2.3 Altitudes Between 1000 and 2000 Feet

In this region, the results from the 1000ft low altitude model is linearly interpolated with the results from the 2000ft high altitude model.

Table 4.6: Wind turbulence model severity lookup table value sets.

Level	**Turbulence Intensity σ [ft/s], Altitude h [kft]**
2×10^{-1}	$\sigma = [\ 3.64 \quad 2.05 \quad 0.00\ ]$ $h = [\ 0.00 \quad 2.00 \quad 7.33\ ]$
10^{-1}	$\sigma = [\ 4.32 \quad 3.64 \quad 3.30 \quad 1.59 \quad 0.00\ ]$ $h = [\ 0.00 \quad 2.00 \quad 4.00 \quad 7.33 \quad 14.67\ ]$
10^{-2}	$\sigma = [\ 6.36 \quad 7.27 \quad 6.60 \quad 4.55 \quad 2.73 \quad 0.45 \quad 0.00\ ]$ $h = [\ 0.00 \quad 4.00 \quad 8.00 \quad 14.67 \quad 24.67 \quad 34.67 \quad 44.67\ ]$
10^{-3}	$\sigma = [\ 8.41 \quad 10.68 \quad 10.00 \quad 7.95 \quad 6.59 \quad 5.00 \quad 4.09 \quad 2.73 \quad 0.00\ ]$ $h = [\ 0.00 \quad 4.00 \quad 8.00 \quad 14.67 \quad 24.67 \quad 34.67 \quad 44.67 \quad 54.67 \quad 64.67\ ]$
10^{-4}	$\sigma = [\ 11.36 \quad 12.95 \quad 15.91 \quad 15.00 \quad 11.59 \quad 7.95 \quad 8.18 \quad 7.73 \quad 5.00$ $3.18 \quad 2.05\ ]$ $h = [\ 0.00 \quad 2.00 \quad 4.00 \quad 8.00 \quad 14.67 \quad 34.67 \quad 45.33 \quad 54.67 \quad 64.67$ $75.33 \quad 80.00\ ]$
10^{-5}	$\sigma = [\ 15.00 \quad 17.95 \quad 22.73 \quad 23.41 \quad 19.77 \quad 15.91 \quad 15.00 \quad 11.82 \quad 7.95$ $5.91 \quad 5.00\ ]$ $h = [\ 0.00 \quad 2.00 \quad 4.00 \quad 7.33 \quad 25.33 \quad 35.33 \quad 45.33 \quad 55.33 \quad 65.33$ $75.33 \quad 80.00\ ]$
10^{-6}	$\sigma = [\ 17.95 \quad 21.36 \quad 28.18 \quad 30.00 \quad 30.45 \quad 30.91 \quad 25.00 \quad 22.95 \quad 17.50$ $10.68 \quad 7.27\ ]$ $h = [\ 0.00 \quad 2.00 \quad 4.00 \quad 7.33 \quad 16.00 \quad 25.33 \quad 35.33 \quad 45.33 \quad 54.67$ $64.67 \quad 80.00\ ]$

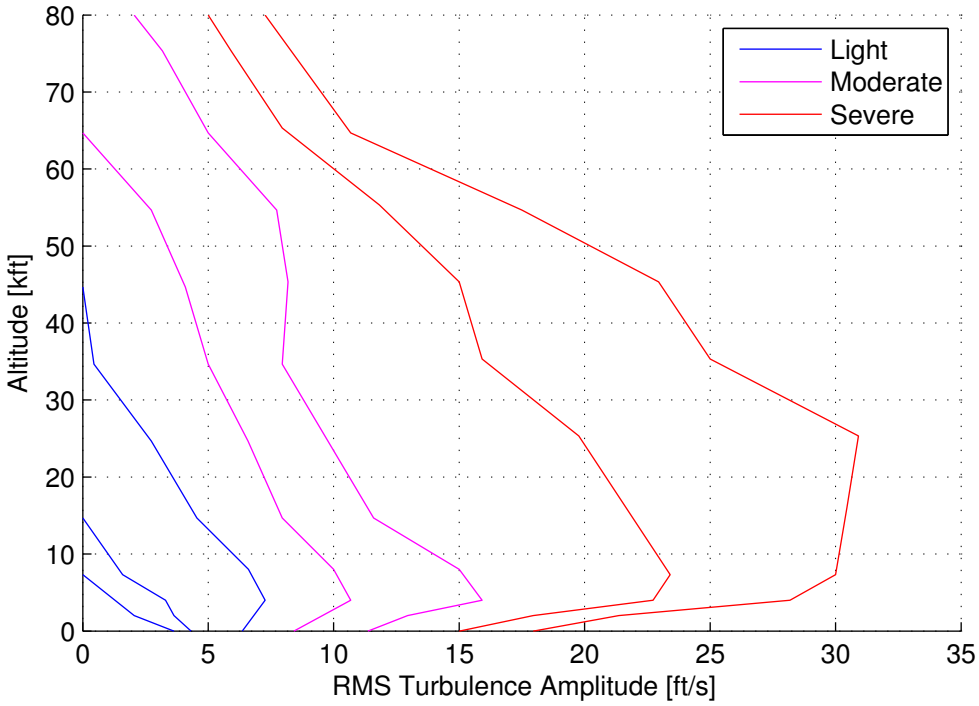

Figure 4.10: Medium/High altitude turbulence intensities (probability of exceedance) used as a lookup table [6].

4.4.2.4 Dryden vs. Von Kármán Models

From the references, it was found that the most significant difference between the two spectra are that:

- the Dryden implementation approximates the spectral characteristics, but is more computationally realisable and convenient; and
- the Von Kármán implementation more accurately describes the spectral characteristics, but is more computationally cumbersome.

The military standards states that the Dryden model retains the essential features found to be useful in many piloted simulator handling quality investigations. It is therefore chosen to be the model used in the simulations for this project.

4.4.2.5 Results

The models were implemented in Simulink and used in HIL simulations the verify the aircraft control systems against these environmental disturbances. Figure 4.11 and 4.12 show the turbulence velocity and angular rate, respectively, for the aircraft flying at approximately a constant altitude of 20m and velocity of 18m/s in a HIL simulation. The settings were configured as $V_{20} = 2.7\text{m/s}$, $\sigma = 10^{-1}$ severity, and the Dryden $(-q,\ +r)$ spectral type.

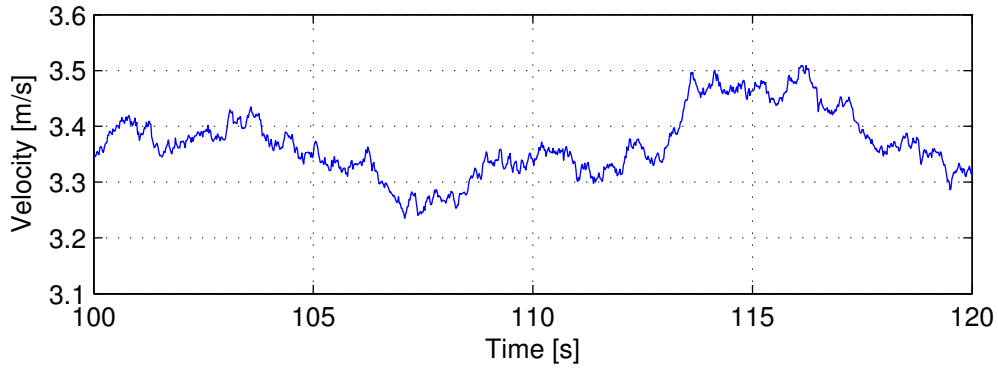

Figure 4.11: Wind turbulence velocity magnitude for straight and level flight.

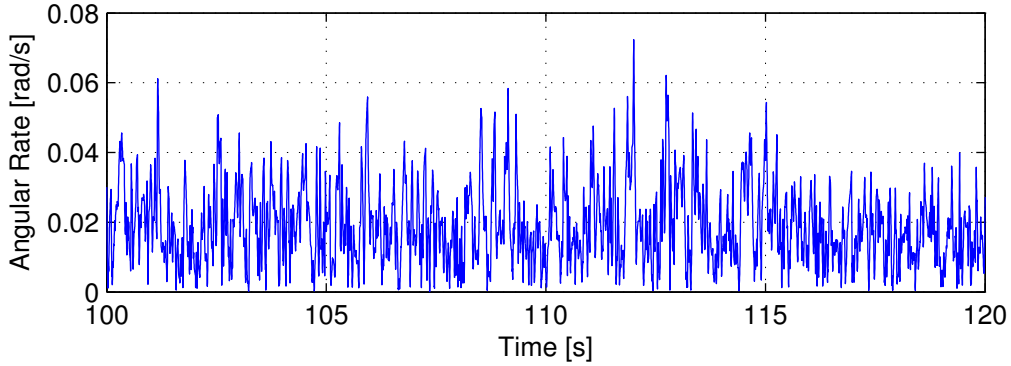

Figure 4.12: Wind turbulence angular rate magnitude for straight and level flight.

4.4.3 Wind Shear

Wind shear is a phenomenon described as gradients in horizontal airspeed at different altitudes. The severity of wind shear increases significantly in unfavourable weather, such as thunderstorms. An illustration of this effect can be seen in Figure 4.13, where the wind speed at a higher altitude is faster than those at a lower altitude. The model presented in this section is based on the specifications given in [47, 48].

The magnitude of the wind shear for the mean wind profile as a function of the aircraft altitude is given by

$$\overline{v}_{shear} = V_{20}\frac{\ln\left(\frac{h}{z_0}\right)}{\ln\left(\frac{20}{z_0}\right)}, \qquad 3 \text{ ft} < h < 1000 \text{ ft} \tag{4.83}$$

where $\overline{v}_{shear}$ is the mean wind speed, V_{20} is the measured wind speed at an altitude of 20ft, h is the current altitude of the aircraft, and z_0 is a constant dependant on the flight phase, which is equal to 0.15ft for Category C flight phases (takeoff, approach, and landing) and 2.0ft for all others. The simulation block that was implemented allows for the setting of each parameter as well as an inertial direction component. Figure 4.14 shows how the wind velocity decreases as the aircraft reduces altitude during the landing phase in a HIL simulation.

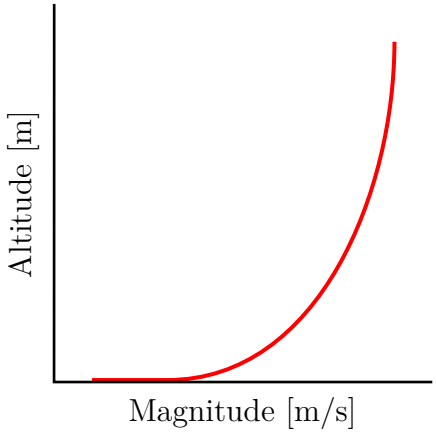

Figure 4.13: Illustration of wind shear as implemented in the simulation model.

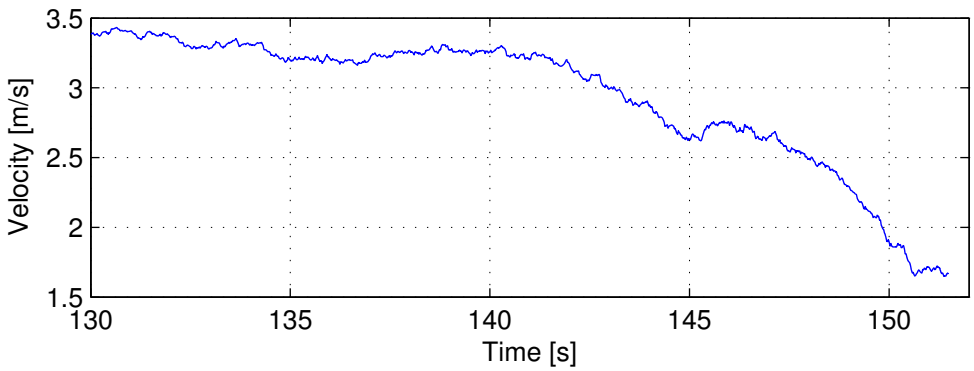

Figure 4.14: Wind velocity magnitude during a landing showing the diminishing effect due to wind shear in a HIL simulation. The noise visible is caused by the turbulence model.

4.4.4 Carrier Landing Disturbance

The military references also describe the following environmental effects related to a carrier based landing:

1. free-air turbulence — independent of the relative aircraft position;
2. steady carrier airwake — a reduction in the steady wind and a predominant upwash aft of the ship, dependent on the aircraft distance from the ship;
3. periodic carrier airwake — a periodic component that varies with the ship pitching frequency, pitch magnitude, wind over the deck and aircraft distance from the ship; and
4. random carrier airwake — random velocity components relating to the ship motion.

These components are all modelled by passing white noise through the appropriate shaping filters. Although these effects are important in the carrier-based landing scenario, they are deemed out of scope for this project. Additionally, the wake created by the platform used in this project should be of a significantly smaller magnitude due to the small size of the vehicles involved and elevated positioning of the platform.

4.5 Summary

This chapter presented the mathematical models used in this project. The different axes and notation systems used were explained on which all subsequent models were based. The six degrees of freedom model was divided into the kinetic and kinematic models. A platform model was derived consisting of very basic modes of motion. The implementation of an environmental model was presented which includes significantly more complexity than previous models used for autonomous landing projects in the ESL.

§ 5

Trim & Stability Analysis

This chapter presents the linearisation of the aircraft model to be used in the control system design, as well as an analysis of the open-loop dynamics and selected trim conditions.

Section 5.1 presents the linearisation of the aircraft dynamic model. Section 5.2 outlines the natural modes of motion of the aircraft related to the open-loop poles of the system. Section 5.3 discusses the glide slope trim conditions. Section 5.4 provides a summary of the chapter.

5.1 Linearisation

When designing the control system, it is useful to linearise the aircraft dynamics around an equilibrium condition to analyse stability, give insight into the aircraft dynamics and allow the use of the tools available for linear systems theory. Although many trim conditions exist, such as a constant bank angle, perpetual barrel roll, or linear climb, the most useful trim condition for a UAV in this application is straight and level flight, which is the condition that the aircraft would be under during the majority of its flight envelope. The linearisation process presented in this section is based on [4].

During the trim flight equilibrium state, the sum of all forces and the sum of all moments acting on the aircraft are zero. The assumption of symmetry in the XZ-plane and level wing flight implies that all lateral motion and control variables $(v,\ p,\ r,\ \phi,\ \delta_a,\ \delta_r)_T$ are zero. This reduces the required solutions to the longitudinal motion and control variables $(u,\ w,\ q,\ \theta,\ \delta_e,\ \delta_t)_T$, or equivalently $(\overline{v},\ \alpha,\ q,\ \theta,\ \delta_e,\ \delta_t)_T$. The variables $(\psi,\ p_N,\ p_E,\ p_D)_T$ are not included as they are arbitrary and do not feed back into the dynamics.

The force and moment equations from Sections 4.2.2, 4.2.3 and 4.2.4 can be used to calculate the trim parameter values. For the trim force and moment diagram shown in Figure 5.1, the trim dynamic pressure and straight and level flight pitch angle are

$$q_{p_T} = \frac{1}{2}\rho\overline{v}_T^2 \tag{5.1}$$

$$\theta_T = \alpha_T \tag{5.2}$$

respectively. Typically, the trim airspeed is a desired known value, therefore q_T is known for a

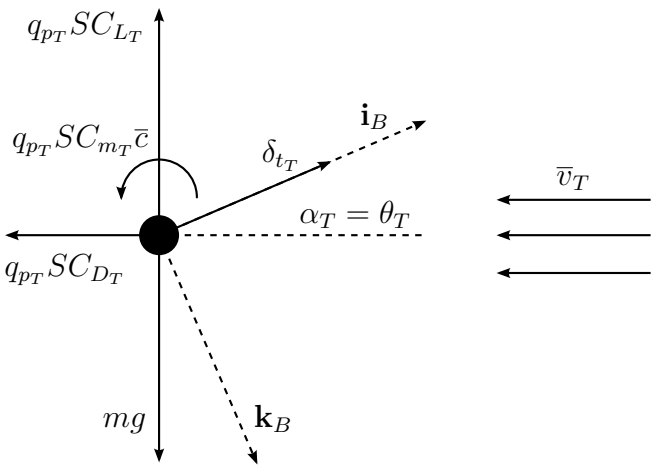

Figure 5.1: Trim forces and moments diagram from the body Y-axis perspective. Adapted from [2].

specific air density at a trim altitude. Since the pitch rate must be zero for straight and level flight, the remaining longitudinal variables $(\alpha, \delta_e, \delta_t)_T$ can now be calculated by balancing the forces and moments in the X- and Z-axes. This results in

$$0 = -q_{p_T} S C_{D_T} \cos\alpha_T + q_{p_T} S C_{L_T} \sin\alpha_T + \delta_{T_T} - mg \sin\theta_T \tag{5.3}$$

$$0 = -q_{p_T} S C_{L_T} \cos\alpha_T - q_{p_T} S C_{D_T} \sin\alpha_T + mg \cos\theta_T \tag{5.4}$$

$$0 = q_{p_T} S \overline{c} C_{m_T} \tag{5.5}$$

By assuming that the trim angle of attack is very small and that the trim lift is an order of magnitude greater than the trim drag, Equations 5.4 and 5.5 can be simplified to

$$0 = -q_{p_T} S C_{L_T} + mg \tag{5.6}$$

$$0 = q_{p_T} S \overline{c} C_{m_T}$$

Substituting Equations 4.44 and 4.46 into Equations 5.5 and 5.6 and rearranging the terms, the lift and pitching moment coefficients can now be calculated as

$$\begin{bmatrix} C_{L_0} \\ C_{m_0} \end{bmatrix} + \begin{bmatrix} C_{L_\alpha} & C_{L_{\delta_e}} \\ C_{m_\alpha} & C_{m_{\delta_e}} \end{bmatrix} \begin{bmatrix} \alpha_T \\ \delta_{e_T} \end{bmatrix} = \begin{bmatrix} \frac{mg}{q_{p_T} S} \\ 0 \end{bmatrix} \tag{5.7}$$

which can be rearranged to

$$\begin{bmatrix} \alpha_T \\ \delta_{e_T} \end{bmatrix} = \begin{bmatrix} C_{L_\alpha} & C_{L_{\delta_e}} \\ C_{m_\alpha} & C_{m_{\delta_e}} \end{bmatrix}^{-1} \begin{bmatrix} \frac{mg}{q_{p_T} S} - C_{L_0} \\ -C_{m_0} \end{bmatrix} \tag{5.8}$$

to solve the trim angle of attack and elevator setting. Finally, rearranging Equation 5.3, the trim thrust can now be calculated with

$$\delta_{t_T} = q_{p_T} S C_{D_T} \cos\alpha_T - q_{p_T} S C_{L_T} \sin\alpha_T + mg \sin\alpha_T \tag{5.9}$$

where

$$C_{D_T} = C_{D_0} + \frac{C_{L_T}^2}{\pi A e} \tag{5.10}$$

The trim flight conditions of the aircraft are now fully defined and the force and moment dynamic models can be linearised around these working points.

In Section 4.2.1.1, six state equations were defined, namely ($\dot{u}$, $\dot{v}$, $\dot{w}$, $\dot{p}$, $\dot{q}$, $\dot{r}$). Two additional state equations can now be defined as

$$\dot{\phi} = p + q\sin\phi\tan\theta + r\cos\phi\tan\theta \tag{5.11}$$

$$\dot{\theta} = q\cos\phi - r\sin\phi \tag{5.12}$$

These eight states form the coupled set of differential equations and describe the primary dynamics of the aircraft. The states (ψ, p_N, p_E, p_D) do not couple back into the above dynamics and are therefore left out of the linearisation process. The states of Equations 4.7 through 4.12, 5.11, and 5.12 can be expressed in state-space form

$$\dot{\boldsymbol{x}} = \boldsymbol{f}(\boldsymbol{x}, \boldsymbol{u}) \tag{5.13}$$

where

$$\boldsymbol{x} = \begin{bmatrix} u & v & w & p & q & r & \phi & \theta \end{bmatrix}^T \tag{5.14}$$

$$\boldsymbol{u} = \begin{bmatrix} \delta_a & \delta_e & \delta_r & \delta_t \end{bmatrix}^T \tag{5.15}$$

and $\boldsymbol{f}$ is the vector function representing the dynamic equations respective to each state. Adding perturbations about trim yields

$$\boldsymbol{x} = \boldsymbol{x}_T + \Delta\boldsymbol{x} \tag{5.16}$$

$$\boldsymbol{u} = \boldsymbol{u}_T + \Delta\boldsymbol{u} \tag{5.17}$$

where

$$\Delta\boldsymbol{x} = \Delta\begin{bmatrix} u & v & w & p & q & r & \phi & \theta \end{bmatrix}^T \tag{5.18}$$

$$\Delta\boldsymbol{u} = \Delta\begin{bmatrix} \delta_a & \delta_e & \delta_r & \delta_t \end{bmatrix}^T \tag{5.19}$$

Equation 5.13 can now be expanded in a Taylor series about the trim conditions, which yields

$$\dot{\boldsymbol{x}}_T + \Delta\dot{\boldsymbol{x}} = \boldsymbol{f}(\boldsymbol{x}_T + \Delta\boldsymbol{x},\ \boldsymbol{u}_T + \Delta\boldsymbol{u}) \tag{5.20}$$

$$= \boldsymbol{f}(\boldsymbol{x}_T, \boldsymbol{u}_T) + \left.\frac{\partial \boldsymbol{f}}{\partial \boldsymbol{x}}\right|_T \Delta\boldsymbol{x} + \left.\frac{\partial \boldsymbol{f}}{\partial \boldsymbol{u}}\right|_T \Delta\boldsymbol{u} + \text{higher order terms} \tag{5.21}$$

By assuming that perturbations from trim are small, the higher order terms can be ignored

and the dynamics approximated as

$$\Delta\dot{\boldsymbol{x}} \approx \boldsymbol{A}_T\Delta\boldsymbol{x} + \boldsymbol{B}_T\Delta\boldsymbol{u} \tag{5.22}$$

where

$$\boldsymbol{A}_T = \left.\frac{\partial \boldsymbol{f}}{\partial \boldsymbol{x}}\right|_T \tag{5.23}$$

$$\boldsymbol{B}_T = \left.\frac{\partial \boldsymbol{f}}{\partial \boldsymbol{u}}\right|_T \tag{5.24}$$

At trim conditions, it should hold that

$$\dot{\boldsymbol{x}}_T = \boldsymbol{f}(\boldsymbol{x}_T, \boldsymbol{u}_T) = 0 \tag{5.25}$$

Linearisation of the dynamics is now only the problem of determining the vector partial derivatives of Equations 5.23 and 5.24. With the state and control vectors as

$$\Delta\boldsymbol{x} = \begin{bmatrix}\Delta\boldsymbol{x}_{lon} & \Delta\boldsymbol{x}_{lat}\end{bmatrix}^T \tag{5.26}$$

$$\Delta\boldsymbol{u} = \begin{bmatrix}\Delta\boldsymbol{u}_{lon} & \Delta\boldsymbol{u}_{lat}\end{bmatrix}^T \tag{5.27}$$

where

$$\Delta\boldsymbol{x}_{lon} = \Delta\begin{bmatrix}u & w & q & \theta\end{bmatrix}^T \tag{5.28}$$

$$\Delta\boldsymbol{x}_{lat} = \Delta\begin{bmatrix}v & p & r & \phi\end{bmatrix}^T \tag{5.29}$$

$$\Delta\boldsymbol{u}_{lon} = \Delta\begin{bmatrix}\delta_e & \delta_t\end{bmatrix}^T \tag{5.30}$$

$$\Delta\boldsymbol{u}_{lat} = \Delta\begin{bmatrix}\delta_a & \delta_r\end{bmatrix}^T \tag{5.31}$$

the dynamics of Equation 5.22 become

$$\begin{bmatrix}\Delta\dot{\boldsymbol{x}}_{lon}\\ \Delta\dot{\boldsymbol{x}}_{lat}\end{bmatrix} = \begin{bmatrix}\boldsymbol{A}_{T_{11}} & \boldsymbol{A}_{T_{12}}\\ \boldsymbol{A}_{T_{21}} & \boldsymbol{A}_{T_{22}}\end{bmatrix}\begin{bmatrix}\Delta\boldsymbol{x}_{lon}\\ \Delta\boldsymbol{x}_{lat}\end{bmatrix} + \begin{bmatrix}\boldsymbol{B}_{T_{11}} & \boldsymbol{B}_{T_{12}}\\ \boldsymbol{B}_{T_{21}} & \boldsymbol{B}_{T_{22}}\end{bmatrix}\begin{bmatrix}\Delta\boldsymbol{u}_{lon}\\ \Delta\boldsymbol{u}_{lat}\end{bmatrix} \tag{5.32}$$

Since the aircraft is symmetrical about its XZ-plane, the perturbations in the longitudinal dynamics will not affect the lateral dynamics, and it can therefore be stated that

$$\boldsymbol{A}_{T_{21}} = \boldsymbol{0} \tag{5.33}$$

$$\boldsymbol{B}_{T_{21}} = \boldsymbol{0} \tag{5.34}$$

If deviations from trim are small as required by the linearisation assumption, and in particular small deviations in roll angle, a good approximation is that

$$\boldsymbol{A}_{T_{12}} \approx \boldsymbol{0} \tag{5.35}$$

$$\boldsymbol{B}_{T_{12}} \approx \mathbf{0} \tag{5.36}$$

The decoupled longitudinal and lateral dynamics are now, respectively,

$$\Delta\dot{\boldsymbol{x}}_{lon} = \boldsymbol{A}_{T_{11}}\Delta\boldsymbol{x}_{lon} + \boldsymbol{B}_{T_{11}}\Delta\boldsymbol{u}_{lon} \tag{5.37}$$

$$\Delta\dot{\boldsymbol{x}}_{lat} = \boldsymbol{A}_{T_{22}}\Delta\boldsymbol{x}_{lat} + \boldsymbol{B}_{T_{22}}\Delta\boldsymbol{u}_{lat} \tag{5.38}$$

The dynamics can now be expanded and rewritten as

$$\begin{bmatrix}\dot{u}\\ \dot{w}\\ \dot{q}\\ \dot{\theta}\end{bmatrix} = \begin{bmatrix}\frac{\partial\dot{u}}{\partial u} & \frac{\partial\dot{u}}{\partial w} & \frac{\partial\dot{u}}{\partial q} & \frac{\partial\dot{u}}{\partial\theta}\\ \frac{\partial\dot{w}}{\partial u} & \frac{\partial\dot{w}}{\partial w} & \frac{\partial\dot{w}}{\partial q} & \frac{\partial\dot{w}}{\partial\theta}\\ \frac{\partial\dot{q}}{\partial u} & \frac{\partial\dot{q}}{\partial w} & \frac{\partial\dot{q}}{\partial q} & \frac{\partial\dot{q}}{\partial\theta}\\ \frac{\partial\dot{\theta}}{\partial u} & \frac{\partial\dot{\theta}}{\partial w} & \frac{\partial\dot{\theta}}{\partial q} & \frac{\partial\dot{\theta}}{\partial\theta}\end{bmatrix}\begin{bmatrix}u\\ w\\ q\\ \theta\end{bmatrix} + \begin{bmatrix}\frac{\partial\dot{u}}{\partial\delta_e} & \frac{\partial\dot{u}}{\partial\delta_t}\\ \frac{\partial\dot{w}}{\partial\delta_e} & \frac{\partial\dot{w}}{\partial\delta_t}\\ \frac{\partial\dot{q}}{\partial\delta_e} & \frac{\partial\dot{q}}{\partial\delta_t}\\ \frac{\partial\dot{\theta}}{\partial\delta_e} & \frac{\partial\dot{\theta}}{\partial\delta_t}\end{bmatrix}\begin{bmatrix}\delta_e\\ \delta_t\end{bmatrix} \tag{5.39}$$

$$\begin{bmatrix}\dot{v}\\ \dot{p}\\ \dot{r}\\ \dot{\phi}\end{bmatrix} = \begin{bmatrix}\frac{\partial\dot{v}}{\partial v} & \frac{\partial\dot{v}}{\partial p} & \frac{\partial\dot{v}}{\partial r} & \frac{\partial\dot{v}}{\partial\phi}\\ \frac{\partial\dot{p}}{\partial v} & \frac{\partial\dot{p}}{\partial p} & \frac{\partial\dot{p}}{\partial r} & \frac{\partial\dot{p}}{\partial\phi}\\ \frac{\partial\dot{r}}{\partial v} & \frac{\partial\dot{r}}{\partial p} & \frac{\partial\dot{r}}{\partial r} & \frac{\partial\dot{r}}{\partial\phi}\\ \frac{\partial\dot{\phi}}{\partial v} & \frac{\partial\dot{\phi}}{\partial p} & \frac{\partial\dot{\phi}}{\partial r} & \frac{\partial\dot{\phi}}{\partial\phi}\end{bmatrix}\begin{bmatrix}v\\ p\\ r\\ \phi\end{bmatrix} + \begin{bmatrix}\frac{\partial\dot{v}}{\partial\delta_a} & \frac{\partial\dot{v}}{\partial\delta_r}\\ \frac{\partial\dot{p}}{\partial\delta_a} & \frac{\partial\dot{p}}{\partial\delta_r}\\ \frac{\partial\dot{r}}{\partial\delta_a} & \frac{\partial\dot{r}}{\partial\delta_r}\\ \frac{\partial\dot{\phi}}{\partial\delta_a} & \frac{\partial\dot{\phi}}{\partial\delta_r}\end{bmatrix}\begin{bmatrix}\delta_a\\ \delta_r\end{bmatrix} \tag{5.40}$$

for longitudinal and lateral dynamics respectively.

In the state vector equation, it is common to work with the velocity magnitude and angle of attack rather than axial and normal velocity. For the trim condition chosen as straight and level flight and given that the angle of attack is small, the approximations can be made that

$$\overline{v} = \sqrt{u^2 + v^2 + w^2} \approx \sqrt{u^2} = u \tag{5.41}$$

$$w \approx u\alpha = (u_T + \Delta u)\alpha \approx u_T\alpha \approx v_T\alpha \tag{5.42}$$

The derivatives of Equations 5.41 and 5.42 can then be calculated as

$$\dot{\overline{v}} = \dot{u} \tag{5.43}$$

$$\dot{w} = v_T\dot{\alpha} \tag{5.44}$$

In the state vector equation, it is also common to work with the angle of sideslip rather than the lateral velocity. For the trim condition chosen as straight and level flight and given that the angle of sideslip is small, the approximations can be made that

$$v = \overline{v}\sin\beta \approx \overline{v}\beta = (\overline{v}_T + \overline{v})\beta \approx \overline{v}_T\beta \tag{5.45}$$

The derivative of Equation 5.45 can then be calculated as

$$\dot{v} = \overline{v}_T\dot{\beta} \tag{5.46}$$

Finally, with these simplifications, the partial derivatives can be calculated. The end result of this process yield the linearised models as

$$\begin{bmatrix} \dot{\overline{v}} \\ \dot{\alpha} \\ \dot{q} \\ \dot{\theta} \end{bmatrix} = \begin{bmatrix} \frac{\rho \overline{v}_T S C_{X_T}}{m} & \frac{q_{p_T} S}{m}\left(C_{L_\alpha}\alpha_T + C_{L_T} - \frac{2C_{L_T}C_{L_\alpha}}{\pi A e}\right) & 0 & -g\cos\theta_T \\ -\frac{\rho S C_{L_T}}{m} & -\frac{q_{p_T} S}{m\overline{v}_T}C_{L_\alpha} & 1 - \frac{q_{p_T} S}{m\overline{v}_T}\frac{\overline{c}}{2\overline{v}_T}C_{L_Q} & -\frac{g}{\overline{v}_T}\sin\theta_T \\ 0 & \frac{q_{p_T} S\overline{c}}{I_{yy}}C_{m_\alpha} & \frac{q_{p_T} S\overline{c}}{I_{yy}}\frac{\overline{c}}{2\overline{v}_T}C_{m_Q} & 0 \\ 0 & 0 & 1 & 0 \end{bmatrix} \begin{bmatrix} \overline{v} \\ \alpha \\ q \\ \theta \end{bmatrix} + \begin{bmatrix} 0 & \frac{1}{m} \\ -\frac{q_{p_T} S}{m\overline{v}_T}C_{L_{\delta_e}} & 0 \\ \frac{q_{p_T} S\overline{c}}{I_{yy}}C_{m_{\delta_e}} & 0 \\ 0 & 0 \end{bmatrix} \begin{bmatrix} \delta_e \\ \delta_t \end{bmatrix} \tag{5.47}$$

$$\begin{bmatrix} \dot{\beta} \\ \dot{p} \\ \dot{r} \\ \dot{\phi} \end{bmatrix} = \begin{bmatrix} \frac{q_{p_T} S}{m\overline{V}_T}C_{y_\beta} & \frac{q_{p_T} S}{m\overline{v}_T}\frac{b}{2\overline{v}_T}C_{y_P} & \frac{q_{p_T} S}{m\overline{v}_T}C_{y_R} - 1 & \frac{g}{\overline{v}_T}\cos\theta_T \\ \frac{q_{p_T} Sb}{I_{xx}}C_{l_\beta} & \frac{q_{p_T} Sb}{I_{xx}}\frac{b}{2\overline{v}_T}C_{l_P} & \frac{q_{p_T} Sb}{I_{xx}}\frac{b}{2\overline{V}_T}C_{l_R} & 0 \\ \frac{q_{p_T} Sb}{I_{zz}}C_{n_\beta} & \frac{q_{p_T} Sb}{I_{zz}}\frac{b}{2\overline{v}_T}C_{n_P} & \frac{q_{p_T} Sb}{I_{zz}}\frac{b}{2\overline{v}_T}C_{n_R} & 0 \\ 0 & 1 & \tan\theta_T & 0 \end{bmatrix} \begin{bmatrix} \beta \\ p \\ r \\ \phi \end{bmatrix} + \begin{bmatrix} \frac{q_{p_T} S}{m\overline{v}_T}C_{y_{\delta_a}} & \frac{q_{p_T} S}{m\overline{v}_T}C_{y_{\delta_r}} \\ \frac{q_{p_T} Sb}{I_{xx}}C_{l_{\delta_a}} & \frac{q_{p_T} Sb}{I_{xx}}C_{l_{\delta_r}} \\ \frac{q_{p_T} Sb}{I_{zz}}C_{n_{\delta_a}} & \frac{q_{p_T} Sb}{I_{zz}}C_{n_{\delta_r}} \\ 0 & 0 \end{bmatrix} \begin{bmatrix} \delta_a \\ \delta_r \end{bmatrix} \tag{5.48}$$

for the longitudinal and lateral model, respectively.

5.2 Analysis of the Linearised Dynamics

In order to design a control system for the aircraft, knowledge of the system dynamics is required. This involves obtaining the poles and zeroes of the plant, which governs the modes of motion of the system. The analysis in this section is based on [4] unless indicated otherwise.

For this project, the state-space form is predominantly used which is represented by the vectors and matrices

$$\dot{\boldsymbol{x}} = \boldsymbol{A}\boldsymbol{x} + \boldsymbol{B}\boldsymbol{u} \tag{5.49}$$

$$\boldsymbol{y} = \boldsymbol{C}\boldsymbol{x} + \boldsymbol{D} \tag{5.50}$$

for both the longitudinal and lateral systems. Matrix $\boldsymbol{C}$ is used to extract the desired output state, while the feed-forward matrix $\boldsymbol{D}$ is generally zero. Applying the Laplace transform to both equations yield

$$s\boldsymbol{X}(s) = \boldsymbol{A}\boldsymbol{X}(s) + \boldsymbol{B}\boldsymbol{U}(s) \tag{5.51}$$

$$\boldsymbol{Y}(s) = \boldsymbol{C}\boldsymbol{X}(s) \tag{5.52}$$

Rearrangement and substitution of $\boldsymbol{X}(s)$ yields the transfer function

$$\frac{\boldsymbol{Y}(s)}{\boldsymbol{U}(s)} = \boldsymbol{C}\left(s\boldsymbol{I} - \boldsymbol{A}\right)^{-1}\boldsymbol{B} \tag{5.53}$$

$$= \frac{\boldsymbol{C}\mathrm{adj}\left(s\boldsymbol{I} - \boldsymbol{A}\right)\boldsymbol{B}}{\det\left(s\boldsymbol{I} - \boldsymbol{A}\right)} \tag{5.54}$$

The characteristic equation shows the dynamics of the system and is obtained by determining

where the transfer function tends to infinity. Therefore, the poles of the system can be obtained by solving for the values of s in

$$\det\left(s\boldsymbol{I} - \boldsymbol{A}\right) = 0 \tag{5.55}$$

The subsequent sections use Equations 5.47, 5.48 and 5.55 to determine the poles of the longitudinal and lateral systems.

For a given complex pole pair $s = \sigma + j\omega$, the natural frequency and damping ratio can be calculated, respectively, by

$$\omega_n = \sqrt{\sigma^2 + \omega^2} \tag{5.56}$$

$$\zeta = \cos(\theta) \tag{5.57}$$

where θ is the angle between the real (σ) and imaginary ($j\omega$) parts of the vector and the imaginary axis.

5.2.1 Natural Longitudinal Dynamics

Substitution of the aircraft parameters into Equation 5.47 yield

$$\boldsymbol{A}_{lon} = \begin{bmatrix} -0.1214 & 13.4969 & 0 & -9.7616 \\ -0.0606 & -5.8739 & 0.9019 & -0.0540 \\ 0 & -64.3073 & -7.3940 & 0 \\ 0 & 0 & 1.0000 & 0 \end{bmatrix} \tag{5.58}$$

$$\boldsymbol{B}_{lon} = \begin{bmatrix} 0 & 0.1637 \\ -0.5571 & 0 \\ -92.5869 & 0 \\ 0 & 0 \end{bmatrix} \tag{5.59}$$

From Equations 5.55 and 5.58, the open-loop poles can be obtained as

$$s_{lon_1} = -6.6458 \pm 7.6175j \tag{5.60}$$

$$s_{lon_2} = -0.0489 \pm 0.6045j \tag{5.61}$$

The poles are shown graphically on an s-plane map in Figure 5.2.

5.2.1.1 Short Period Mode

The short period mode describes the tendency of the aircraft to realign itself longitudinally with its velocity vector through incoming airflow after perturbation. Its characteristics are determined by the high frequency complex pole pair at s_{lon_1}. In a statically stable aircraft, the restoring pitching moment (quantified by C_{m_α}) will rotate the aircraft back towards its trim

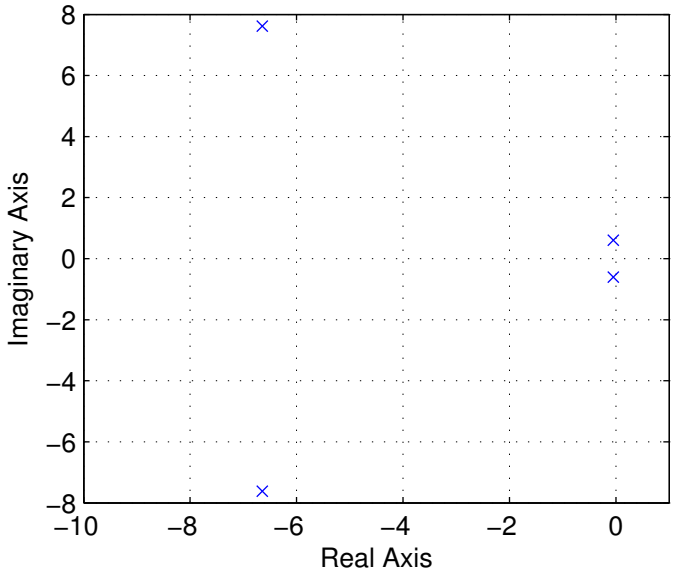

Figure 5.2: Open-loop poles of the longitudinal aircraft model showing two complex pole pairs on an s-plane.

position, while the damping from the pitch rate motion (quantified by C_{m_q}) will remove energy from the system, causing dynamically stable behaviour. For this aircraft, the short period mode is naturally very stable and well damped. It has a natural frequency and damping ratio of

$$\omega_n = 10.1091 \text{ rad/s} \tag{5.62}$$

$$\zeta = 0.6574 \tag{5.63}$$

5.2.1.2 Phugoid Mode

The phugoid mode describes the tendency of the aircraft to exchange its potential and kinetic energy after perturbation. Its characteristics are determined by the low frequency complex pole pair at s_{lon_2}. This exchange between kinetic energy (or velocity, which affects lift) and potential energy (or altitude) causes the aircraft to follow a sinusoidal flight trajectory. For this aircraft, the phugoid mode is almost marginally stable and very poorly damped. It has a natural frequency and damping ratio of

$$\omega_n = 0.6065 \text{ rad/s} \tag{5.64}$$

$$\zeta = 0.0806 \tag{5.65}$$

5.2.2 Natural Lateral Dynamics

Substitution of the aircraft parameters into Equation 5.48 yields

$$\boldsymbol{A}_{lat} = \begin{bmatrix} -0.2046 & 0.0089 & -0.8611 & 0.5423 \\ -22.4182 & -8.1595 & 2.6947 & 0 \\ 16.2790 & -0.4486 & -0.9363 & 0 \\ 0 & 1.0000 & 0.0997 & 0 \end{bmatrix} \tag{5.66}$$

$$\boldsymbol{B}_{lat} = \begin{bmatrix} 0.0041 & 0.1143 \\ -94.4846 & 0.7748 \\ 2.4473 & -11.4618 \\ 0 & 0 \end{bmatrix} \tag{5.67}$$

From Equations 5.55 and 5.66, the open-loop poles can be obtained as

$$s_{lat_1} = -8.3048 \tag{5.68}$$

$$s_{lat_2} = -0.5699 \pm 4.0617j \tag{5.69}$$

$$s_{lat_3} = 0.1441 \tag{5.70}$$

The poles are shown graphically on an s-plane map in Figure 5.3.

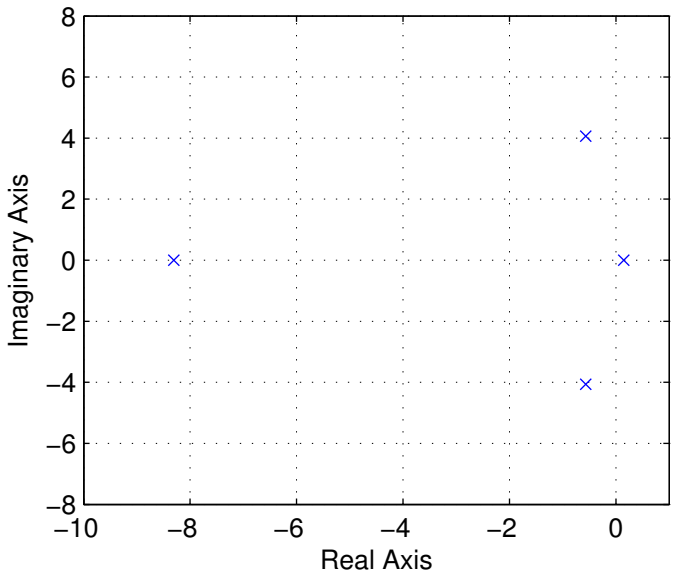

Figure 5.3: Open-loop poles of the lateral aircraft model showing two real poles and one complex pole pair on an s-plane.

5.2.2.1 Roll Mode

The roll mode describes the roll rate dynamics of the aircraft after perturbation. Its characteristics are determined by the high frequency real pole at s_{lat_1}. Upon disturbance, the roll rate will quickly grow until the natural damping provided by the wing (quantified by C_{l_p}) counters

the rolling moment disturbance, causing the aircraft to continue flying at a constant roll rate. For this aircraft, the roll mode is very stable and has a natural frequency of

$$\omega_n = 8.3048 \text{ rad/s} \tag{5.71}$$

5.2.2.2 Dutch Roll Mode

The Dutch roll mode describes the tendency of the aircraft to realign itself laterally with its velocity vector through incoming airflow after perturbation. Its characteristics are determined by the complex pole pair at s_{lat_2}. The vertical stabiliser causes a restoring yaw moment (quantified by C_{n_β}) which rotates the nose into the direction of incoming airflow while the yaw rate (quantified by C_{n_r}) provides damping. Due to the two wings experiencing differential velocities during the yawing motion, they each contribute differentially in terms of lift and drag (quantified partially by C_{l_r} and C_{n_r}). This causes additional roll rate perturbations which in turn causes differential lift and drag perturbations through C_{l_p} and C_{n_p}, where the drag additions cause additional damping. With these effects combined, the aircraft will experience oscillations in both yaw and roll along the X-axis. For this aircraft, the Dutch roll mode is stable and poorly damped. It has a natural frequency and damping ratio of

$$\omega_n = 4.1015 \text{ rad/s} \tag{5.72}$$

$$\zeta = 0.1389 \tag{5.73}$$

5.2.2.3 Spiral Mode

The spiral mode describes the tendency of the aircraft to restore itself to or diverge from wings level flight after perturbation. Its characteristics are determined by the low frequency real pole at s_{lat_3}. Upon disturbance, the effect on roll angle will either relieve or worsen the disturbance, depending on the sign of C_{l_β}, which is influenced by factors such as dihedral, wing sweep and high or low wing design. The induced roll angle also causes differential wing velocity and therefore differential lift (quantified by C_{l_r}), which tends to amplify the disturbance. For this aircraft, the spiral mode is slightly unstable and has a natural frequency of

$$\omega_n = 0.1441 \text{ rad/s} \tag{5.74}$$

5.3 Glide Path Angle Tracking

In simulation, it was found that the longitudinal control system was unable to maintain the airspeed of 16m/s and flight path angle of -8.2° commanded for the first steep glide path slope as shown in Table 5.1. Instead, the control system settled to an undesired steady state which saturated as the glide slope became steeper. This can be ascribed to the following:

1. The aircraft is unable to give negative thrust and limits at the minimum thrust value that can be commanded. In Chapter 6, it will be seen that the airspeed is mainly controlled

by the thrust, and to keep the airspeed from increasing in a steep glide slope, the thrust must be reduced significantly.

2. The controller starts reducing the aircraft angle of attack to maintain the flight path angle, but in doing so decreases the drag and thereby increases the velocity.

Table 5.1: Trim conditions over flight path angle with $\overline{v}_c = 16$m/s.

γ_T [°]	$\overline{v}_T$ $[m/s]$	α_T [°]	θ_t [°]	δ_{t_T} $[N]$	δ_{e_T} [°]	$\dot{h}$ $[m/s]$	γ [°]
0	16.00	7.316	7.316	11.10	-5.081	0.000	0.000
-1	16.00	7.331	6.331	10.02	-5.092	-0.279	-1.000
-2	16.00	7.344	5.344	8.933	-5.101	-0.558	-2.000
-3	16.00	7.355	4.355	7.846	-5.108	-0.837	-2.999
-4	16.00	7.363	3.363	6.758	-5.114	-1.116	-3.997
-5	16.00	7.370	2.370	5.669	-5.119	-1.394	-4.994
-6	16.00	7.374	1.374	4.581	-5.122	-1.672	-5.989
-7	16.00	7.376	0.376	3.493	-5.123	-1.950	-6.983
-8	16.00	7.376	-0.624	2.406	-5.123	-2.227	-7.974
-9	16.51	6.920	-1.613	2.225	-4.807	-2.450	-8.503
-10	16.51	6.920	-1.612	2.225	-4.806	-2.450	-8.501

The results from this simulation prompted the decision to change from a steep and subsequent shallow glide slope to a single glide slope approach for the autonomous landing state machine as discussed in Section 3.3.1.2.

5.4 Summary

This chapter presented the linearised aircraft dynamics in order to use it in the design of the control systems. The natural modes of motion of the aircraft related to the open-loop poles of the system were discussed. A trim condition analysis showed that the longitudinal controllers were unable to follow a steep glide slope while regulating both flight path angle and airspeed, prompting the change towards a single glide slope approach for the autonomous landing.

§ 6

Control System Design

This chapter describes the controller architectures and presents the controller designs for both longitudinal and lateral control systems.

Section 6.1 gives an overview of the control architectures and why they were chosen for this project, as well as how the controllers fit together. Section 6.2 details the design of the longitudinal controllers. Section 6.3 details the design of the lateral controllers. Section 6.4 provides a summary of the chapter.

6.1 Architecture Overview

The autonomous flight control and landing problem is, as a whole, a very complex task. It is often divided into small separate problems, each evaluated and solved individually. When all the separate problems are solved, the subsystems are merged and integrated to form one all-encompassing controller structure. The structure for the controller used in this project is illustrated in Figure 6.1 and discussed in this chapter.

For this project, it was decided to not investigate very complex control methods such as dynamic inversion or robust control techniques such as H_2/H_∞. A summary of research using these methods was discussed in Chapter 1 and has achieved results of varying success. In terms of cost, it was decided that control methods of this complexity would significantly increase the scope of research for this project, as well as progressing into further complexities. This would also incur additional time penalties as research, implementation and testing would have more uncertainties and would not further the goals of the research environment.

It was decided to investigate the Total Energy Control System method for longitudinal control in order to diversify the longitudinal control knowledge of the ESL. Although complex controller design methods are possible, it was decided to attempt simple methods to build a foundation for future projects. This control system architecture includes controllers for

1. altitude;
2. climb rate;
3. flight path angle;

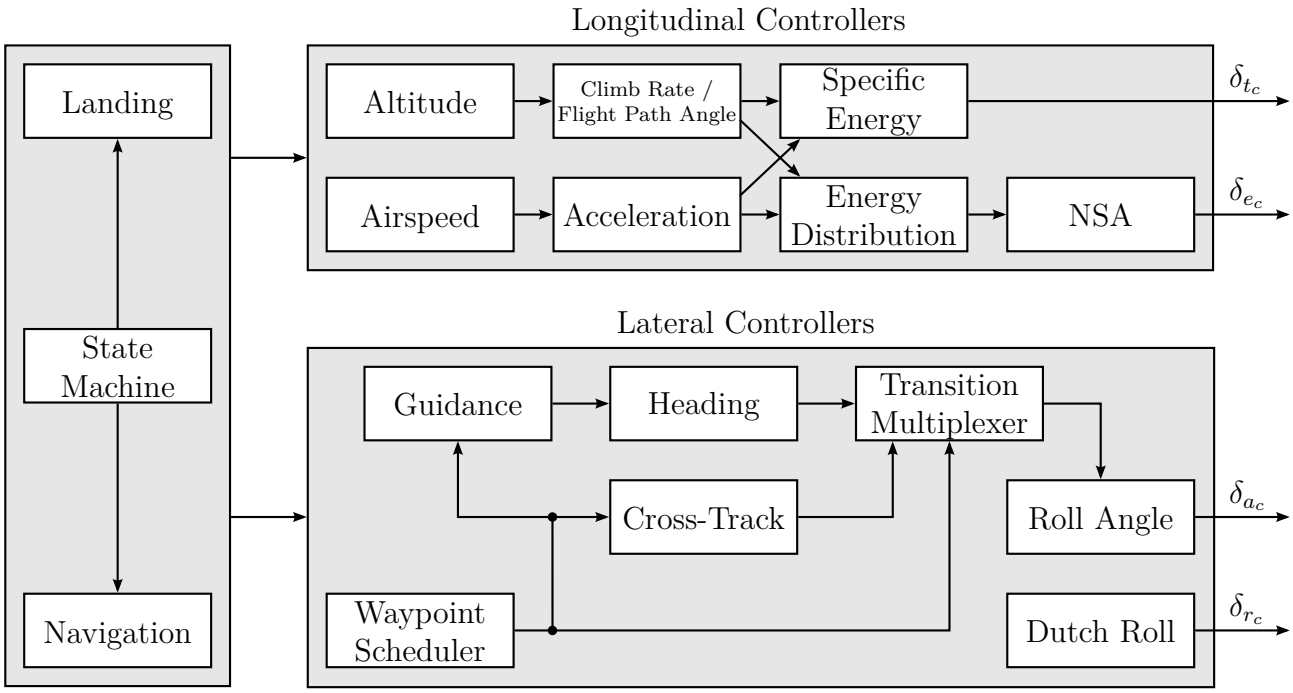

Figure 6.1: Overview of the control architecture.

4. airspeed;
5. acceleration;
6. total energy;
7. total energy distribution;
8. pitch angle; and
9. pitch rate.

Classical controller methods were to be used for the lateral controllers as these are already well understood in the ESL through previous projects. These controllers can be designed using the root locus method with successive loop closure. This control system architecture includes controllers for

1. Dutch roll;
2. roll angle;
3. heading;
4. guidance; and
5. waypoint scheduling.

The GCS, as discussed in Chapter 2, is used to dynamically upload commands and parameters to the aircraft in mid-flight. Commands are interpreted by the state machine, the core of the decision-making on the aircraft. Parameters and waypoints are kept in memory in the MCU

and are overwritten with new data as it is uploaded from the GCS. Since the state machine determines the landing waypoints, it also has the authority to modify waypoint parameters as required, determined by the distance and altitude from the intended touchdown point. When the state machine determines the final reference values, they are transferred to the longitudinal and lateral controllers for further processing. These controllers are discussed in more detail in Sections 6.2 and 6.3.

6.2 Longitudinal Control

In conventional aircraft controllers, the longitudinal controller is responsible for regulating the altitude and airspeed values to track the given references. While many such controllers exist and have been successfully implemented, the focus of this project was to use energy principles to expand and diversify knowledge inside the ESL.

The concept of an energy controller was pioneered and patented by Lambregts [7] in 1985, resulting in the longitudinal TECS architecture. Initially developed for large passenger aircraft, the main purpose of this controller is to balance the kinetic and potential energy of the aircraft with an integrated and simplified control system architecture.

Earlier flight systems were developed in a piecemeal fashion which lacked proper integration. Several deficiencies in these controllers were highlighted verbatim as [7]:

1. *low reliability and availability*;
2. *high procurement and maintenance costs*;
3. *excessive number of sensors*;
4. *undesired flight path and speed control coupling*;
5. *command capture overshoots and poor tracking*;
6. *excessive controller activity and turbulence resulting in poor ride quality, engine wear and waste of fuel*;
7. *loss of speed control when thrust limits*;
8. *mode switching transients*;
9. *inadequate stall/overspeed protection*; and
10. *unsatisfactory performance in wind shear.*

At the time of this invention, there was a need for a fully integrated vertical flight control system that could provide coordinated elevator and throttle control to overcome known limitations. TECS solved some of these issues by using the throttle to control the total energy error of the aircraft and the elevator to control the energy distribution error between flight path angle and airspeed. The core TECS concept is detailed in Section 6.2.1 according to [7] with a simplified overview as shown in Figure 6.2. Lambregts also made the following claims verbatim:

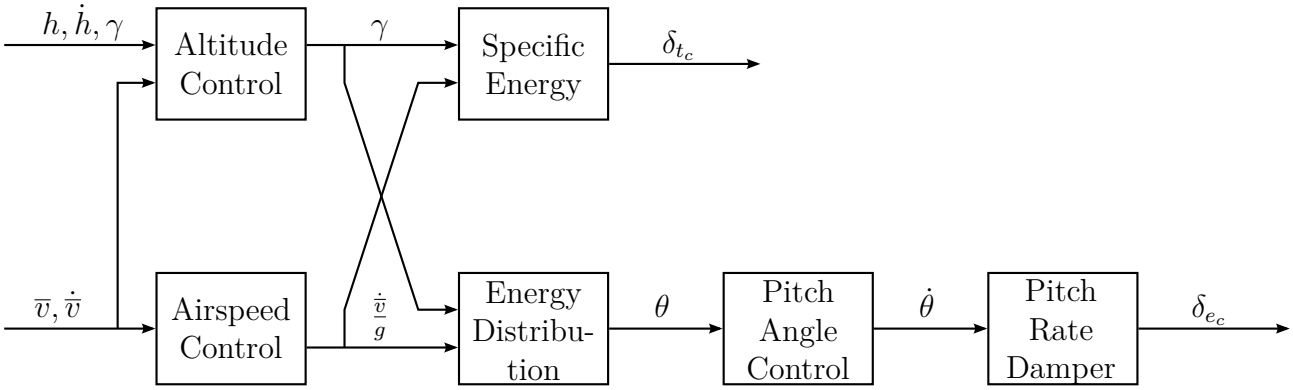

Figure 6.2: Simplified TECS structure showing the separate controller blocks.

1. *all flight control modes share the same generalised thrust and elevator signal processing*;

2. *the forward feed of flight path and speed commands to both throttle and elevator command processors, using signal normalisations based on energy considerations, provides a mechanism for developing precisely coordinated thrust and elevator commands that decouple the the flight path response from the speed commands and the speed response from the flight path commands*;

3. *since thrust is only used to control the total aircraft energy, flight path perturbation will not induce throttle activity*;

4. *all feedback loops, except the extreme outer loops, are "hard-wired" and therefore identical for each mode, yielding uniform control characteristics for all control modes*;

5. *only the outer loop error feedback signal, which is characteristic for each mode and processed in the integral signal path, is switched. As a result, control switching between each mode is accomplished transient free, without the need for synchronisation circuitry and reinitialisation of the command integrators*;

6. *step changes in the flight path or speed commands result in initial rate responses of the controllers, making the command capture responses smooth*;

7. *identical outer loops gains K_h and K_v are used to normalise the altitude and speed error signals into energy related errors. As a result, the throttle responds minimally in case of a "zoom" manoeuvre (simultaneous climb and deceleration command)*;

8. *the outer loop altitude and vertical speed normalisation provides inherent gain scheduling, yielding virtually constant control bandwidth and damping over the entire flight regime*;

9. *as a result of the use of a generalised control law processing scheme, duplication of functions is avoided and control law reconfiguration from one mode to another is minimised. As a result, the system's software and hardware demands are sharply reduced compared to previous state-of-the-art systems*; and

10. *the generalised and integrated speed and flight path control law based on the total energy control concept makes the design largely aircraft independent. Only the inner loop thrust and elevator control need to be designed specifically for each aircraft. Thus large time and money savings accrue when applying the design to other aircraft.*

6.2.1 TECS Concept

Thrust is the most effective actuator to control the energy state of the aircraft in all flight conditions, while the elevator provides an effective means to modulate the energy distribution between flight path angle and airspeed, thereby stabilising the attitude of the aircraft during flight. The total energy of the aircraft E, which is the sum of the potential and kinetic energy components, can be expressed as

$$E = mgh + \frac{1}{2}m\overline{v}^2 \tag{6.1}$$

where m is the mass, g is the gravitational acceleration, h is the current altitude, and $\overline{v}$ is the current velocity. By assuming a constant weight of $W = mg$, Equation 6.1 can be rewritten and differentiated by time to form

$$E = Wh + \frac{1}{2}\frac{W\overline{v}^2}{g} \tag{6.2}$$

$$\dot{E} = W\left(\dot{h} + \frac{\overline{v}\,\dot{\overline{v}}}{g}\right) \tag{6.3}$$

where $\dot{E}$ is the total energy rate, $\dot{h}$ is the climb rate and $\dot{\overline{v}}$ is the acceleration. The flight path angle γ can be calculated as

$$\sin\gamma = \frac{\dot{h}}{\overline{v}} \tag{6.4}$$

By using the small angle approximation $\sin\gamma \approx \gamma$, Equation 6.4 can be linearised to

$$\gamma = \frac{\dot{h}}{\overline{v}} \tag{6.5}$$

Substituting Equation 6.5 into Equation 6.3 and scaling the result by $\overline{v}$, an energy rate equation normalised by velocity is obtained and can be expressed as

$$\frac{\dot{E}}{\overline{v}} = W\left(\gamma + \frac{\dot{\overline{v}}}{g}\right) \tag{6.6}$$

This reveals that, at a given airspeed, the energy rate of change of the aircraft is dependant only on the flight path angle and longitudinal acceleration.

The second law of Newton states that the total force applied to an object is equal to the product of its mass and acceleration, or mathematically as $F = ma$. The longitudinal equations

of motion of the aircraft is then expressed, mass-acceleration first, as

$$\frac{W}{g}\dot{\overline{v}} = \delta_t - F_d - W\sin\gamma \tag{6.7}$$

where δ_t is the total thrust applied and F_d is the total resulting drag. By again assuming a small flight path angle, Equation 6.7 can be rewritten as

$$W\left(\gamma + \frac{\dot{\overline{v}}}{g}\right) = \delta_t - F_d \tag{6.8}$$

This resembles Equation 6.6, concluding that the energy rate of change of the aircraft is proportional to the difference between thrust and drag. The required thrust can then be written as

$$\delta_{t_{req}} = W\left(\gamma + \frac{\dot{\overline{v}}}{g}\right) + F_d \tag{6.9}$$

$$= \frac{\dot{E}}{\overline{v}} + F_d \tag{6.10}$$

$$= \frac{\dot{E}_s W}{\overline{v}} + F_d \tag{6.11}$$

where $\dot{E}_s$ is the specific energy rate of the aircraft.

For a given airspeed and drag configuration, the incremental thrust required is directly proportional to the aircraft weight and the sum of the incremental flight path angle and the longitudinal acceleration. At a specific thrust level, it is possible to exchange between flight path angle and acceleration by using only the elevator. It therefore becomes apparent that a flight path angle and speed control concept is obtained in the form of total specific energy rate, where the throttle is driven until the total specific energy rate error relative to the target flight path angle and acceleration is zero. This controller equation is given by

$$\dot{E}_{se} = \gamma_e + \frac{\dot{\overline{v}}_e}{g} \tag{6.12}$$

where $\dot{E}_{se}$ is the total specific energy rate error, γ_e is the error between the reference and present flight path angle as expressed by $\gamma_e = \gamma_c - \gamma$, and $\dot{\overline{v}}_e$ is the error between the reference and present acceleration as expressed by $\dot{\overline{v}}_e = \dot{\overline{v}}_c - \dot{\overline{v}}$. The elevator is to be driven until the energy rate distribution error relative to the target flight path angle and acceleration is zero. This controller equation is given by

$$\dot{D}_e = -\gamma_e + \frac{\dot{\overline{v}}_e}{g} \tag{6.13}$$

where $\dot{D}_e$ is the energy rate distribution error between the potential and kinetic energy contributions in relative energy terms.

Using these control mechanisms, the altitude and speed errors are now scaled in relative

energy terms. The specific energy rate error is used directly in the computation of the thrust command δ_t, and the energy rate distribution error is similarly applied to the elevator command δ_e. This forms a generalised total energy based thrust and elevator command processor that can be used by multiple aircraft flight modes by simply coupling in the correct reference at the desired loop. This control scheme allows the aircraft to be precisely guided from one flight path angle and longitudinal acceleration to new reference values in any combination of specific speed and flight path control modes and under any flight condition.

In most cases, it is desired to command the aircraft altitude and airspeed rather than the flight path angle and acceleration. To realise this, the command and feedback signals are normalised to form the standard flight path angle command and acceleration command signals. The required modifications are discussed further in Section 6.2.2.

6.2.2 Traditional TECS Architecture

In this section, the original TECS architecture is divided into its subsystems. Each controller is detailed individually from the outermost to the innermost loops to obtain the necessary insight into how each controller functions. Each explanation is accompanied by a small diagram for reference. This section is primarily based on [7] with some explanatory concepts from [25]. As this section only covers the original architecture, the adaptations to the TECS to fit the purposes of this project will be discussed in Section 6.2.3.

6.2.2.1 Altitude Control

Under regular flight conditions, altitude is ultimately one of the most desired states to be controlled. As one of the outermost loops, it is also naturally one of the slowest in dynamic response.

The TECS altitude controller is a regular proportional controller as illustrated in Figure 6.3. The altitude error equation is formed by using an adder circuit to obtain

$$h_e = h_c - h \tag{6.14}$$

where h_e is the altitude error, h_c is the altitude command, and h is the altitude measurement. The output of this controller is a climb rate command which is formed by multiplying the altitude error signal with a suitable gain, which yields

$$\dot{h}_c = K_h h_e \tag{6.15}$$

where h_c is the climb rate command and K_h is the proportional controller gain. The value of K_h determines the error delay time constant of the altitude response, typically chosen to be the same value as K_v in Section 6.2.2.3 to yield identical dynamic responses between altitude and airspeed reference steps.

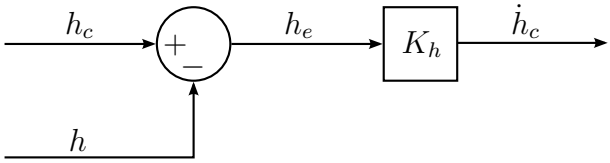

Figure 6.3: Traditional TECS altitude controller structure.

6.2.2.2 Climb Rate Control

Control over the climb rate of the aircraft is not achieved through a traditional control system. Instead, the structure acts as a proxy to the inner loop energy controllers as discussed in Section 6.2.2.5. This structure is illustrated in Figure 6.4.

The flight path angle command is formed by assuming a small angle and using a simple divider circuit. The divider is expressed by

$$\gamma_c = \frac{\dot{h}_c}{\overline{v}} \tag{6.16}$$

where γ_c is the flight path angle command, $\dot{h}_c$ is the climb rate command, and $\overline{v}$ is the airspeed measurement. This structure shows that the altitude controller outer loop can easily be circumvented by directly supplying the climb rate command, thereby allowing for more flexibility in the control system.

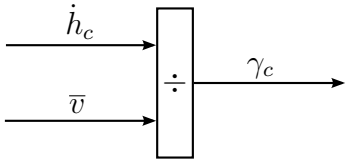

Figure 6.4: Traditional TECS climb rate controller structure.

6.2.2.3 Airspeed Control

Under regular flight conditions, airspeed is ultimately one of the most desired states to be controlled. As one of the outermost loops, it is also naturally one of the slowest in dynamic response.

The TECS airspeed controller is a regular proportional controller as illustrated in Figure 6.5. The airspeed error equation is formed by using an adder circuit to obtain

$$\overline{v}_e = \overline{v}_c - \overline{v} \tag{6.17}$$

where $\overline{v}_e$ is the airspeed error, $\overline{v}_c$ is the airspeed command, and $\overline{v}$ is the airspeed measurement. The output of this controller is an acceleration command which is formed by multiplying the airspeed error signal with a suitable gain, which yields

$$\dot{\overline{v}}_c = K_v \overline{v}_e \tag{6.18}$$

where $\dot{\overline{v}}_c$ is the acceleration command and K_v is the proportional controller gain. The value of K_v determines the error delay time constant of the airspeed response, typically chosen to be the same value as K_h in Section 6.2.2.1 to yield identical dynamic responses between airspeed and altitude reference steps.

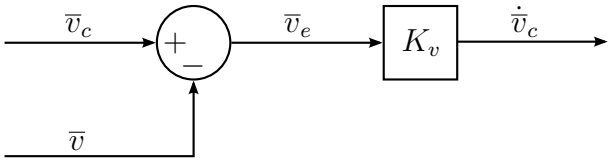

Figure 6.5: Traditional TECS airspeed controller structure.

6.2.2.4 Acceleration Control

Control over the acceleration of the aircraft is not achieved through a traditional control system. Instead, the structure acts as an intermediary step to normalise the signals for use in the inner loop energy controllers as discussed in Section 6.2.2.5. This structure is illustrated in Figure 6.6.

The acceleration error equation is formed by using an adder circuit to obtain

$$\dot{\overline{v}}_e = \dot{\overline{v}}_c - \dot{\overline{v}} \tag{6.19}$$

where $\dot{\overline{v}}_e$ is the acceleration error, $\dot{\overline{v}}_c$ is the acceleration command, and $\dot{\overline{v}}$ is the acceleration measurement. The acceleration error is divided by gravity as a normalisation factor and used as an input signal to the subsequent inner loop controllers. This structure shows that the airspeed controller outer loop can easily be circumvented by directly supplying the acceleration command, although this is usually not a desired input.

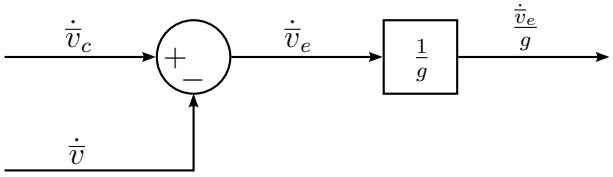

Figure 6.6: Traditional TECS acceleration controller structure.

6.2.2.5 Energy Controllers

The energy controllers are the core of the TECS architecture. These controllers generate a throttle output command from the specific energy controller and an elevator output command from the energy distribution controller. Furthermore, two additional controllers, the pitch angle controller and pitch rate damper, act as intermediary controllers between the energy distribution controller output and the final elevator deflection angle command. The energy controller structure is illustrated in Figure 6.7.

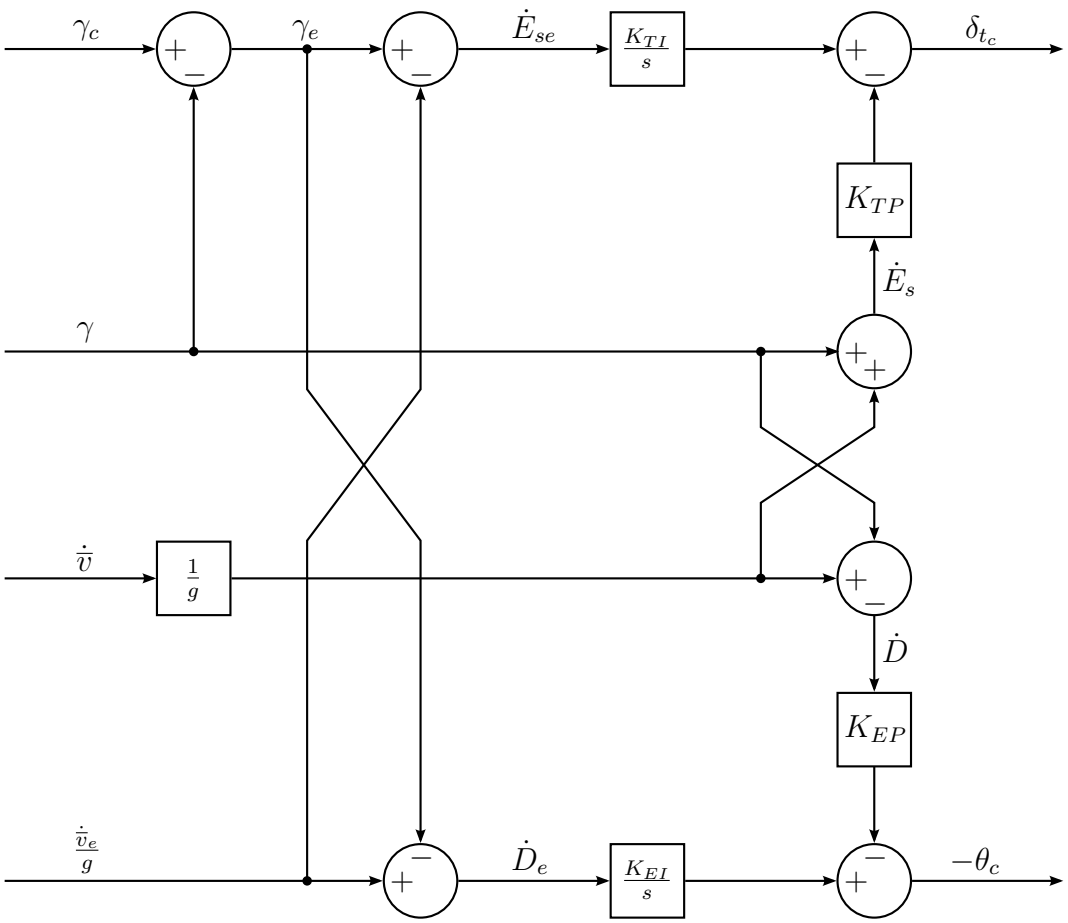

Figure 6.7: Traditional TECS energy controller structures showing the specific energy and energy distribution controllers. Adapted from [7].

The climb rate measurement equation is formed by using a divider circuit and the small angle approximation of $\sin\gamma \approx \gamma$ to obtain

$$\gamma = \frac{\dot{h}}{\overline{v}} \tag{6.20}$$

where γ is the flight path angle measurement. The flight path angle command signal is obtained from the climb rate controller as discussed in Section 6.2.2.2. This can be used to obtain the flight path error equation as

$$\gamma_e = \gamma_c - \gamma \tag{6.21}$$

where γ_e is the flight path angle error. This structure shows that the climb rate controller outer loop can easily be circumvented by directly supplying the flight path angle command, thereby allowing for more flexibility in the control system.

From the acceleration controller outer loop, the normalised acceleration error is obtained. Additionally, the acceleration measurement is also normalised by gravity in the same fashion. At this point, the γ_e and $\frac{\dot{\overline{v}}_e}{g}$ signals can be used to form the specific energy rate and energy rate distribution signals as shown in Equations 6.12 and 6.13. The γ and $\frac{\dot{\overline{v}}}{g}$ signals will be used to provide damping to the proportional-integral architecture of both inner loop controllers.

The specific energy rate error is formed by an adder circuit and is expressed by

$$\dot{E}_{se} = \gamma_e + \frac{\dot{\bar{v}}}{g} \tag{6.22}$$

where $\dot{E}_{se}$ is the specific energy rate error. The specific energy error is formed by amplifying the rate error signal though a suitable gain and integrated over time to form

$$E_{se} = K_{TI} \int \dot{E}_{se}\, \mathrm{d}t \tag{6.23}$$

where E_{se} is the specific energy error and K_{TI} is the integrator gain. The specific energy rate is formed by an adder circuit and is expressed by

$$\dot{E}_s = \gamma + \frac{\dot{\bar{v}}}{g} \tag{6.24}$$

where $\dot{E}_s$ is the specific energy rate. This signal is amplified and passed through an adder circuit to provide damping to the proportional-integral controller. Thus, the net thrust command is formed as

$$\delta_{t_c} = E_{se} - K_{TP}\dot{E}_s \tag{6.25}$$

where δ_{t_c} is the thrust command and K_{TP} is the proportional gain. This controller now fully controls the total energy of the aircraft by using the throttle only with a first-order time constant of $\tau_E = \frac{K_{TP}}{K_{TI}}$.

The energy rate distribution error is formed by an adder circuit and is expressed by

$$\dot{D}_e = -\gamma_e + \frac{\dot{\bar{v}}}{g} \tag{6.26}$$

where $\dot{D}_e$ is the energy rate distribution error. The energy distribution error is formed by amplifying the rate error signal though a suitable gain and integrated over time to form

$$D_e = K_{EI} \int \dot{D}_e\, \mathrm{d}t \tag{6.27}$$

where D_e is the energy distribution error and K_{EI} is the integrator gain. The energy rate distribution is formed by an adder circuit and is expressed by

$$\dot{D} = -\gamma + \frac{\dot{\bar{v}}}{g} \tag{6.28}$$

where $\dot{D}$ is the energy rate distribution. This signal is amplified and passed through an adder circuit to provide damping to the proportional-integral controller. Thus, the net elevator de-

flection angle command is formed as

$$\delta_{e_c} = D_e - K_{EP}\dot{D} \tag{6.29}$$

where δ_{e_c} is the elevator deflection angle command and K_{EP} is the proportional gain. This controller now fully controls the energy distribution of the aircraft by using the elevator only with a first order time constant of $\tau_D = \frac{K_{EP}}{K_{EI}}$.

However, it is often not desired to drive the elevator from this signal directly as additional stabilisation is preferred. The output of this controller is used as the input for a pitch angle controller as discussed in Section 6.2.2.6. Thus, the net pitch angle command is formed as

$$-\theta_c = D_e - K_{EP}\dot{D} \tag{6.30}$$

where $-\theta_c$ is the pitch angle command, inverted as per convention. Optionally, the elevator effectiveness can be compensated for by gain scheduling via a function of the dynamic pressure.

To ensure a coordinated response to both airspeed and flight path angle changes, the specific energy rate error and energy rate distribution error should be controlled to zero simultaneously. This can be enforced by choosing the gains so that $\tau_e = \tau_D$ and $K_{TI} = K_{EI}$.

6.2.2.6 Pitch Angle Controller

From the energy distribution controller outer loop, the negative pitch angle command is obtained. The reason for a negative pitch command is that, according to sign conventions commonly used, a negative elevator deflection angle command induces a positive pitching moment. The TECS pitch angle controller is a regular proportional controller as illustrated in Figure 6.8. The pitch angle error equation is formed by using an adder circuit to obtain

$$\theta_e = \theta - \theta_c \tag{6.31}$$

where θ_e is the pitch angle error, θ is the pitch angle measurement, and θ_c is the pitch angle command. The output of this controller is a pitch rate command which is formed by multiplying the pitch angle error signal with a suitable gain, which yields

$$\dot{\theta}_c = K_\theta \theta_e \tag{6.32}$$

where $\dot{\theta}_c$ is the pitch rate command and K_θ is the proportional controller gain.

This controller, together with the pitch rate damper, forms part of a loop to stabilise and augment the short period mode dynamics. The gains should be chosen to match thrust inner loop dynamics.

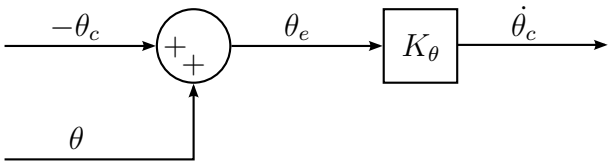

Figure 6.8: Traditional TECS pitch angle controller structure.

6.2.2.7 Pitch Rate Damper

From the pitch angle controller outer loop, the pitch rate command is obtained. The TECS pitch rate controller is a regular proportional controller as illustrated in Figure 6.9. The pitch rate error equation is formed by using an adder circuit to obtain

$$\dot{\theta}_e = \dot{\theta}_c + \dot{\theta} \tag{6.33}$$

where $\dot{\theta}_e$ is the pitch rate error, $\dot{\theta}_c$ is the pitch rate command, and $\dot{\theta}$ is the pitch rate measurement. The output of this controller is an elevator deflection angle command which is formed by multiplying the pitch rate error signal with a suitable gain, which yields

$$\delta_{e_c} = K_{\dot{\theta}}\dot{\theta}_e \tag{6.34}$$

where δ_{e_c} is the elevator deflection angle command and $K_{\dot{\theta}}$ is the proportional controller gain.

This controller, together with the pitch rate damper, forms part of a loop to stabilise and augment the short period mode dynamics. The gains should be chosen to match thrust inner loop dynamics.

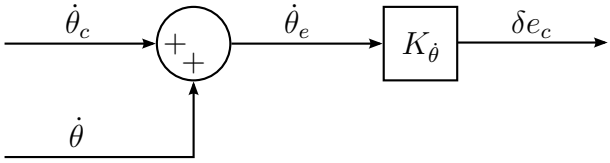

Figure 6.9: Traditional TECS pitch rate damper structure.

6.2.3 TECS Architecture Modifications

During the SIL and HIL simulations, detailed in Chapter 7, it was found that the control system can still be improved. This section discusses the modifications and optimisations made to the original TECS architecture.

6.2.3.1 Climb Rate Feed Forward

For the purposes of this project, it is preferred to land at a very specific and predetermined sink rate to avoid damage to the aircraft undercarriage. To this end, the original climb rate

command is rather treated as a preliminary climb rate command, given by

$$\dot{h}_c' = K_h h_e \tag{6.35}$$

where $\dot{h}_c'$ is the preliminary climb rate command. A feed-forward climb rate is introduced to this design to ensure that a safe sink rate is followed upon touchdown. This concept allows the use of a ramp reference value which slowly decreases in altitude towards the intended touchdown point on the runway, thereby creating a predetermined glide path. The new climb rate command is given by

$$\dot{h}_c = \dot{h}_c' + \dot{h}_c'' \tag{6.36}$$

where $\dot{h}_c''$ is the feed-forward climb rate, negative in sign for the purposes of landing and forcing a sink rate. In this fashion, when the aircraft is at the correct ramp altitude command, a constant sink rate is supplied to the climb rate controller. Note that this feed-forward is only a modification of a reference signal and therefore does not contribute any dynamic behaviour.

6.2.3.2 Reference Modifications

For convenience, the calculation of the flight path angle in the original architecture is restated as

$$\gamma_c = \frac{\dot{h}_c}{\overline{v}}$$

In the original architecture, the flight path angle is calculated by using either the calculated or directly commanded climb rate and dividing by the measured airspeed. In conventional control systems, it is preferred to keep the command signals and measurement signals apart for such calculations to reduce the effect of disturbances in the generation of reference signals. For this project, the flight path angle calculation is rather performed by

$$\gamma_c = \frac{\dot{h}_c}{\overline{v}_c} \tag{6.37}$$

using only command signals. Through simulation, it was found that this does not have a negative impact on the control system, and in many cases showed improved performance.

6.2.3.3 Damping Improvements

For convenience, the calculation of the energy controller outputs in the original architecture are restated as

$$\delta_{t_c} = K_{TI} \int \dot{E}_{se}\, \mathrm{d}t - K_{TP} \dot{E}_s \tag{6.38}$$

$$\delta_{e_c} = K_{EI} \int \dot{D}_e\, \mathrm{d}t - K_{EP} \dot{D} \tag{6.39}$$

with substitution of parameters to indicate the integral and proportional parts. In the original architecture, the error signals are integrated while the measured signals are used to provide the damping. Since the measured signals are used, the damping components are subtracted to achieve the desired result.

In conventional control systems, the same error signal is used for the integration, derivative and proportional parts of the controller. For this project, the energy controller outputs are also calculated, in the s-plane representation, as

$$\delta_{t_c} = \left(K_{TP} + \frac{K_{TI}}{s}\right) \dot{E}_{se} \tag{6.40}$$

$$\delta_{e_c} = \left(K_{EP} + \frac{K_{EI}}{s}\right) \dot{D}_e \tag{6.41}$$

therefore using the error signal for both the proportional and integral components, achieving the more familiar proportional-integral controller form. Note that the sign of the proportional part is now positive as only the error signals, not the measurements, are used for both the proportional and integral parts to achieve the desired result. This form showed better results in SIL simulations during initial testing, and retains the first order time constant quality as expressed by

$$\tau_E = \frac{K_{TP}}{K_{TI}} \tag{6.42}$$

$$\tau_D = \frac{K_{EP}}{K_{EI}} \tag{6.43}$$

The design will attempt to keep the two time constants equal to achieve the same dynamic response.

6.2.3.4 Normal Specific Acceleration Control

In the original TECS architecture, the elevator inner loop control consists of a pitch angle controller and a pitch rate damper as discussed in Sections 6.2.2.6 and 6.2.2.7. These controllers were both designed using the root locus method with successive loop closure and tested in a nonlinear simulation, although the designs and results are omitted. Although the design was successful, it was speculated that the controllers aim to achieve load factor control by using pitch angle as a proxy.

It was decided to replace these inner loops with the NSA controller and a pitch rate feedback loop, specifically the system developed in [11] and refined in [16]. This modification is also proposed by [7] as it does not deviate from the integrated longitudinal controller goal of the original TECS.

6.2.4 Longitudinal Design

The majority of the controllers were designed using the root locus method with successive loop closure. Designs started at the innermost loops, which are the fastest in terms of dynamic response, and worked towards the outer loops, which are the slowest in terms of dynamic response.

The first loop designed is the NSA as presented in Section 6.2.4.1. Because of the complex TECS architecture, it is first simplified in Section 6.2.4.2 in order to design a control system using conventional methods. The inner and outer loop designs are subsequently presented in Sections 6.2.4.3 and 6.2.4.4, respectively. As the TECS controls the flight path angle and acceleration through energy controllers and due to the design method of the altitude and airspeed controllers, the step responses of these traditional flight control references will only be shown in Chapter 7.

6.2.4.1 NSA Design

The design of the NSA controller presented in this section is the work of [16], which was based on [4]. Since the exact same airframe was used with the same controller, both an identical design and implementation were used for this project.

The following assumptions were made to simplify the linearised longitudinal model from Equation 5.47:

1. standard trigonometric small angle assumptions for α and β, and that the product of small angles are zero;

2. the aircraft will perform coordinated turns so that the sideslip remains approximately zero, therefore no coupling into roll and yaw rates occur;

3. the zero angle of attack lift and pitching moment coefficients C_{L_0} and C_{m_0} can be removed from the model because the controller will negate the steady state errors caused by their omission; and

4. coupling of thrust into the normal dynamics can be discarded based on the large time-scale separation between the thrust and normal dynamics.

The simplified longitudinal model for the NSA now becomes:

$$\begin{bmatrix} \dot{\alpha} \\ \dot{q} \end{bmatrix} = \begin{bmatrix} -\frac{q_{pT}S}{m\bar{v}_T}C_{L_\alpha} & 1 - \frac{q_{pT}S}{m\bar{v}_T}\frac{\bar{c}}{2\bar{v}_T}C_{L_Q} \\ \frac{q_{pT}S\bar{c}}{I_{yy}}C_{m_\alpha} & \frac{q_{pT}S\bar{c}}{I_{yy}}\frac{\bar{c}}{2\bar{v}_T}C_{m_Q} \end{bmatrix} \begin{bmatrix} \alpha \\ q \end{bmatrix} + \begin{bmatrix} -\frac{q_{pT}S}{m\bar{v}_T}C_{L_{\delta_e}} \\ \frac{q_{pT}S\bar{c}}{I_{yy}}C_{m_{\delta_e}} \end{bmatrix} \begin{bmatrix} \delta_e \end{bmatrix} \tag{6.44}$$

To simplify the equations, the following terms are defined as

$$L_\alpha = q_{p_T} S C_{L_\alpha} \tag{6.45}$$

$$L_q = q_{p_T} S \frac{\overline{c}}{2\overline{v}_T} C_{L_q} \tag{6.46}$$

$$L_{\delta_e} = q_{p_T} S C_{L_{\delta_e}} \tag{6.47}$$

$$M_\alpha = q_{p_T} S \overline{c} C_{m_\alpha} \tag{6.48}$$

$$M_q = q_{p_T} S \overline{c} \frac{\overline{c}}{2\overline{v}_T} C_{m_q} \tag{6.49}$$

$$M_{\delta_e} = q_{p_T} S \overline{c} C_{m_{\delta_e}} \tag{6.50}$$

It was shown by [50] that if the flight path angle remains small, which is the case for trim flight, the effect of gravitational acceleration can be considered as a constant force. If this constant force is treated as a disturbance, it can be assumed that the controllers will correct any errors caused by its omission under steady state conditions. Furthermore, it is assumed that

$$\left| \frac{L_q}{m\overline{v}_T} \right| \ll 1 \tag{6.51}$$

since its effect is negligibly small for conventional aircraft as shown by [44]. By substituting these values into Equation 6.44, the dynamics are now given by

$$\begin{bmatrix} \dot{\alpha} \\ \dot{q} \end{bmatrix} = \begin{bmatrix} -\frac{L_\alpha}{m\overline{v}_T} & 1 \\ \frac{M_\alpha}{I_{yy}} & \frac{M_q}{I_{yy}} \end{bmatrix} \begin{bmatrix} \alpha \\ q \end{bmatrix} + \begin{bmatrix} -\frac{L_{\delta_e}}{m\overline{v}_T} \\ \frac{M_{\delta_e}}{I_{yy}} \end{bmatrix} \begin{bmatrix} \delta_e \end{bmatrix} \tag{6.52}$$

$$\begin{bmatrix} C_w \\ q \end{bmatrix} = \begin{bmatrix} -\frac{L_\alpha}{m} & -\frac{L_q}{m} \\ 0 & 1 \end{bmatrix} \begin{bmatrix} \alpha \\ q \end{bmatrix} + \begin{bmatrix} -\frac{L_{\delta_e}}{m} \\ 0 \end{bmatrix} \begin{bmatrix} \delta_e \end{bmatrix} \tag{6.53}$$

During the analysis of this plant, [16] investigated the effect of a non-minimum phase (NMP) zero located at approximately $s = 35$ rad/s. This zero is caused by the elevator during actuation where a small amount of lift is generated in the opposite direction than what is intended. It was shown by [5] that the NMP nature of the NSA controller can be ignored if both the open-loop and closed-loop dominant poles are at least three times slower than the NMP zero. The open-loop poles meet this criteria, and it is assumed that the designed closed-loop poles will do as well. From these assumptions, the effect of the NMP zero can be ignored by letting

$$C_{L_{\delta_e}} = 0 \tag{6.54}$$

Furthermore, [16] also found a zero in the left-half plane at a much higher frequency than that of the dominant NSA pole dynamics. It was concluded that its effect will be negligible in the presence of other high-frequency poles such as those from servo lag, which are currently not

modelled. The zero represents lift generated by the aircraft due to an induced angle of attack created when it experiences a pitch rate. Therefore, it is assumed that

$$C_{L_q} = 0 \tag{6.55}$$

Incorporating these assumptions, the final simplified NSA dynamics are represented by

$$\begin{bmatrix} \dot{\alpha} \\ \dot{q} \end{bmatrix} = \begin{bmatrix} -\frac{L_\alpha}{m\bar{v}_T} & 1 \\ \frac{M_\alpha}{I_{yy}} & \frac{M_q}{I_{yy}} \end{bmatrix} \begin{bmatrix} \alpha \\ q \end{bmatrix} + \begin{bmatrix} 0 \\ \frac{M_{\delta_e}}{I_{yy}} \end{bmatrix} \begin{bmatrix} \delta_e \end{bmatrix} \tag{6.56}$$

$$\begin{bmatrix} C_w \\ q \end{bmatrix} = \begin{bmatrix} -\frac{L_\alpha}{m} & 0 \\ 0 & 1 \end{bmatrix} \begin{bmatrix} \alpha \\ q \end{bmatrix} + \begin{bmatrix} 0 \\ 0 \end{bmatrix} \begin{bmatrix} \delta_e \end{bmatrix} \tag{6.57}$$

For the state-space representation, this results in

$$\boldsymbol{A} = \begin{bmatrix} -\frac{L_\alpha}{m\bar{v}_T} & 1 \\ \frac{M_\alpha}{I_{yy}} & \frac{M_q}{I_{yy}} \end{bmatrix} \tag{6.58}$$

$$\boldsymbol{B} = \begin{bmatrix} 0 \\ \frac{M_{\delta_e}}{I_{yy}} \end{bmatrix} \tag{6.59}$$

$$\boldsymbol{C} = \begin{bmatrix} -\frac{L_\alpha}{m} & 0 \end{bmatrix} \tag{6.60}$$

$$D = 0 \tag{6.61}$$

The characteristic equation can now be determined by

$$G(s) = \boldsymbol{C}\left(s\boldsymbol{I} - \boldsymbol{A}\right)^{-1}\boldsymbol{B} + D \tag{6.62}$$

$$= \begin{bmatrix} -\frac{L_\alpha}{m} & 0 \end{bmatrix} \left[\begin{bmatrix} s & 0 \\ 0 & s \end{bmatrix} - \begin{bmatrix} -\frac{L_\alpha}{m\bar{v}_T} & 1 \\ \frac{M_\alpha}{I_{yy}} & \frac{M_q}{I_{yy}} \end{bmatrix} \right]^{-1} \begin{bmatrix} 0 \\ \frac{M_{\delta_e}}{I_{yy}} \end{bmatrix} + 0 \tag{6.63}$$

$$= \frac{-\frac{L_\alpha}{m}\frac{M_{\delta_e}}{I_{yy}}}{s^2 + \left(\frac{L_\alpha}{m\bar{v}_T} - \frac{M_q}{I_{yy}}\right)s - \left(\frac{L_\alpha}{m\bar{v}_T}\frac{M_q}{I_{yy}} + \frac{M_q}{I_{yy}}\right)} \tag{6.64}$$

The NSA controller is augmented with an integrator to negate any steady state errors. This integrator is implemented by the following equation

$$\dot{x}_I = C_w - C_w^{ref} \tag{6.65}$$

The augmented dynamics are now given by

$$\begin{bmatrix} \dot{x}_I \\ \dot{\alpha} \\ \dot{q} \end{bmatrix} = \begin{bmatrix} 0 & -\frac{L_\alpha}{m} & 0 \\ 0 & -\frac{L_\alpha}{m\bar{v}_T} & 1 \\ 0 & \frac{M_\alpha}{I_{yy}} & \frac{M_q}{I_{yy}} \end{bmatrix} \begin{bmatrix} x_I \\ \alpha \\ q \end{bmatrix} + \begin{bmatrix} 0 \\ 0 \\ \frac{M_{\delta_e}}{I_{yy}} \end{bmatrix} \delta_e - \begin{bmatrix} 1 \\ 0 \\ 0 \end{bmatrix} C_w^{ref} \tag{6.66}$$

$$\begin{bmatrix} C_w \\ q \end{bmatrix} = \begin{bmatrix} 0 & -\frac{L_\alpha}{m} & 0 \\ 0 & 0 & 1 \end{bmatrix} \begin{bmatrix} x_I \\ \alpha \\ q \end{bmatrix} + \begin{bmatrix} 0 \\ 0 \end{bmatrix} \begin{bmatrix} \delta_e \end{bmatrix} \tag{6.67}$$

Due to difficulties encountered when using feedback directly from the NSA, the following strategies are followed to improve performance [51]:

- Feedback of the integrator state ensures that steady state errors are negated in the closed-loop system.
- Feedback from the pitch rate sensors allows for damping of the NSA dynamics.
- A feed-forward of the reference input allows for the placement of a closed-loop zero.

An elevator control law can now be defined as

$$u = \boldsymbol{kx} + r \tag{6.68}$$

$$\delta_e = \begin{bmatrix} K_I & 0 & K_q \end{bmatrix} \begin{bmatrix} x_I \\ \alpha \\ q \end{bmatrix} + N_c C_w^{ref} \tag{6.69}$$

which can be substituted into the dynamics to obtain the characteristic equation as

$$|sI - A + BK| = \left| \begin{bmatrix} s & 0 & 0 \\ 0 & s & 0 \\ 0 & 0 & s \end{bmatrix} - \begin{bmatrix} 0 & -\frac{L_\alpha}{m} & 0 \\ 0 & -\frac{L_\alpha}{m\bar{v}_T} & 1 \\ 0 & \frac{M_\alpha}{I_{yy}} & \frac{M_q}{I_{yy}} \end{bmatrix} + \begin{bmatrix} 0 \\ 0 \\ \frac{M_{\delta_e}}{I_{yy}} \end{bmatrix} \begin{bmatrix} K_I & 0 & K_q \end{bmatrix} \right| \tag{6.70}$$

$$= \begin{vmatrix} s & \frac{L_\alpha}{m} & 0 \\ 0 & s + \frac{L_\alpha}{m\bar{v}_T} & -1 \\ K_I \frac{M_{\delta_e}}{I_{yy}} & -\frac{M_\alpha}{I_{yy}} & s - \frac{M_q}{I_{yy}} + K_q \frac{M_{\delta_e}}{I_{yy}} \end{vmatrix} \tag{6.71}$$

$$\begin{aligned} &= s^3 + \left(\frac{L_\alpha}{m\bar{v}_T} - \frac{M_q}{I_{yy}} + \frac{M_{\delta_e}}{I_{yy}} K_q \right) s^2 + \\ &\quad \left(-\frac{L_\alpha}{m\bar{v}_T} \frac{M_q}{I_{yy}} + \frac{L_\alpha}{m\bar{v}_T} \frac{M_{\delta_e}}{I_{yy}} K_q - \frac{M_\alpha}{I_{yy}} \right) s - \frac{L_\alpha}{m} \frac{M_{\delta_e}}{I_{yy}} K_I \end{aligned} \tag{6.72}$$

To place one complex pole pair and one real pole, the dynamics of the closed-loop NSA controller

should conform to

$$p_{cl} = \left(s^2 + 2\zeta\omega_n s + \omega_n^2\right)(s+a) \tag{6.73}$$

$$= s^3 + (2\zeta\omega_n + a)s^2 + \left(s\zeta\omega_n a + \omega_n^2\right)s + \omega_n^2 a \tag{6.74}$$

Comparing the coefficients of Equations 6.72 and 6.74 means that the following should hold true for the desired controller:

$$\frac{L_\alpha}{m\bar{v}_T} - \frac{M_q}{I_{yy}} + \frac{M_{\delta_e}}{I_y y}K_q = 2\zeta\omega_n + a \tag{6.75}$$

$$-\frac{L_\alpha}{m\bar{v}_T}\frac{M_q}{I_{yy}} + \frac{L_\alpha}{m\bar{v}_T}\frac{M_{\delta_e}}{m\bar{v}_T}\frac{M_{\delta_e}}{I_{yy}}K_q - \frac{M_\alpha}{I_{yy}} = 2\zeta\omega_n a + \omega_n^2 \tag{6.76}$$

which can be rearranged to

$$K_q = \left(2\zeta\omega_n + a - \frac{L_\alpha}{m\bar{v}_T} + \frac{M_q}{I_{yy}}\right)\frac{I_{yy}}{M_{\delta_e}} \tag{6.77}$$

$$K_q = \left(2\zeta\omega_n a + \omega_n^2 + \frac{L_\alpha}{m\bar{v}_T}\frac{M_q}{I_{yy}} + \frac{M_\alpha}{I_{yy}}\right)\frac{m\bar{v}_T}{L_\alpha}\frac{I_{yy}}{M_{\delta_e}} \tag{6.78}$$

From Equations 6.77 and 6.78, the damping of the short period mode ζ and the location of the augmented integrator pole a can be chosen. Since the two equations are equal, the positive root of the natural frequency can subsequently be calculated as

$$\omega_n^2 + \left(2\zeta a - 2\zeta\frac{L_\alpha}{m\bar{v}_T}\right)\omega_n + \left(\frac{M_\alpha}{I_{yy}} + \left(\frac{L_\alpha}{m\bar{v}_T}\right)^2 - a\frac{L_\alpha}{m\bar{v}_T}\right) = 0 \tag{6.79}$$

$$\omega_n = \frac{-2\zeta\left(a - \frac{L_\alpha}{m\bar{v}_T}\right) + \sqrt{\left(2\zeta\left(a - \frac{L_\alpha}{m\bar{v}_T}\right)\right)^2 - 4\left(\frac{M_\alpha}{I_{yy}} + \left(\frac{L_\alpha}{m\bar{v}_T}\right)^2 - a\frac{L_\alpha}{m\bar{v}_T}\right)}}{2} \tag{6.80}$$

$$= \zeta\eta + \sqrt{(\zeta\eta)^2 - \frac{M_\alpha}{I_{yy}} - \frac{L_\alpha}{m\bar{v}_T}\eta} \tag{6.81}$$

where

$$\eta = \frac{L_\alpha}{m\bar{v}_T} - a \tag{6.82}$$

After the damping and pole location have been chosen, the value of K_q can be determined by substituting the chosen values into any one of Equations 6.77 or 6.78.

From the coefficient comparison and the chosen parameters, the integrator gain can now also be determined by evaluating

$$-\frac{L_\alpha}{m}\frac{M_{\delta_e}}{I_{yy}}K_I = \omega_n^2 a \tag{6.83}$$

$$K_I = -\frac{\omega_n^2 a m I_{yy}}{L_\alpha M_{\delta_e}} \tag{6.84}$$

It is not desired to have the response of the integrator in the reference input, which can be removed by placing a feed-forward zero such that

$$N_c = -\frac{K_I}{z_f} \tag{6.85}$$

where z_f is the location of the desired zero.

For convenience, the open-loop natural frequency and damping of the NSA dynamics are restated as

$$\omega_{n_{ol}} = 10.1091 \text{ rad/s}$$
$$\zeta_{ol} = 0.6574$$

which is similar to the values as determined by [16]. The integrator pole is placed at a frequency lower than that of the short period mode. The feed-forward zero is placed at twice the frequency of the integrator pole to remove some of the integrator dynamics from the reference input while avoiding excessive feed-forward. These chosen values are

$$a = -4 \text{ rad/s} \tag{6.86}$$
$$z_f = -8 \text{ rad/s} \tag{6.87}$$

The assumption made regarding the NMP zero remains valid as the dominant open-loop and closed-loop poles are still at least three times slower than that of the NMP zero.

The poles are shown graphically on an s-plane map in Figure 6.10. It can be observed that the damping of the short period mode complex pole pair has slightly improved. The integrator pole and feed-forward zero are also present. The NSA step response is well damped with a rise time of $t_{r_{63\%}} = 0.3s$ and a settling time of $t_{s_{2\%}} = 0.95s$, shown graphically in Figure 6.11. These results correlate well with the foundation project [16], although minor deviations are observed. These are likely due to slightly different values used for some parameters, as well as errors due to rounding.

6.2.4.2 TECS Simplification

As shown in Section 6.2.1, the total energy and energy distribution of the aircraft is given, respectively, by

$$E = mgh + \frac{1}{2}m\bar{v}^2 \tag{6.88}$$
$$D = -mgh + \frac{1}{2}m\bar{v}^2 \tag{6.89}$$

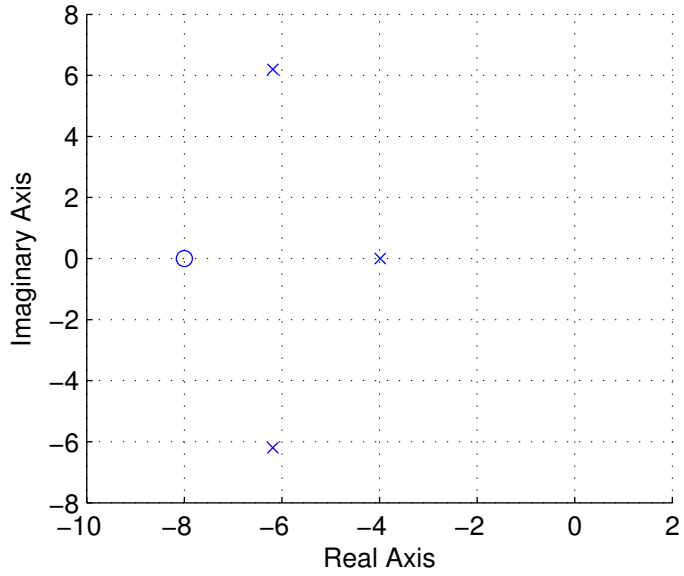

Figure 6.10: Closed-loop poles of the NSA dynamics on an s-plane.

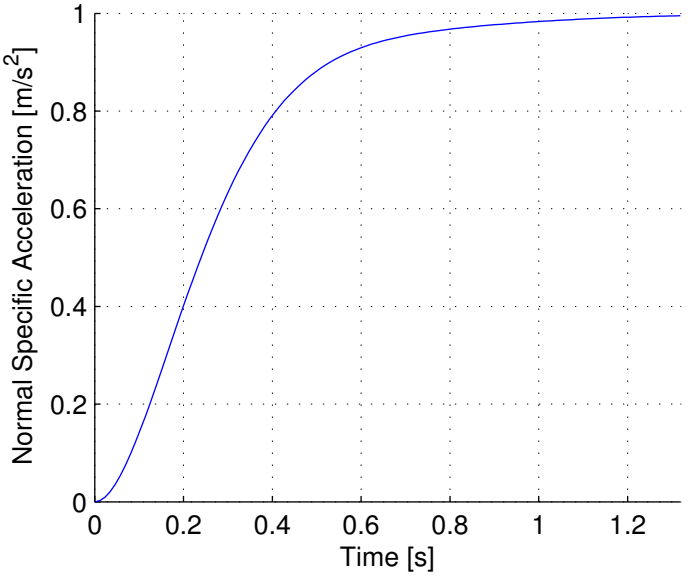

Figure 6.11: Step response of the NSA controller.

It was also shown that the time derivatives of each can be calculated to obtain the total energy rate and energy distribution rate as

$$\dot{E} = mg\dot{h} + m\overline{v}\,\dot{\overline{v}} \tag{6.90}$$

$$\dot{D} = -mg\dot{h} + m\overline{v}\,\dot{\overline{v}} \tag{6.91}$$

Applying the normalisation by airspeed and the small angle approximation $\gamma \approx \frac{\dot{h}}{\overline{v}}$, these equations now contain the flight path angle as

$$\frac{\dot{E}}{\overline{v}} = mg\gamma + m\dot{\overline{v}} \tag{6.92}$$

$$\frac{\dot{D}}{\overline{v}} = -mg\gamma + m\dot{\overline{v}} \tag{6.93}$$

By factoring out the weight, forms similar to [7] are obtained as

$$\frac{\dot{E}}{\overline{v}} = mg\left(\gamma + \frac{\dot{\overline{v}}}{g}\right) \tag{6.94}$$

$$\frac{\dot{D}}{\overline{v}} = mg\left(-\gamma + \frac{\dot{\overline{v}}}{g}\right) \tag{6.95}$$

By controlling the values of $\dot{E}$ and $\dot{D}$, the values of γ and $\overline{v}$ are in effect controlled.

The specific total energy rate and energy distribution rate are obtained by dividing by the force of gravity and are now defined for a given airspeed as

$$\dot{E}_s = \frac{\dot{E}}{mg\overline{v}} \tag{6.96}$$

$$\dot{D}_s = \frac{\dot{D}}{mg\overline{v}} \tag{6.97}$$

where $\dot{E}_s$ is the specific total energy rate and $\dot{D}_s$ is the specific energy distribution rate. Combining Equations 6.94 through 6.97 yield

$$\dot{E}_s = \gamma + \frac{\dot{\overline{v}}}{g} \tag{6.98}$$

$$\dot{D}_s = -\gamma + \frac{\dot{\overline{v}}}{g} \tag{6.99}$$

To control $\dot{E}_s$ and $\dot{D}_s$, the thrust and elevator signals can be used as discussed in Section 6.2.1. The longitudinal force and moment equations of motion can be stated as

$$m\dot{\overline{v}} = \delta_t - F_d - mg\sin\gamma \tag{6.100}$$

Rearrangement of Equation 6.100 and subsequent substitution into Equation 6.98 yield

$$\dot{\bar{v}} = \frac{1}{m}\left(\delta_t - F_d - mg\sin\gamma\right) \tag{6.101}$$

$$\dot{E}_s = \gamma + \frac{1}{mg}\left(\delta_t - F_d - mg\sin\gamma\right) \tag{6.102}$$

$$\dot{E}_s = \gamma + \frac{1}{mg}\left(\delta_t - F_d\right) - \sin\gamma \tag{6.103}$$

By assuming the small angle approximation $\sin\gamma \approx \gamma$, Equation 6.103 can be simplified to

$$\dot{E}_s = \frac{1}{mg}\left(\delta_t - F_d\right) \tag{6.104}$$

It is now evident that $\dot{E}_s$ can be controlled using δ_t only and that it is independent of γ. A PI controller can therefore be designed with the reference from Equation 6.98 as

$$\dot{E}_{sc} = \gamma_c + \frac{\dot{\bar{v}}_c}{g} \tag{6.105}$$

where $\dot{E}_{sc}$ is the specific total energy command, γ_c is the flight path angle command and $\bar{v}_c$ is the airspeed command. The drag is treated as a disturbance reducing the effect of the thrust applied. This controller form is illustrated in Figure 6.12.

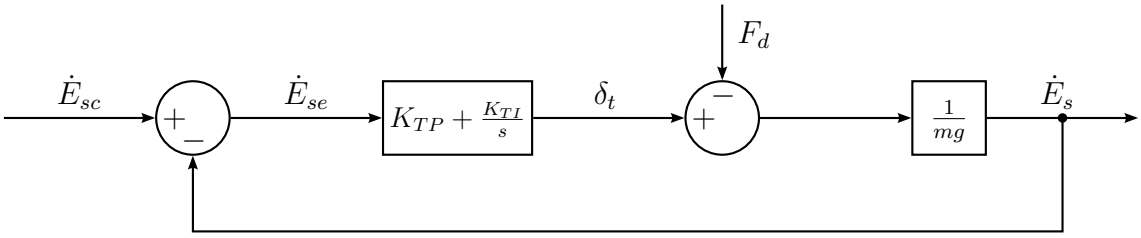

Figure 6.12: Simplified TECS specific energy loop.

Taking the time derivative of Equation 6.99 yields

$$\ddot{D}_s = -\dot{\gamma} + \frac{\ddot{\bar{v}}}{g} \tag{6.106}$$

The flight path angle rate $\dot{\gamma}$ can be controlled using δ_e, while $\frac{\ddot{\bar{v}}}{g}$ can be regarded as a disturbance that needs to be rejected. A PI controller can therefore be designed with the reference from Equation 6.99 as

$$\dot{D}_{sc} = -\gamma_c + \frac{\dot{\bar{v}}_c}{g} \tag{6.107}$$

where $\dot{D}_{sc}$ is the energy distribution rate command. This controller form is illustrated in Figure 6.13, assuming unity gain for the dynamics of the innermost loops.

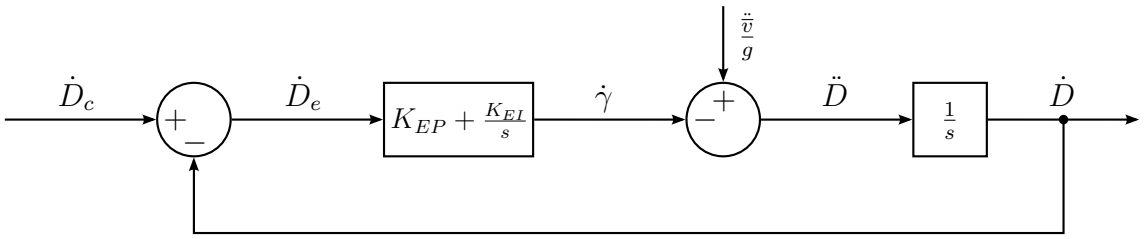

Figure 6.13: Simplified TECS energy distribution loop.

To control $\dot{\gamma}$, consider the equation of motion given by

$$\dot{\gamma} = \frac{\frac{F_l}{m} - g\cos\gamma}{\overline{v}} \tag{6.108}$$

where F_l is the force caused by lift. This equation can be simplified to

$$\dot{\gamma} = \frac{1}{\overline{v}}\left(-a_z - g\cos\gamma\right) \tag{6.109}$$

where a_z is the NSA measurement. The flight path angle rate $\dot{\gamma}$ can thus be controlled through controlling the NSA.

6.2.4.3 TECS Inner Loop Design

The simplification presented in Section 6.2.4.2 can be used as a starting point to design the TECS inner loop controllers. The design will attempt to reach optimal damping and keeping the time constant for both controllers equal as suggested by [7] to achieve a similar response to thrust and elevator command signals. The output of the specific energy controller will be a thrust command signal whereas the energy distribution controller now outputs an NSA command signal instead of the traditional pitch angle command.

It should be noted that the designs presented in this section are a subset of all the attempted designs. These designs were chosen to illustrate the steps performed to reach the final implemented controllers. Continuous integration and testing in a SIL/HIL environment accompanied these steps to visually verify that the responses are acceptable.

Energy Distribution Controller It was shown that the modified energy distribution plant can be simplified to a single integrator system with the transfer function

$$G_D(s) = \frac{1}{s} \tag{6.110}$$

by assuming unity gain for the innermost loops. With the plant being so heavily simplified, it initially appears that the poles can be placed anywhere to achieve the desired dynamic response. In reality, it should be kept in mind that the inner loop dynamics will affect all outer loops. To that end, the time-scale separation between the controllers will be used to determine where poles can be placed realistically. In addition, this controller is designed in conjunction with the specific energy controller in an attempt to achieve a similar dynamic response.

Figure 6.14 shows the initial energy distribution controller design root locus and step response, with its characteristics detailed in Table 6.1. This attempt tried to achieve optimal damping at a reasonably fast settling time. It can be seen that the optimal damping ratio has been achieved, but significantly more overshoot is present due to the placement of a zero. The transient response peaks within 0.8s and settles under 1.8s, which is very fast. When taking the inner loop NSA controller settling time of 0.95s into consideration, it can be seen that the outer loop settling time is approximately double that of the inner loop, which falls significantly short of the five-times target [5]. It can therefore be concluded that this design will cause interference with the inner loop, which is behaviour that should be avoided.

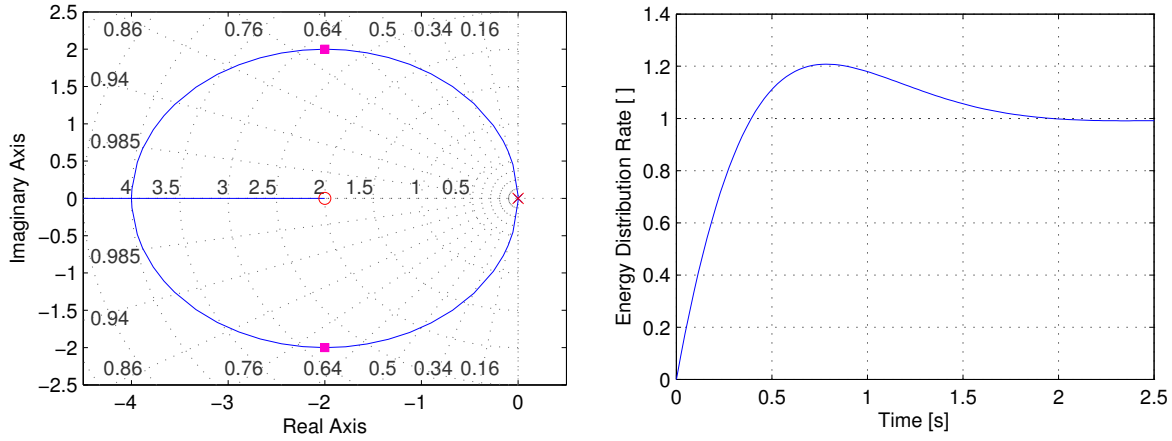

Figure 6.14: Initial TECS energy distribution controller design root locus and step response.

Table 6.1: Initial energy distribution controller design characteristics.

$D(s) = 4\dfrac{(s+2)}{s}$			
p_{cl}:	$-1 \pm 2j$	M_p:	21%
ζ:	0.707	t_p:	0.775 s
ω_n:	2.83 rad/s	$t_{s_{2\%}}$:	1.78 s

Figure 6.15 shows the second energy distribution controller design root locus and steps response, with its characteristics detailed in Table 6.2. This attempt tried to reduce the settling time by reducing the controller gain, thereby bringing the closed-loop poles closer to the origin. Although this worsened the damping ratio to 0.5 and increased overshoot to 30%, it did increase the settling time to 3.75s, which is approximately four times that of the NSA inner loop, which is nearing acceptable behaviour.

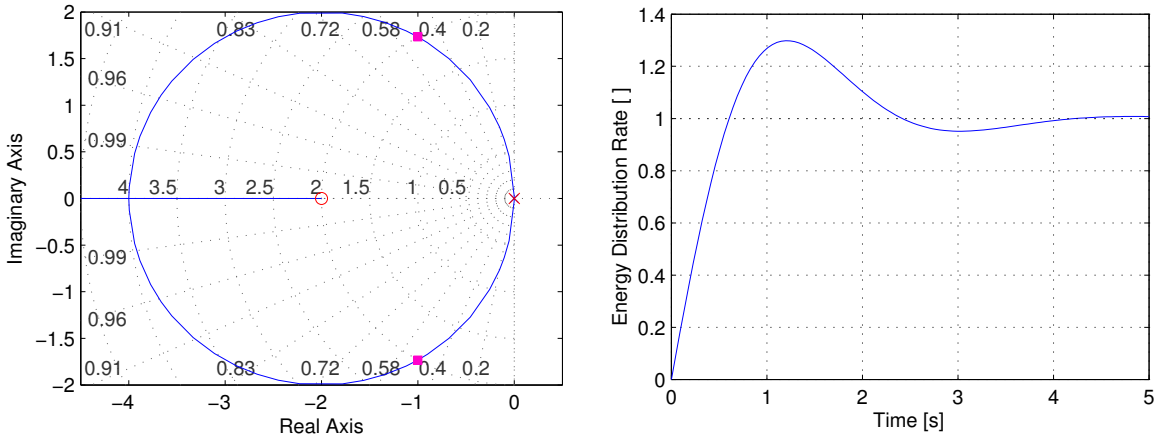

Figure 6.15: Second TECS energy distribution controller design root locus and step response.

Table 6.2: Second energy distribution controller design characteristics.

$D(s) = 2\dfrac{(s+2)}{s}$			
p_{cl}:	$-1 \pm 1.73j$	M_p:	30%
ζ:	0.5	t_p:	1.30 s
ω_n:	3.75 rad/s	$t_{s_{2\%}}$:	3.75 s

Figure 6.16 shows the third energy distribution controller design root locus and steps response, with its characteristics detailed in Table 6.3. This attempt tried to reduce the overshoot and improve the damping ratio while retaining the increased settling time. By moving the placed zero closer to the origin, the circular shape of the root locus became much smaller and closer to the origin, allowing for closed-loop pole placements which yield a much more gentle response. The damping ratio target of 0.707 has been achieved, although the overshoot remains a moderately high 21% due to the zero. The settling time is now just over 7s, which is more than the required five-times slower rule for acceptable time-scale separation. The peak time is just over 3s, which should yield acceptable results.

Table 6.3: Third (and implemented) energy distribution controller design characteristics.

$D(s) = \dfrac{(s+0.5)}{s}$			
p_{cl}:	$-0.5 \pm 0.5j$	M_p:	21%
ζ:	0.707	t_p:	3.16 s
ω_n:	0.707 rad/s	$t_{s_{2\%}}$:	7.10 s

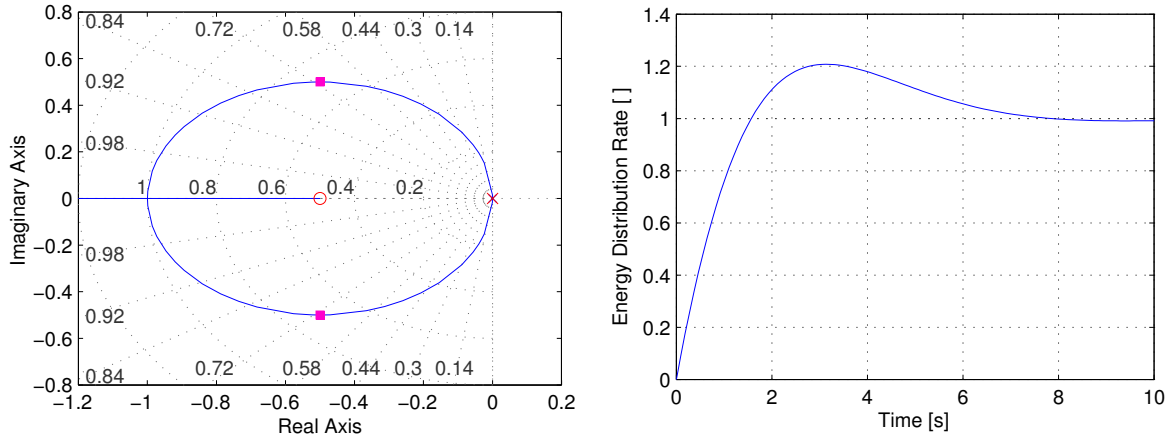

Figure 6.16: Third TECS energy distribution controller design root locus and step response.

Figure 6.17 shows the fourth energy distribution controller design root locus and steps response, with its characteristics detailed in Table 6.4. This attempt tried to further reduce damping while retaining the increased settling time. By increasing the gain, the damping ratio was increased to 0.866 with an overshoot of 16%. The settling time reduced to just under 6.3s, which still allows very good time-scale separation. However, this design looked too aggressive in HIL and was therefore discarded in favour of the previous design attempt.

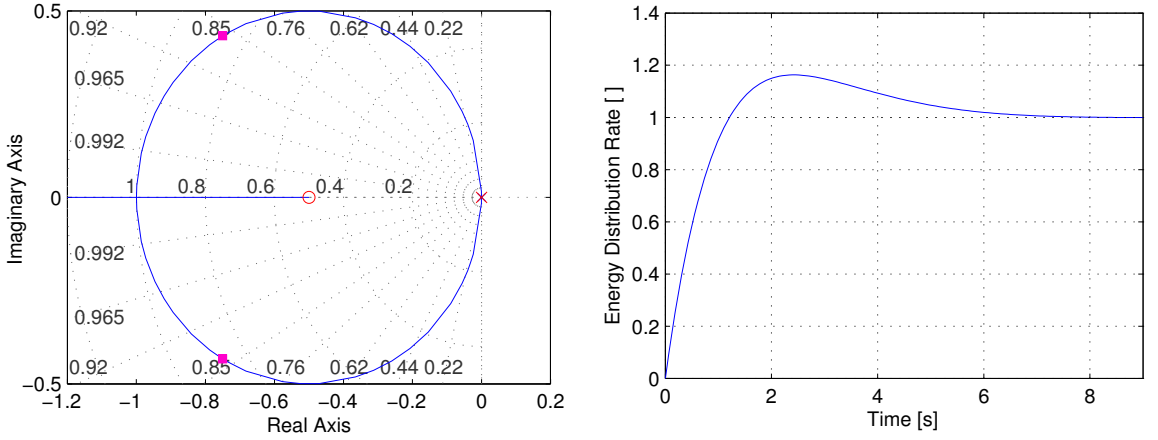

Figure 6.17: Fourth TECS energy distribution controller design root locus and step response.

Table 6.4: Fourth energy distribution controller design characteristics.

$D(s) = 1.5\dfrac{(s+0.5)}{s}$			
p_{cl}:	$-0.75 \pm 0.433j$	M_p:	16%
ζ:	0.866	t_p:	2.43 s
ω_n:	0.866 rad/s	$t_{s_{2\%}}$:	6.26 s

With the fine tuning performed in HIL, it was decided to settle on the third attempted controller. The final controller gains and time constant as per [7] were implemented as

$$K_{EP} = -1 \tag{6.111}$$

$$K_{EI} = -0.5 \tag{6.112}$$

$$\tau_D = 2 \text{ s} \tag{6.113}$$

Note that the gains are required to be negative in sign due to the controller output signal being an NSA command which is implemented around $-g$ as a zero point with a signal greater than $-g$ that would result in an upwards motion.

Specific Energy Controller It was shown that the modified specific energy plant can be simplified to a gain system with the transfer function

$$G_E(s) = \frac{1}{mg} \tag{6.114}$$

With the plant being so heavily simplified, it initially appears that the poles can be placed anywhere to achieve the desired dynamic response. It reality, it should be kept in mind that this controller should roughly match the energy distribution controller to achieve a similar response. This controller is therefore designed in conjunction with the energy distribution controller in an attempt to achieve this similar dynamic response.

Figure 6.18 shows the initial specific energy controller design root locus and steps response, with its characteristics detailed in Table 6.5. This attempt tried to match the settling time and time constant of the energy distribution controller. As expected, this controller and plant combination yields a first-order response, and the time at which it enters the 2% region will therefore be considered as the settling time. It can be seen that the time constant is very close to that of the energy distribution controller and that the settling time matches exactly. However, through HIL simulations it was found that this controller performed relatively poorly with such low gains, especially during landings.

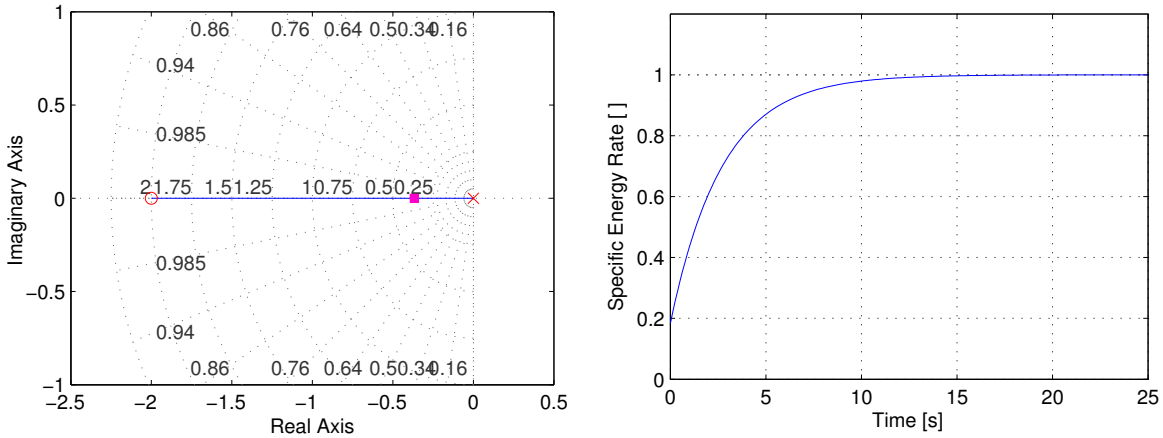

Figure 6.18: Initial TECS specific energy controller design root locus and step response.

Table 6.5: Initial specific energy controller design characteristics.

$D(s) = 13.5\frac{(s+2)}{s}$			
p_{cl}:	-0.368	τ:	2.17 s
ω_n:	0.368 rad/s	$t_{s_{2\%}}$:	6.26 s

Figure 6.19 shows the second specific energy controller design root locus and steps response, with its characteristics detailed in Table 6.6. This attempt tried to make the controller more aggressive by moving the location of the placed zero. This moved the closed-loop pole further away from the origin, thereby increasing the overall speed of the response. It should be noted that the system now no longer conforms to the similar time constant ratio specification as the value has now halved. The settling time is also faster, although it remains in proportion to that of the energy distribution controller. When examining the specific inputs, it can be seen that the integrator contributes the most to the final command signal. For the case where one of the inputs is zero, the following instantaneous integrator contributions are determined as

$$\left.\frac{\dot{\overline{v}}_e}{g}\right|_0 \rightarrow \frac{\delta_t}{\gamma_e} = \frac{0.95 \text{ N}}{1^\circ} \tag{6.115}$$

$$\left.\gamma_e\right|_0 \rightarrow \frac{\delta_t}{\dot{\overline{v}}_e} = \frac{5.4 \text{ N}}{0.1\text{m/s}^2} \tag{6.116}$$

These command values per error measurement seem reasonable and not too excessive, therefore it can be concluded that the design is practically acceptable given the simulated dynamic responses.

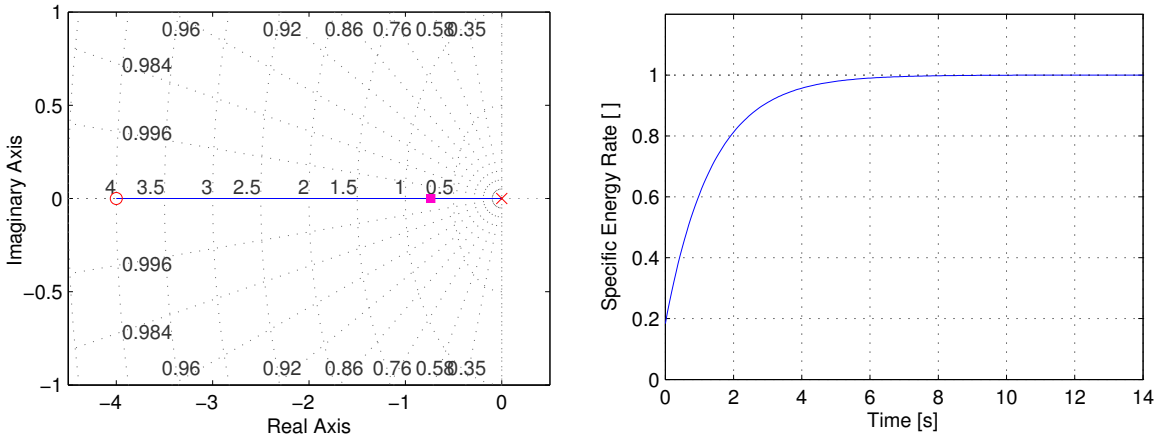

Figure 6.19: Second TECS specific energy controller design root locus and step response.

Table 6.6: Second (and implemented) specific energy controller design characteristics.

$D(s) = 13.5\frac{(s+4)}{s}$			
p_{cl}:	-0.735	τ:	1.08 s
ω_n:	0.735 rad/s	$t_{s_{2\%}}$:	5.02 s

Figure 6.20 shows the third specific energy controller design root locus and steps response, with its characteristics detailed in Table 6.7. This attempt tried to look at the effect of further increasing the controller gain. As can be seen, this sped up the dynamic response. Both the time constant and settling time are now much too fast to allow for a matched response with the energy distribution controller. For the case where one of the inputs is zero, the following instantaneous integrator contributions are determined as

$$\left.\frac{\dot{\overline{v}}_e}{g}\right|_0 \rightarrow \frac{\delta_t}{\gamma_e} = \frac{2.24 \text{ N}}{1^\circ} \tag{6.117}$$

$$\gamma_e|_0 \rightarrow \frac{\delta_t}{\dot{\overline{v}}_e} = \frac{12.80 \text{ N}}{0.1\text{m/s}^2} \tag{6.118}$$

Intuitively, these command signals are too aggressive. When sensor noise and vibration are considered, these gains will likely cause excessive throttle activity and the design is therefore discarded in favour of the second design attempt.

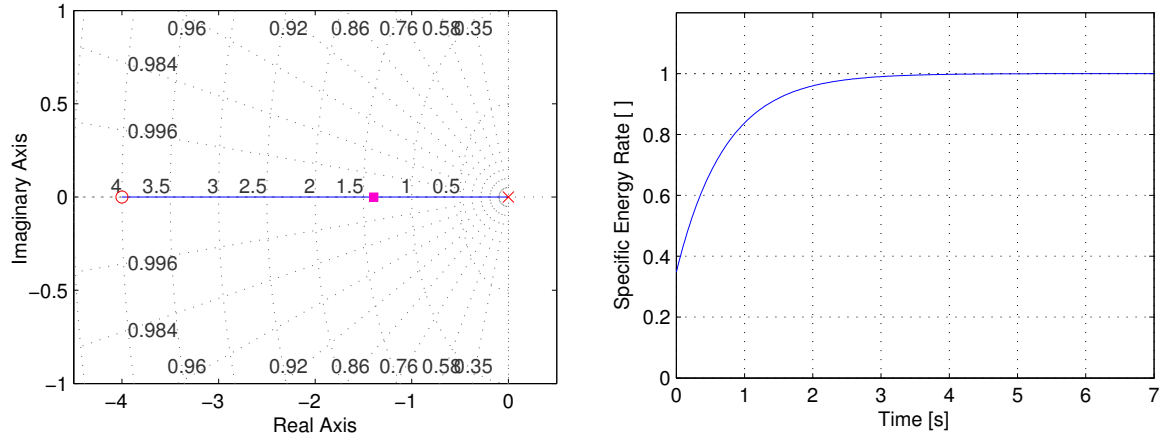

Figure 6.20: Third TECS specific energy controller design root locus and step response.

Table 6.7: Third specific energy controller design characteristics.

$D(s) = 32\frac{(s+4)}{s}$			
p_{cl}:	-1.39	τ:	0.41 s
ω_n:	1.39 rad/s	$t_{s_{2\%}}$:	2.49 s

With the fine tuning performed in HIL, the final controller gains and time constant were implemented as

$$K_{EP} = 13.5 \tag{6.119}$$
$$K_{EI} = 54 \tag{6.120}$$
$$\tau_D = 1.08 \text{ s} \quad \text{as per Matlab design} \tag{6.121}$$
$$= 4.0 \text{ s} \quad \text{as per [7]} \tag{6.122}$$

6.2.4.4 TECS Outer Loop Design

Due to the complexity of the inner loop controller structure, it was decided to design the outer loops in a heuristic fashion similar to some of the research presented in Chapter 1. This method heavily involved the SIL/HIL environments to evaluate the performance of each gain set. It was decided to keep the gains equal as suggested by [7], especially since the inner loop gains already deviated from the design suggestions.

The gains of the two outer loop controllers essentially determines the error decay time of the responses. It shows second-order behaviour, especially evident with higher gain values. It also seemed that the inner loops heavily dominate the dynamic response, as significant gain changes were required in order to observe a relatively small change in response. The final gain values were implemented as

$$K_h = 0.5 \tag{6.123}$$
$$K_v = 0.5 \tag{6.124}$$

6.3 Lateral Control

In conventional aircraft controllers, the lateral controller is responsible for matching the bank angle and heading of the aircraft to the reference values in order to perform steering as well as providing stability. While many such controllers exist and have been successfully implemented, the focus of this project was to use aggressive control to settle on the intended landing path as quickly as possible. For this goal, classical control methods were used and augmented as required.

For the classical controller method, the following four controllers are typically implemented in a successive loop closure fashion:

1. Dutch Roll Damper, which improves yaw rate stability by improving the damping of the Dutch roll natural mode of motion;
2. Roll Angle Controller, which controls the roll angle of the aircraft and is used to bank the aircraft to change flight direction by rotating the angle of the lift vector;
3. Heading Controller, which controls the compass heading of the aircraft; and a
4. Guidance Controller, which controls the cross-track error to follow a ground track between two points.

Although this approach has been proven to work adequately, the time-scale separation required between these controllers causes the system to respond very slowly, as well as reducing its ability to reject constant disturbances fast enough for accurate landings. An aggressive control method is therefore proposed, which is discussed in more detail in Section 6.3.4. The designs in this chapter are primarily based on the work of [4].

6.3.1 Dutch Roll Damper

The Dutch Roll Damper attempts to suppress the oscillations in both yaw and induced roll rates as discussed in Section 5.2.2.2 by providing additional artificial damping. This effect is achieved by a feedback loop that modifies the rudder command according to the currently experienced yaw rate, mainly filtered directly from the yaw rate gyroscope. However, during constant turns the aircraft will also experience a desired yaw rate which should not be damped by the rudder signal. To enable the desired damping behaviour, a high-pass filter (HPF) is used so that the rudder is commanded to oppose the higher frequency yaw rates of the Dutch roll mode, but is not commanded to oppose the low frequency yaw rates of a constant turn. It is therefore important to select the cut-off frequency of the filter appropriately — high enough to sufficiently damp Dutch roll motions, but low enough to allow constant turns.

For this aircraft, the Dutch roll mode is stable but poorly damped as seen in Figure 5.3. The pole pair corresponding to this mode, as well as its natural frequency and damping ratio, are restated for convenience as

$$\begin{aligned} s &= -0.5699 \pm 4.0617j \\ \omega_n &= 4.1015 \text{ rad/s} \\ \zeta &= 0.1389 \end{aligned}$$

The Dutch Roll Damper has a simple structure, using only the filtered yaw rate measurement for damping as illustrated in Figure 5.5. The design entails choosing the gain and cut-off frequency of the HPF.

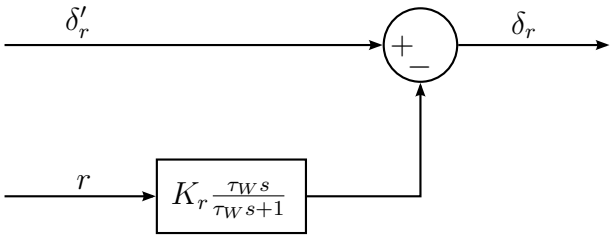

Figure 6.21: Dutch Roll Damper block diagram.

The rudder deflection angle to yaw rate transfer function can be obtained from the state-space representation as

$$\frac{r(s)}{\delta_r(s)} = \boldsymbol{C}_r \left(s\boldsymbol{I} - \boldsymbol{A}_{lat}\right)^{-1} \boldsymbol{B}_{\delta_r} \tag{6.125}$$

where

$$\boldsymbol{B}_{\delta_r} = \begin{bmatrix} \frac{q_{p_T} S}{m\bar{v}_T} C_{y_{\delta_r}} & \frac{q_{p_T} Sb}{I_{xx}} C_{l_{\delta_r}} & \frac{q_{p_T} Sb}{I_{zz}} C_{n_{\delta_r}} & 0 \end{bmatrix}^T \tag{6.126}$$

$$\boldsymbol{C}_r = \begin{bmatrix} 0 & 0 & 1 & 0 \end{bmatrix} \tag{6.127}$$

For an initial starting point, it is suggested to set the filter cut-off frequency to

$$\tau_W = \frac{\omega_n}{4} \tag{6.128}$$

$$= 1.025 \tag{6.129}$$

$$\approx 1.0 \text{ rad/s} \tag{6.130}$$

The filter can then be added to the plant and a gain can subsequently be designed using the root locus. For this design, the gain value was set to

$$K_r = -0.6 \tag{6.131}$$

Note that the value is negative as a positive deflection causes a negative moment, with a negative feedback loop being a requirement for a stable system. Figure 6.22 shows the controller design root locus and impulse response, with its characteristics detailed in Table 6.8. For the impulse response, the zero/pole combination for the spiral mode was ignored as it will be attended to with a subsequent loop closure design. The settling time was considered at the point where the magnitude enters 2% of the maximum deviation. As can be seen, the damping and maximum deviation has been significantly improved from the open-loop response with the oscillations settling in under 3s and deviates 12% of the original maximum.

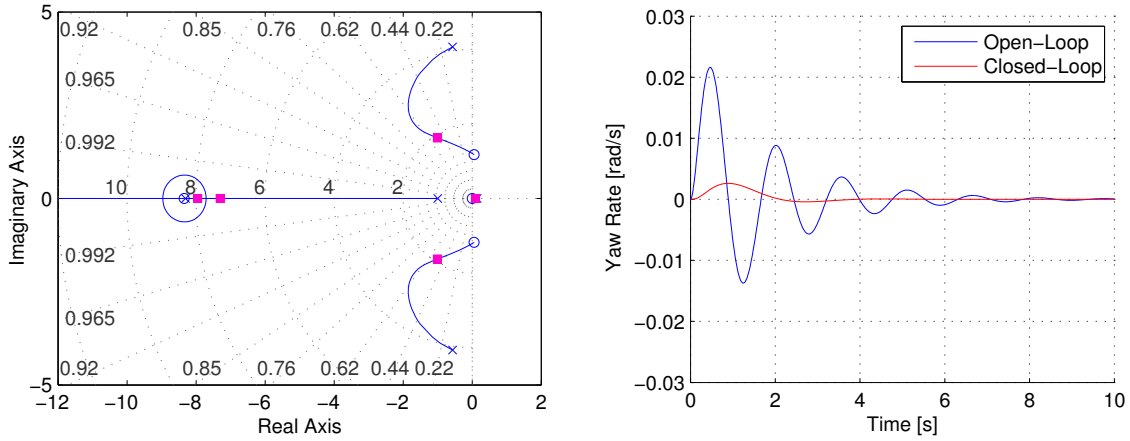

Figure 6.22: Dutch Roll Damper design root locus and impulse response.

Table 6.8: Dutch Roll Damper design characteristics.

$D(s) = -0.6\dfrac{s}{s+1}$			
p_{cl}:	$-1.0 \pm 1.73j$	ω_n:	1.91 rad/s
ζ:	0.528	$t_{s_{2\%}}$:	2.85 s

The closed-loop system will now serve as the inner loop for the subsequent controller loop. The augmented plant is now given by

$$\dot{\boldsymbol{x}}_{DRD} = \boldsymbol{A}_{DRD}\boldsymbol{x}_{DRD} + \boldsymbol{B}_{DRD}\boldsymbol{u}_{lat} \tag{6.132}$$

with

$$\boldsymbol{A}_{DRD} = \begin{bmatrix} \boldsymbol{A}_{lat} - \boldsymbol{B}_{\delta_r} D_W \boldsymbol{C}_r & -\boldsymbol{B}_{\delta_r} C_W \\ B_W \boldsymbol{C}_r & B_W \end{bmatrix} \tag{6.133}$$

$$\boldsymbol{B}_{DRD} = \begin{bmatrix} \boldsymbol{B}_{lat} \\ 0 \end{bmatrix} \tag{6.134}$$

$$\boldsymbol{x}_{DRD} = \begin{bmatrix} \beta & p & r & \phi & x_W \end{bmatrix}^T \tag{6.135}$$

$$\boldsymbol{u}_{lat} = \begin{bmatrix} \delta_a & \delta_r' \end{bmatrix}^T \tag{6.136}$$

During HIL simulations, the controller underwent further tuning. The following value was altered for the final implementation:

$$\tau_W = 1.5 \text{ rad/s} \tag{6.137}$$

6.3.2 Roll Angle Controller

The Roll Angle Controller uses the ailerons to regulate the bank angle of the aircraft. The roll angle has the most profound effect on turning the aircraft and is therefore used to guide the aircraft laterally. Since it is difficult to measure the roll angle, complex estimation methods are commonly used to obtain its value. Furthermore, roll angle controllers usually add an integrator to obtain zero steady state error.

For this aircraft, the roll mode has a fast and stable pole as seen in Figure 5.3. The pole corresponding to this mode and its natural frequency are restated for convenience as

$$s = -8.3048$$
$$\omega_n = 8.3048 \text{ rad/s}$$

The Roll Angle Controller has the traditional PI controller structure, except for the output signal sign inversion as illustrated in Figure 6.23. This sign inversion is necessary to acquire a negative feedback loop given the sign conventions.

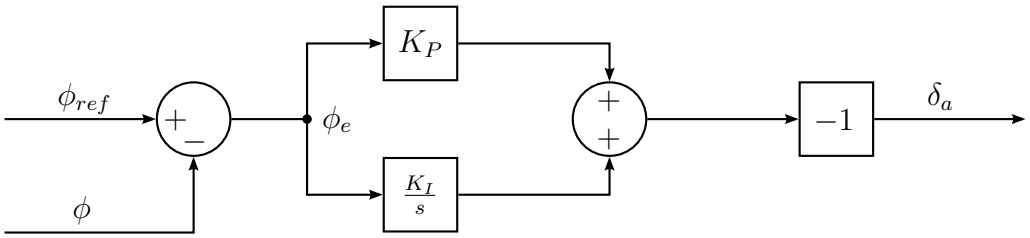

Figure 6.23: Roll Angle Controller block diagram.

The aileron deflection angle to roll angle transfer function can be obtained from the state-space representation as

$$\frac{\phi(s)}{\delta_a(s)} = \boldsymbol{C}_\phi \left(s\boldsymbol{I} - \boldsymbol{A}_{DRD}\right)^{-1} \boldsymbol{B}_{\delta_a} \tag{6.138}$$

where

$$\boldsymbol{B}_{\delta_a} = \begin{bmatrix} \frac{q_{p_T} S}{m\bar{v}_T} C_{y_{\delta_a}} & \frac{q_{p_T} Sb}{I_{xx}} C_{l_{\delta_a}} & \frac{q_{p_T} Sb}{I_{zz}} C_{n_{\delta_a}} & 0 & 0 \end{bmatrix}^T \tag{6.139}$$

$$\boldsymbol{C}_\phi = \begin{bmatrix} 0 & 0 & 0 & 1 & 0 \end{bmatrix} \tag{6.140}$$

For this design, the values were set to

$$z = -0.4 \tag{6.141}$$
$$K_P = 0.2 \tag{6.142}$$
$$K_I = 0.08 \qquad \text{(by implication)} \tag{6.143}$$

Figure 6.24 shows the controller design root locus and step response, with its characteristics detailed in Table 6.9. This designed attempted to slow down the roll angle response due to

practical flight test concerns that sprouted from the HIL visualisation. The unusual looking response is due to the dominant spiral mode pole that also affects this response. A moderate amount of overshoot is present at 28% after 4.4s which was difficult to reduce while keeping an average speed of response. Although the response appears to settle very slowly, it rises extremely quickly. This was deemed an acceptable trade-off since the controller would continuously get new command signals.

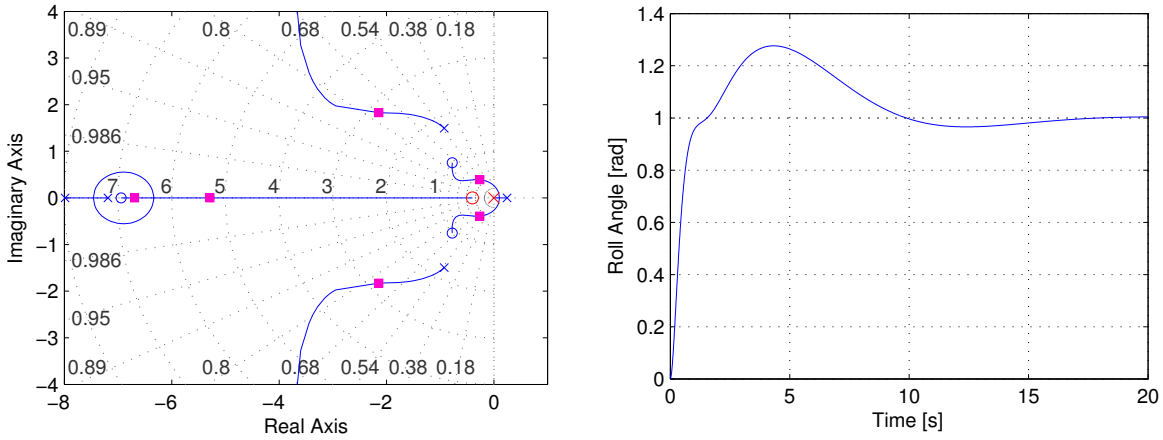

Figure 6.24: Roll Angle Controller design root locus and step response.

Table 6.9: Roll Angle Controller design characteristics with the dominant and relevant poles.

$D(s) = 0.2\dfrac{(s+0.4)}{s}$			
p_{cl_1}:	$-0.259 \pm -0.389j$	p_{cl_2}:	-5.29
ζ:	0.554	p_{cl_3}:	-6.69
ω_n:	0.467 rad/s	t_p:	4.4 s
M_p:	28%	$t_{s_{2\%}}$:	14.9 s

The closed-loop system will now serve as the inner loop for the subsequent controller loop. The augmented plant is now given by

$$\dot{\boldsymbol{x}}_{RAC} = \boldsymbol{A}_{RAC}\boldsymbol{x}_{RAC} + \boldsymbol{B}_{RAC}\phi_{ref} \tag{6.144}$$

with

$$\boldsymbol{A}_{RAC} = \begin{bmatrix} \boldsymbol{A}_{DRD} + \boldsymbol{B}_{\delta_a} K_P \boldsymbol{C}_\phi & -\boldsymbol{B}_{\delta_a} K_I \\ -\boldsymbol{C}_\phi & 0 \end{bmatrix} \tag{6.145}$$

$$\boldsymbol{B}_{RAC} = \begin{bmatrix} -K_P \boldsymbol{B}_{\delta_a} \\ 1 \end{bmatrix} \tag{6.146}$$

$$\boldsymbol{x}_{RAC} = \begin{bmatrix} \beta & p & r & \phi & x_W & x_I \end{bmatrix}^T \tag{6.147}$$

During HIL simulations, the controller underwent further tuning. The following value was altered for the final implementation:

$$K_P = 0.15 \tag{6.148}$$

6.3.3 Heading & Guidance Controllers

Due to the inherent problem of the Cross-Track Controller discovered in Section 6.3.4, heading and guidance controllers were implemented to aid waypoint navigation. The controllers in this section run in tandem with the Cross-Track Controller, but the final roll angle reference value consists of mixing between the two output signals. An ideal switching distance exists and can be calculated, which is presented in Section 6.3.4.2.

6.3.3.1 Heading Controller

The Heading Controller supplies the Roll Angle Controller with a roll angle command which is proportional to the current heading error. In turn, the Roll Angle Controller would produce a heading rate which is naturally integrated to yield the heading. This controller can be thought of as steering the aircraft into a specified direction.

The Heading Controller has the traditional proportional controller structure as illustrated in Figure 6.25. With the inner loops now stabilised, the only purpose of this controller is to steer the aircraft in the reference direction as quickly as possible with an acceptable transient and avoiding excessive roll angle commands.

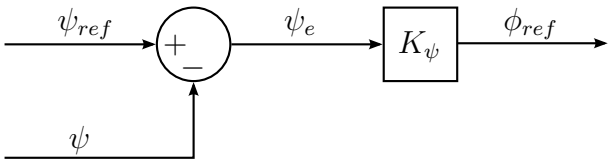

Figure 6.25: Heading Controller block diagram.

In a steady turn with a constant, nonzero roll angle, the lift vector provides both a counter to the weight of the aircraft as well as centripetal acceleration to perform the turn. For such a case, the lateral acceleration is given by

$$a_L = \overline{v}_T \dot{\psi} \tag{6.149}$$

$$= g \tan \phi \tag{6.150}$$

With the small angle assumption that $\tan \phi \approx \phi$, Equations 6.149 and 6.150 can be rewritten

to form

$$\dot{\psi} = \frac{g}{\overline{v}_T}\phi \tag{6.151}$$

This equation is used to relate the roll angle to the heading rate. Due to the natural integration from the heading rate to the heading angle, the system is of type 1 and should be able to follow a constant heading reference with zero steady state error, assuming that there is no bias error in the roll angle measurement as observed by [16].

The Roll Angle Controller inner loop is now augmented with the heading dynamics to obtain

$$\begin{bmatrix} \dot{\boldsymbol{x}}_{RAC} \\ \dot{\psi} \end{bmatrix} = \begin{bmatrix} \boldsymbol{A}_{RAC} & 0 \\ \boldsymbol{C}_{\dot{\psi}} & 0 \end{bmatrix} \begin{bmatrix} \boldsymbol{x}_{RAC} \\ \psi \end{bmatrix} + \begin{bmatrix} \dot{\boldsymbol{B}}_{RAC} \\ 0 \end{bmatrix} \phi_{ref} \tag{6.152}$$

The roll angle to heading angle transfer function can be obtained from the state-space representation as

$$\frac{\psi(s)}{\phi_{ref}(s)} = \frac{1}{s}\boldsymbol{C}_{\dot{\psi}} \left(s\boldsymbol{I} - \boldsymbol{A}_{RAC}\right)^{-1} \boldsymbol{B}_{RAC} \tag{6.153}$$

where

$$\boldsymbol{C}_{\dot{\psi}} = \begin{bmatrix} \boldsymbol{0}_3 & \frac{g}{\overline{v}_T} & \boldsymbol{0}_2 \end{bmatrix} \tag{6.154}$$

For this design, the value was set to

$$K_{\psi} = 1.25 \tag{6.155}$$

Figure 6.26 shows the controller design root locus and step response, with its characteristics detailed in Table 6.10. The response is reasonably well damped with 11% overshoot while settling in under 12s. The undershoot after the overshoot is fairly large, but diminishes quickly. This response is likely due to the interaction between the many poles and zeroes near the origin.

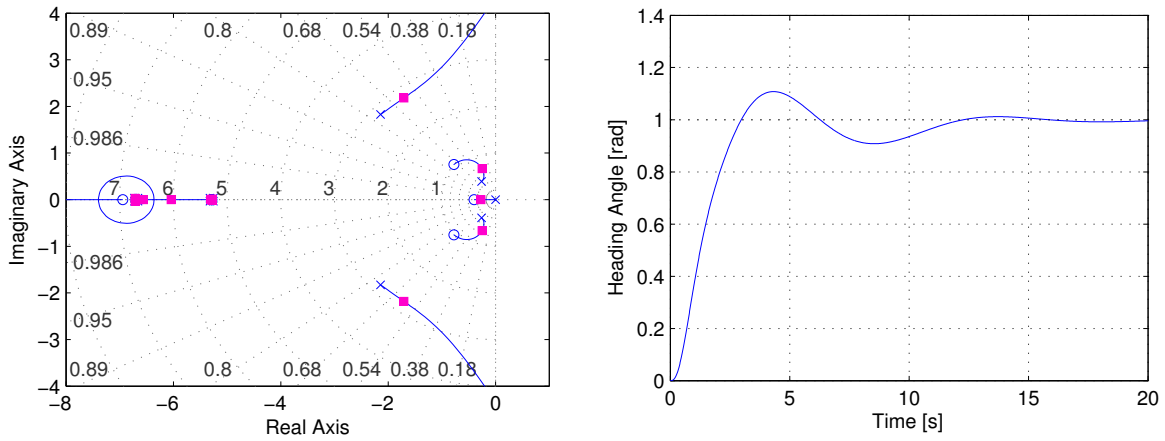

Figure 6.26: Heading Controller design root locus and step response.

Table 6.10: Heading Controller design characteristics with the dominant pole.

$D(s) = 1.25$			
p_{cl}:	-0.271	M_p:	11%
ζ:	1.0	t_p:	4.15 s
ω_n:	0.271 rad/s	$t_{s_{2\%}}$:	11.4 s

The closed-loop system will now serve as the inner loop for the subsequent controller loop. The augmented plant is now given by

$$\dot{\boldsymbol{x}}_{HC} = \boldsymbol{A}_{HC}\boldsymbol{x}_{HC} + \boldsymbol{B}_{HC}\psi_{ref} \tag{6.156}$$

with

$$\boldsymbol{A}_{HC} = \begin{bmatrix} \boldsymbol{A}_{RAC} & -\boldsymbol{B}_{RAC}K_\psi \\ \boldsymbol{C}_{\dot{\psi}} & 0 \end{bmatrix} \tag{6.157}$$

$$\boldsymbol{B}_{HC} = \begin{bmatrix} \boldsymbol{B}_{RAC}K_\psi \\ 0 \end{bmatrix} \tag{6.158}$$

$$\boldsymbol{x}_{HC} = \begin{bmatrix} \beta & p & r & \phi & x_W & x_I & \psi \end{bmatrix}^T \tag{6.159}$$

During HIL simulations, the controller underwent further tuning. The following value was altered for the final implementation:

$$K_\psi = 1.20 \tag{6.160}$$

6.3.3.2 Guidance Controller

The Guidance Controller steers the aircraft onto a heading track between two points in inertial space. For this project, these sets of points will create a series of straight line segments over the ground. The end points of these segments are the waypoints of the track. To keep the aircraft on this ground track, the Guidance Controller reduces the distance between the current location of the aircraft and the ground track.

The Guidance Controller has the traditional proportional controller structure, except for the addition of the track heading as illustrated in Figure 6.27. In order to design this controller, a guidance axes system and accompanying parameters need to be defined.
The guidance axes system and its parameters are illustrated in Figure 6.28. The track heading

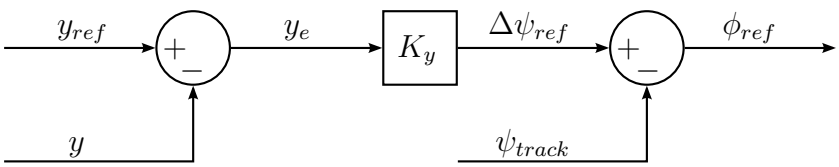

Figure 6.27: Guidance Controller block diagram.

and track length is defined as

$$\tan\psi_{track} = \frac{E_{dest} - E_{src}}{N_{dest} - N_{src}} \tag{6.161}$$

$$L_{track} = \sqrt{(N_{dest} - N_{src})^2 + (E_{dest} - E_{src})^2} \tag{6.162}$$

The in-track distance is defined as the length of the projection of the aircraft perpendicular onto the track from the source waypoint. The cross-track error is defined as the perpendicular distance from the aircraft to its projection on the ground track. The guidance axes system is defined with the following characteristics:

- The origin is located at the source waypoint coordinates.
- The X-axis is parallel to the ground track and points towards the destination waypoint.
- The Y-axis is perpendicular to the X-axis towards its starboard side in the horizontal plane.
- The Z-axis coincides with that of the inertial axes, although this axis irrelevant.

The inertial position coordinates are transformed through a matrix to obtain

$$\begin{bmatrix} x \\ y \end{bmatrix} = \begin{bmatrix} \cos\psi_{track} & \sin\psi_{track} \\ -\sin\psi_{track} & \cos\psi_{track} \end{bmatrix} \begin{bmatrix} N_{cur} - N_{src} \\ E_{cur} - E_{src} \end{bmatrix} \tag{6.163}$$

where x is the in-track distance and y is the cross-track error. The controller generates a heading command proportional to the cross-track error for the Heading Controller inner loop. The subsequent changes in heading causes a rate of change in the cross-track error. This rate of change can be calculated by

$$\dot{y} = \overline{v}\sin(\psi - \psi_{track}) \tag{6.164}$$

and simplified with the small angle assumption to

$$\dot{y} = \overline{v}(\psi - \psi_{track}) \tag{6.165}$$

Due to the natural integration from the cross-track rate to a cross-track distance, the system is of type 1 and should be able to follow a constant cross-track reference with zero steady state error, assuming that there is no bias error in the heading angle measurement. Since the

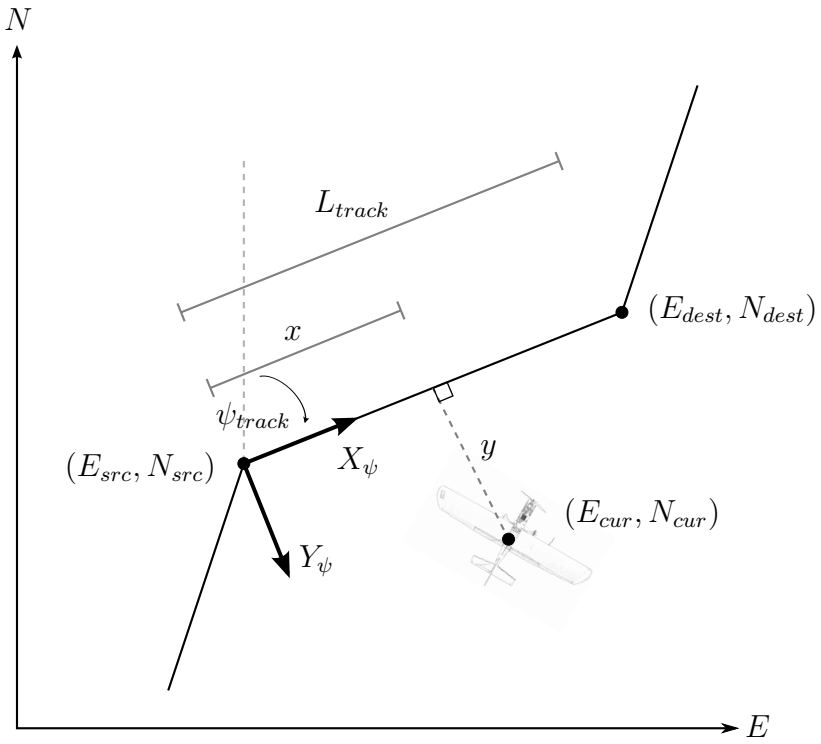

Figure 6.28: Guidance axes system showing the waypoints, track heading, cross-track error and in-track distance.

Heading Controller requires a heading reference relative to North and not that of the guidance axes system, it is required to add the track heading to the Guidance Controller output as given by

$$\psi_{ref} = \Delta\psi + \psi_{track} \tag{6.166}$$

The relative heading should be limited to remain within $\pm 90°$ or the aircraft may fly in the wrong in-track direction.

The Heading Controller inner loop is now augmented with the cross-track dynamics to obtain

$$\begin{bmatrix} \dot{\boldsymbol{x}}_{HC} \\ \dot{y} \end{bmatrix} = \begin{bmatrix} \boldsymbol{A}_{HC} & 0 \\ \boldsymbol{C}_{\dot{y}} & 0 \end{bmatrix} \begin{bmatrix} \boldsymbol{x}_{HC} \\ y \end{bmatrix} + \begin{bmatrix} \dot{\boldsymbol{B}}_{HC} \\ 0 \end{bmatrix} \psi_{ref} + \begin{bmatrix} \mathbf{0}_6 \\ -1 \end{bmatrix} \psi_{track} \tag{6.167}$$

The relative heading angle reference to cross-track distance transfer function can be obtained from the state-space representation as

$$\frac{y(s)}{\Delta\psi_{ref}(s)} = \frac{1}{s}\boldsymbol{C}_{\dot{y}} \left(s\boldsymbol{I} - \boldsymbol{A}_{HC}\right)^{-1} \boldsymbol{B}_{HC} \tag{6.168}$$

where

$$\boldsymbol{C}_{\dot{y}} = \begin{bmatrix} \mathbf{0}_6 & \overline{v}_T \end{bmatrix} \tag{6.169}$$

For this design, the value was set to

$$K_y = 0.02 \tag{6.170}$$

Figure 6.29 shows the controller design root locus and step response, with its characteristics detailed in Table 6.11. The response is very well damped with only 8% overshoot, although wide oscillation persists fairly long into the transient. This large initial oscillation response is likely due to interaction between the many poles and zeroes near the origin. It must be noted that the dominant pole location is not an order of magnitude less than the inner Heading Controller loop, which means that adequate time-scale separation is not achieved. However, since this loop has a significant 50% slower peak and settling time, it is regarded as safe. The controller is also merely used to push the aircraft into the correct direction until the Cross-Track Controller can engage and will therefore not be used during any landing attempts.

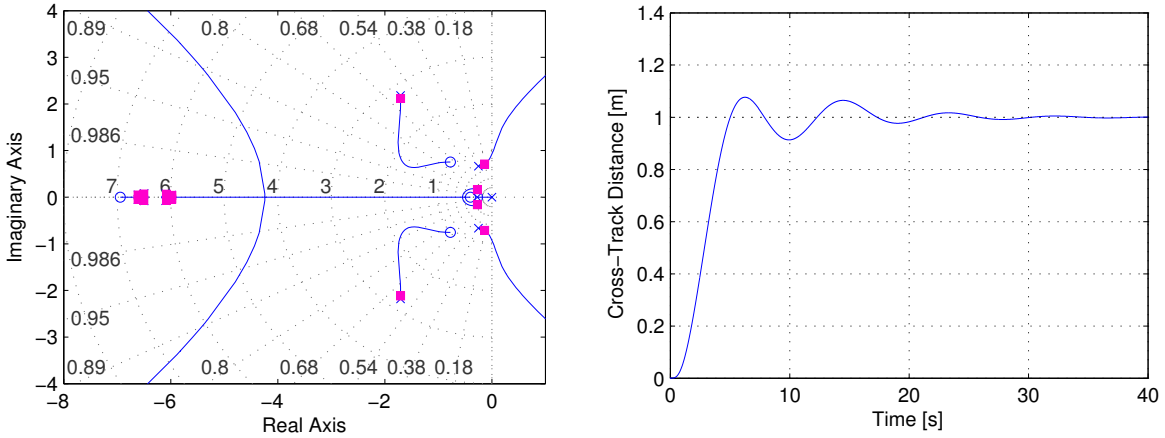

Figure 6.29: Guidance Controller design root locus and step response with the dominant pole.

Table 6.11: Guidance Controller design characteristics.

$D(s) = 0.02$			
p_{cl}:	$-0.269 \pm 0.162j$	M_p:	8%
ζ:	0.856	t_p:	6.29 s
ω_n:	0.314 rad/s	$t_{s_{2\%}}$:	19.7 s

The closed-loop system is the final loop in the successive loop closure design and therefore has no reference input. The augmented plant can now be given by

$$\dot{\boldsymbol{x}}_{GC} = \boldsymbol{A}_{GC}\boldsymbol{x}_{GC} \tag{6.171}$$

with

$$\boldsymbol{A}_{GC} = \begin{bmatrix} \boldsymbol{A}_{HC} & -\boldsymbol{B}_{HC}K_y \\ \boldsymbol{C}_{\dot{y}} & 0 \end{bmatrix} \tag{6.172}$$

$$\boldsymbol{x}_{GC} = \begin{bmatrix} \beta & p & r & \phi & x_W & x_I & \psi & y \end{bmatrix}^T \tag{6.173}$$

During HIL simulations, the controller underwent further tuning. The following value was altered for the final implementation:

$$K_y = 0.01 \tag{6.174}$$

6.3.4 Cross-Track Controller

The Cross-Track Controller is proposed as a substitute to the traditional Heading and Guidance Controllers. It uses the same cross-track signals as described in Section 6.3.3.2 to directly command the Roll Angle Controller. By reducing two successive loop closure designs into one, the controller can act much more aggressively due to less time-scale separation between loops.

The Cross-Track Controller has the traditional PID controller structure, except that the derivative component uses the time derivative of the output signal instead of the time derivative of the error signal as illustrated in Figure 6.23. This change is included to avoid large spikes every time the reference changes when the aircraft passes a waypoint, therefore a near constant reference signal is assumed.

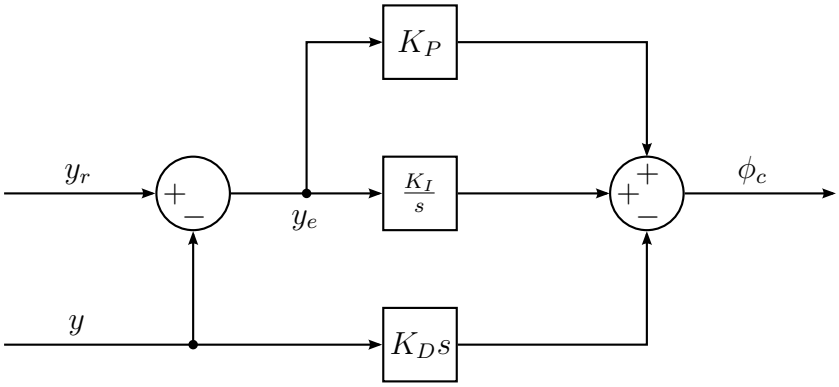

Figure 6.30: Cross-Track Controller block diagram.

The Roll Angle Controller is augmented with both the heading and cross-track dynamics from Sections 6.3.3.1 and 6.3.3.2 in a single augmentation to obtain the cross-track error. The roll angle to cross-track distance transfer function can subsequently be written as

$$\frac{y(s)}{\phi_{ref}(s)} = \frac{\overline{v}_T}{s^2}\boldsymbol{C}_{\psi}\left(s\boldsymbol{I} - \boldsymbol{A}_{RAC}\right)^{-1}\boldsymbol{B}_{RAC} \tag{6.175}$$

where

$$\boldsymbol{C}_{\dot{\psi}} = \begin{bmatrix} \mathbf{0}_3 & \frac{g}{\bar{v}_T} & \mathbf{0}_2 \end{bmatrix} \tag{6.176}$$

Note that the small angle assumption made to obtain Equation 6.165 applies to this augmentation as well. Initially, the controller was designed as a PD controller only. For this design, the values were set to

$$K_P = 0.075 \tag{6.177}$$

$$K_D = 0.15 \tag{6.178}$$

Figure 6.31 shows the controller design root locus and step response, with its characteristics detailed in Table 6.12. Although the dominant pole pair is highly damped, the response still shows a major 47% overshoot after just 2s. This is likely due to the many zeroes located close to the origin, which typically increase overshoot due to predictive behaviour. Fortunately, the oscillation settles fairly quickly in under 13s. Given that the system will only perform regulation towards zero error, this is deemed acceptable.

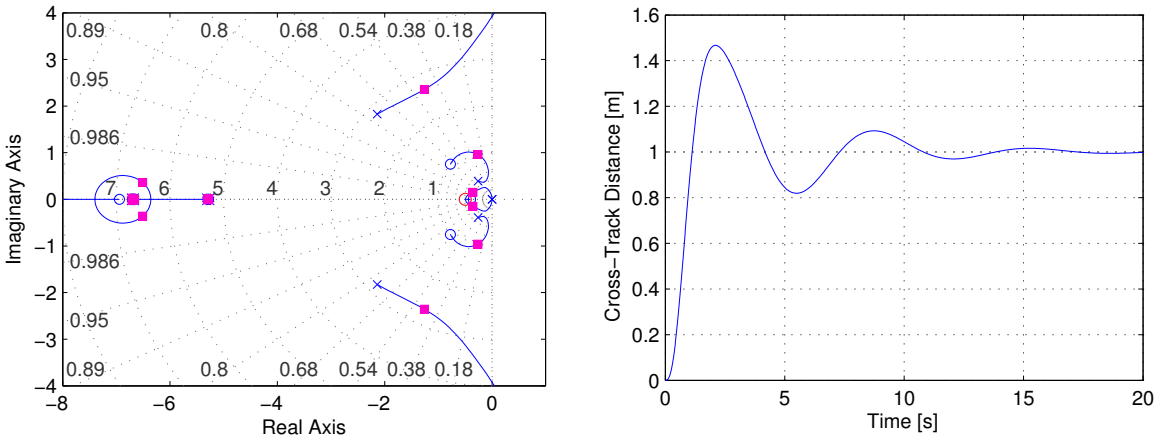

Figure 6.31: Cross-track Controller design root locus and step response.

Table 6.12: Cross-track Controller design characteristics.

$D(s) = 0.15s + 0.075$			
p_{cl}:	$0.356 \pm 0.149j$	M_p:	47%
ζ:	0.923	t_p:	2.06 s
ω_n:	0.386 rad/s	$t_{s_{2\%}}$:	12.9 s

In previous projects, it was found that there exists a sensor bias in the Roll Angle Controller inner loop. To ensure zero steady state error in the presence of this bias, a limited integrator

is added to the controller. The integrator limit was set to only contribute a maximum of 4° to the roll angle command output, which was the maximum bias estimated from the previous projects. For this design, the gain value was set to

$$K_I = 0.01 \tag{6.179}$$

Figure 6.32 shows the controller design root locus and step response, with its characteristics detailed in Table 6.13. The effect of the integrator on the transient response was to be minimised and was therefore mostly tuned through HIL. This caused the chosen value to place the zeroes at a non-real location. It can be seen that the integrator caused slightly more overshoot, which increased to 51%. As expected, it also slowed down the system so that it now settles within 14s. Due to the many poles around the origin, designing this controller proved to be very difficult to tune in order to get a fast, yet acceptably damped response.

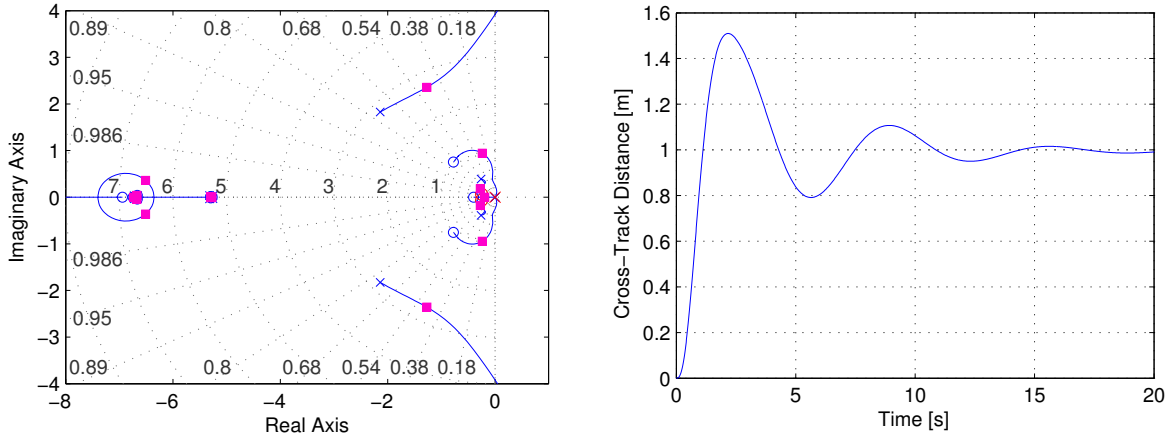

Figure 6.32: Cross-track Controller with a limited integrator design root locus and step response.

Table 6.13: Cross-track Controller with a limited integrator design characteristics.

$D(s) = 0.15\dfrac{(s+0.25+0.0645j)(s+0.25-0.0645j)}{s}$			
p_{cl}:	$0.275 \pm 0.178j$	M_p:	51%
ζ:	0.839	t_p:	2.14 s
ω_n:	0.328 rad/s	$t_{s_{2\%}}$:	13.7 s

During HIL simulations, the controller underwent further tuning. The following value was altered for the final implementation:

$$K_I = 0.02 \tag{6.180}$$

6.3.4.1 Tracking Issue

During the simulation testing, it was found that this controller could not reduce the cross-track error to zero when the aircraft is initialised at a position that is far away from the track or if it deviates into such a position. Instead, it performs constant circling around a particular location, never closing the cross-track gap. Further investigation presented in Section 6.3.4.2 shows that this behaviour is caused by constant roll angle commands given by the Cross-Track Controller when the cross-track error is sufficiently large. This command is so large that the aircraft turns too far and continues on this banked angle forever, never being able to return to the track. This problem stems from the fact that the Cross-Track Controller assumes that the aircraft is sufficiently close to the track and flying in the correct direction so that the small angle approximation holds where the cross-track rate is proportional to the relative heading between the aircraft and the ground track. Thus, when the aircraft is too far away from the track, this assumption is no longer valid. Unfortunately, this problem can not simply be tuned away through control system design as this would negatively impact system performance and merely change the point at which it would start affecting the system.

Initially, it was attempted to incorporate a set of rules to override the controller behaviour. However, the way in which the references and measurements are calculated, the rule set became very large and difficult to design and test, especially since the aircraft should be able to fly anywhere and change circuit direction at any time.

To address this problem, it was proposed that the traditional Heading and Guidance Controller be added to the system and used in conjunction with the Cross-Track Controller. By switching between the two sets, the aircraft can be brought into range where a switch to the Cross-Track Controller would allow it to negate the cross-track error as intended. This switching method is further discussed in Section 6.3.4.2.

6.3.4.2 Integration with the Heading & Guidance Controllers

As discussed in Section 6.3.4.1, it was found that the Cross-Track Controller can not reduce a cross-track error to zero when the aircraft is sufficiently far away from the track. This can be deduced from the controller command generation equation. The controller command output can be written without the integrator component as

$$\phi_c = K_P y_e - K_D \dot{y} \tag{6.181}$$

with positive values for the gains K_P and K_D. Consider the aircraft flying at a constant speed from a positive East position perpendicular towards a track aligned with the South-North axis and the destination waypoint at the northern coordinate. For this scenario, Equation 6.181 can be written as

$$\phi_c = \underbrace{K_P y_e}_{<0} - \underbrace{K_D \left(-\overline{v}_g\right)}_{<0} \tag{6.182}$$

$$= \underbrace{K_P y_e}_{<0} + \underbrace{C}_{>0} \tag{6.183}$$

It becomes obvious that if $K_P y_e < C$, the aircraft will be commanded to roll towards the port side. If the aircraft is sufficiently far away in the stated scenario, it will always be commanded such a turn and continue to perform a counter-clockwise loop.

Since the gains and trim speed are constants, this issue will always manifest at a predictable cross-track error. It was initially attempted to check against predetermined rules to prevent the aircraft from performing certain actions in these scenarios. Unfortunately, the way in which some of the parameters are calculated, it became difficult to ensure correct operation under all possible scenarios of this rule-based system. Instead, the combination of the Cross-Track Controller and Heading and Guidance Controllers was proposed. The switching point can be determined from the cross-track error at the point where the roll angle is commanded a zero angle. Again, ignoring the integrator, it can be stated that

$$\phi_c = K_P y_e - K_D \dot{y} \tag{6.184}$$

$$(0) = K_P y_e - K_D \overline{v} \tag{6.185}$$

$$|y_e| = \frac{K_D}{K_P} \overline{v} \tag{6.186}$$

which is the maximum absolute distance at the which the Cross-Track Controller will produce the correct command signal.

In order to perform a gradual transition, a sinusoidal weighting between the Cross-Track Controller and Heading and Guidance Controllers was proposed. This transition is illustrated in Figure 6.33. The following regions are defined:

- Outer region, beyond the upper bound. In this region, the Cross-Track Controller could produce an incorrect command, therefore only the Heading and Guidance Controller should be used.
- Transition region, between the lower and upper bound. In this region, both the controllers would produce the correct result. The closer the aircraft is to the lower bound, the more weight should be placed on the Cross-Track Controller.
- Inner region, nearer than the lower bound. In this region, both controllers would produce the correct command, but preference is given completely to the more aggressive Cross-Track Controller.

The upper bound of the switching region should therefore be the maximum cross-track error for which the Cross-track Controller will produce the correct roll angle command signal, thus

$$b_u = \frac{K_D}{K_P} \overline{v}_g \tag{6.187}$$

Stability for such a dual controller scheme can not be proven. However, given the defined behaviour per bounding region, the final mixed controller output will always push the aircraft

towards the inner region and the operation of a single stable controller, therefore a stable response should be achieved. The final transition weighting multipliers can be written in terms of the percentage weight to be placed on the Heading and Guidance Controller and is expressed by

$$d_r = b_u - b_l \tag{6.188}$$

$$r_{HG} = \sin\left(\frac{\pi}{2}\frac{|y_e| - b_l}{b_u - b_l}\right) \tag{6.189}$$

$$r_{CTC} = 1 - r_{HG} \tag{6.190}$$

Furthermore, it was felt that the Cross-Track Controller behaves very aggressively under the

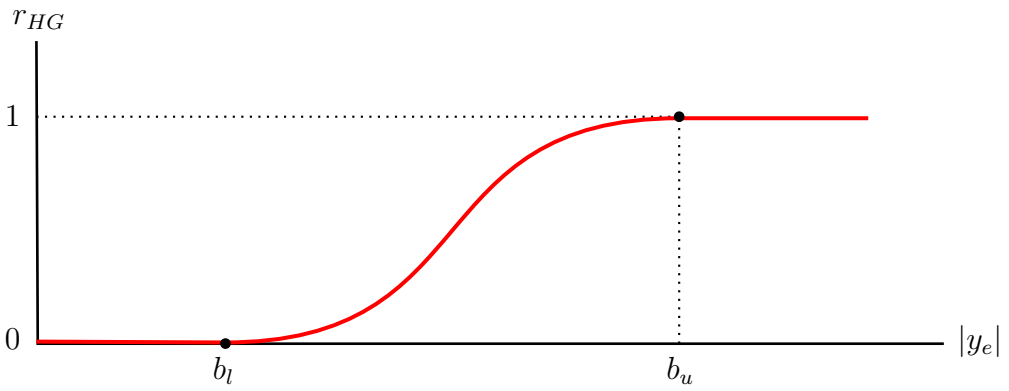

Figure 6.33: Transition curve between the Cross-Track Error and Heading and Guidance Controllers.

waypoint navigation system when switching waypoints only when it passes through them, in other words when the in-track distance is reached. This is especially noticeable when compared with the nonlinear navigation as used by [16]. It was thus proposed to perform an early switch when nearing the destination waypoint by looking ahead at the distance towards the target waypoint. Intuitively, it can be seen that the time to negate the cross-track error could also be reduced by using the scheme as illustrated on Figure 6.34. This is because the aircraft maximum roll angle is limited to reduce excessive loss of lift during turns, therefore a maximum turn rate is enforced. Using the proposed scheme, the aircraft will not first increase its cross-track error while turning when the target waypoint has been passed, but will instead immediately start reducing the cross-track error when switching to the new destination waypoint. The distance to the destination waypoint at which the switch should occur can be empirically determined and adjusted for ground speed.

6.4 Summary

This chapter presented the concept and traditional TECS architecture with the innermost loops subsequently replaced by a reimplementation of the NSA controller. A reduced order, simplified model of the TECS dynamics was used as the basis for the control system design with

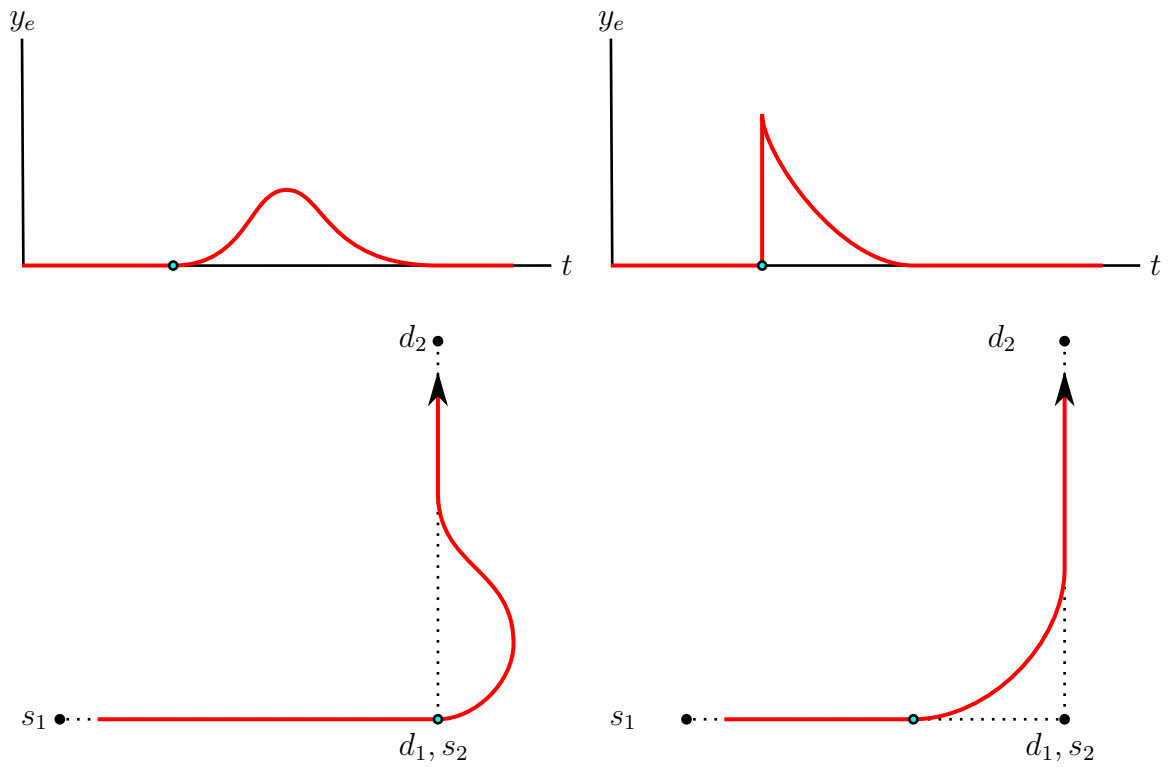

(a) Waypoint-passed method, showing the response when changing the destination when the target waypoint is passed.

(b) Proposed look-ahead method, showing the response when changing the destination before reaching the target waypoint.

Figure 6.34: Comparison between the waypoint-passed and look-ahead waypoint switching methods.

the outermost loops designed in a heuristic fashion using HIL simulations. The design of the TECS entailed a significant tuning process. The lateral controller designs were presented using simple successive loop closure. The Cross-Track Controller design did not operate correctly when the aircraft was sufficiently far away from the ground track and was supplemented with the Heading and Guidance Controllers using a sinusoidal transition curve. This was further improved using an early switching scheme when approaching the destination waypoint.

§ 7

Nonlinear Simulation

This chapter presents the results from simulations for the longitudinal and lateral controllers as well as the results from stationary and moving platform landings.

Section 7.1 discusses the setup and software used for both the SIL and HIL nonlinear simulations. Section 7.2 presents the results obtained from the HIL simulations for both longitudinal and lateral controllers as well as the performance of the landing strategy. Section 7.3 provides a summary of the chapter.

7.1 Simulation Setup

This section describes the different simulation platforms used to verify the system before any practical flight tests were performed. The controller structures were initially tested using Simulink M-code blocks to see if the architecture will be viable. The code was subsequently tested in a SIL simulation to verify the C-code implementation. Finally, the system was ported to the actual hardware to include the complexities of the hardware components. When the HIL simulation shows acceptable performance, the system is scheduled for practical testing.

It is important to note that the simulation is only as accurate as the model that is used as the representation of the system. Therefore, as many models as possible are included to achieve a realistic simulation environment. These additions include wind disturbances, system delays and sensor noise. If these are modelled accurately, the simulated and practical results should correlate very well.

7.1.1 Software-in-the-Loop

The aim of the SIL simulations are to verify that the control system implementation in C-code matches the behaviour of the Matlab designs. The controllers were initially implemented as Matlab M-code, then ported to C-code and compiled with the Matlab MEX tool for direct inclusion into Simulink models. For this project, MPLABX was used as the hardware integrated development environment (IDE). It was decided to develop in the same IDE for SIL, but make the code compatible to be compiled with both the MPLABX GCC and the Matlab LCC compilers.

The SIL environment can be described with reference to Figure 7.1. The aim was to use the same source files for compiling both the simulation binaries as well as those that will be loaded onto the hardware. This means that the `.c` and `.h` files must be compatible with both environments. The SIL functions act as wrappers to pack received data into the format used on the OBC by the hardware sensors. This compatibility is accomplished by utilising hash-defines, commonly used in C-based source code. A primary hash-define serves as a switch to toggle between "compile-for-SIL" and "compile-for-HIL" modes.

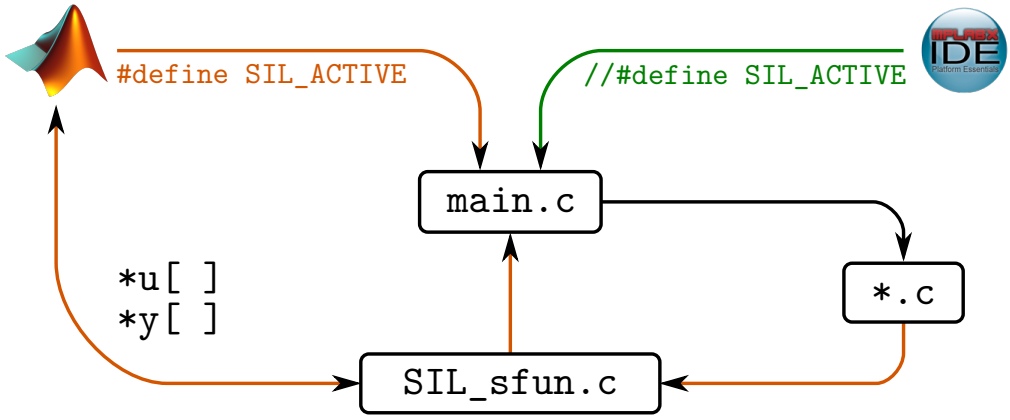

Figure 7.1: Integration between Simulink and MPLABX in the SIL environment.

When the code is compiled for SIL simulations, the "`#define SIL_ACTIVE`" statement is inserted to indicate compilation should be done for SIL. In this mode, the Matlab LCC compiler is used to compile the source code to create a `.mex32` binary file. This binary can be called directly from Simulink to simulate the code that would run on the OBC. When the code is compiled for loading onto the MCU, the hash-define is omitted to indicate compilation should be done for the MCU. In this mode, the MPLABX GCC compiler is used to compile the source code to create a `.hex` binary file. This file can then be loaded onto the OBC for either HIL simulations or practical flights using the Microchip PICkit3 programmer device.

Additional functionality is included when the hash-define is active. The `main.c` file then includes the SIL headers and source, which have functions to set initial conditions, send and receive pointers to data, and make various other system calls. For debugging purposes, special `#ifdefs` are included to perform logging to a file, the Matlab console, or both. The SIL procedure can be summarised as follow:

1. Data is generated from the aircraft model blocks (six degrees of freedom, external disturbances).
2. The six degrees of freedom data is passed through sensor disturbance models.
3. The sensor data is sent to the `mdlOutputs(...)` S-Function.
4. A wrapper function packs the data into data structures as used on the OBC.
5. Functions inside the `while(1)` loop are called to run the controllers and write the data to the relevant OBC structures.

6. A wrapper function reads the actuator data from the OBC data structures and outputs it to Simulink.

7. The actuator data is sent to the aircraft model blocks and the process repeats.

The biggest advantage of the SIL simulations is that the software can very easily be debugged before attempting to run it on the real hardware. This allows for reduced development time, rapid prototyping, better coding practices, easier refactoring, and builds confidence through more thorough testing of the subroutines.

7.1.2 Hardware-in-the-Loop

The aim of the HIL simulations are to verify that the control system implementation on the OBC and all accompanying subsystems are functioning as intended. This includes RF communication, sensors readings, state machine switching and the general signal processing required. The data transfer between the simulation software and the OBC is facilitated by an external HIL board which is wire-connected to both systems. An illustrative overview of the system is given in Figure 2.1.

Additional advantages of the HIL system are that it allows for the visual tuning of the controllers. This was especially useful for controllers that were difficult to design, such as the TECS. During this phase, several of the practical aspects of flight tests were also tuned, such as the reference limits, integrator limits, integrator wind-up and pre-set values, and actuator command limits.

For this project, all controllers were completely rewritten except for the NSA controller implementation. Almost all other integration systems were used as-is, although some required minor tweaks for updated RF commands and the platform integration between the RC and the Simulink model. During this phase, the aircraft also underwent calibration, discussed briefly in Section 8.1.1, to ensure that the HIL system values correspond to the actual values for sensor parameters and actuator commands. The HIL procedure can be summarised as follow:

1. The OBC is placed into HIL mode through the GCS.

2. Data is generated from the aircraft model blocks (six degrees of freedom, external disturbances).

3. The six degrees of freedom data is passed through sensor disturbance models.

4. The sensor data is sent through a USB connection to the HIL board.

5. The HIL board sends the sensor data to the OBC via the CAN bus and UART connections.

6. The OBC acts on the data and sends actuator commands to the Servo Board, which is also read by the HIL board.

7. The HIL board sends the actuator data to the computer through USB.

8. The actuator data is sent to the aircraft model blocks and the process repeats from step 2.

7.2 Simulation Results

This section presents the final results obtained from the HIL simulations for the longitudinal and lateral controllers as well as the stationary and moving platform landings. The simulations were executed with full sensor and environmental disturbance models activated unless otherwise specified. Comparisons are drawn with respect to the designs from Chapter 6.

7.2.1 Longitudinal Controllers

This section presents the results obtained from the HIL simulations for the longitudinal controllers. For these simulations, the Dutch Roll Damper and Roll Angle Controller were armed to diminish the effect of yaw rates and nonzero roll angles on the longitudinal controllers.

7.2.1.1 NSA

The NSA controller was only tested for regulation of a given reference signal which was typically equal to gravity to command straight and level flight. Even though it was not directly tested for step responses, a varying controller reference signal is given by the outer loop TECS Energy Distribution Controller. As shown in Figure 7.2, the NSA Controller appears to closely follow the 0.3s rise time and settles slightly faster than 0.95s as per its design. The exact values are however more difficult to see given that the reference signal is curved rather than a discrete step.

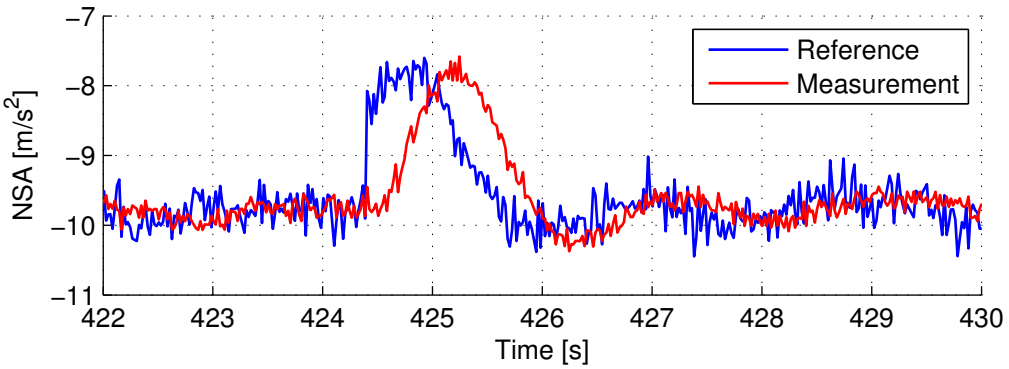

Figure 7.2: NSA regulation during HIL simulations.

As shown in Figure 7.3, the controller was engaged mid-flight with the greyed part indicating the area in which the controller was active. It can be seen that the reference signal is warped due to compensation for the magnitude of the gravity vector that is reduced when the aircraft experiences a nonzero roll angle. Additionally, it can be seen that the NSA integrator is not given an initial value on activation but rather has to wind up until it reaches steady state conditions in which it follows the reference with zero error.

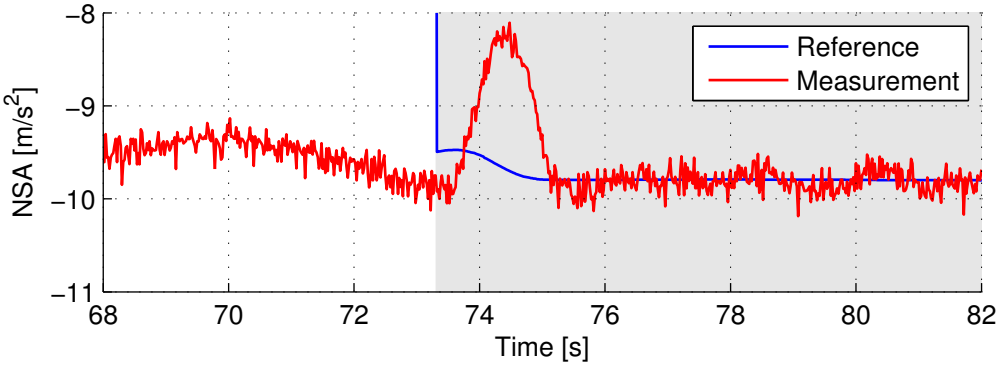

Figure 7.3: NSA regulation showing roll angle compensation and zero steady state error during HIL simulations.

7.2.1.2 Airspeed

The Airspeed Controller was simply given airspeed steps to evaluate its response while the Flight Path Angle Controller was engaged to maintain flight path angle. As shown in Figure 7.4, this controller yields a response with very little overshoot which is virtually indistinguishable from the disturbances. It has a rise time of approximately 2.5s and settles within 10s. The acceleration inner loop was not evaluated separately, but the response for the same step is shown in Figure 7.5. The response appears to settle in about 2.5s, making it fast enough to avoid time-scale separation problems with the airspeed outer loop.

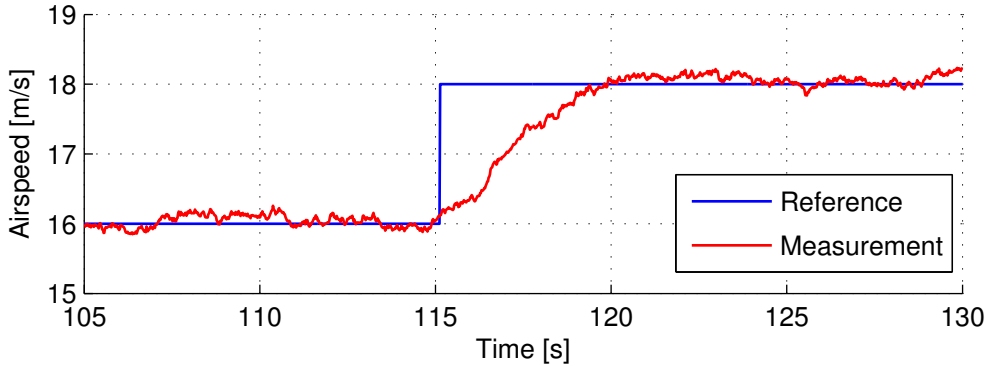

Figure 7.4: Airspeed step response during HIL simulations.

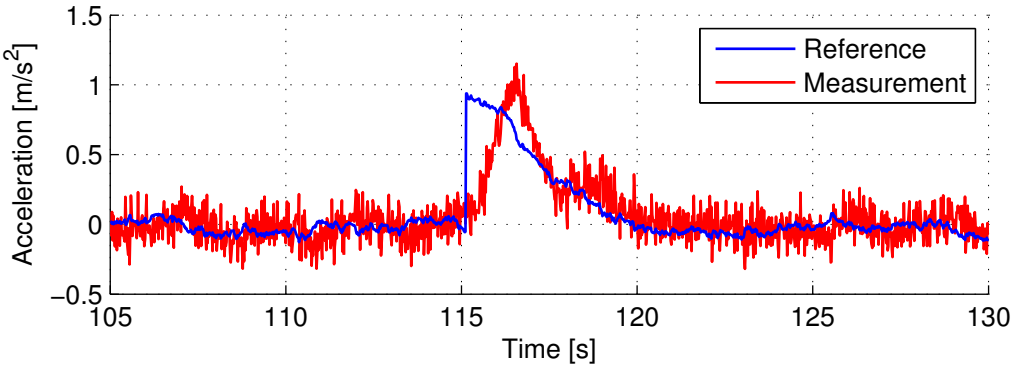

Figure 7.5: Acceleration response during HIL simulations.

The flight path angle and altitude responses for the same step are shown in Figures 7.6 and 7.7, respectively. It can be seen that the aircraft slightly lowered its flight path angle in order to quickly exchange potential energy for kinetic energy until the Specific Energy Controller corrected the error. This is somewhat in contrast to [7] which claimed that the airspeed and flight path angle responses should not significantly affect each other. This response is likely due to the unequal controller time constants as the one error may be corrected faster than the other. It was shown in Section 6.2.4.3 that the time constant of the Specific Energy Controller is double that of the Energy Distribution controller as per the time constant equations from [7]. The two energy controller responses shown in Figures 7.8 and 7.9 indicate that the Energy Distribution Controller settles faster than the Specific Energy Controller which matches more closely with the design characteristics given by [7] than the Matlab settling time estimation.

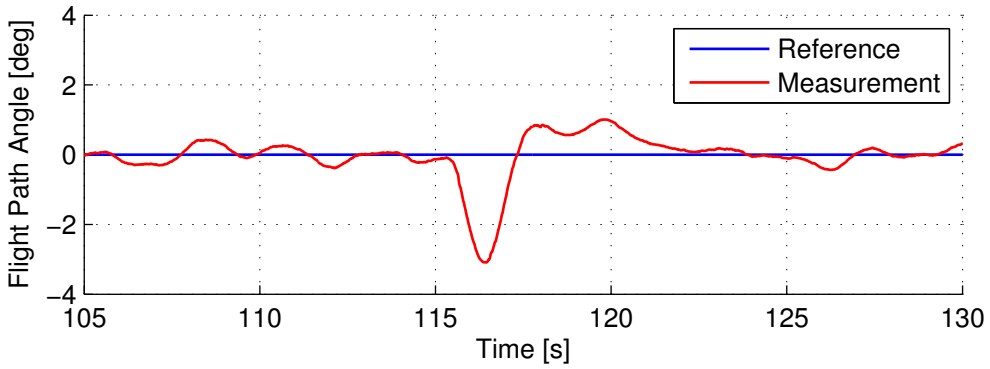

Figure 7.6: Effect on flight path angle from an airspeed step response during HIL simulations.

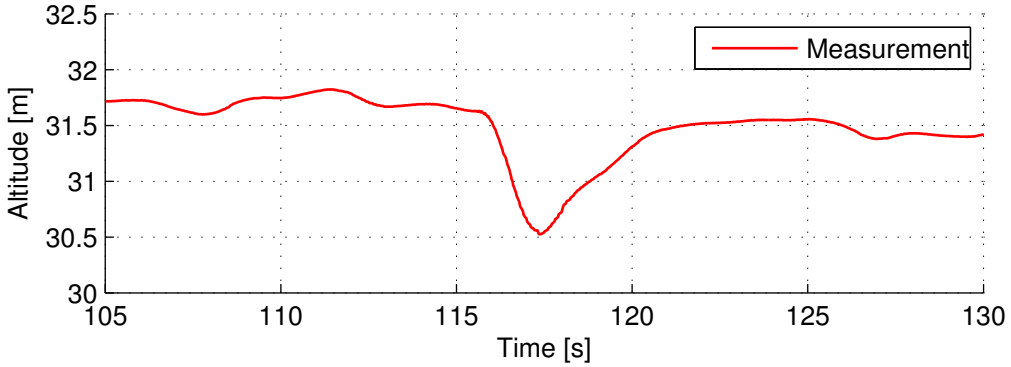

Figure 7.7: Effect on altitude from an airspeed step response during HIL simulations.

The system was also tested under different wind conditions. As shown in Figures 7.10 and 7.11, the system is resilient against wind disturbances. The slightly more overshoot from the tailwind simulation is most likely due to sensor noise as the headwind simulation shows the same deviation even after settling.

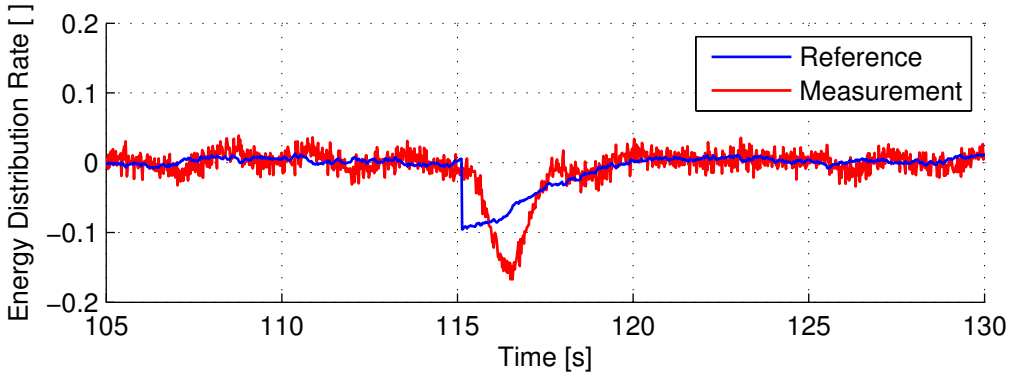

Figure 7.8: Energy distribution rate regulation for an airspeed step during HIL simulations.

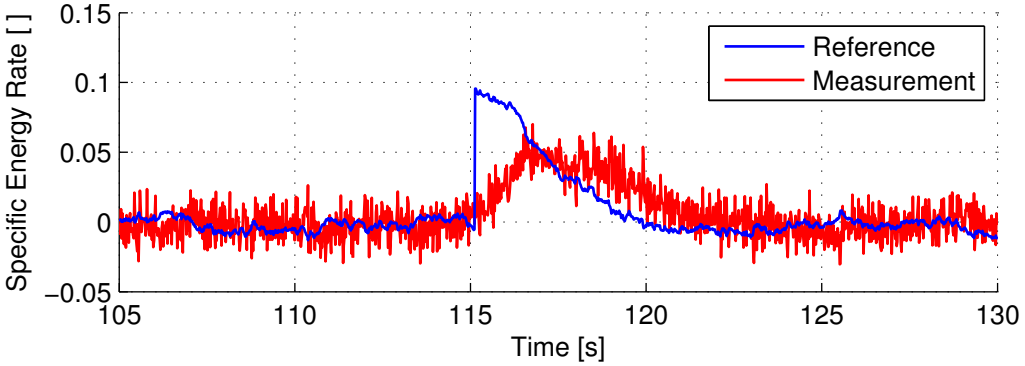

Figure 7.9: Specific energy rate regulation for an airspeed step during HIL simulations.

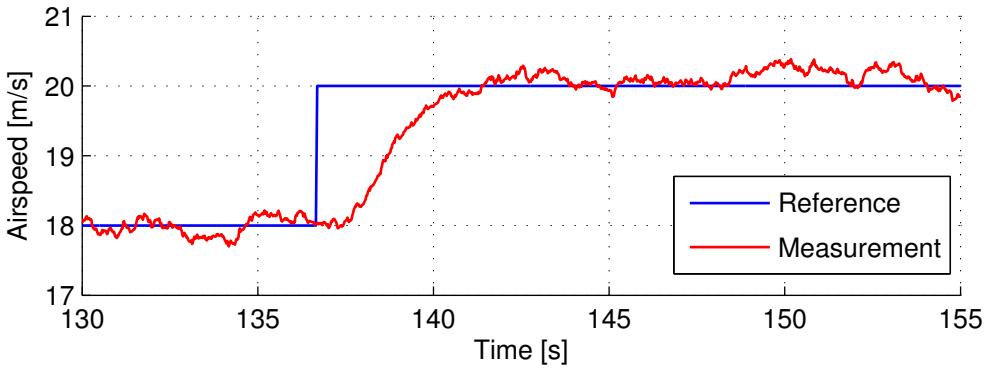

Figure 7.10: Airspeed step response under headwind conditions during HIL simulations.

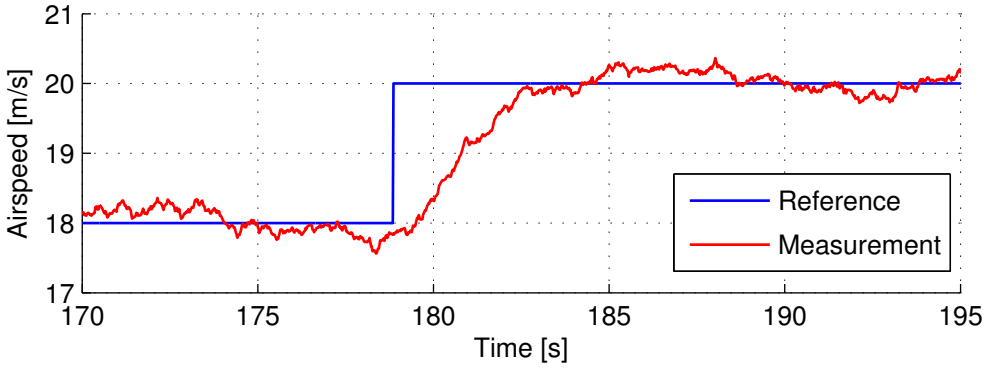

Figure 7.11: Airspeed step response under tailwind conditions during HIL simulations.

7.2.1.3 Flight Path Angle

The Flight Path Angle Controller was given flight path angle steps to evaluate its response while the Airspeed Controller was engaged to maintain airspeed. As shown in Figure 7.12, this system yields a response with very little overshoot which is virtually indistinguishable from the disturbances. It has a rise time of approximately 1.5s and settles in approximately 6s. This is similar to the response of the Airspeed Controller, although quite faster.

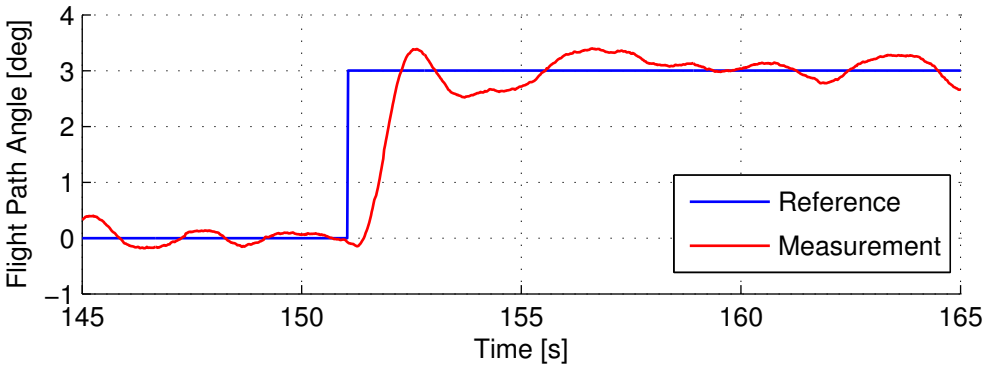

Figure 7.12: Flight path angle step response during HIL simulations.

The airspeed response for the same step is shown in Figure 7.13. It is observed that the effect on the airspeed is much less profound when given a flight path angle step command than that of the flight path angle when given an airspeed command as shown in Figure 7.6. This could be due the Energy Distribution Controller settling slightly faster than the Specific Energy Controller as shown in Figures 7.14 and 7.15. It is speculated that the elevator deflection has less of an effect on the airspeed than the throttle setting has on the flight path angle even though both the Energy Distribution Controller and Specific Energy Controller contribute to the steady state. The delay in responses could be ascribed to the speed of the following chain of events: an elevator deflection angle would first cause a pitch rate, which would in turn cause an increased angle of attack, which would lead to increased drag, which would finally lead to a reduction in airspeed. Similarly, the throttle settings, coupled with an additional engine time constant would first cause an increase in airspeed, which would in turn cause an increase in lift, which would cause an upwards force, which would finally cause an increase in altitude.

It is also noted that the Energy Distribution Controller and Specific Energy Controller do follow the second and first-order responses, respectively, as per the design in Section 6.2.4.3. The Energy Distribution controller appears to have more overshoot than expected and rises more quickly, although not by too large a factor. Furthermore, the Specific Energy Controller appears to conform to the Matlab-estimated rise time and settling time of 1.08s and 5.02s, respectively. This gives more validity to the simplifications of the plant and design methodology as presented in Section 6.2.4.2.

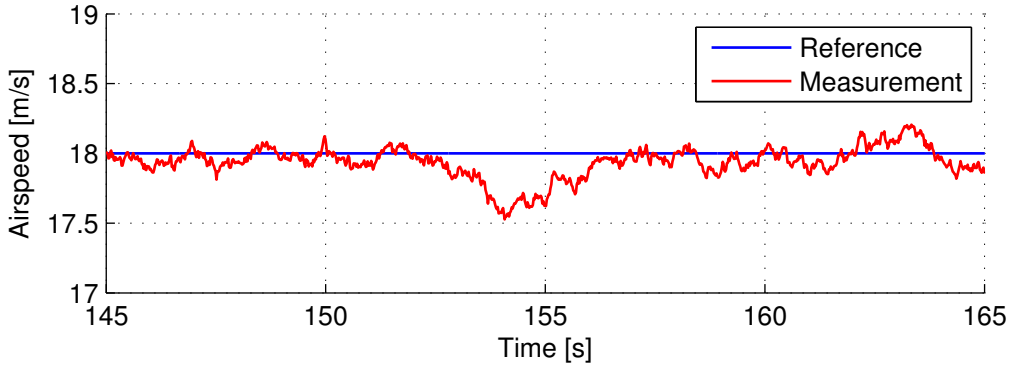

Figure 7.13: Effect on airspeed from a flight path angle step during HIL simulations.

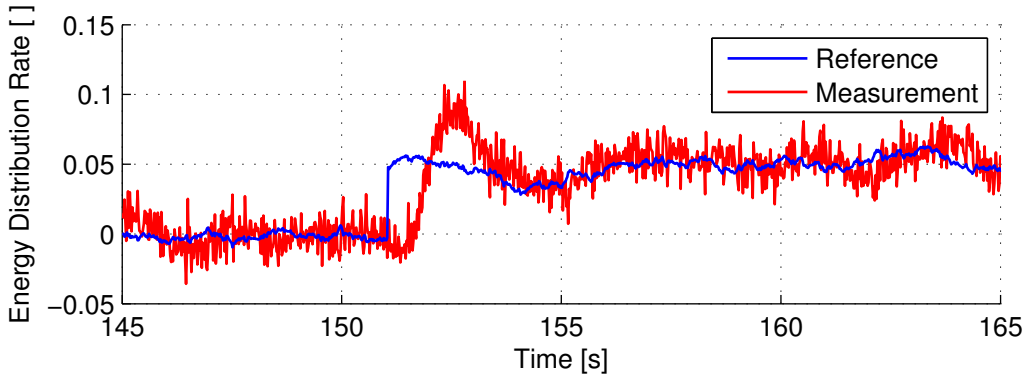

Figure 7.14: Energy distribution rate regulation for a flight path angle step during HIL simulations.

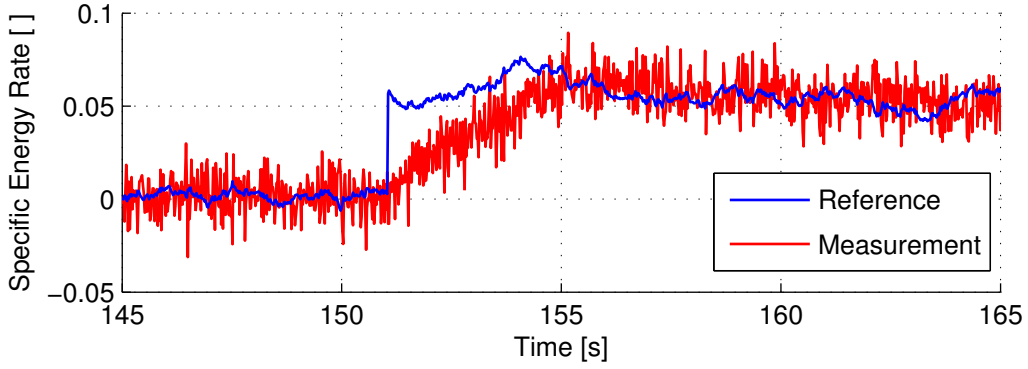

Figure 7.15: Specific energy rate regulation for a flight path angle step during HIL simulations.

7.2.1.4 Climb Rate

The Climb Rate system was given climb rate steps to evaluate its response while the Airspeed Controller was engaged to maintain airspeed. As shown in Figure 7.16, this system yields a response with very little overshoot which is virtually indistinguishable from the disturbances. This response is expected to match the response of the Flight Path Angle system as the climb rate command is merely converted to a flight path angle command. This is indeed true and therefore confirms the notion that the same inner loop control architecture can be used for both climb rate and flight path angle commands.

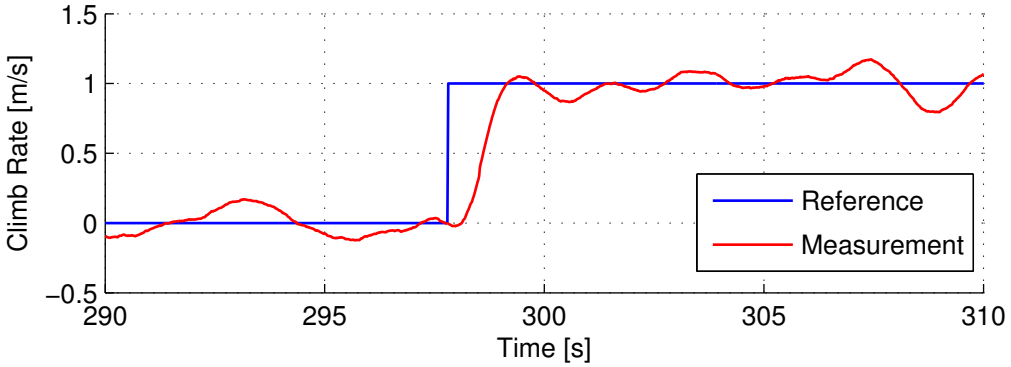

Figure 7.16: Climb rate step response during HIL simulations.

7.2.1.5 Altitude

The Altitude Controller was given altitude steps to evaluate its response while the Airspeed Controller was engaged to maintain airspeed. As shown in Figure 7.17, this controller yields a response with very little overshoot. It has a rise time of approximately 2s and settles in approximately 9s. This is very similar to the response of the Airspeed Controller, although marginally faster. This validates the claim by [7] that the two controllers should yield the same response if given identical gains. The cause of the slight difference is likely due to the inner loops not conforming to the design guidelines.

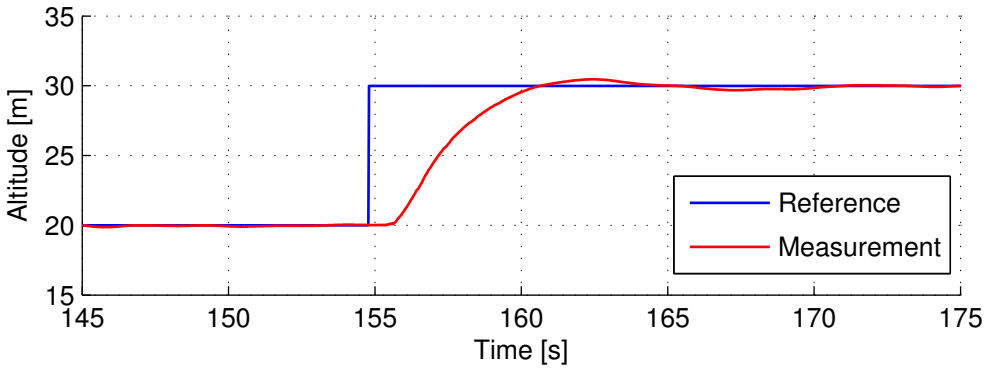

Figure 7.17: Altitude step response during HIL simulations.

As shown in Figure 7.18, this controller handles a simultaneous airspeed and altitude command without any negative impact on the altitude response. However, the airspeed response

appears to be more affected and yields significantly more overshoot and a slightly slower settling time as shown in Figure 7.19. This could again be due to the unmatched inner loop controller gains, causing an exacerbated difference in response when subjected to a large step command.

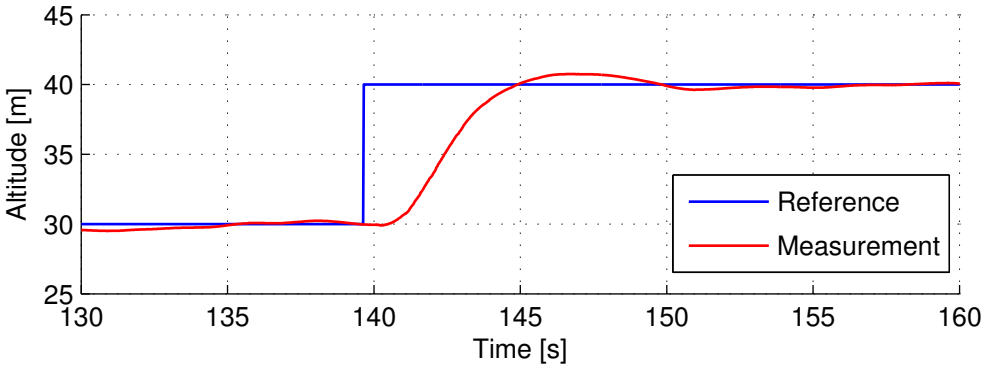

Figure 7.18: Altitude step response for a combined airspeed and altitude step during HIL simulations.

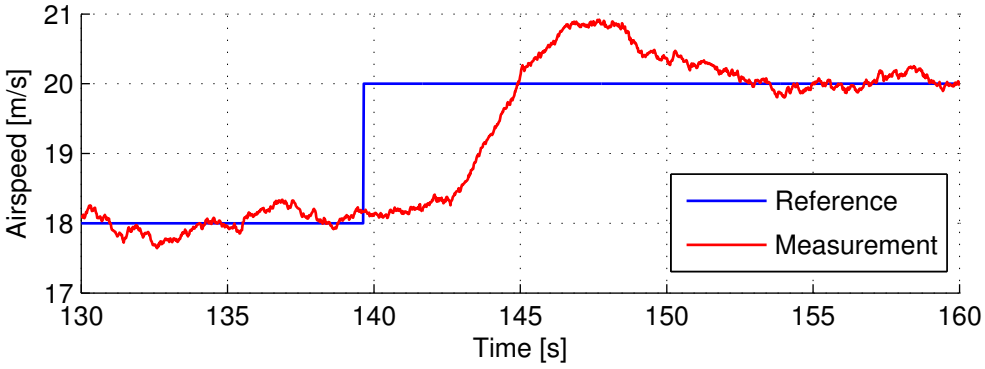

Figure 7.19: Airspeed step response for a combined airspeed and altitude step during HIL simulations.

The system was also tested under different wind conditions. As shown in Figures 7.20 and 7.21, the system is fairly resilient against wind disturbances. The improved response in headwind conditions compared to tailwind conditions is likely due to the aircraft better rejecting noise from incoming airflow, causing the response to be more stable.

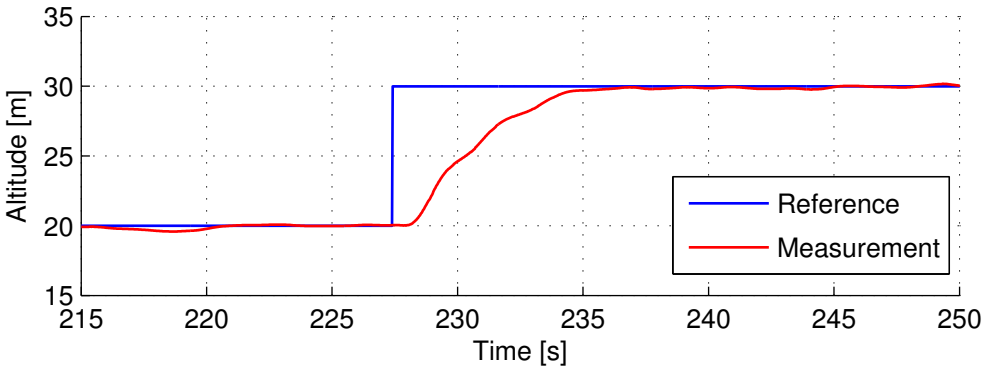

Figure 7.20: Altitude step response under headwind conditions during HIL simulations.

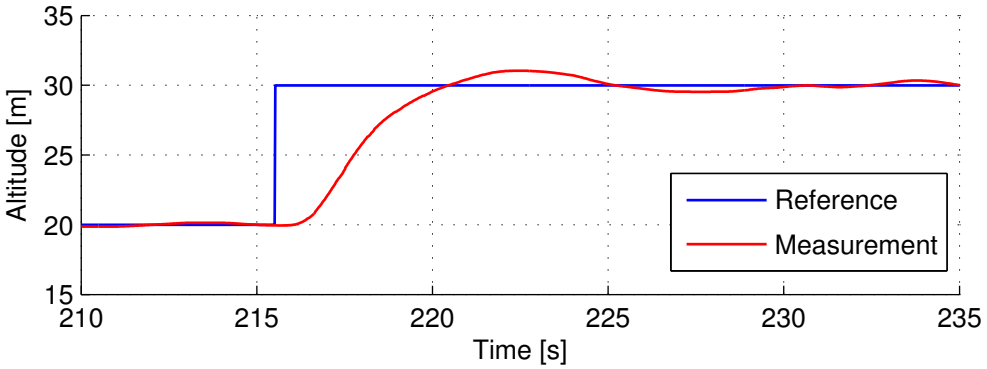

Figure 7.21: Altitude step response under tailwind conditions during HIL simulations.

7.2.2 Lateral Controllers

This section presents the results obtained from the HIL simulations for the lateral controllers. For these simulations, the Airspeed Controller and Altitude Controller were armed to diminish the effect of longitudinal perturbations on the lateral controllers.

7.2.2.1 Dutch Roll Damper

To test the Dutch Roll Damper, the aircraft was given a set of rudder doublets — quickly alternating the commanded deflection angles for the rudder control surface in order to introduce a perturbation. During this sequence, both the RC and the control system can command the rudder with their separate signals added together to produce the final reference value. The doublet shown in Figure 7.22a was supplied to the system without the controller activated, which produced the lightly damped oscillation shown in Figure 7.22b. This oscillation is only sufficiently suppressed naturally after about 6s, which corresponds well with the uncontrolled impulse response as presented in Figure 6.22.

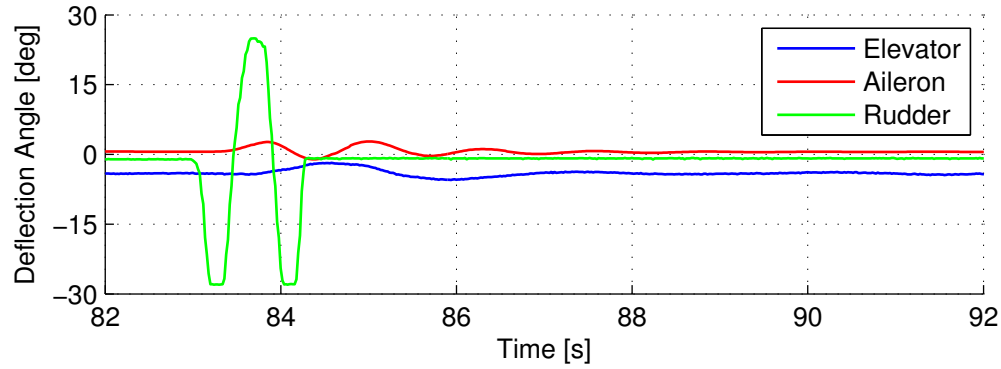

(a) Control surface command signals showing a doublet input.

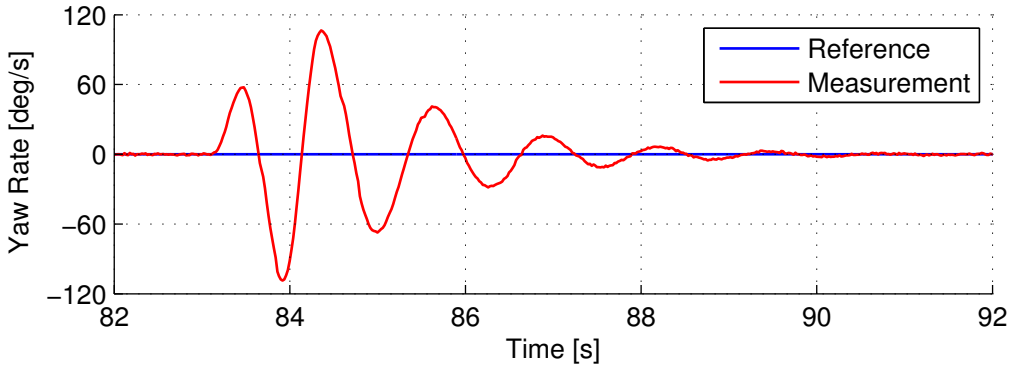

(b) Natural yaw rate response.

Figure 7.22: Evaluation of the natural yaw rate response during HIL simulations.

The doublet shown in Figure 7.23a was supplied to the system with the controller activated, which produced the well damped oscillation as shown in Figure 7.23b. This oscillation is sufficiently suppressed after about 2s, which also corresponds well with the controlled impulse response as presented in Figure 6.22. It should be noted that the controller does reach the much more strict deflection limits when under autopilot control. It is also evident that the controller

would have supplied a larger deflection angle if possible as the command signal reaches the limits even after the doublets were supplied. Additionally, there is much less aileron command activity from the Roll Angle Controller, showing that the Dutch Roll Damper also reduced the induced roll rates.

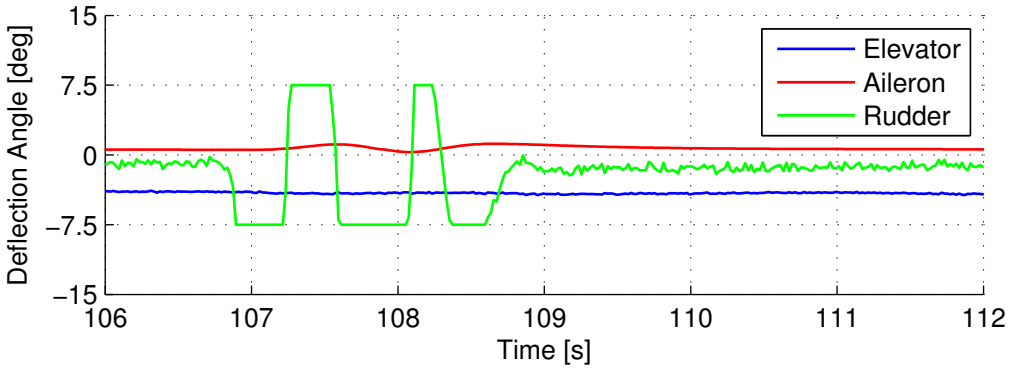

(a) Control surface command signals showing a doublet input.

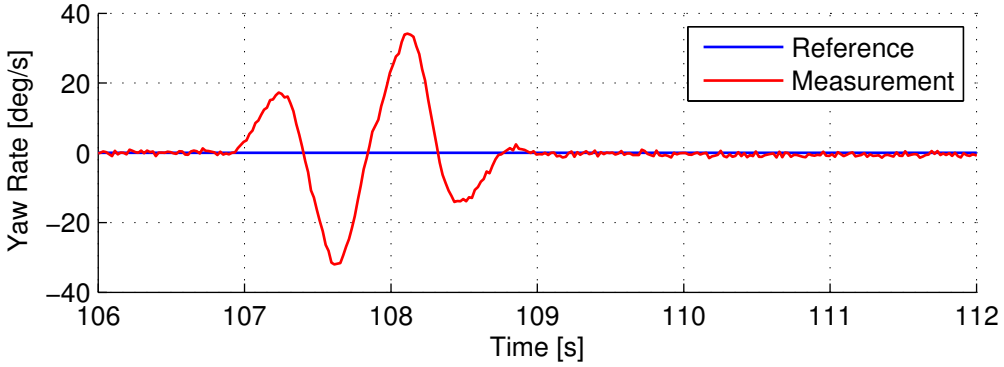

(b) Damped yaw rate response.

Figure 7.23: Evaluation of the damped yaw rate response during HIL simulations.

As shown in Figure 7.24, the controller behaves similarly when subjected to wind disturbances. Under the headwind condition, the response is almost identical and settles marginally faster, likely due to the added natural stability provided by the aircraft weathercocking into the incoming airflow.

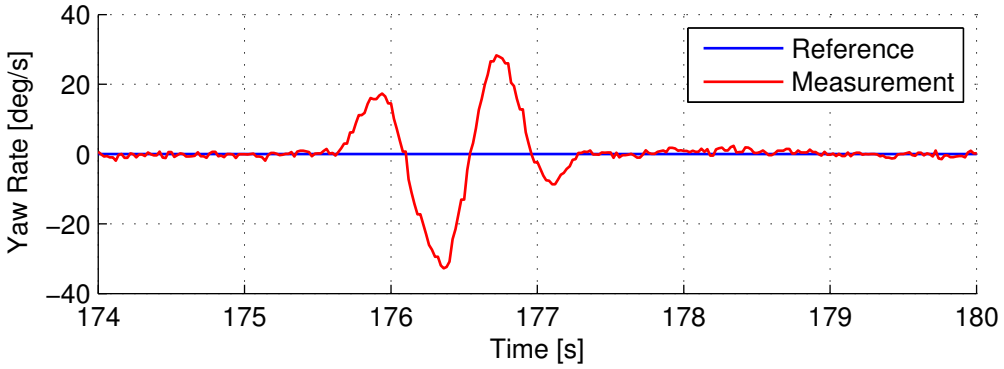

Figure 7.24: Damped yaw rate response during HIL simulations under headwind conditions.

7.2.2.2 Roll Angle Controller

The Roll Angle Controller was given roll angle steps to evaluate its response. As shown in Figure 7.25, this controller exhibits the same unusual response as presented in Figure 6.24. This response rises very quickly, then flattens out to a long overshoot and eventually settles. The lower peak is reached at approximately 1s, while the main peak is reached at approximately 5s, both in accordance with the design. The simulation appears to settle slightly earlier at about 10s. This may be due to the implicit lowering of the integrator gain when the total loop gain was reduced during HIL tuning.

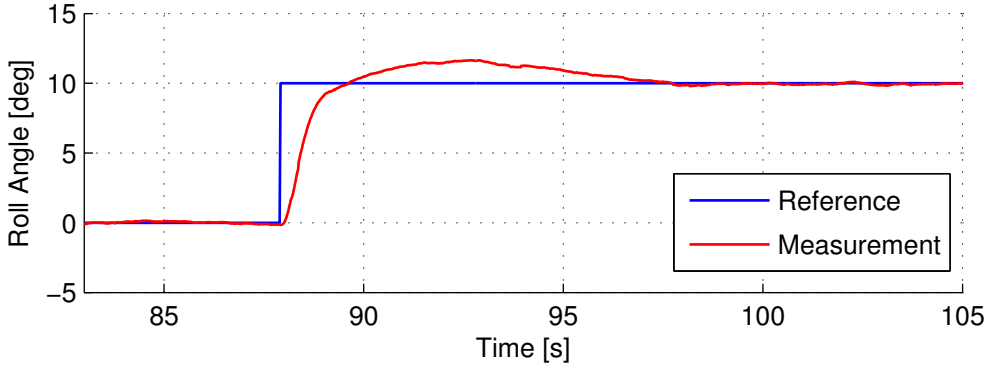

Figure 7.25: Roll Angle Controller step response during HIL simulations.

7.2.2.3 Cross-Track Controller

The Cross-Track Controller was given cross-track steps to evaluate its response. As shown in Figure 7.26, this controller does not completely conform to its designed response as presented in Figure 6.32. The overshoot has halved to only 25% while the peak time more than doubled to 5s. This could be due to the poles negating the effect of the zeroes, thereby significantly reducing the amount of overshoot and slowing down the response. The settling time remained approximately the same at 14s.

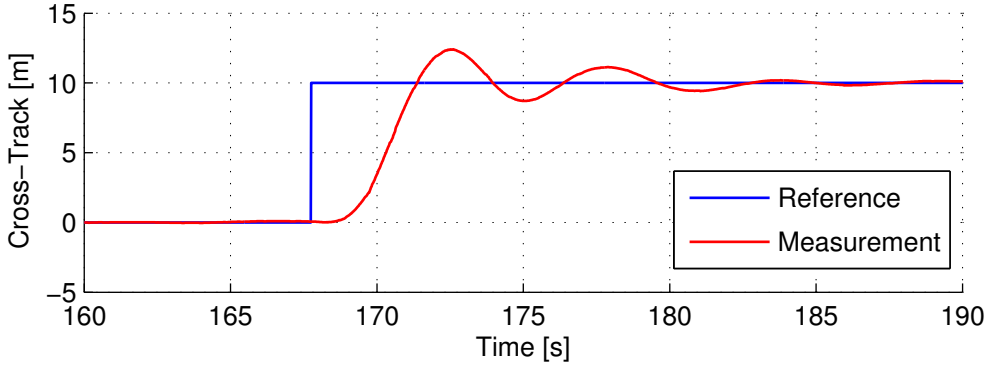

Figure 7.26: Cross-Track Controller step response during HIL simulations.

7.2.2.4 Heading & Guidance Controllers and Navigation

The Heading and Guidance Controllers were tightly integrated with the Cross-Track Controller and were therefore not given separate steps to evaluate their responses. The relevant heading signals are shown in Figure 7.27a for the ideal track scenario. It can be seen that the controller guides the aircraft to the given reference so that the Cross-Track Controller can engage and aggressively negate the error. The roll angle regulation during this simulation is shown in Figure 7.27b. As the aircraft consistently followed the waypoint ground track and the controller regulated the roll angle to zero, it can be concluded that the transition scheme from the Heading and Guidance Controllers to the Cross-Track Controller behaves correctly, irrelevant of its position with respect to the track and current waypoint set.

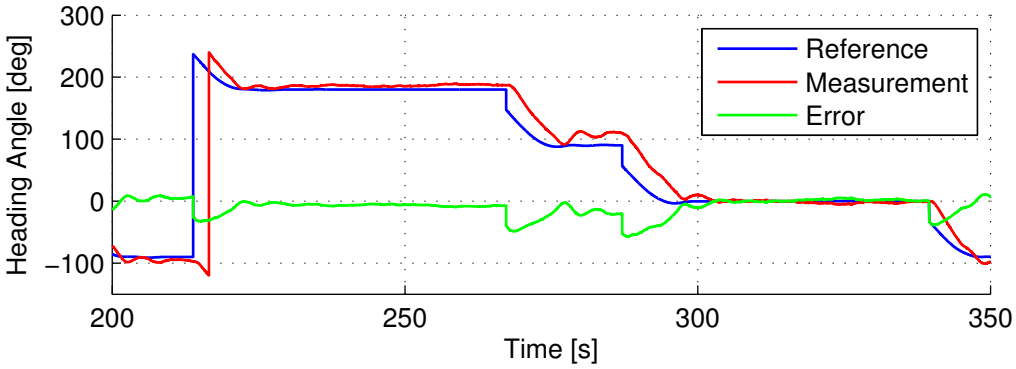

(a) Heading angle response.

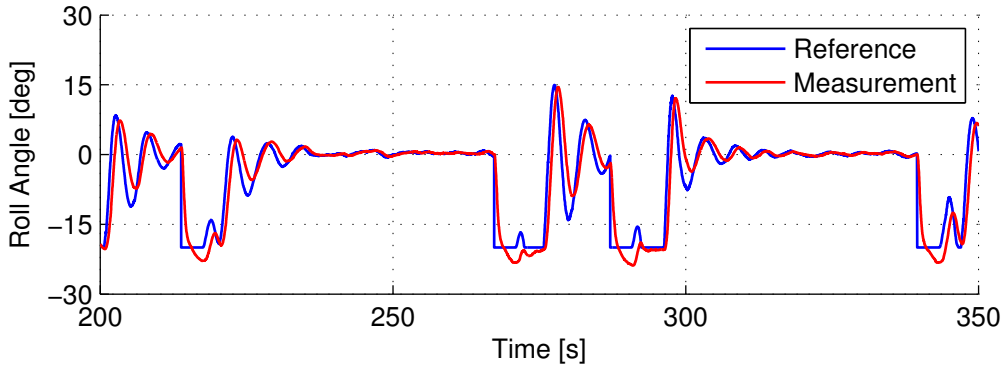

(b) Roll angle regulation.

Figure 7.27: Evaluation of the heading response for the ideal track during HIL simulations.

Figure 7.28 shows the aircraft following the ideal track extremely well using the dual-controller implementation and early waypoint switching scheme. It can therefore be concluded that the early switching scheme is a valid approach to improve the cross-track transient response.

For the realistic track scenario shown in Figure 7.29, it is clearly visible that the aircraft performs a peculiar overshoot when entering the final waypoint set. This behaviour was consistently repeated, even when reversing the waypoint direction. Further investigation into this issue revealed that a problem exists with the current OBC firmware. For reference, Figure 7.30 shows the aircraft inertial position during successive go-arounds. As shown in Figure 7.31, it

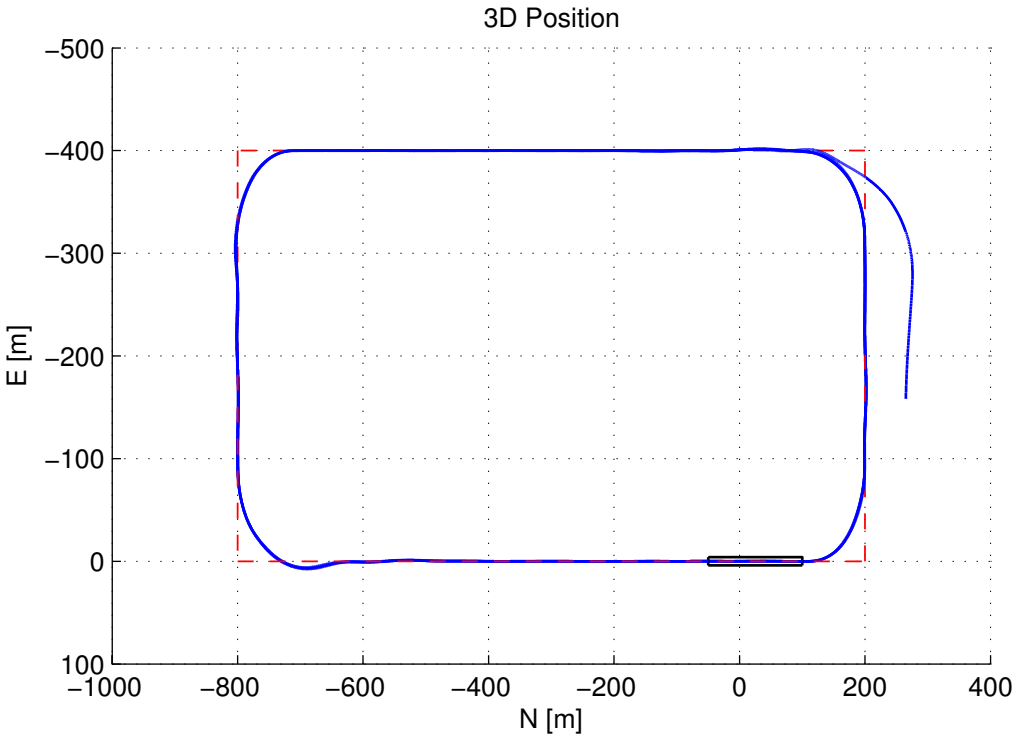

Figure 7.28: Navigation path for the ideal track during HIL simulations.

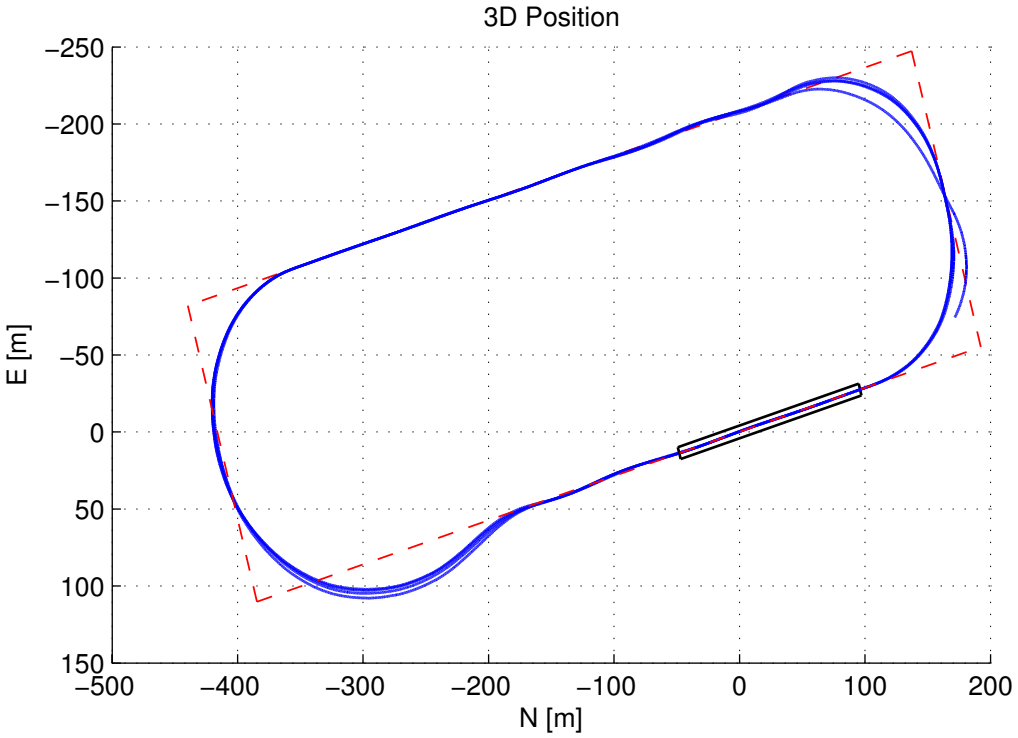

Figure 7.29: Navigation path for the realistic track during HIL simulations.

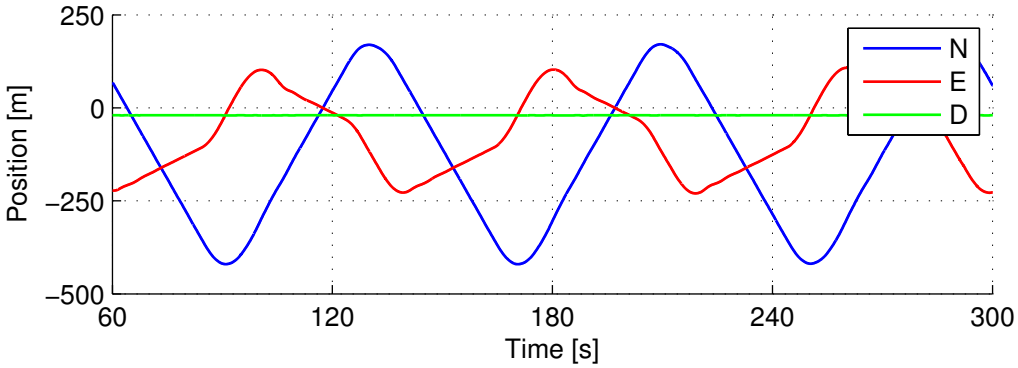

Figure 7.30: Position measurements for the realistic track navigation response during HIL simulations.

was noted that the aircraft increases its airspeed significantly around this final waypoint turn, even though the airspeed reference remains constant throughout the flight. This increase in

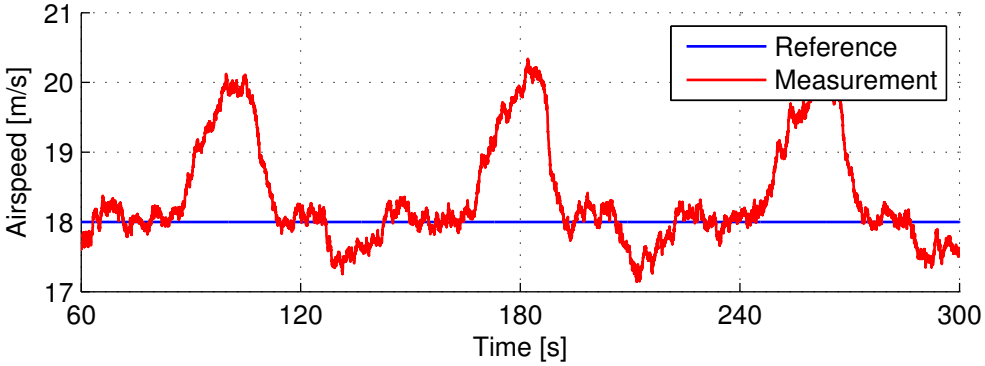

Figure 7.31: Airspeed signals for the realistic track navigation response during HIL simulations.

airspeed was opposed by the commanded forward acceleration as shown in Figure 7.32, which attempted to rapidly reduce the airspeed. It was also noticed that continuous NSA offsets followed by spikes were also present at these locations as shown in Figure 7.33. Finally, it was determined that the origin of this issue is likely caused by an erroneous pitch angle estimation. As shown in Figure 7.34, a significant difference between the pitch angle estimated by the OBC and the true pitch angle from the Matlab simulation is present. Figures 7.35 and 7.36 show the simulated gyroscope and accelerometer measurements, which are the only sensors used in the estimator to estimate the pitch angle. Since they do not show abnormal behaviour with respect to the whole flight envelope, it is believed that they are not the source of the pitch angle estimation error.

Although this issue may have been present in previous projects, it may not have had a significant influence as they only used airspeed feedback to control the airspeed whereas this project uses an inner loop with an acceleration measurement. Since the calculated acceleration in the axial and normal axes are determined by using the pitch angle estimation, any pitch angle errors would cause errors in the calculation of the gravity vector in the estimator, which would introduce errors in the estimation of the other state variables. This error would therefore affect both the NSA and the airspeed controllers, especially since the NSA command signal also

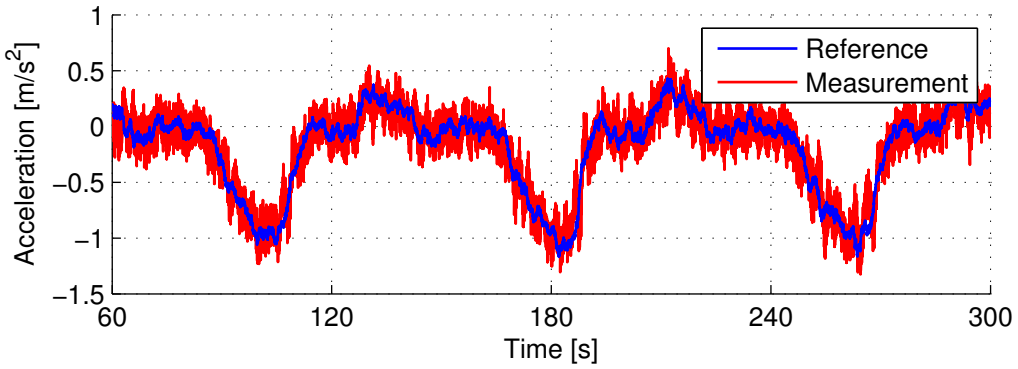

Figure 7.32: Acceleration signals for the realistic track navigation response during HIL simulations.

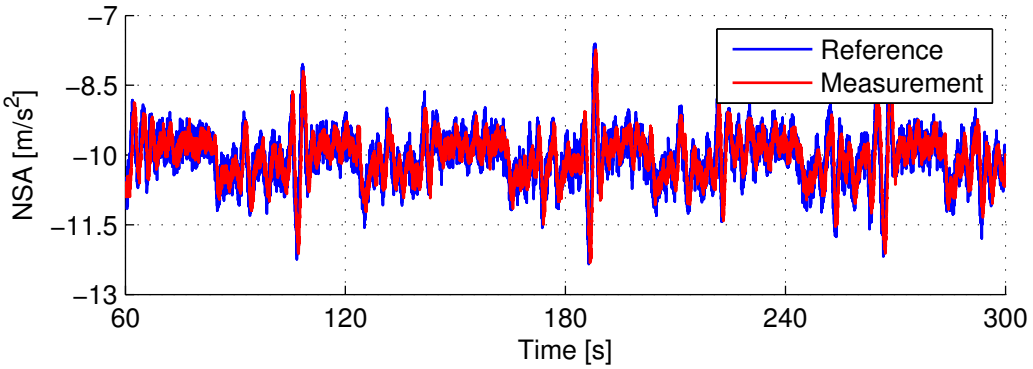

Figure 7.33: NSA signals for the realistic track navigation response during HIL simulations.

compensates for pitch angle. It is reasoned that this incorrect pitch angle estimation causes the system to underestimate the real acceleration as the large gravity coupling is now subtracted. Even though the system does command the aircraft to slow down, it is still not enough to sufficiently reduce the error until the pitch angle is restored to trim. Unfortunately, this issue was never resolved due to insufficient time and therefore remains open for investigation.

The system was also tested under different wind conditions. As shown in Figure 7.37, it is observed that the system can fail to effectively reduce the cross-track error to zero under strong wind conditions, especially if the wind direction is such that it prevents the Cross-Track

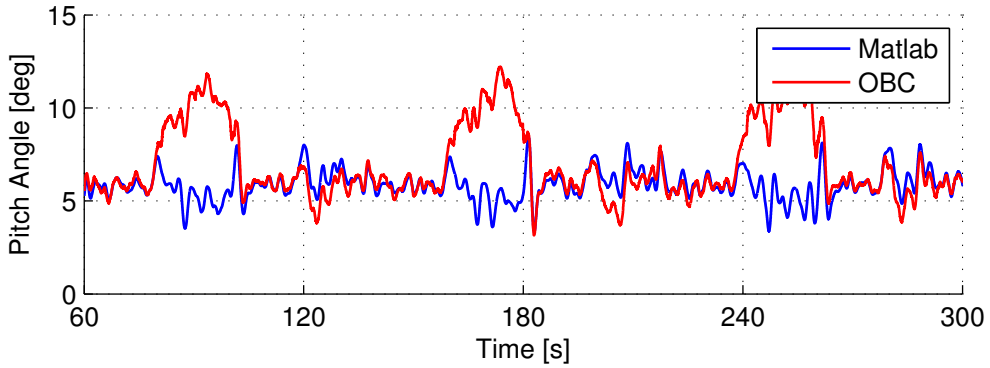

Figure 7.34: Pitch angle measurement comparison between the OBC and Matlab for the realistic track navigation response during HIL simulations.

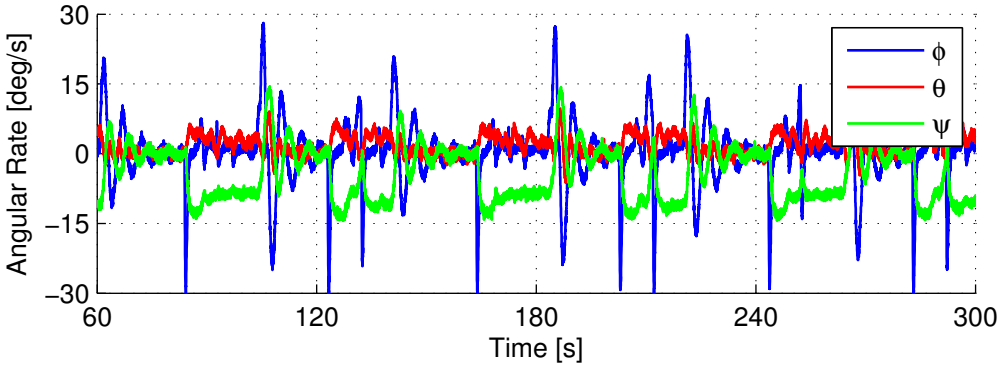

Figure 7.35: Angular rate measurements for the realistic track navigation response during HIL simulations.

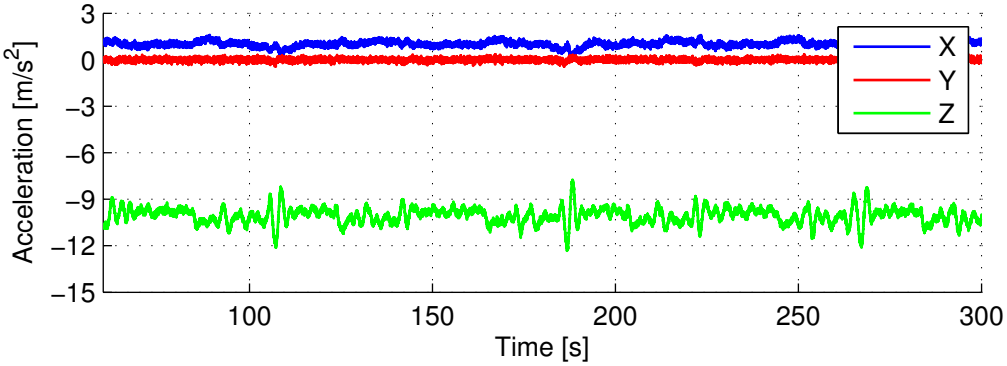

Figure 7.36: Acceleration measurements for the realistic track navigation response during HIL simulations.

Controller from engaging. In this scenario, the Heading and Guidance Controllers are very slow to guide the aircraft to the transition region. If the track is sufficiently small, the aircraft may reach the destination waypoint before the Cross-Track Controller has been activated. The overshoot at the North-Western point is not due to the pitch angle problem, but rather the aircraft being pushed beyond the track due to excessive wind force. Overall, the system responded relatively well under wind conditions that remained within the safety pilot comfort level.

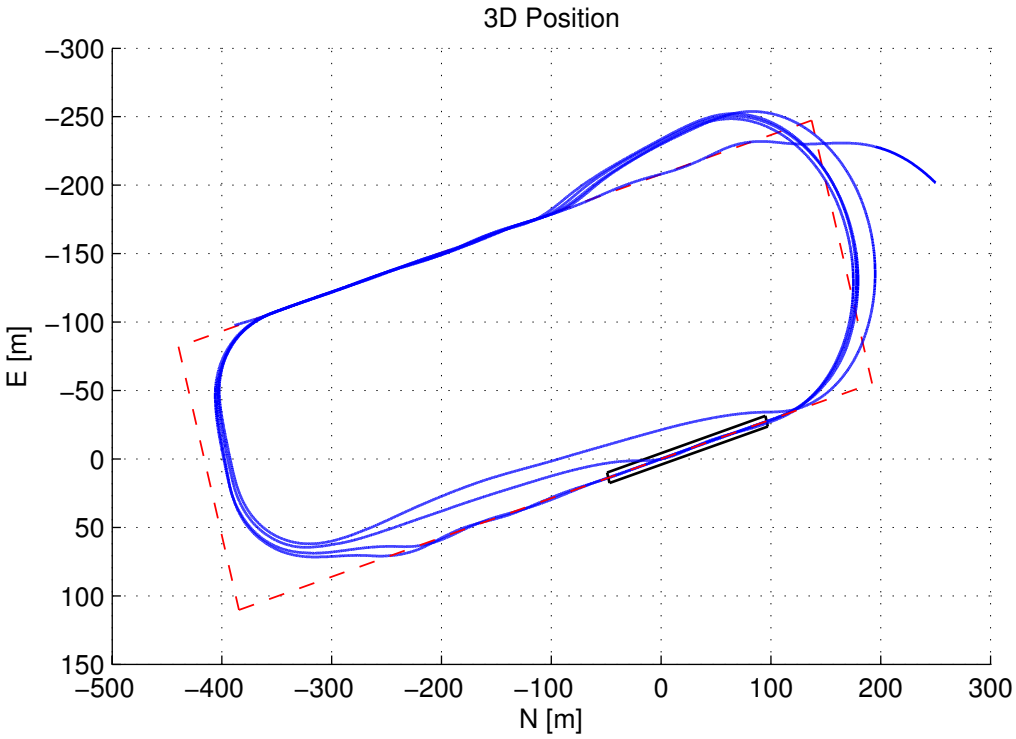

Figure 7.37: Navigation path for the realistic track with a starboard wind during HIL simulations.

7.2.3 Stationary Platform Landings

This section presents the results of the HIL simulations for the stationary platform landings. It should be noted that some simulations were paused upon touchdown, therefore data logged by the OBC after that point should be disregarded unless stated otherwise.

7.2.3.1 Ideal Scenario

For the ideal scenario, a more elongated waypoint set was used to ensure more time for the controllers to settle before the landing glide path was initiated. This set would be feasible in the scenario where the aircraft would have sufficient approach distance to set up the landing track unobstructed, such as an aircraft carrier and open sea scenario. The waypoint set used is given in Table 7.1.

An isometric view of the landing is presented in Figure 7.38. The aircraft lands on the point where the estimator was initialised, which is typically one third onto the runway to

Table 7.1: Ideal landing scenario waypoint set.

WP	North [m]	East [m]
0	200	0
1	200	-400
2	-400	-200
3	-400	0

ensure sufficient clearance before the landing point, but also enough remaining runway to bring the aircraft to a halt. The same principles will be used for the moving platform landing, except that a constant offset is added to the inertial reference points between the aircraft and the DGPS base station antenna.

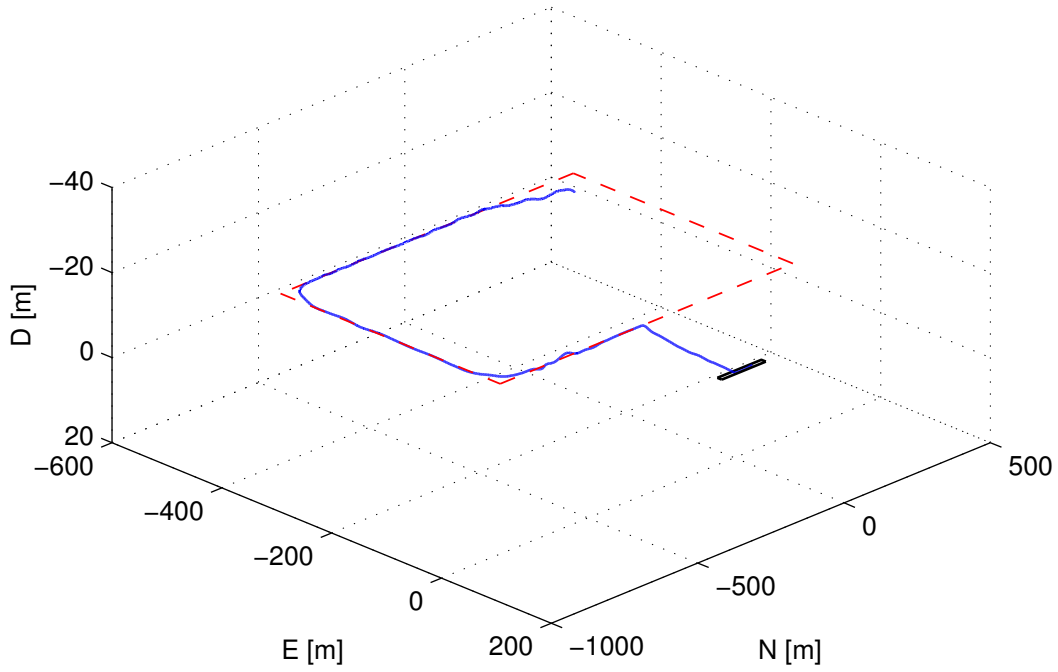

Figure 7.38: Isometric view of a landing for the ideal scenario track.

Figure 7.39 shows the altitude profile during the landing phase. It can be seen that the aircraft is able to follow the ramp reference very well after the initial transient. The aircraft is able to hit the intended target point with nearly no error in the longitudinal axis.

As shown in Figure 7.40, the intended landing climb rate of -1.1m/s is tracked well and ensures a safe landing speed of descent. The error is controlled to remain within approximately 0.1m/s. As shown in Figure 7.41, the constant airspeed reference is also tracked well up to the landing point, except for the initial transition where a small increase is observed due to the exchange from potential to kinetic energy. The error is controlled to remain within approximately 0.25m/s. As shown in Figure 7.42, the cross-track error is also tracked well up to the landing point. The error is controlled to remain within approximately 0.15m. The aircraft is thus able to hit the intended target point with nearly no error in the lateral axis.

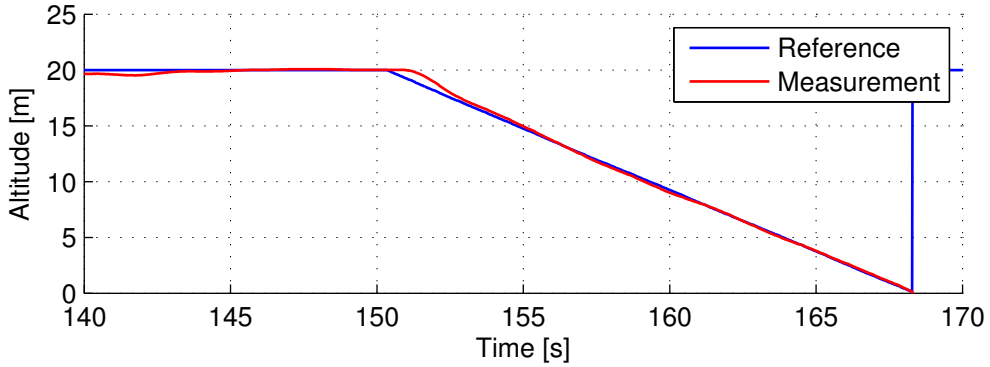

Figure 7.39: Altitude response of a landing for the ideal scenario track.

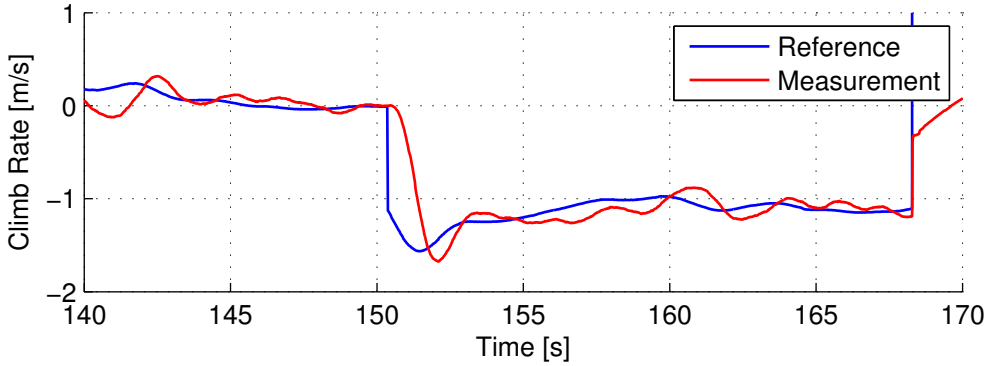

Figure 7.40: Climb rate response of a landing for the ideal scenario track.

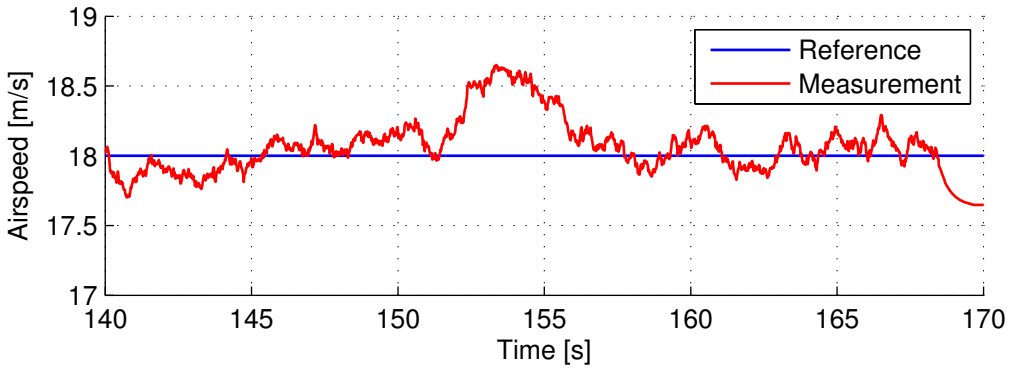

Figure 7.41: Airspeed response of a landing for the ideal scenario track.

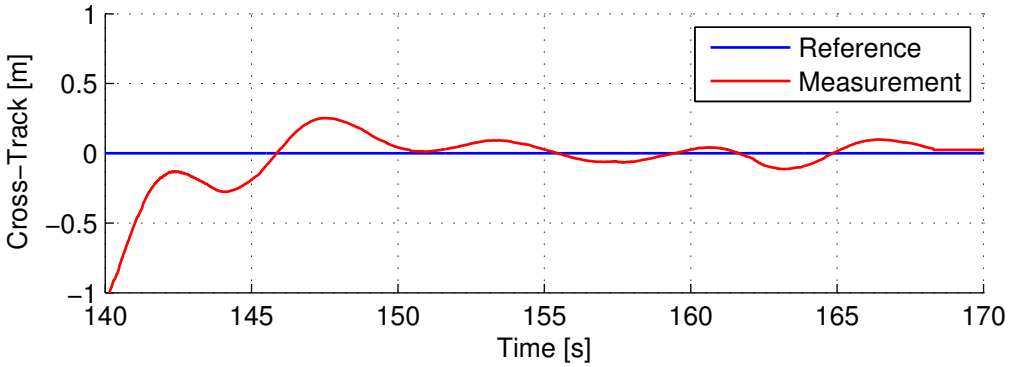

Figure 7.42: Cross-Track response of a landing for the ideal scenario track.

7.2.3.2 Realistic Scenario

For the realistic scenario, a short waypoint set was used that would have been practically feasible to perform at the available flight test facilities. To ensure correct behaviour during practical tests, the track heading angle is rotated by

$$\psi_{track} = -16^{\circ} \tag{7.1}$$

to align the track with the GPS and magnetometer measurements. The waypoint set used is given in Table 7.2. The aircraft was subjected to wind conditions with the wind model set to 3.6m/s (20% of flight speed) and a severity of 10^{-1} using the Dryden $-q + r$ sequence.

Table 7.2: Realistic landing scenario waypoint set. These points are rotated by ψ_{track} on the OBC.

WP	**North [m]**	**East [m]**
0	200	0
1	200	-200
2	-200	-200
3	-400	0

A top-down view of the landing is presented in Figure 7.43. The aircraft was subjected to crosswind conditions which clearly influenced the navigation path. As the aircraft attempts to reach the base leg, it is pushed back by the incoming airflow. This continues as the aircraft makes the turn towards the final leg, therefore it takes longer for the Cross-Track Controller to engage and negate the steady state error. The aircraft is still able to land on the point where the estimator was initialised, although the responses up to the touchdown point are less favourable.

Figure 7.44 shows the altitude profile during the landing phase. It can be seen that the aircraft is able to follow the ramp reference fairly well after the initial transient, however a slight oscillation persists throughout the sequence. The aircraft is able to hit the intended target point, but slight errors in altitude cause more inaccuracy in the longitudinal axis. As shown in Figure 7.45, the intended landing climb rate of -1.1m/s is tracked to ensure a safe landing sink rate. The error is not controlled as well as in the ideal condition, but remains within approximately 0.2m/s and improves towards the landing point. As shown in Figure 7.46, the constant airspeed reference is tracked poorly during the initial landing phases, but this improves towards the end of the sequence. This is due to the pitch angle estimation error as discussed in Section 7.2.2.4 that causes a large airspeed increase. The increased airspeed significantly reduces the distance and time in which the controller can settle the response, therefore the controller is still in its transient when beginning the landing sequence and hits the target point before the oscillations have been sufficiently damped. The error is however controlled to remain within approximately 0.25m/s near the final stages of the sequence. As shown in Figure 7.47, the cross-track error is tracked well from the point where the Cross-Track Controller takes over from the Heading and Guidance Controllers up to the touchdown point. The error is controlled

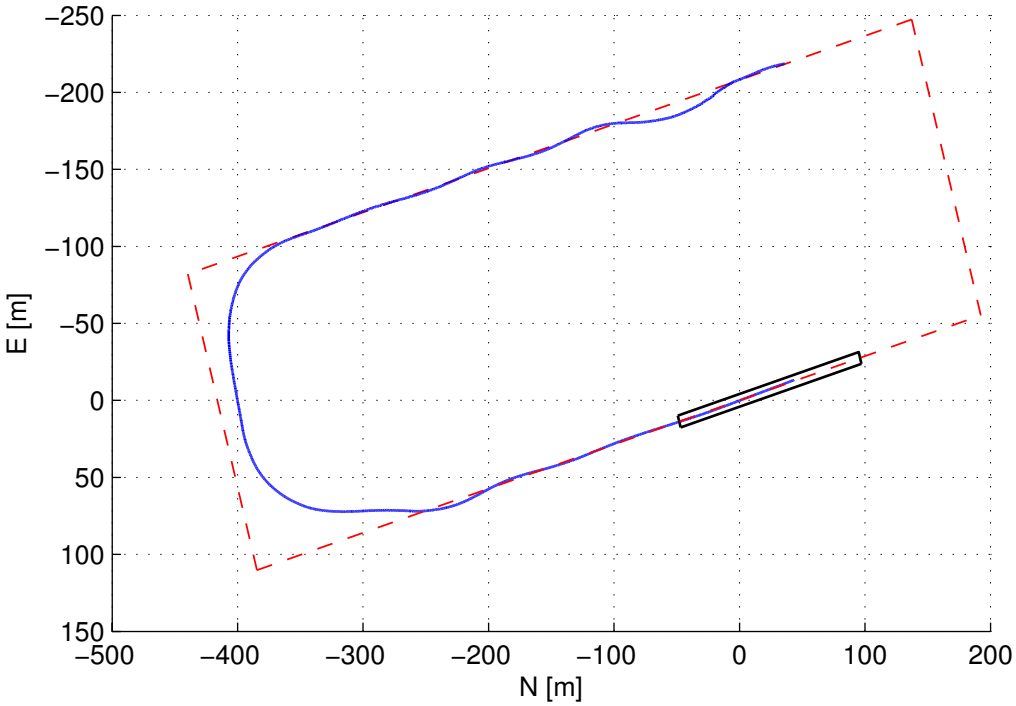

Figure 7.43: Top-Down view of a landing for the realistic scenario track under crosswind conditions.

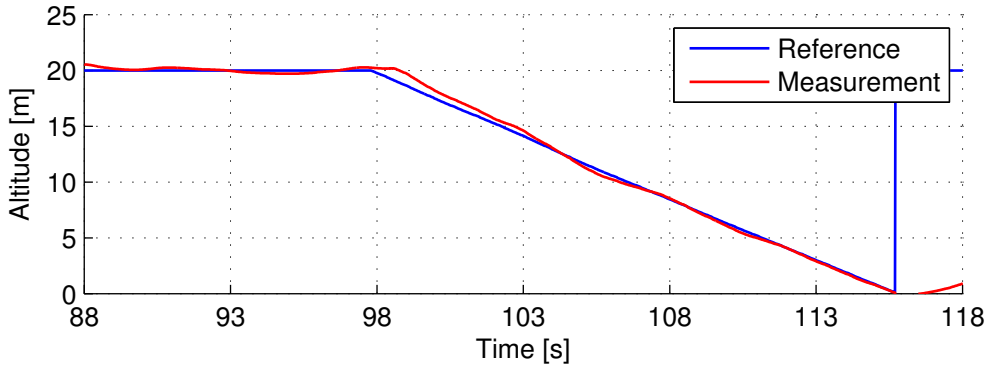

Figure 7.44: Altitude response of a landing for the realistic scenario track.

to remain within approximately 1m during these final stages, although poorer tracking is caused by the pitch angle estimation problem which causes an increase in airspeed and subsequently large lateral path deviations on the final leg. The aircraft is still able to hit the intended target point, although a larger error is observed in the lateral axis with the smaller track.

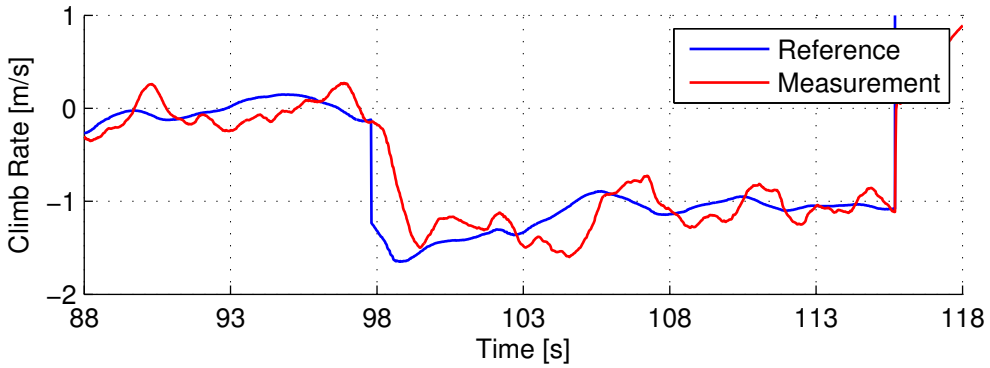

Figure 7.45: Climb rate response of a landing for the realistic scenario track.

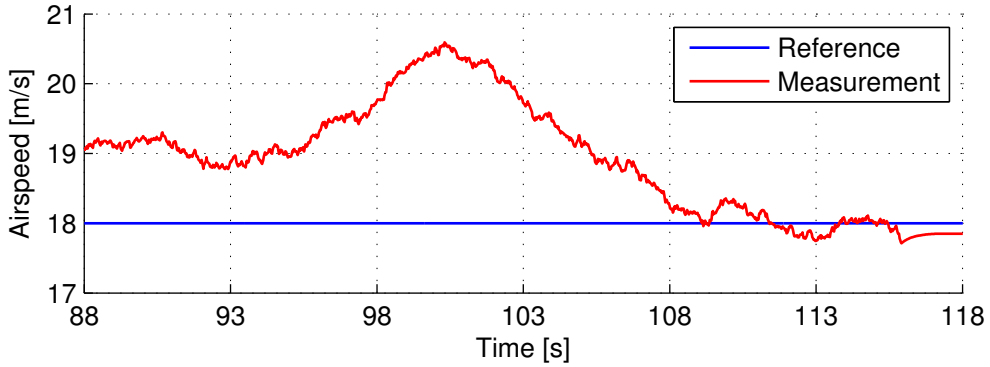

Figure 7.46: Airspeed response of a landing for the realistic scenario track.

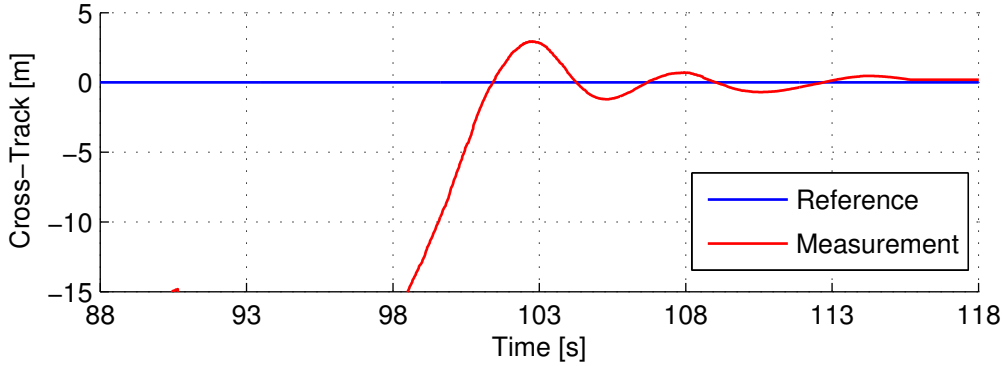

Figure 7.47: Cross-Track response of a landing for the realistic scenario track.

7.2.4 Moving Platform Landings

This section presents the results of the HIL simulations for the moving platform landings. It should be noted that some simulations were paused upon touchdown, therefore data logged by the OBC after that point should be disregarded unless stated otherwise. The platform motion was initiated at a predetermined point in the simulation and at a constant rate of 10m/s.

The Figures 7.48, 7.49 and 7.50 show the aircraft NSA, airspeed and altitude responses, respectively, when performing a touch-and-go manoeuvre. This manoeuvre is necessary as the intended practical platform is too small to allow the aircraft to stop naturally as no assisted braking is available. The large negative acceleration spike is clearly visible about 128s into the flight. This value was fairly consistent throughout simulations, but was also practically verified when the aircraft was landed under safety pilot control. The state machine was therefore programmed to continuously evaluate the normal acceleration for a spike lower than $-2g$ to transition from the descent phase into the recovery phase. The chosen value was regarded safe as it provided a buffer for false positives but not so large that it would result in a false negative. Figure 7.49 shows the altitude profile for the touch-and-go manoeuvre. The aircraft

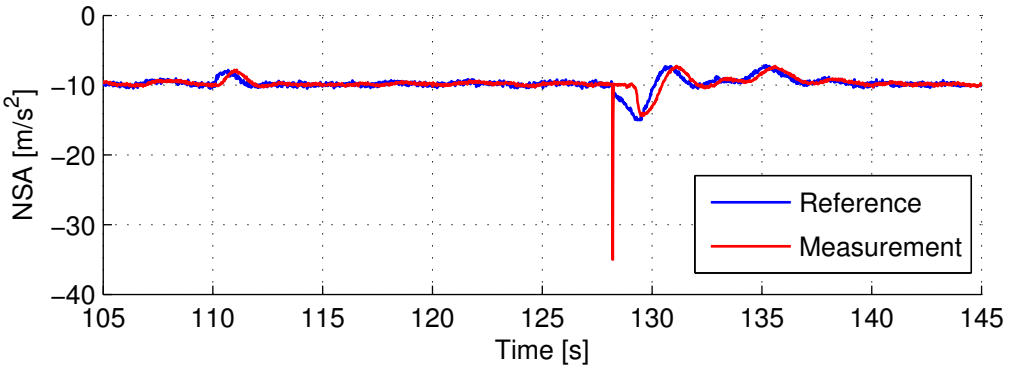

Figure 7.48: NSA spike for a moving platform landing and recovery during HIL simulations.

was simply commanded to track the trim altitude after the touchdown was detected, while the roll angle was commanded to remain wings-level. It was decided to not command a high pitch angle to quickly increase angle of attack and therefore gain additional lift during this procedure. The resulting large pitch rate may cause the tail to strike the platform, thereby damaging the undercarriage, elevator or the servo motors. Figure 7.50 shows the large deviation in airspeed during the touch-and-go manoeuvre. The reason for this is twofold. Firstly, the aircraft experiences a large backwards force due to dynamic friction when the wheels come into contact with the platform surface, especially since the wheels are prone to bending under large downwards forces. Secondly, the large altitude step also causes the controllers to exchange some kinetic energy for potential energy, thus lowering the airspeed. The specific energy integrator may not wind down fast enough after the altitude is reached, therefore causing the overshoot in airspeed. The manoeuvre is however performed successfully and deemed acceptable for practical flight.

As shown in Figure 7.51, the system is able to adapt its glide path in accordance with the platform speed. At approximately 113s, it can be observed that the aircraft starts to descend

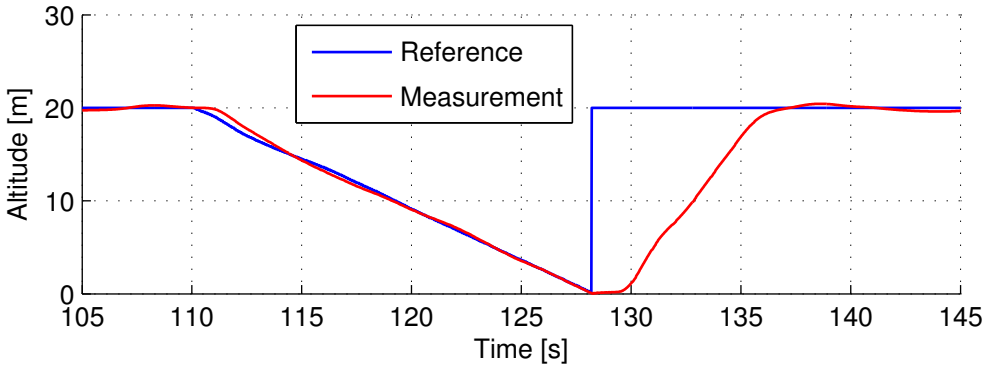

Figure 7.49: Altitude profile for a moving platform landing and recovery during HIL simulations.

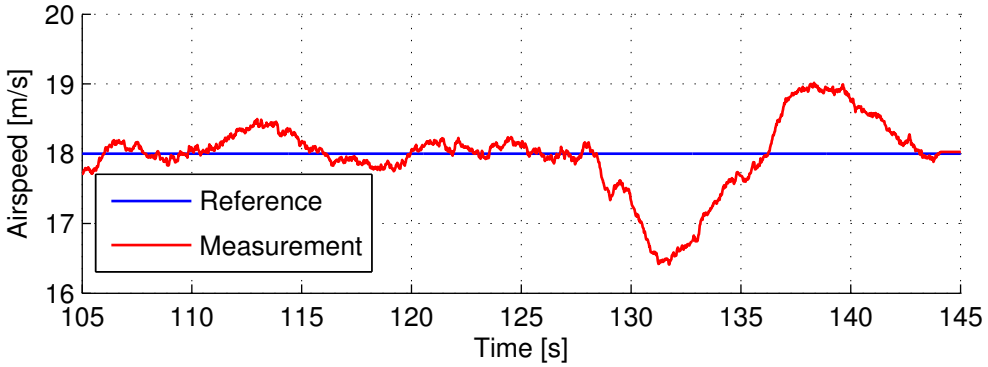

Figure 7.50: Airspeed response for a moving platform landing and recovery during HIL simulations.

towards the point where it predicts that the platform will be at the time of touchdown. The platform however starts moving at 117s and the aircraft redetermines the correct glide path in order to hit the target correctly. This procedure was necessary for practical flight tests as it is virtually impossible to maintain an exact constant speed with the platform, but it also makes the system more robust in general.

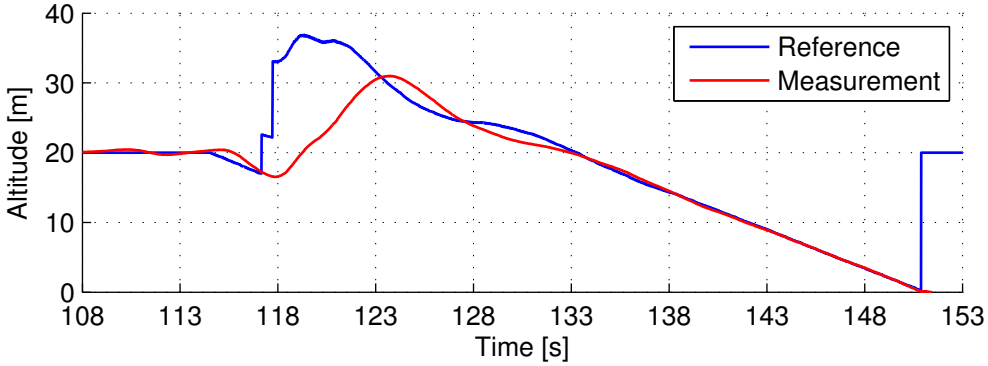

Figure 7.51: Replan manoeuvre for a moving platform landing during HIL simulations.

7.2.4.1 Ideal Scenario

The ideal moving platform scenario makes use of the same waypoint set as the ideal stationary landing scenario. The waypoint set used is given in Table 7.1. For the final landing sequence,

only the first and final waypoints are relevant as they form the final leg track.

Figure 7.52 shows the altitude profile during the landing phase. It can be seen that the aircraft is able to follow the ramp reference very well after the initial transient. The aircraft is able to hit the intended target point with nearly no error in the longitudinal axis. The response is virtually identical to the stationary landing scenario. This happens because the glide path to the touchdown point is predetermined, therefore the aircraft would attempt to cover the same distance to the touchdown point, regardless of the stationary or moving nature of the platform.

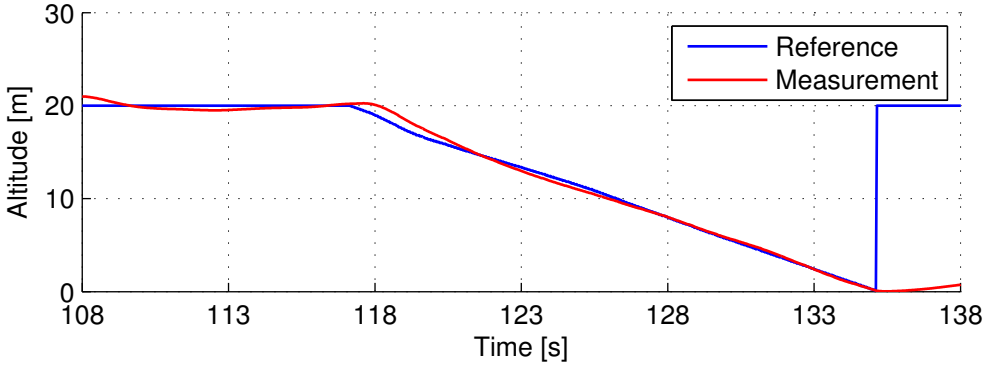

Figure 7.52: Altitude response of a landing for the ideal moving platform scenario.

As shown in Figure 7.53, the intended landing climb rate of -1.1m/s is tracked well and ensures a safe landing sink rate. The error is controlled to remain within approximately 0.2m/s. Upon close examination, it can be seen that the reference signal follows a jagged pattern. This is the result of the climb rate calculation using a different measurement source for the moving platform landings than for the stationary landings. Instead of using the estimator for position and velocity measurements, the slower sample rate DGPS measurements are used which are held between samples. The reference ramps up or down during the held period, but is corrected every 100ms by the new DGPS sample.

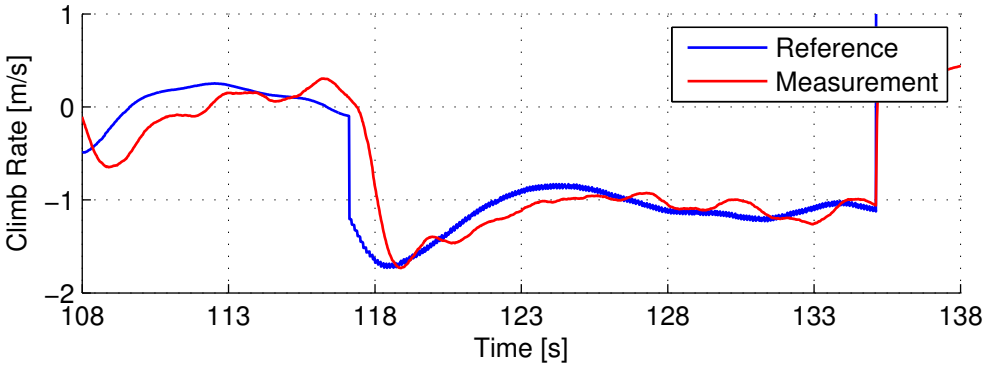

Figure 7.53: Climb rate response of a landing for the ideal moving platform scenario.

As shown in Figure 7.54, the constant airspeed reference is tracked fairly well up to the landing point, except for the initial transition where a small increase is observed due to the exchange from potential to kinetic energy. The error is controlled to remain within approximately 0.4m/s.

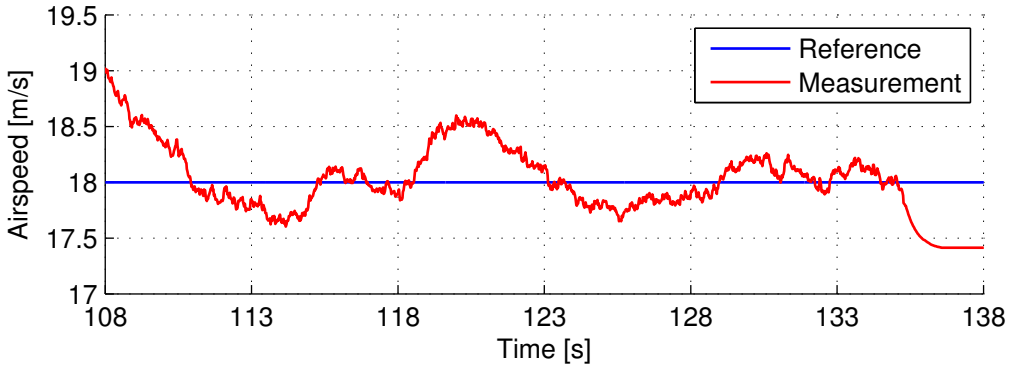

Figure 7.54: Airspeed response of a landing on the ideal moving platform scenario.

As shown in Figure 7.55, the cross-track error is tracked very well up to the landing point. The error is controlled to remain within approximately 0.15m. The aircraft is thus able to hit the intended target point with nearly no error in the lateral axis. The good tracking performance during the final stages is owed to the long track distance available that provides enough time to allow the transient responses of the controllers to settle before initiating the landing sequence.

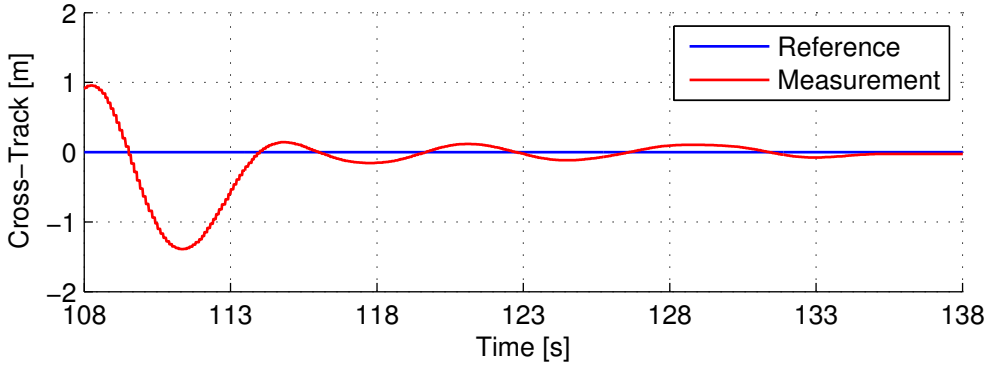

Figure 7.55: Cross-Track response of a landing for the ideal moving platform scenario.

Figure 7.56 shows the relative position measurements from the DGPS. It is clearly visible how the North, East and Down coordinates go through the zero relative position, indicating a successful platform landing. This figure also matches well with Figure 7.52, verifying the DGPS implementation against that of the position estimates.

7.2.4.2 Realistic Scenario

The realistic moving platform scenario makes use of the same waypoint set as the realistic stationary landing scenario. The waypoint set used is given in Table 7.2. For the final landing sequence, only the first and final waypoints are relevant as they form the final leg track. The aircraft was subjected to wind conditions with the wind model set to 3.6m/s (20% of flight speed) and a severity of 10^{-1} using the Dryden $-q + r$ sequence.

Figure 7.57 shows the altitude profile during the landing phase. It can be seen that the aircraft is able to follow the ramp reference fairly well after the initial transient, however a

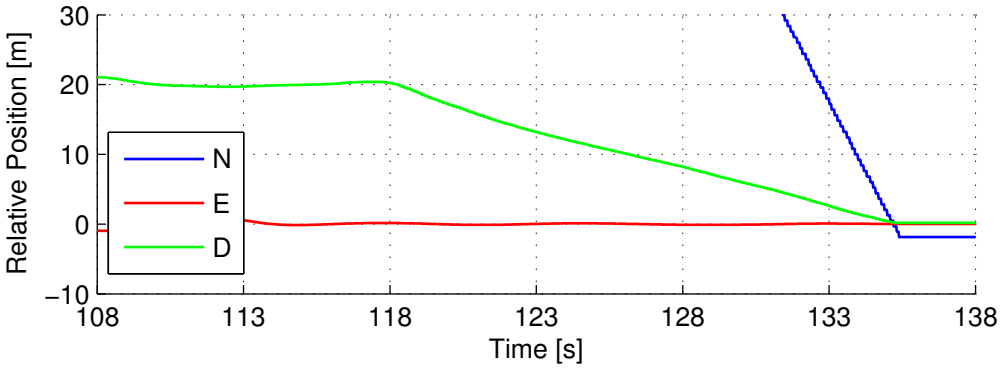

Figure 7.56: DGPS relative position measurements of a landing for the ideal moving platform scenario.

slight oscillation persists throughout the sequence. The aircraft is able to hit the intended target point, but slight errors in altitude cause more inaccuracy in the longitudinal axis. As

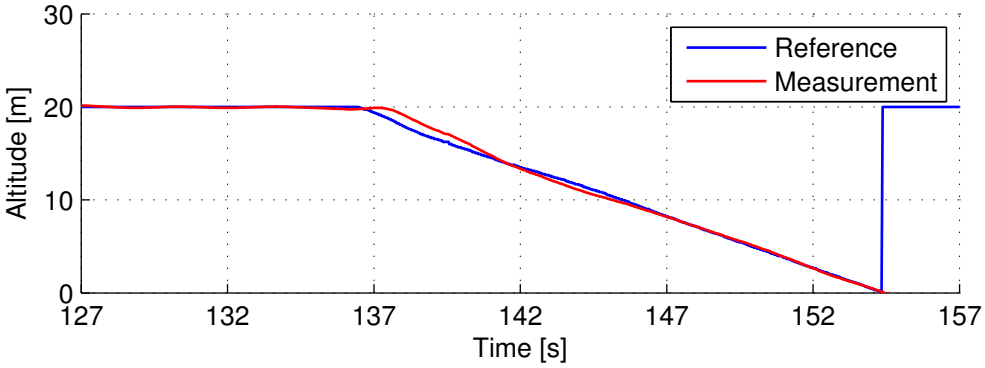

Figure 7.57: Altitude response of a landing for the realistic moving platform scenario.

shown in Figure 7.58, the intended landing climb rate of -1.1m/s is tracked to ensure a safe landing sink rate. The error is not controlled as well as in the ideal condition, but remains within approximately 0.2m/s towards the landing point. It is observed that the tracking remains significantly better than under the stationary platform conditions. As shown in Figure 7.59,

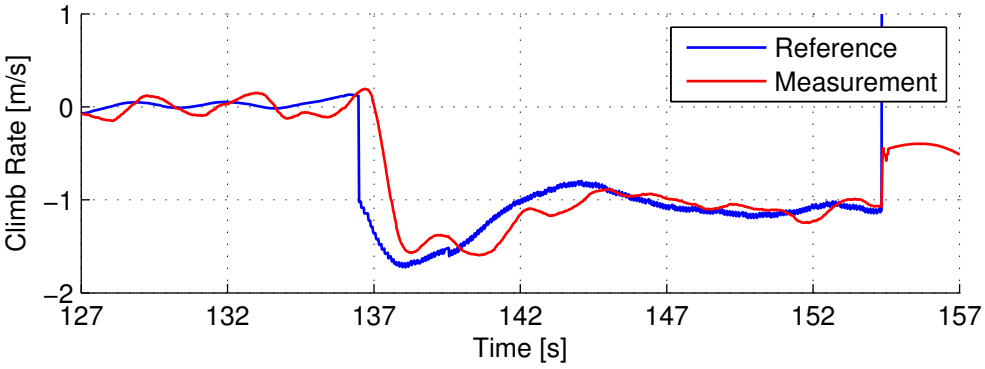

Figure 7.58: Climb rate response of a landing for the realistic moving platform scenario.

the constant airspeed reference is also tracked fairly well up to the landing point, except for the initial transition where a small increase is observed due to the exchange from potential to

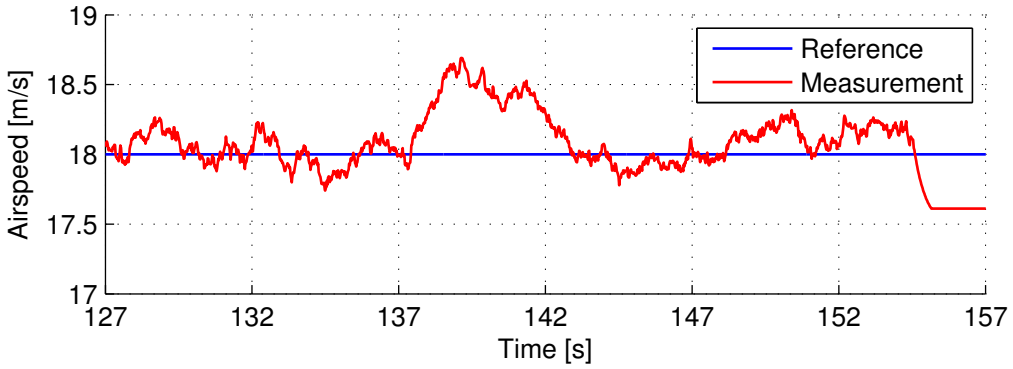

Figure 7.59: Airspeed response of a landing for the realistic moving platform scenario.

kinetic energy. The error is controlled to remain within approximately 0.4m/s. As shown in Figure 7.60, the cross-track error is also tracked well up to the landing point. The error is controlled to remain within approximately 0.2m. The aircraft is thus able to hit the intended target point with nearly no error in the lateral axis. The good tracking performance during the final stages is owed to the long track distance available that provides enough time to allow the transient responses of the controllers to settle before initiating the landing sequence. The small spikes observed in the measurements appear to be instances where the OBC failed to receive a DGPS base station packet with updated position and velocity information, causing erroneous estimates. This can be especially critical when delta values and rotation matrices between control cycles are used for estimation. Figure 7.61 shows the relative position measurements

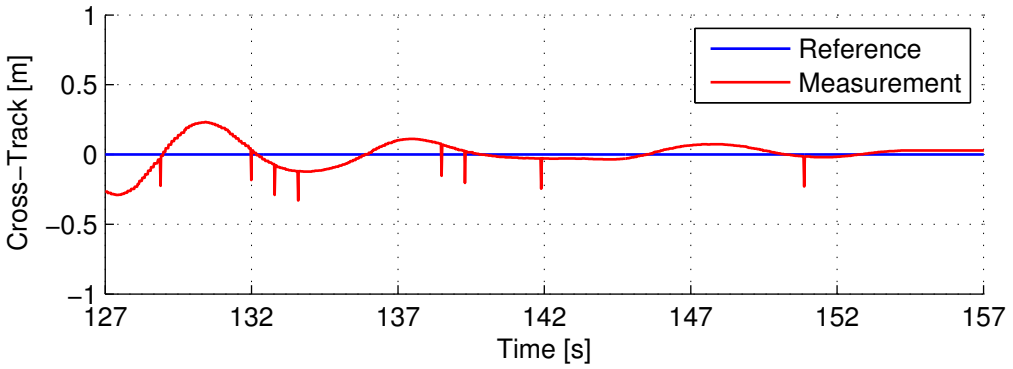

Figure 7.60: Cross-Track response of a landing for the realistic moving platform scenario.

from the DGPS. It is clearly visible how the North, East and Down coordinates go through the zero relative position, indicating a successful platform landing. This figure also matches well with Figure 7.57, verifying the DGPS implementation against that of the position estimates.

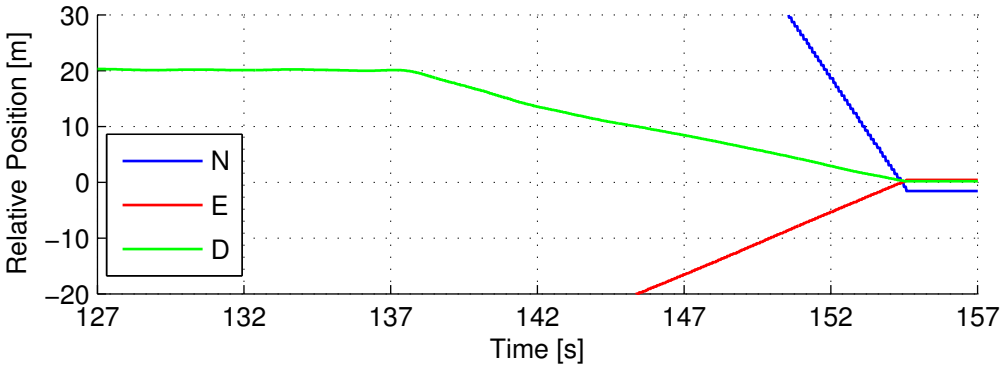

Figure 7.61: DGPS relative position measurements of a landing for the realistic moving platform scenario.

7.2.5 Landing Accuracy

The landing accuracy was evaluated using the results from a significant number of simulations. Although the typical Monte Carlo method requires many times more simulations to be truly representative, this was practically infeasible as it takes a large amount of time to set up each simulation, perform it, and extract the data afterwards. This task also required manual intervention and therefore could not be automated. The simulations were therefore limited to ten runs for each scenario considered, assuming that there is an equal probability that the aircraft will be subjected to each scenario in practice. The scenarios included zero wind and wind from every direction for both stationary and moving platform landings, resulting in one hundred total tests which was deemed sufficient to perform an analysis upon. For the simulations under wind conditions, the wind model was set to 2.7m/s (15% of flight speed) and a severity of 10^{-1} using the Dryden $-q + r$ sequence. The landing accuracy is colour-coded according to the physically required specifications given in Table 3.1, where landings within the inner bounds are marked green, landings between the inner and outer bounds are marked yellow, and landings outside of the outer bounds are marked red. To analyse these touchdown points, the statistical mean and standard deviation are used as symbols $\overline{p}_t$ and σ_t, respectively. For all landings, the standard deviation in the longitudinal axis was much larger than in the lateral axis. This is due to the fact that a slight altitude offset causes a large horizontal offset in the landing point due to the small glide path angle followed.

7.2.5.1 Stationary Platform Landings

The stationary platform landing points presented in Figure 7.62 with their statistical distribution shown in Table 7.3 gives an indication of what can be expected under ideal environmental conditions. Since no wind disturbances are present, it is expected that the aircraft should touch down at the centre point of the platform. This is indeed evident from the fact that the mean values of both North and East coordinates of the touchdown point are near zero. The standard deviation indicates that the aircraft will land within 0.93m longitudinally and 0.07m laterally in 95% of attempts.

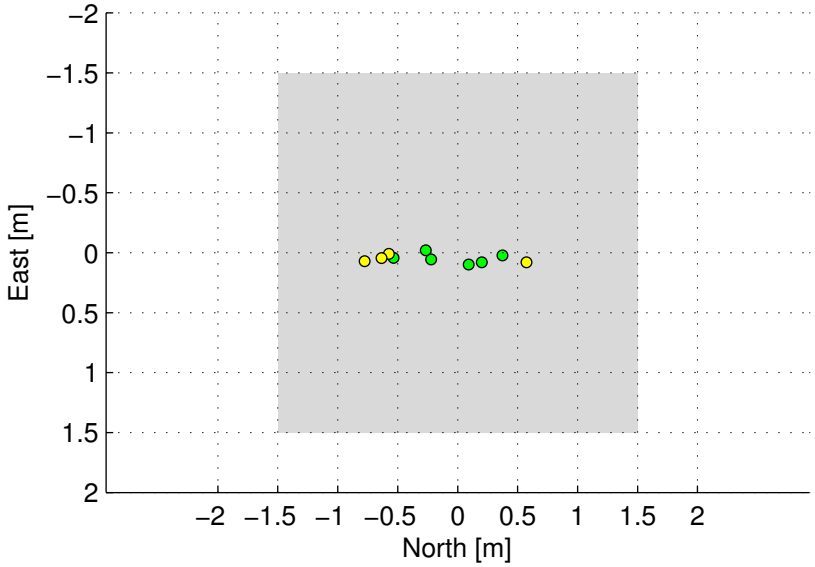

Figure 7.62: Stationary platform touchdown points under zero wind conditions.

Table 7.3: Stationary platform touchdown point statistical distribution under zero wind conditions.

Parameter	**North [m]**	**East [m]**
$\overline{p}_t$	-0.1764	0.0481
σ_t	0.4650	0.0363

Figure 7.63 and Table 7.4 present the stationary platform landing points and their statistical distribution under headwind conditions. It is observed that the mean has shifted more uprange, while the standard deviation increased significantly. This indicates that the aircraft was pushed back by the wind, therefore flying behind the ramp reference and landing short of the target point. The increased deviation is likely caused by the randomness of the wind which pushes the aircraft in the longitudinal axis, resulting in more deviations from the reference glide path.

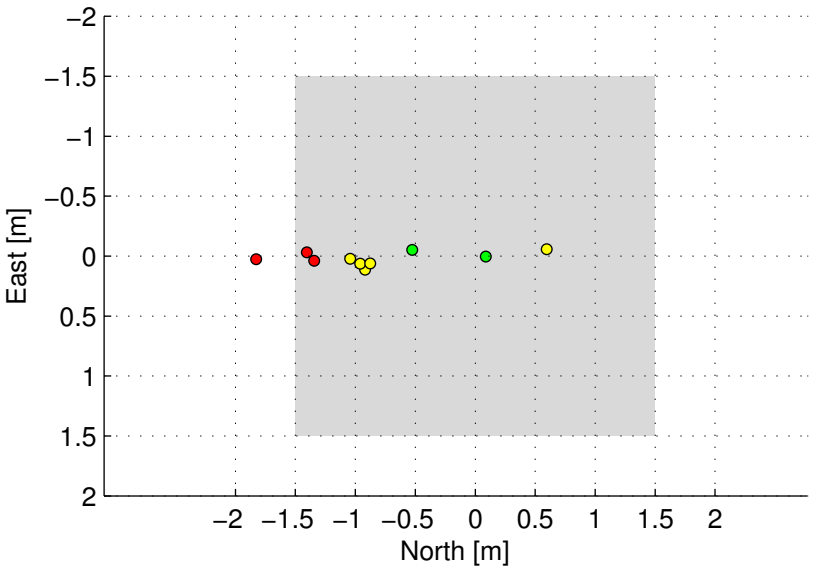

Figure 7.63: Stationary platform touchdown points under headwind conditions.

Table 7.4: Stationary platform touchdown point statistical distribution under headwind conditions.

Parameter	**North [m]**	**East [m]**
$\overline{p}_t$	-0.8212	0.0189
σ_t	0.7172	0.0543

Figure 7.64 and Table 7.5 present the stationary platform landing points and their statistical distribution under tailwind conditions. It is observed that the mean has shifted much further downrange, while the standard deviation increased significantly. This indicates that the aircraft was pushed forward by the wind, therefore flying in front of the ramp reference and landing beyond the target point. The increased deviation is likely caused by the randomness of the wind which pushes the aircraft in the longitudinal axis, resulting in more deviations from the reference glide path.

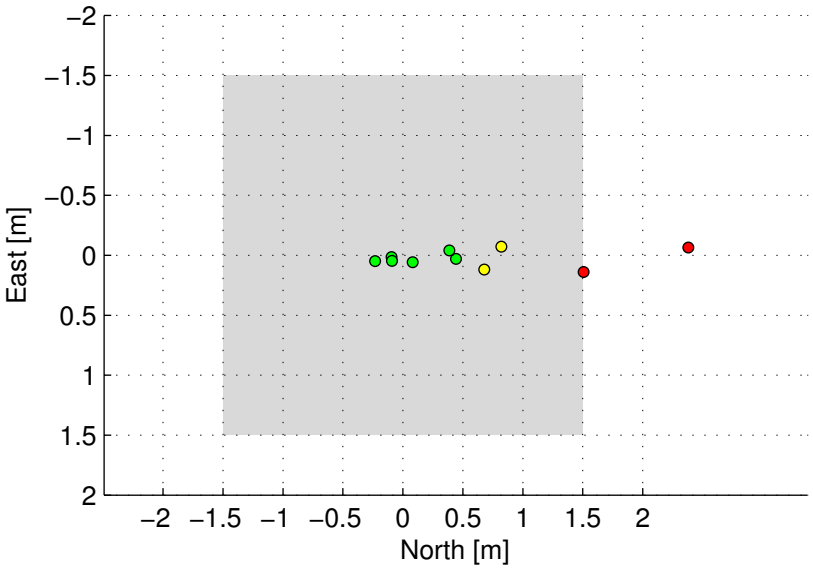

Figure 7.64: Stationary platform touchdown points under tailwind conditions.

Table 7.5: Stationary platform touchdown point statistical distribution under tailwind conditions.

Parameter	**North [m]**	**East [m]**
$\overline{p}_t$	0.5880	0.0277
σ_t	0.8189	0.0712

Figure 7.65 and Table 7.6 present the stationary platform landing points and their statistical distribution under starboard-side wind conditions. It is observed that the mean is nearly identical, while the standard deviation increased significantly in the longitudinal axis. This behaviour is caused by the lateral transients that have not been sufficiently suppressed by the time that the aircraft initiates the landing sequence. The slight gain and loss of lift by uneven wing levels therefore causes a disturbance into the longitudinal controllers, resulting in the aircraft being unable to accurately track the glide path ramp reference. This is exacerbated by the randomness of the wind causing lateral disturbances.

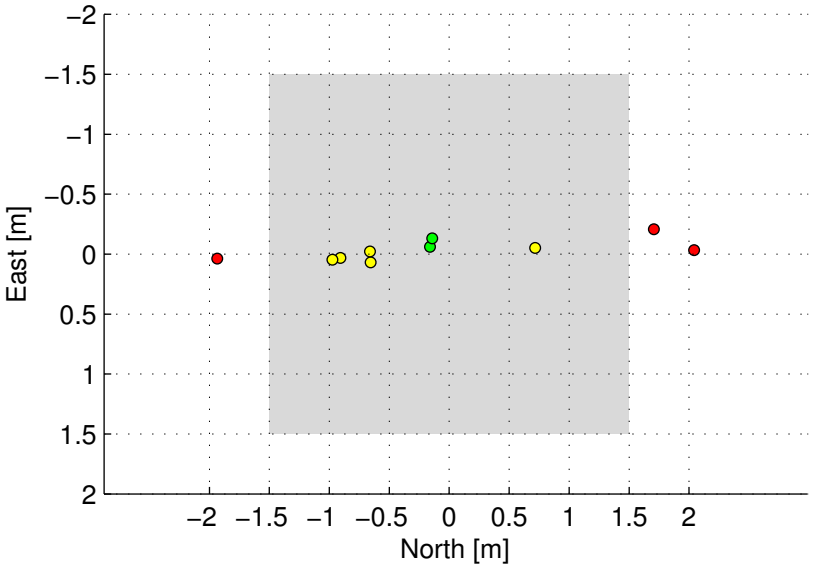

Figure 7.65: Stationary platform touchdown points under starboard-side wind conditions.

Table 7.6: Stationary platform touchdown point statistical distribution under starboard-side wind conditions.

Parameter	**North [m]**	**East [m]**
$\overline{p}_t$	-0.0968	-0.0325
σ_t	1.2443	0.0865

Figure 7.66 and Table 7.7 present the stationary platform landing points and their statistical distribution under port-side wind conditions. It is observed that the mean is slightly uprange, while the standard deviation increased significantly in the longitudinal axis. This behaviour is caused by the lateral transients that has not been sufficiently suppressed by the time that the aircraft initiates the landing sequence. The slight gain and loss of lift by uneven wing levels therefore causes a disturbance into the longitudinal controllers, resulting in the aircraft being unable to accurately track the glide path ramp reference. This is exacerbated by the randomness of the wind causing lateral disturbances.

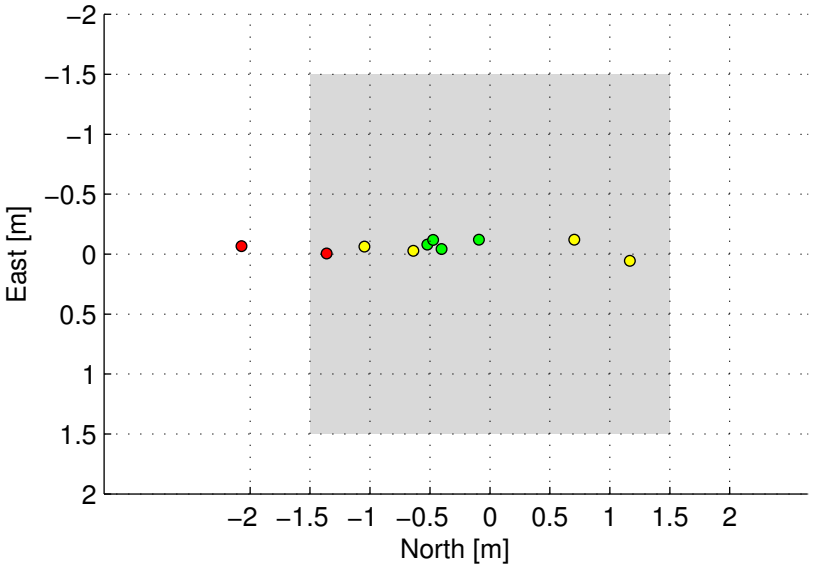

Figure 7.66: Stationary platform touchdown points under port-side wind conditions.

Table 7.7: Stationary platform touchdown point statistical distribution under port-side wind conditions.

Parameter	**North [m]**	**East [m]**
$\overline{p}_t$	-0.4735	-0.0587
σ_t	0.9387	0.0567

Figure 7.67 and Table 7.8 present the combined stationary platform landing points and their statistical distribution. It is clear that the mean is very close to zero for both the North and East coordinates, indicating very good average landing point accuracy. Given the dimensions of the physical platform, the standard deviation in the longitudinal axis indicates that the aircraft should land safely approximately 80% of the time, while laterally it would land safely nearly 100% of the time with exceptional accuracy. The longitudinal deviation was nearly double that of the ideal value, while the lateral deviation was less than half of the ideal value. It can be concluded that for stationary landings, the lateral touchdown point will not be an issue. The longitudinal touchdown point however is a concern in terms of repeatability as the results show that the system can easily be negatively impacted by disturbances in this axis.

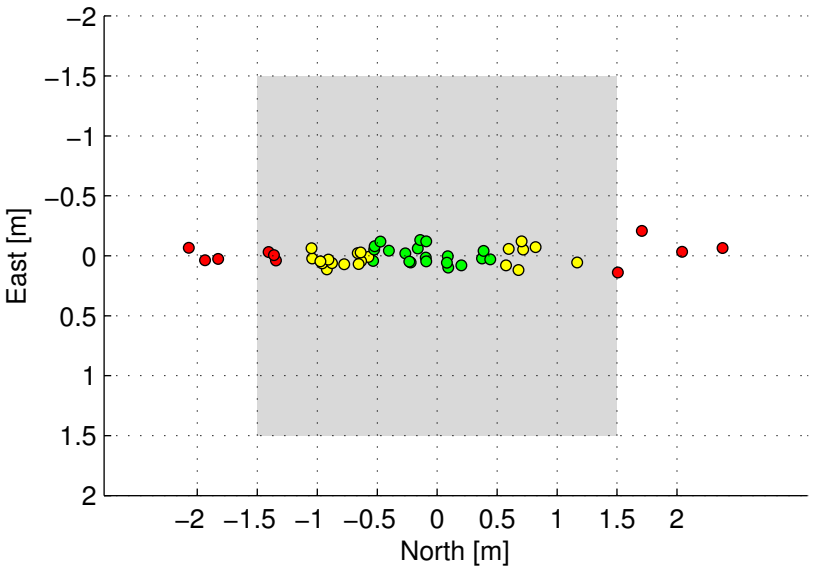

Figure 7.67: Combined stationary platform touchdown points.

Table 7.8: Combined stationary platform touchdown point statistical distribution.

Parameter	**North [m]**	**East [m]**
$\overline{p}_t$	-0.1960	0.0007
σ_t	0.9626	0.0728

7.2.5.2 Moving Platform Landings

The moving platform landing points presented in Figure 7.68 with their statistical distribution shown in Table 7.9 gives an indication of what can be expected under ideal environmental conditions. Since no wind disturbances are present, it is expected that the aircraft should touch down at the centre point of the platform. This is indeed evident from the fact that the mean values of both North and East coordinates of the touchdown point are near zero. The standard deviation indicates that the aircraft will land within 1.20m longitudinally and 0.08m laterally in 95% of attempts.

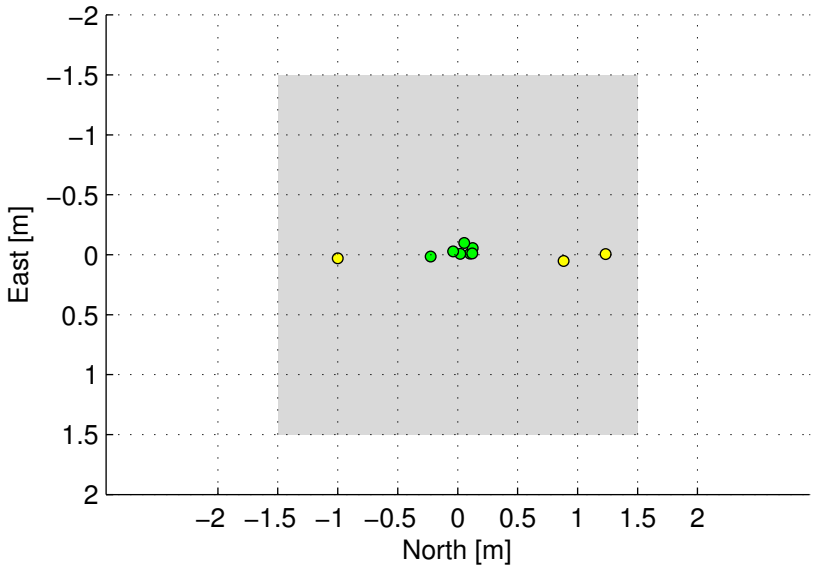

Figure 7.68: Moving platform touchdown points under zero wind conditions.

Table 7.9: Moving platform touchdown point statistical distribution under zero wind conditions.

Parameter	**North [m]**	**East [m]**
$\overline{p}_t$	0.1278	-0.0117
σ_t	0.5993	0.0423

Figure 7.69 and Table 7.10 present the moving platform landing points and their statistical distribution under headwind conditions. It is observed that the mean touchdown point has shifted much further uprange, while the standard deviation decreased. This indicates that the aircraft was pushed back by the wind, therefore flying behind the ramp reference and landing short of the target point. The smaller standard deviation may indicate that the headwind improved stability by allowing the aircraft to better align its velocity vector with incoming airflow over the long distance in which the controller was allowed to settle.

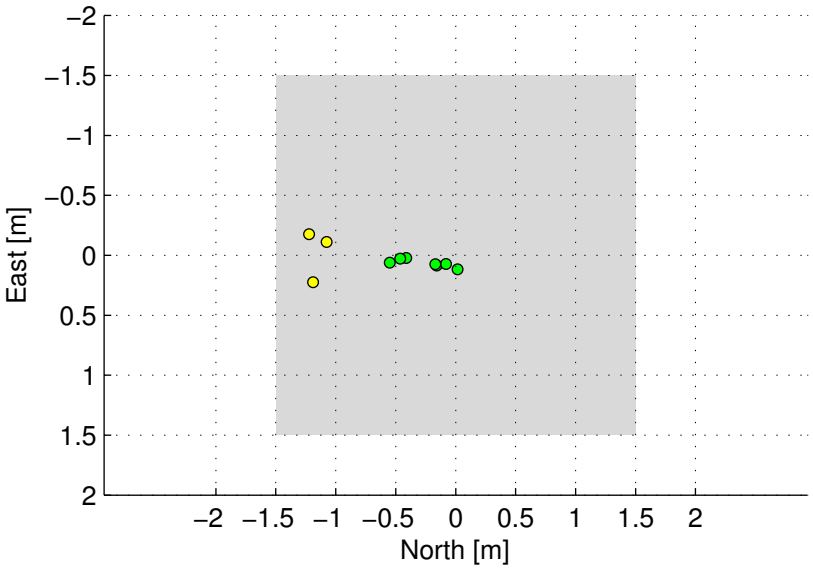

Figure 7.69: Moving platform touchdown points under headwind conditions.

Table 7.10: Moving platform touchdown point statistical distribution under headwind conditions.

Parameter	**North [m]**	**East [m]**
$\overline{p}_t$	-0.5301	0.0397
σ_t	0.4714	0.1130

Figure 7.70 and Table 7.11 present the moving platform landing points and their statistical distribution under tailwind conditions. It is observed that the mean touchdown point has shifted further downrange, while the standard deviation increased. This indicates that the aircraft was pushed forward by the wind, therefore flying in front of the ramp reference and landing beyond the target point. The larger standard deviation may indicate that the tailwind worsened stability by reducing the ability of the aircraft to align its velocity vector with incoming airflow, resulting in more deviations from the reference glide path.

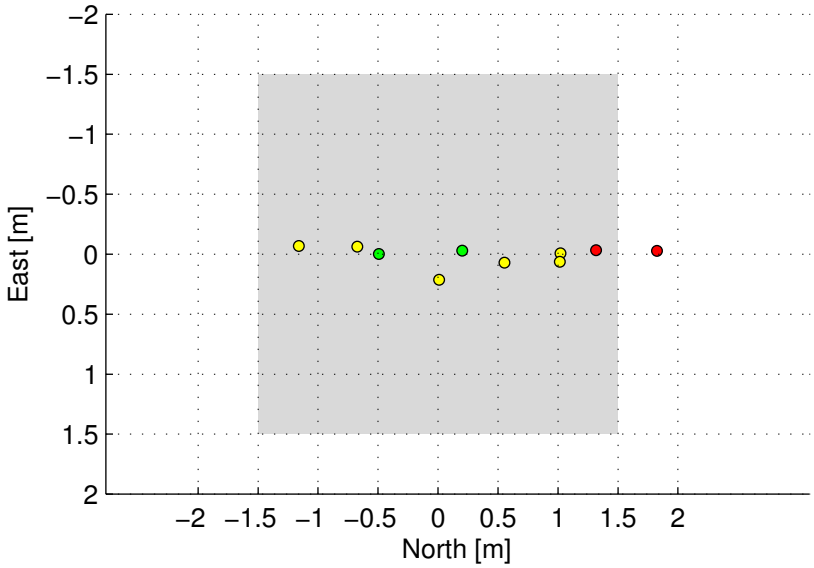

Figure 7.70: Moving platform touchdown points under tailwind conditions.

Table 7.11: Moving platform touchdown point statistical distribution under tailwind conditions.

Parameter	**North [m]**	**East [m]**
$\overline{p}_t$	0.3619	0.0115
σ_t	0.9561	0.0847

Figure 7.71 and Table 7.12 present the moving platform landing points and their statistical distribution under starboard-side wind conditions. It is observed that the mean has shifted uprange, while the standard deviation remained nearly the same. It is suspected that the starboard-side wind caused less overshoot of the navigation path on the final leg, therefore allowing the Cross-Track Controller to engage earlier. This would cause an earlier settling of the transients, therefore better control is achieved in the longitudinal axis. The single point far beyond the the mean is considered an outlier caused by large disturbances during that particular simulation.

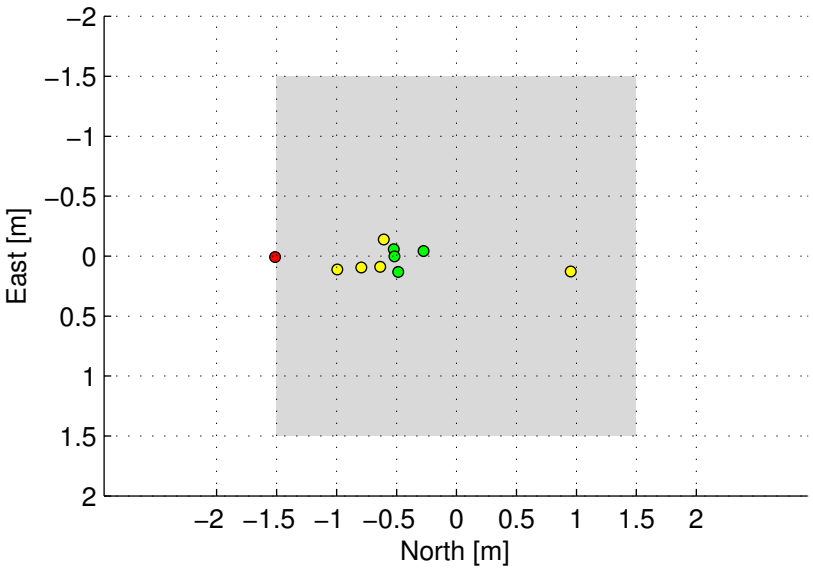

Figure 7.71: Moving platform touchdown points under starboard-side wind conditions.

Table 7.12: Moving platform touchdown point statistical distribution under starboard-side wind conditions.

Parameter	**North [m]**	**East [m]**
$\overline{p}_t$	-0.5395	0.0326
σ_t	0.6265	0.0926

Figure 7.72 and Table 7.13 present the moving platform landing points and their statistical distribution under port-side wind conditions. It is observed that the mean is nearly identical, while the standard deviation increased significantly in both axes. It is suspected that the portside-side wind caused more overshoot of the navigation path on the final leg, therefore not allowing the Cross-Track Controller to engage as early. This would cause a late settling of the transients, therefore poor control is achieved in the longitudinal axis. Since some transients remained in the lateral axis, a larger deviation is obtained.

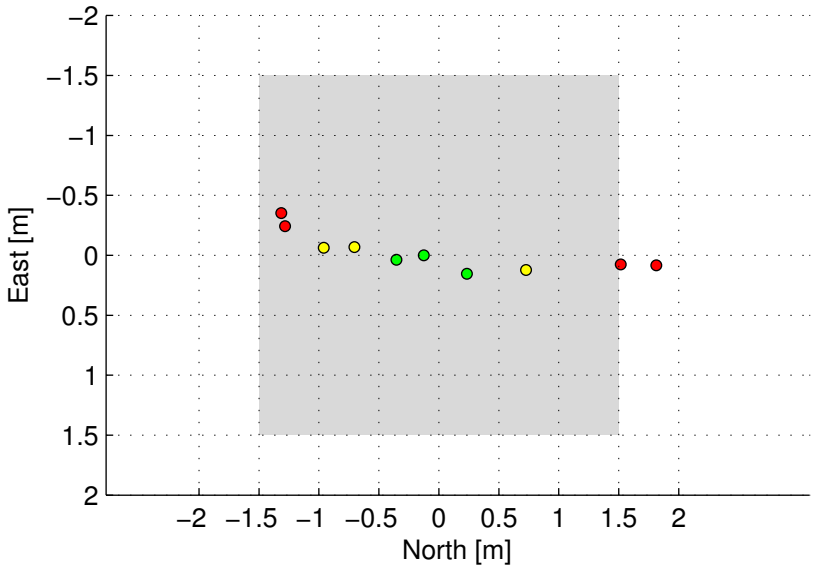

Figure 7.72: Moving platform touchdown points under port-side wind conditions.

Table 7.13: Moving platform touchdown point statistical distribution under port-side wind conditions.

Parameter	**North [m]**	**East [m]**
$\overline{p}_t$	-0.0455	-0.0254
σ_t	1.1099	0.1628

Figure 7.73 and Table 7.14 present the combined moving platform landing points and their statistical distribution. It is clear that the mean is very close to zero for both the North and East coordinates, indicating very good average landing point accuracy. Given the dimensions of the physical platform, the standard deviation in the longitudinal axis indicates that the aircraft should land safely approximately 86% of the time, while laterally it would land safely nearly 100% of the time with exceptional accuracy. The longitudinal deviation was one and a half times that of the ideal value, while the lateral deviation was half of the ideal value. It can be concluded that for moving platform landings, the lateral touchdown point will not be an issue. The longitudinal touchdown point however is a concern in terms of repeatability as the results show that the system can easily be negatively impacted by disturbances in this axis. Additionally, disturbances in the lateral axis manifest as disturbances in the longitudinal axis which can cause further inaccuracies.

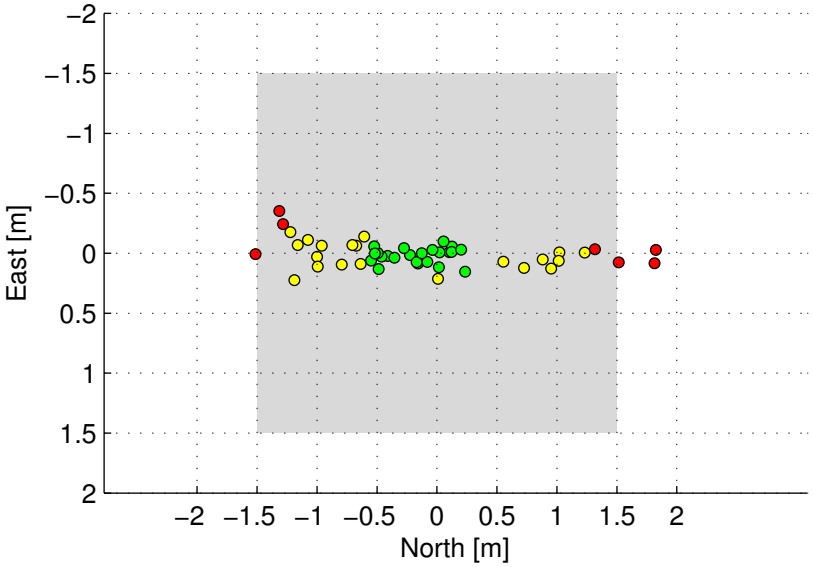

Figure 7.73: Combined moving platform touchdown points.

Table 7.14: Combined moving platform touchdown point statistical distribution.

Parameter	**North [m]**	**East [m]**
$\overline{p}_t$	-0.1251	0.0093
σ_t	0.8392	0.1052

Initially, it may appear strange that the moving platform landings yield statistically better results than the stationary platform landings. If analysed more closely, it becomes clear that the system performs better when the controllers are allowed to settle all transients before the landing sequence is initiated. This minimises the coupling between the longitudinal and lateral dynamics and allows the controllers to achieve higher tracking performance, resulting in more accurate landings. In many cases, the results seem so similar that deviations are more likely due to sensor noise rather than any actual phenomena. From the results obtained, it is believed

that the system performs well enough to achieve the goal of accurately landing on a moving platform.

7.3 Summary

This chapter briefly discussed the implementation of a fully integrated SIL simulation, although it could not be fully implemented due to the already strict implementation of HIL firmware. An analysis of the HIL simulation results for all controllers as well as a Monte Carlo style approach for the evaluation of the landing performance were presented. It was shown that most controllers correspond well with their respective designs. Of particular interest was the TECS controllers whose simulation results did not significantly deviate from the designs, validating the TECS simplification and design methodology, although improvements can be made by including the inner loops. A significant issue was highlighted in that an erroneous pitch angle estimation could cause deviations in airspeed and subsequently influence the landing accuracy by allowing transients of the navigation controller into the landing sequence. The landing results proved to be accurate enough to allow for practical testing as the aircraft should hit a moving platform 86% of the time within the allowed tolerances. It was however found that it would be essential that sufficient time be allowed for the transients of the lateral controllers to settle before the landing sequence is initiated as these transients couple into the longitudinal controllers as additional disturbances which could cause larger touchdown point deviations.

§ 8

Flight Tests

This chapter presents the results from practical flight tests for selected longitudinal and lateral controllers.

Section 8.1 describes the setup, systems and procedures used for the flight tests. Section 8.2 presents the results of selected flight tests. Section 8.3 provides a summary of the chapter.

8.1 Flight Test Setup

Before any flight tests were performed, the system had to undergo configuration, integration and testing. Not only did this process reduce the risks of practical testing, but it also made the tests more targeted and result-driven to ensure that essential data was captured correctly. This section will further discuss these details.

8.1.1 Aircraft Calibration

Before the aircraft was flight tested, the actuators were calibrated with respect to the RC and the automatic controllers. This ensured that the actuators followed the commanded control surface deflections and that they could not be commanded to an unreachable or dangerous state. The procedure is performed during the HIL simulation step as the HIL setup takes these calibration parameters into account.

Typically, the control surfaces are deflected at the maximum possible angles achievable by the servo motors. This is especially important after vehicle maintenance as the servo arms or rods may have suffered accidental damage. The throttle system was tested using a special thrust jig in order to measure the force provided by the motor. After the calibration process, the input commands are scaled by the calibration gains and offsets to provide the correct command signals to the actuators within the predefined limits.

8.1.2 Ground Control Station

As this project used an entirely different control system with respect to previous projects, the OBC and GCS were integrated after every modification made on either side. For the GCS, a

completely new controller interface was developed in order to assess the controllers during flight and to upload reference commands to the OBC. A critical information display was added in order to monitor the landing state and behaviour of the aircraft as well as an override to abort the landing procedure in the event of anomalous behaviour. The transmission transmit and receive procedures were updated to incorporate the new variables passed between the systems. A more detailed overview of the GCS and software changes can be found in Appendix B.

During practical tests, it was found that the RF communication system often failed to successfully transmit or receive data. This significantly impacted the amount of flight tests that could be performed successfully. Often, the aircraft would simply not respond to the step commands, or the aircraft would receive the command when it had already reached a turn in the ground track, causing the coupling between the longitudinal and lateral dynamics to contaminate the response. To improve the successful transmission of telemetry data, the data packet size was reduced as much as possible in order to free up bandwidth for transmissions and also to provide more time for the RF modules to perform additional retries. A detailed overview of the telemetry packet reduction can be found in Appendix B.1.

8.1.3 HIL Testing

In preparation for a flight test, the test procedure is documented and performed in the HIL environment. This reduces the risks involved by ensuring that the OBC can perform the required operations and that physical factors are accounted for, such as the available track distance in which to perform step commands and the flight duration limits due to battery life.

For most controllers, the system is designed to have either a sensible initial state or to capture the current behaviour of the aircraft. This reduces strain on the safety pilot and allows for a smooth and natural transition from manual control to autopilot control.

Once the system has been thoroughly evaluated in HIL simulations, the software and firmware are frozen and physical adjustments are kept to a minimum. The aircraft is then inspected for any defects and prepared for flight.

8.2 Flight Test Results

The flight test phase of this project was heavily hampered by bad RF communications and an intermittently working GPS unit. This section therefore only presents the flight test results obtained from selected flight tests. These tests included different acceleration measurement sources as this was important for the TECS, and the various longitudinal and lateral controllers required to perform an autonomous landing.

8.2.1 Acceleration Measurement Source

From initial longitudinal controller tests, it was determined that the TECS is fairly reliant on acceleration measurements. It was therefore decided to explore different methods to obtain the

acceleration of the aircraft. For the second and third test methods, the acceleration was calculated from both the accelerometers and the estimator, labelled as *Sensor Data* and *Estimator Data*, respectively.

The first method simply uses the axial specific acceleration measurement from the IMU and corrects it for gravity due to the aircraft pitch angle to obtain the body axes X-axis total acceleration. This is expressed mathematically as

$$\dot{\overline{v}} = a_x - g\sin\theta \tag{8.1}$$

where a_x is the specific acceleration measured along the X-axis of the aircraft. This method gave reasonable results and was eventually the method of choice for further tests. A sample of captured data is shown in Figure 8.1.

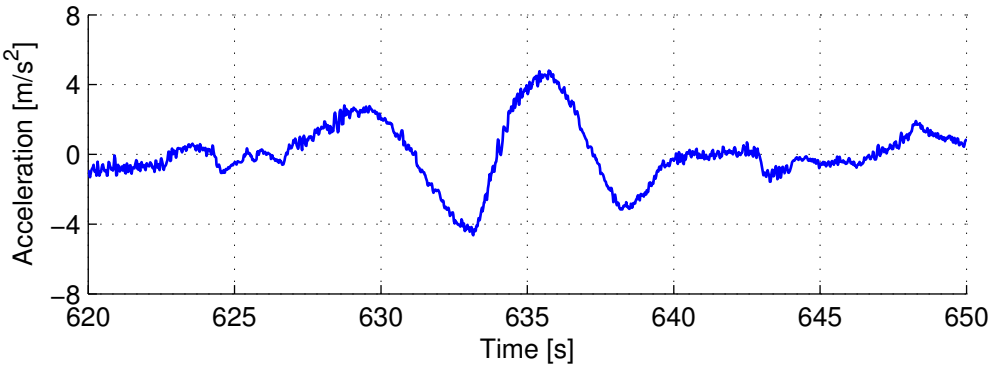

Figure 8.1: Acceleration source test using the first method.

The second method calculated the total rate of change of the velocity magnitude from the acceleration components in the body axes measured by the IMU and the velocity components in the body axes provided by the kinematic state estimator. This equation, obtained from the time derivative of the velocity as shown in Appendix A.2, is expressed mathematically as

$$\dot{\overline{v}} = \frac{1}{\overline{v}}\left(u\dot{u} + v\dot{v} + w\dot{w}\right) \tag{8.2}$$

where

$$\overline{v} = \sqrt{v_N^2 + v_E^2 + v_D^2} \tag{8.3}$$

$$\dot{u} = a_{x_{-g}} \tag{8.4}$$

$$\dot{v} = a_{y_{-g}} \tag{8.5}$$

$$\dot{w} = a_{z_{-g}} \tag{8.6}$$

$$\begin{bmatrix} u \\ v \\ w \end{bmatrix} = \mathrm{DCM}_{i\to b} \begin{bmatrix} v_N \\ v_E \\ v_D \end{bmatrix} \tag{8.7}$$

Here, $a_{x_{-g}}$, $a_{y_{-g}}$ and $a_{z_{-g}}$ are the specific acceleration measurements from the IMU with the gravitational acceleration removed and v_N, v_E and v_D are the coordinates of the aircraft ve-

locity in the inertial axes from the estimator. When using the IMU to obtain the acceleration measurements, as shown by the *Sensor Data* plot, the acceleration looks nearly identical to the first method. It can therefore be concluded that the rate of change of the velocity magnitude is approximately equal to the acceleration measured in the body axes X-axis and that the Y- and Z-axis components are insignificant. When using the estimator to obtain the acceleration measurements, as shown by the *Estimation Data* plot, the acceleration looks similar, although significant spikes are present. This was caused by the estimator inertial acceleration variables being held during cycles in which a GPS update was not received and thus it only propagated the state variables. Upon receiving the new update, the GPS velocity is used to calculate the acceleration by numerical differentiation. As the control cycle executed faster than the sample time of the GPS, it would cause the variable to only update every few control cycles, causing a value that may be much larger or smaller than the previous update to be added to the acceleration measurement. A sample of captured data is shown in Figure 8.2.

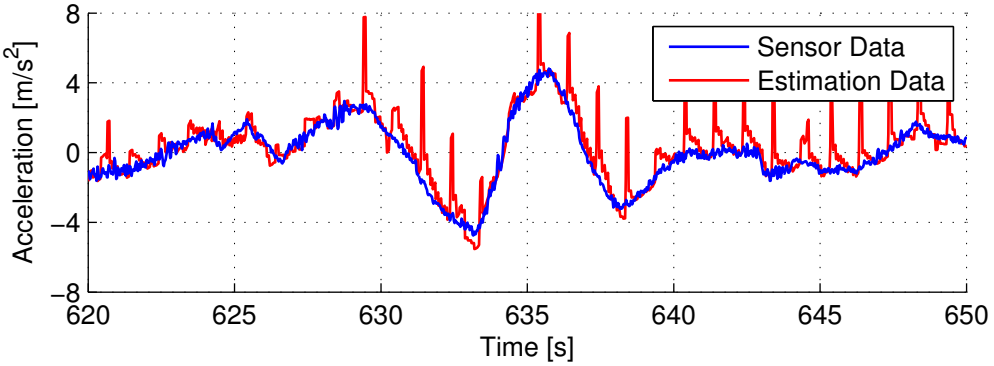

Figure 8.2: Acceleration source test using the second method.

The third method calculated the rate of change of the velocity magnitude from the velocity and acceleration components coordinated in the inertial axes. The velocity coordinates in inertial axes were obtained from the estimator and the acceleration components in inertial axes were were calculated by transforming the acceleration measured in body axes, corrected for gravity, to inertial axes. This equation, obtained in a similar fashion as the second method, is expressed mathematically as

$$\dot{\overline{v}} = \frac{1}{\overline{v}} \left(v_N \dot{v}_N + v_E \dot{v}_E + v_D \dot{v}_D \right) \tag{8.8}$$

where

$$\begin{bmatrix} \dot{v}_N \\ \dot{v}_E \\ \dot{v}_D \end{bmatrix} = \mathrm{DCM}_{b \to i} \begin{bmatrix} a_{x_{-g}} \\ a_{y_{-g}} \\ a_{z_{-g}} \end{bmatrix} \tag{8.9}$$

Both the *Sensor Data* measurements and *Estimator Data* measurements look identical to the second method as expected. The same spikes caused by the GPS updates are also present here. A sample of captured data is shown in Figure 8.3.

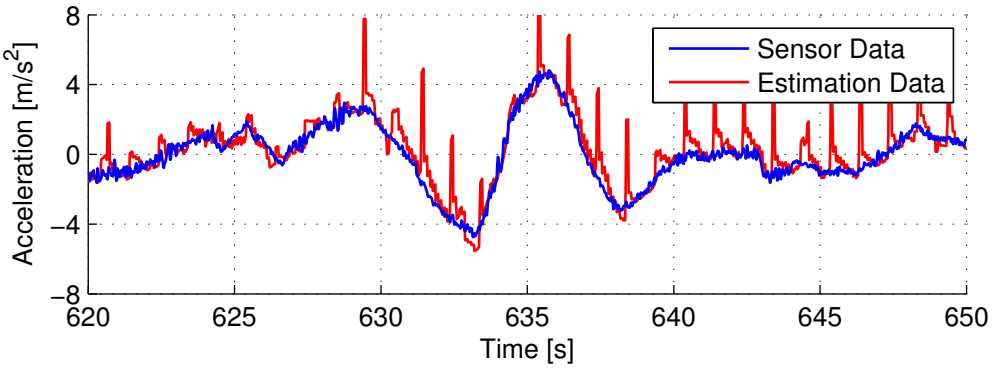

Figure 8.3: Acceleration source test using the third method.

The fourth method calculated the rate of change of the velocity magnitude by numerically differentiating the airspeed measured by the airspeed sensor, or by numerically differentiating the magnitude of the velocity obtained from the estimator. This is expressed mathematically as

$$\dot{\overline{v}} = \frac{1}{T_s}\left(\overline{v}[k] - \overline{v}[k-1]\right) \tag{8.10}$$

$$\overline{v} = \sqrt{v_N^2 + v_E^2 + v_D^2} \tag{8.11}$$

The acceleration calculated by differentiating the airspeed measurement was found to be slightly smaller than the versions calculated with the previous three methods that used the acceleration measurements from the inertial sensors. The reason may be that the airspeed sensor reports a lower airspeed than the actual airspeed, causing the time derivative to also be smaller. The estimator data proved to be totally unusable for this method. The held variables between GPS updates caused constant spikes throughout the flight as the previous measurement and current measurement were often equal, causing a zero derivative. A sample of captured data is shown in Figure 8.4.

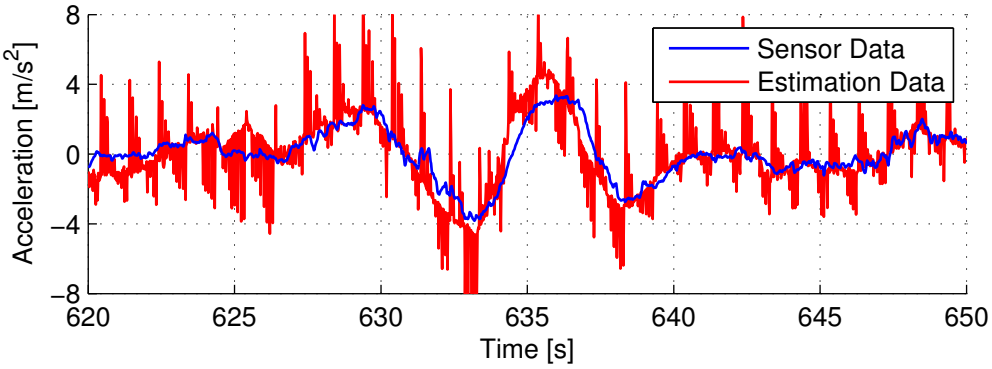

Figure 8.4: Acceleration source test using the fourth method.

These methods were also tested in HIL simulations where they were evaluated against a true simulated acceleration measurement. Since the first method produced acceptable results and was also the simplest method, it was chosen as the method for calculating the acceleration in the flight software. The HIL verification also showed that another good candidate would

have been the numerical differentiation of the airspeed measurement from the pitot sensor as its readings were similar to the true measurements, although it was found that this method resulted in larger deviations when the aircraft performed turns.

8.2.2 Longitudinal Controllers

The NSA Controller was only tested for regulation as giving a constant acceleration step causes the aircraft to pitch up rapidly. As shown in Figure 8.5, the controller appears to follow the 0.3s rise time as per its design. The settling time is difficult to clearly observe, but is estimated to be close to the 0.95s design.

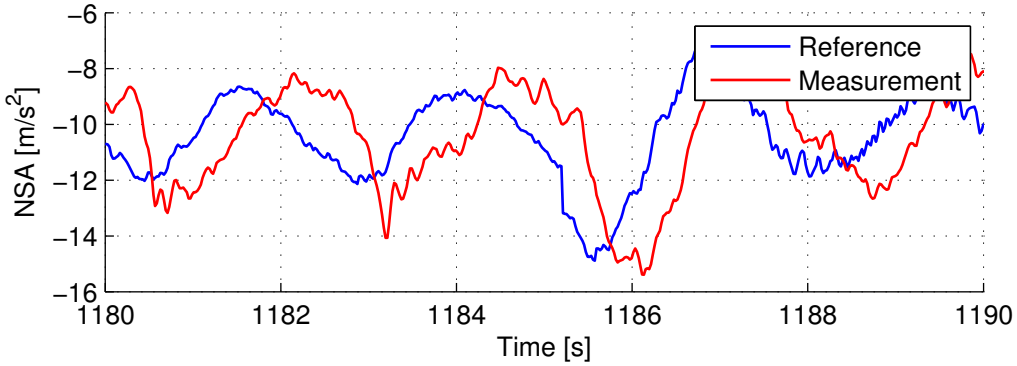

Figure 8.5: NSA regulation during a flight test.

The Energy Distribution Controller was only tested for regulation as the outer loops were given reference signals instead. As shown in Figure 8.6, the controller appears to follow the reference signal with a peak time of approximately 2.5s, although the true value is difficult to observe. This value lies between the Matlab design and the HIL simulations, making it within the expected range of deviation due to small modelling errors and gain tuning.

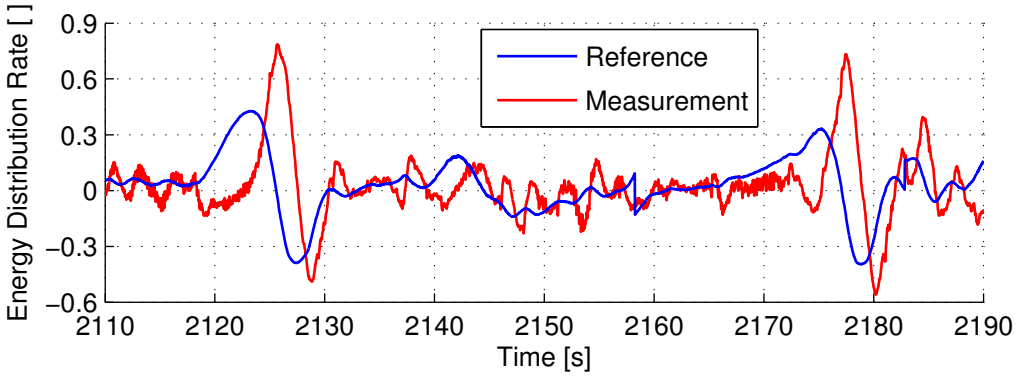

Figure 8.6: Energy distribution regulation during a flight test.

The Specific Energy Controller was only tested for regulation as the outer loops were given reference signals instead. As shown in Figure 8.7, the controller appears to follow the reference signal very well with a rise time and settling time of approximately 1s and 4s, respectively. This is very similar to both the Matlab design and the HIL simulations, further validating the TECS simplification of this loop during the design phase.

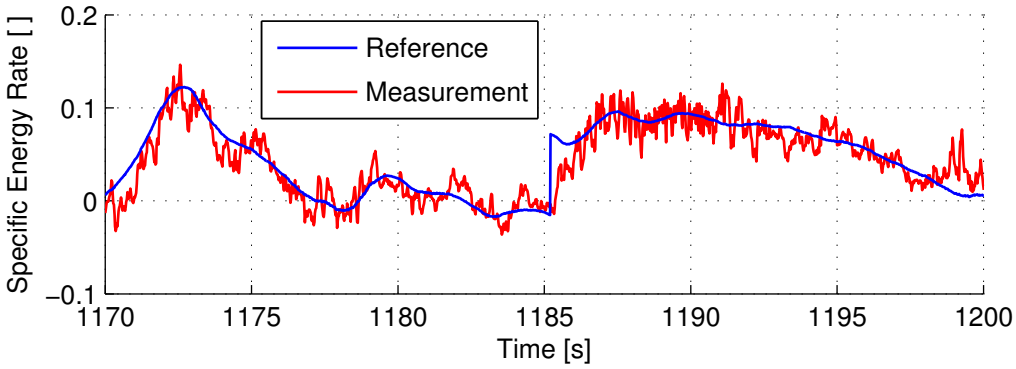

Figure 8.7: Specific energy regulation during a flight test.

The Flight Path Angle Controller was tested for both regulation and step commands. As shown in Figure 8.8, the controller appears to regulate the flight path angle to within ±3°. This is significantly worse than the simulation results and may not be adequate to achieve an accurate landing. As shown in Figure 8.9, the controller seems to have a rise time similar to the 1.5s found in simulation. Additionally, it seems that the settling time may also be close to the simulated 6s, although this is very difficult to observe due to the large continuous oscillations.

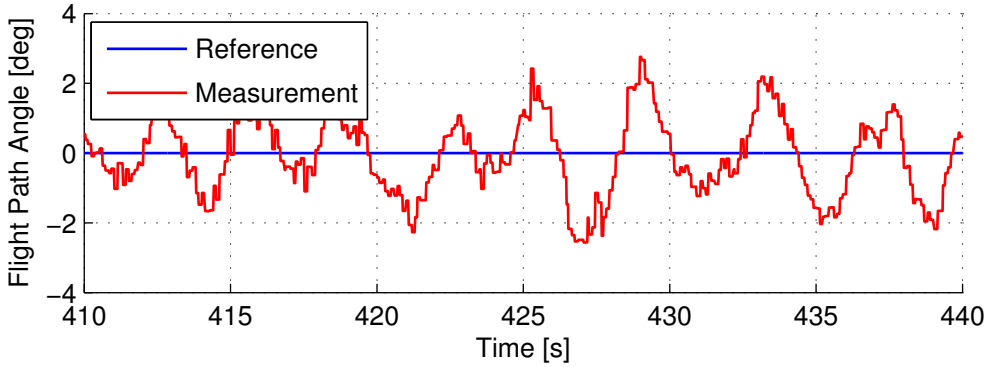

Figure 8.8: Flight path angle regulation during a flight test.

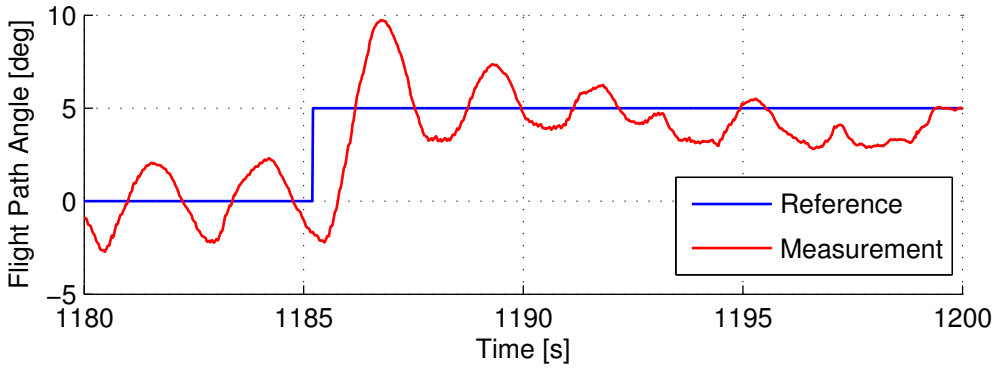

Figure 8.9: Flight path angle step response during a flight test.

The Airspeed Controller was tested for both regulation and step commands. As shown in Figure 8.10, the controller appears to regulate the airspeed, although it also performed significantly worse in practice than in simulation. Regulation was often within ±3m/s, depending

on how the aircraft was manoeuvred, which is considered inadequate for a safe landing. The response shows that the aircraft reached the reference speed after approximately 4s. Although this is close to the simulated 5s, it is unclear if this response was influenced due to an already increasing trend in airspeed. The sudden reduction in airspeed could be caused by the aircraft performing a sharp roll, indicating that the control system is still heavily influenced by the coupling lateral dynamics in this attitude.

The acceleration regulation is shown in Figure 8.11. It is observed that the system responds rapidly to the reference signal. From the given response it is expected that, if the system was given a constant step command, it would have settled in approximately 2.5s as in the simulations.

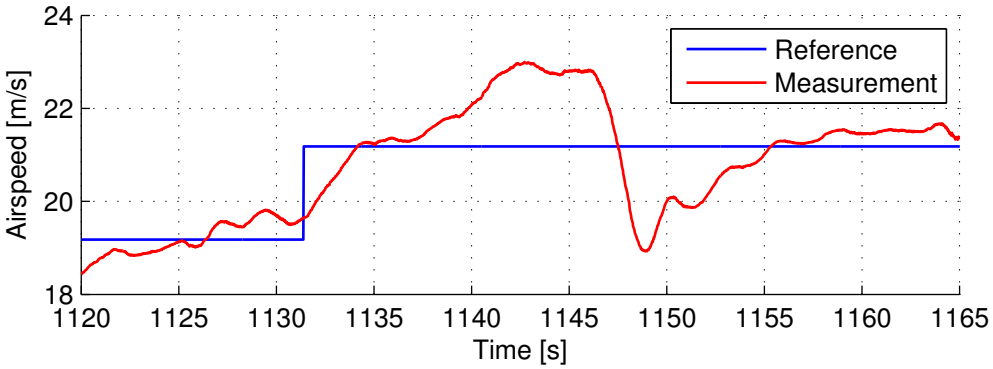

Figure 8.10: Airspeed step response during a flight test.

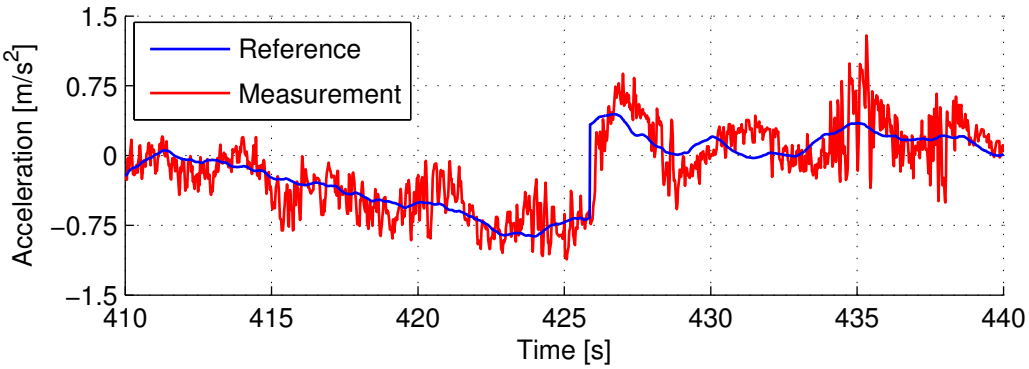

Figure 8.11: Acceleration regulation during a flight test.

The TECS simplification does seem to hold some validity. The poor performance may be due to its reliance on acceleration measurements. Even though the IMU used is well rated, the OBC may have been insufficiently isolated from vibrations. The measurements provided by the IMU are passed through a low pass filter, which was set up during previous projects, before it is sampled and logged by the OBC. Since the previous projects did not require high accuracy acceleration feedback for airspeed control, the filter pass frequency may be set too low for this project. If the noise was of a high enough amplitude and fast enough frequency, the measurements provided may not truly represent the acceleration experienced by the aircraft, resulting in poor controller performance.

8.2.3 Lateral Controllers

The Dutch Roll Damper was tested for regulation by supplying doublets to the rudder in order to cause yaw rate perturbations. An example of this doublet set is shown in Figure 8.12, where it is clearly visible between 341s and 345s as the rudder servo reaches the deflection limits. The large nonzero steady state position is caused by the actuator calibration which compensates for the offset in rudder servo motor installation. As shown in Figure 8.13, the controller sufficiently damps the oscillations after about 1.5s, which is slightly faster than in simulation. This is likely due to the safety pilot flying faster than the designed airspeed, causing the aircraft to have increased natural yaw rate damping.

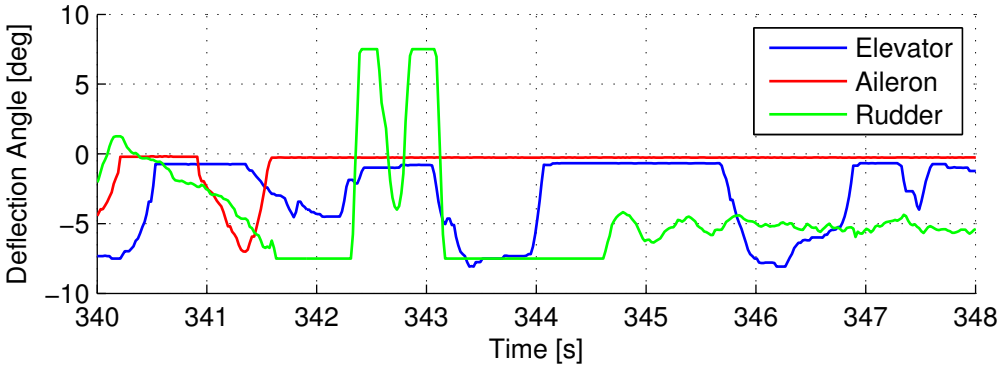

Figure 8.12: Control surface deflections during the Dutch Roll Damper flight test.

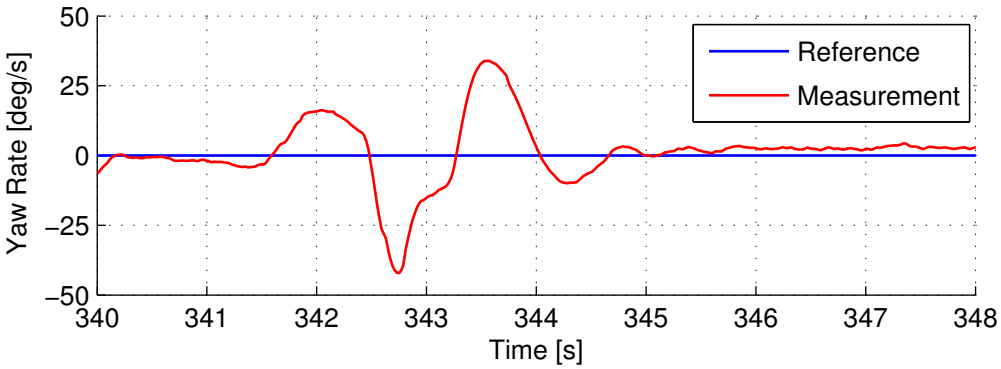

Figure 8.13: Yaw rate regulation during the Dutch Roll Damper flight test.

The Roll Angle Controller was tested for both regulation and step commands. As shown in Figure 8.14, the controller response shows an initial peak after 1s, another peak after approximately 6s, and settling after about 10s, which is behaviour extremely similar to that of the simulations. The overall regulation was considered very good as the roll angle remained within approximately $\pm 3°$.

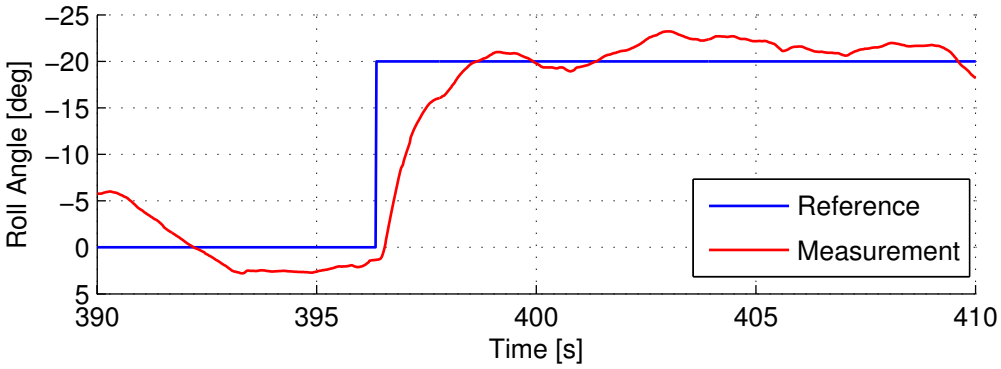

Figure 8.14: Roll angle step response during a flight test.

8.2.4 Crash

During a flight test in which it was scheduled to test the lateral controllers and attempt a runway landing, control of the aircraft was lost and it dived into the ground. The aircraft sustained irreparable damage and the flight testing phase of the project was stopped and subsequently terminated. The exact cause of the crash is unknown as OBC logging data was corrupted and therefore irretrievable. It is suspected that the servo board delayed RC signals to the OBC.

The safety pilot reported sluggish behaviour, although it seemed mostly solved after switching the RC to a more aggressive mode. During the previous flight, it was found that the GPS was reporting data at a rate as low as 0.03Hz. This may have caused the aircraft to believe that it was flying at a higher altitude than the reference command, resulting in the controllers commanding a dive. When the safety pilot took over control of the aircraft, the manual override signal was delayed and full control of the vehicle was granted too late. From the GCS logs, it was found that the pilot did gain control of the aircraft and tried to pull up, but being only a few metres above the ground at that point, it would have been impossible to prevent the crash.

Since the project was at such a late stage and that the cost and time to build a new vehicle was significant, it was decided to cancel further flight testing. It should be noted that the loss of aircraft was not due to the designed control systems, but rather a series of unfortunate events coupled with an elusive software bug as similar events have happened in other projects.

8.3 Summary

This chapter briefly discussed the procedure and integration regarding the flight test setup. Results for selected flight tests were presented. It was shown that the TECS design simplification has merit, although the controllers performed worse in practice than in simulations. This is possibly due to the control system being very reliant on acceleration feedback, which was problematic to accurately measure and could be susceptible to vibrations. The lateral controllers tested reflected the behaviour found in simulation and was therefore verified. The aircraft eventually crashed due to a problem outside of user control and flight testing was terminated. Given the practical results, it is unlikely that the aircraft would have been able to perform an accurate moving platform landing, although a runway landing was feasible.

§ 9

Conclusions

This chapter provides a summary of the work completed, evaluates the project and gives recommendations for future work.

Section 9.1 provides a summary of the work completed for the project. Section 9.2 evaluates the project as a whole and indicates which objectives were achieved and which were left incomplete. Section 9.3 gives recommendations for future projects.

9.1 Summary of Work Completed

This project commenced with a brief investigation into what work has been accomplished in the field of autonomous aircraft landings, especially those that considered moving platform landings and usage of the TECS architecture. It was concluded that many of the methods were quite complex, therefore a simplified approach was preferred.

The physical aircraft and electronics were investigated throughout the project and continuous incremental upgrades were proposed and implemented. This improved general maintainability and allowed focus to be put on other challenges.

An autonomous landing strategy was developed based on the procedures that real pilots follow to achieve a moving platform landing. The strategy scaled values from an actual aircraft to that of the RC model to obtain a set of targets that was deemed realistic. These targets include the parameters such as landing area size, aircraft velocities and environmental influences.

A mathematical dynamic model of the aircraft was presented based on previous work performed in the research environment. These models were linearised and represented in state-space form to be used as the basis for the control design. The wind model that was used in previous projects was expanded to conform to military standards and implemented for use in simulations.

Controllers for the longitudinal and lateral modes of motions were developed. The longitudinal controller focused on the TECS for which a simplification, design methodology and subsequent design were presented. The lateral controllers were based on classical control methods, although an augmentation was proposed and implemented to increase the aggressiveness of the response and improve the steady state tracking. Additionally, a switching scheme be-

tween the new aggressive and classical controllers was proposed and implemented to improve the navigation path transient.

The controllers were initially developed and tested in a SIL environment. It was attempted to merge the code-base to accommodate both software and hardware simulations. Insights into the controllers gave rise to further augmentation of the architecture. The controllers were subsequently implemented in firmware and tested in a HIL environment where it was found that the TECS controllers did not significantly deviate from the designs, validating the TECS simplification and design methodology, and that the lateral controllers generally performed as designed. A Monte Carlo testing approach was performed to evaluate the landing performance consistency under different conditions, which concluded that the autonomous landing system should be able to land on a moving platform 86% of the time.

Flight tests were conducted to test the performance of selected longitudinal and lateral controllers. It was shown that the TECS design simplification has merit, although the controllers performed worse in practice than in simulations, likely due to the system being insufficiently isolated from vibrations which caused noisy acceleration measurements upon which the controller is very reliant. The lateral controllers tested reflected the behaviour found in simulation and were therefore verified. A brief analysis was conducted into a system failure that caused the aircraft to crash and terminate the practical flight testing phase.

9.2 Project Evaluation

The project set out to develop a control system for a UAV and enable autonomous landing onto a moving platform. The longitudinal controllers were to be based on the TECS in an attempt to achieve superior flight control performance. The lateral controllers would be designed for more aggressive behaviour to improve landing accuracy.

The designed longitudinal controllers proved to be very successful in simulation. The simplified TECS design method were reasonably verified by the simulation results. It was found that the controller is sensitive to gain values, a problem highlighted by other researchers who used the same architecture. Flight tests showed that the controllers performed significantly more poorly than in simulation. It was suggested that the acceleration measurements, on which TECS is very reliant, could be the cause of the degraded performance as the IMU was not sufficiently isolated from vibration. The lateral controllers proved to perform as designed in both simulations and in flight tests. Unfortunately, not all controllers could be tested in practice due to electronic failures.

The Monte Carlo approach landing simulations yielded fairly good results. It was found that the system could accurately land on a stationary target 84% of the time while the moving target accuracy improved to 86% under various environmental conditions. This accuracy would possibly improve if the aircraft was allowed more time and distance to settle onto the landing glide path reference. It was found that most deviations came from the longitudinal controllers that had a persistent transient. The longitudinal accuracy was often degraded by transients

from the lateral controllers which caused the dynamics to couple. The lateral accuracy was found to be exceptional under all circumstances. Overall, the goal of designing an autonomous landing system for a moving platform was reached in simulation, although it is unlikely that the system would have been able to achieve this in practice in its current state.

9.3 Recommendations

From a theoretical point of view, the following recommendations are suggested:

1. Data from the safety pilot should be captured and ran through the simulation model in order to verify it. For this project, the foundation projects were trusted for accuracy in this regard.

2. For a solid landing surface, the ground effect should be investigated. This will likely have an influence on landing accuracy and should be taken into account to calculate the glide slope reference.

3. An acceleration model should be set up for the platform by propagating white noise though an appropriate forming filter. The platform can then be more accurately represented and simulated in the HIL environment.

4. An additional carrier or wake model should be included to simulate the wind disturbances caused by the motion of the platform itself to create a more representative model.

5. The nonlinear guidance method as proposed by [24] could be augmented with an integrator to allow for better steady state tracking. The original controller can also replace the Heading and Guidance Controller loops to retain a gentle, yet faster lateral response.

6. The Roll Rate Controller as implemented by [16] showed more design flexibility and a more desired response. It is suggested that this controller be used as an inner loop to the Roll Angle Controller.

7. The NSA inner loop should be included into the TECS design. This will likely allow better matching of the time constants of the Specific Energy Controller and the Energy Distribution Controller.

8. A method to reduce airspeed and flight path angle coupling for the TECS is proposed by [30]. It uses a feedback loop based on an energy cooperation error to reduce the oscillations caused by the differences in dynamics between the total energy path and the energy distribution path. The TECS design presented in this project also did not fully conform to the equal time constant specification, which may have exacerbated flight path angle and airspeed oscillations.

9. The TECS inner loops should be more thoroughly tested by giving the loops separate command signals and evaluating the response of the other. This may indicate why the loops did not fully respond as expected and where modelling simplifications can be improved.

10. Additional wind disturbance tests should be performed to include varying speeds and more severity levels. This would increase confidence in the ability of the system to reject disturbances.

11. The Cross-Track Controller settles on a nonzero angle of sideslip during crosswind landings. An additional controller should be designed and implemented to facilitate decrabbing before touchdown or heading corrections after touchdown.

From a practical point of view, the following recommendations are suggested:

1. The NovAtel system used caused major setbacks throughout the project and likely played a role in the eventual failure of the system. It is suggested that the unit be replaced or further investigated into why it often failed to function properly as this is abnormal behaviour.

2. Even though the DGPS can provide high accuracy measurements, it is suggested that ultrasonic sensors are used during the final stages of landing. They can be sampled at a faster rate at the time when altitude is critical to achieve accuracy.

3. The IMU used should not be calibrated for temperature as it is already sufficiently factory calibrated. Further calibration may cause erroneous samples. Additionally, every effort should be made to mount the IMU in such a way that it is isolated from vibration as the TECS is very reliant on accurate acceleration measurements. Furthermore, additional filtering of the IMU measurements can be attempted, although this may slow down the controller response.

4. The analogue control surface servo motors should be replaced with digital units. These provide much more accuracy and robustness as the flex on the analogue units were often equal to the deflection limits.

5. RF communication should be moved to a different frequency as there is too much interference in the 2.4GHz band. Additionally, the telemetry packets should not be staggered at 0.5s, 1s and 2s as this causes a large cluster of packets to be sent every 2s. These transmissions should be spread out more evenly over the transmission period.

6. The logging system should be improved in order to read OBC logs more reliably, especially in the event that the OBC could not be shut down safely.

7. The main motor power should be more thoroughly investigated and characteristic thrust curves should be set up. Currently, the thrust is assumed to be on a linear scale, which is likely to be a false assumption. Additionally, the available RPM/thrust should be scaled with the current battery voltage supplied to the motor.

8. The intended landing platform would likely have been too small to allow for a sufficient margin of safety. It is suggested that a longer platform be used in order to compensate for longitudinal landing inaccuracy which will remain a problem regardless of the controllers used due to the shallow landing angles involved.

9. An entire redesign and rewrite of the GCS, avionics and SIL/HIL system is recommended. Although the work up to this project has been fairly well done, very few quality control measures have been enforced. This caused deviations in the different projects, resulting in a disconnect between the subsystems. A redesign could increase integration between modern hardware and software design components and principles, resulting in an improved overall quality of work and performance.

Appendix A

Mathematical Derivations

This chapter provides details of mathematical derivations performed during the project.

A.1 Heading Update Low-Pass Filter

The heading angle of the platform is continuously uploaded from the GCS to the OBC, but is filtered to reduce the variations in the positions of the waypoints generated based on the varying heading angle. The filter is derived from the Laplace unity gain low-pass filter equation

$$Y(s) = \frac{1}{\tau s + 1} X(s) \tag{A.1}$$

where $Y(s)$ is the filter output, τ is the time constant and $X(s)$ is the filter input. Using the bilinear transform substitution

$$s = \frac{2}{T} \frac{z-1}{z+1} \tag{A.2}$$

where T is the sample time on Equation A.1, we obtain

$$\begin{aligned} Y(z) &= \frac{1}{\frac{2\tau}{T}\frac{z-1}{z+1} + 1} X(z) \\ &= \frac{1 + z^{-1}}{\frac{2\tau}{T} + 1} X(z) + \frac{\frac{2\tau}{T} - 1}{\frac{2\tau}{T} + 1} Y(z) z^{-1} \end{aligned}$$

The substitution for discrete-space is

$$z^n = k + n \tag{A.3}$$

which can be substituted into Equation A.3 to obtain

$$y[k] = \alpha \left(x[k] + x[k-1] \right) + \beta y[k-1] \tag{A.4}$$

where α and β are filter constants

$$\alpha = \frac{T}{2\tau + T} \tag{A.5}$$

$$\beta = \frac{2\tau - T}{2\tau + T} \tag{A.6}$$

$$\tag{A.7}$$

The 2D heading velocity, stored in $x[k]$ is polled from the GPS base station and subsequently moved to $x[k-1]$ with a new update.

A.2 Acceleration from the Time Derivative of Velocity

For a velocity in the body axes, the total magnitude is the square root of the sum of the squares of its components. This is expressed mathematically as

$$\overline{v} = \sqrt{u^2 + v^2 + w^2} \tag{A.8}$$

$$= \left(u^2 + v^2 + w^2\right)^{\frac{1}{2}} \tag{A.9}$$

where $\overline{v}$ is the total velocity magnitude and u, v and w are the X-, Y- and Z-axis components, respectively. The acceleration is the time derivative of the velocity which is given by

$$\dot{\overline{v}} = \frac{\mathrm{d}}{\mathrm{d}t}\overline{v} \tag{A.10}$$

$$= \frac{\mathrm{d}}{\mathrm{d}t}\left(u^2 + v^2 + w^2\right)^{\frac{1}{2}} \tag{A.11}$$

Following the chain rule, this can be differentiated to give

$$\dot{\overline{v}} = \frac{1}{2}\left(u^2 + v^2 + w^2\right)^{-\frac{1}{2}} \frac{\mathrm{d}}{\mathrm{d}t}\left(u^2 + v^2 + w^2\right) \tag{A.12}$$

$$= \frac{1}{2\left(u^2 + v^2 + w^2\right)^{\frac{1}{2}}} \frac{\mathrm{d}}{\mathrm{d}t}\left(u^2 + v^2 + w^2\right) \tag{A.13}$$

$$= \frac{1}{2\overline{v}} \frac{\mathrm{d}}{\mathrm{d}t}\left(u^2 + v^2 + w^2\right) \tag{A.14}$$

Following the chain rule again, this can be differentiated to give

$$\dot{\overline{v}} = \frac{1}{2\overline{v}}\left(2u\dot{u} + 2v\dot{v} + 2w\dot{w}\right) \tag{A.15}$$

$$= \frac{1}{\overline{v}}\left(u\dot{u} + v\dot{v} + w\dot{w}\right) \tag{A.16}$$

Appendix B

Software

This chapter discusses updates applied to the existing software used in this project.

B.1 Telemetry

The telemetry packets were sent and received over two paired MaxStream 24XStream wireless modules configured to operate at 9600 baud, resulting in a theoretical maximum transfer rate of 1200 bytes per second. The following needs to be taken into consideration:

1. packets may fail due to interference, which can cause resending of lost packets; and
2. transfer of packets is bidirectional.

This means that we can realistically only transfer a maximum of about 600 bytes per second.

After a multitude of tests, it was found that packet loss occurs too often, causing the aircraft to not respond to commands uploaded from the GCS. The number of packets was reduced to the numbers shown in Table B.1.

Table B.1: Size of down-packets after telemetry data reduction.

Set	Start Bits	Data	End Bits	Rate (Hz)	Total	(bytes/sec)
OBC Primary	3	3	2	2	8	16
Estimator	3	18	2	1	23	23
IMU	3	13	2	1	18	18
Control Primary	3	39	2	1	44	44
Control Secondary	3	38	2	1	43	43
Actuators	3	35	2	0.5	40	20
Magnetometers	3	6	2	0.5	11	6
Pressure	3	6	2	0.5	11	6
GPS	3	56	2	0.5	61	32
OBC Secondary	3	7	2	0.5	12	6
Totals:					271	214

The GPS operating in differential mode also consistently transmits and receives packets at 990 bits/sec, or 120 bytes/sec, which totals to 240 bytes/sec. Packets are staged to be sent

every 0.5, 1.0 and 2.0 seconds, which means that every 2 seconds, all packets are staged for sending. This was considered a very poor design decision. Together with all the GPS data, this worst case scenario brings the total number of packets to 511 bytes/sec. Intermittent command uploads are ignored for this evaluation. This is just under half of the theoretical maximum, which should be adequate.

Even though the reduction in packets transmitted and received reduced the number of failed packets, the general communication still performed very poorly even when within line of sight, but especially when the aircraft was far away (over 200m). Possible reasons for this may include that:

1. the units may have been damaged due to improper use (e.g. not using an antenna to attenuate the signal);
2. command uploads were not optimised to the size of a `short int`, but rather transmitted as a much larger `float`, which could become corrupted more easily; and
3. high interference levels at the airfield.

B.2 QtGLEngine

The QtGLEngine is a visualisation tool developed by former students during previous projects using the Qt4 framework and 3DS models. It receives six degrees of freedom information over Ethernet from an in-house developed Simulink block. This information is useful because the behaviour of the aircraft can be inspected and judgements can be made on visual perceptions, e.g. a visual representation shows the aggressiveness of a roll angle manoeuvre better than a Matlab plot. It is also useful to manually fly the aircraft during HIL simulations and testing.

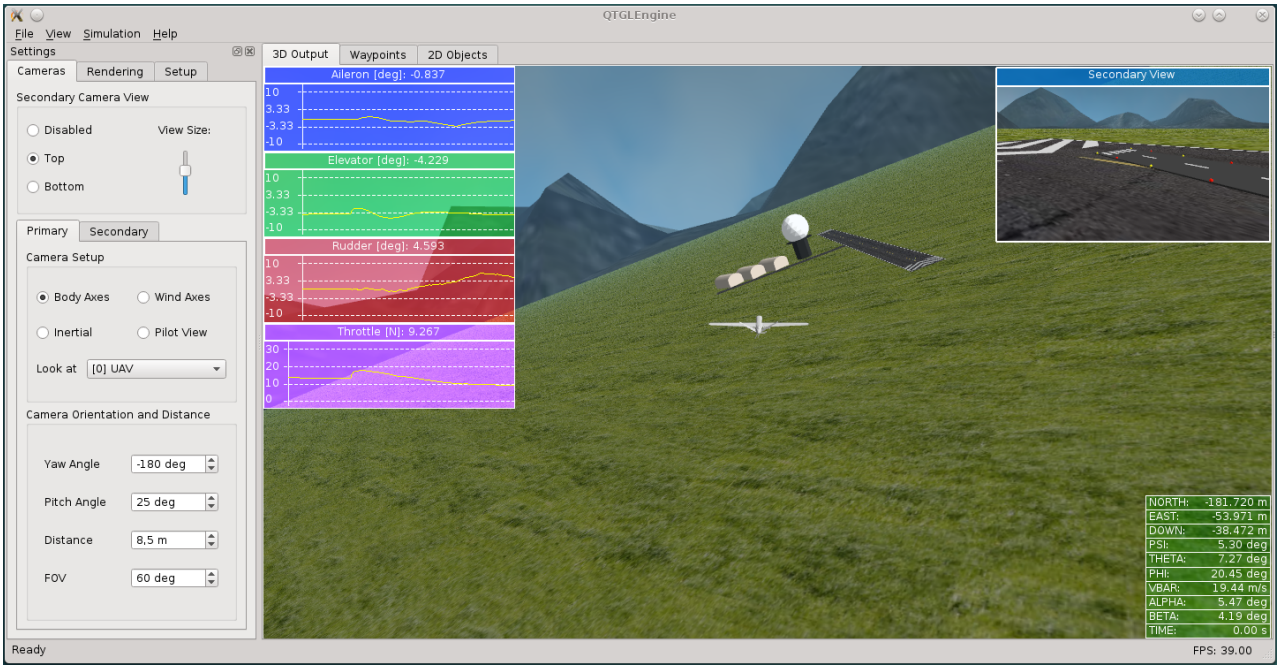

Figure B.1: QtGLEngine running a HIL simulation.

B.3 Ground Control Station

The GCS was written by former students and adapted as the different projects matured, all using the Qt4 framework. The new students have to integrate their work and adapt the system to transmit, receive and display additional data relevant to their own project. In most control system projects, the *Controller* tab is replaced to only show information applicable to that project. The following images show the new subtabs added to the system.

Figure B.2 shows the controller structure for both longitudinal and lateral controllers. The different signal values are highlighted to indicate near-limit or saturated values. This tab is not very useful during practical tests as it is too difficult to differentiate the important information. It is however very useful during HIL simulations to quickly grasp the behaviour of the aircraft when given new commands or investigating the effect of disturbances.

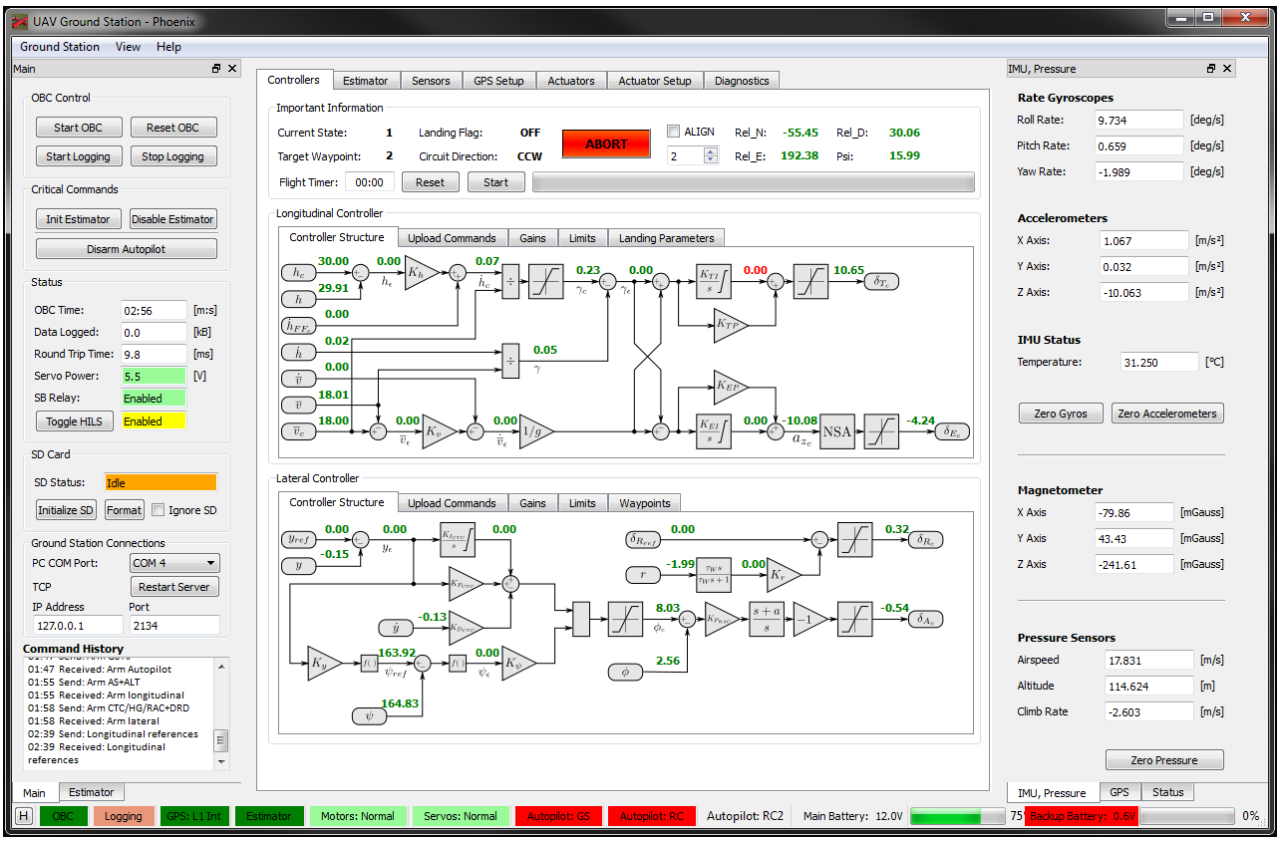

Figure B.2: *Controller Structure* tab in the GCS.

Figure B.2 shows the command fields that can be uploaded for both longitudinal and lateral controllers. This is the tab most often used during practical tests and therefore also include the current measurements so that they can be tracked more easily. New references can be uploaded either as increments (steps) or as a batch to give multiple new references at the same time. New longitudinal and lateral references can not be sent at the same time but rather in succession. The armed state of the different controllers is also indicated by colour to quickly learn the current status.

Figure B.4 shows the controller gains that can be uploaded for both longitudinal and lateral controllers. When a new set is uploaded, it is also immediately requested for download so that

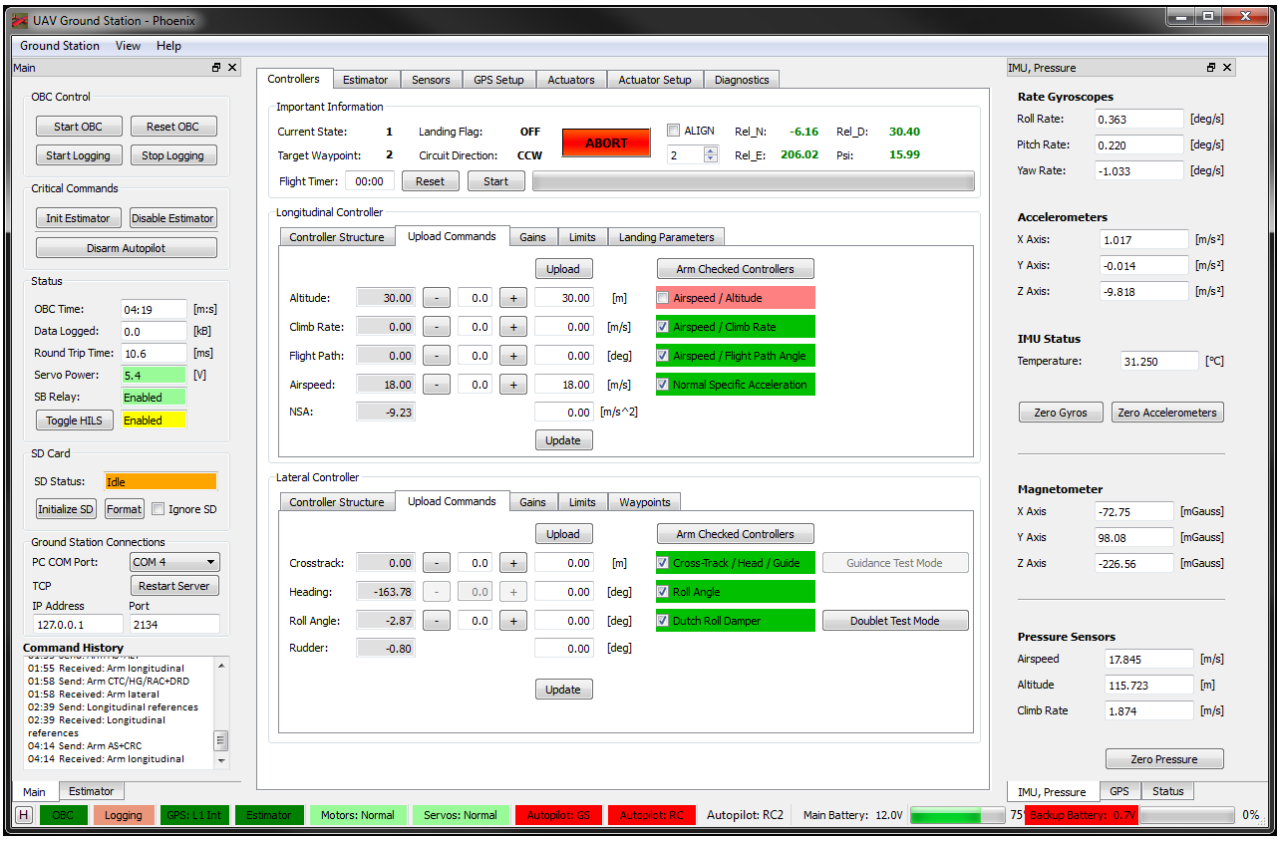

Figure B.3: *Upload Commands* tab in the GCS.

the user can verify that it uploaded correctly. This tab was generally not used during practical flights at it required sending too many floating point numbers, which was difficult due to RF communication issues. It was however useful during HIL simulations for fine-tuning the system. During flight tests, the recommended procedure was to first land the aircraft manually, upload the commands, take off again and re/arm in flight to ensure that the new values are uploaded correctly.

Figure B.5 shows the controller and command limits that can be uploaded for both longitudinal and lateral controllers. When a new set is uploaded, it is also immediately requested for download so that the user can verify that it uploaded correctly. This tab was generally not used during practical flights at it required sending too many floating point numbers, which was difficult due to RF communication issues. It was however useful during HIL simulations for fine-tuning the system. During flight tests, the recommended procedure was to first land the aircraft manually, upload the commands, take off again and re-arm in flight to ensure that the new values are uploaded correctly.

Figure B.6 shows the landing parameters and waypoints that can be uploaded to the longitudinal and lateral controllers, respectively. For the longitudinal controller, it is used to set different landing offsets for the DGPS, landing angles and activation of the landing state machine. For the lateral controller, it is used to set they waypoints in runway coordinates (transformed on the OBC), the target waypoint, the circuit direction, runway heading and the waypoint look-ahead distance. The look-ahead distance feature was removed in favour of a dynamic look-ahead dependant on flight speed.

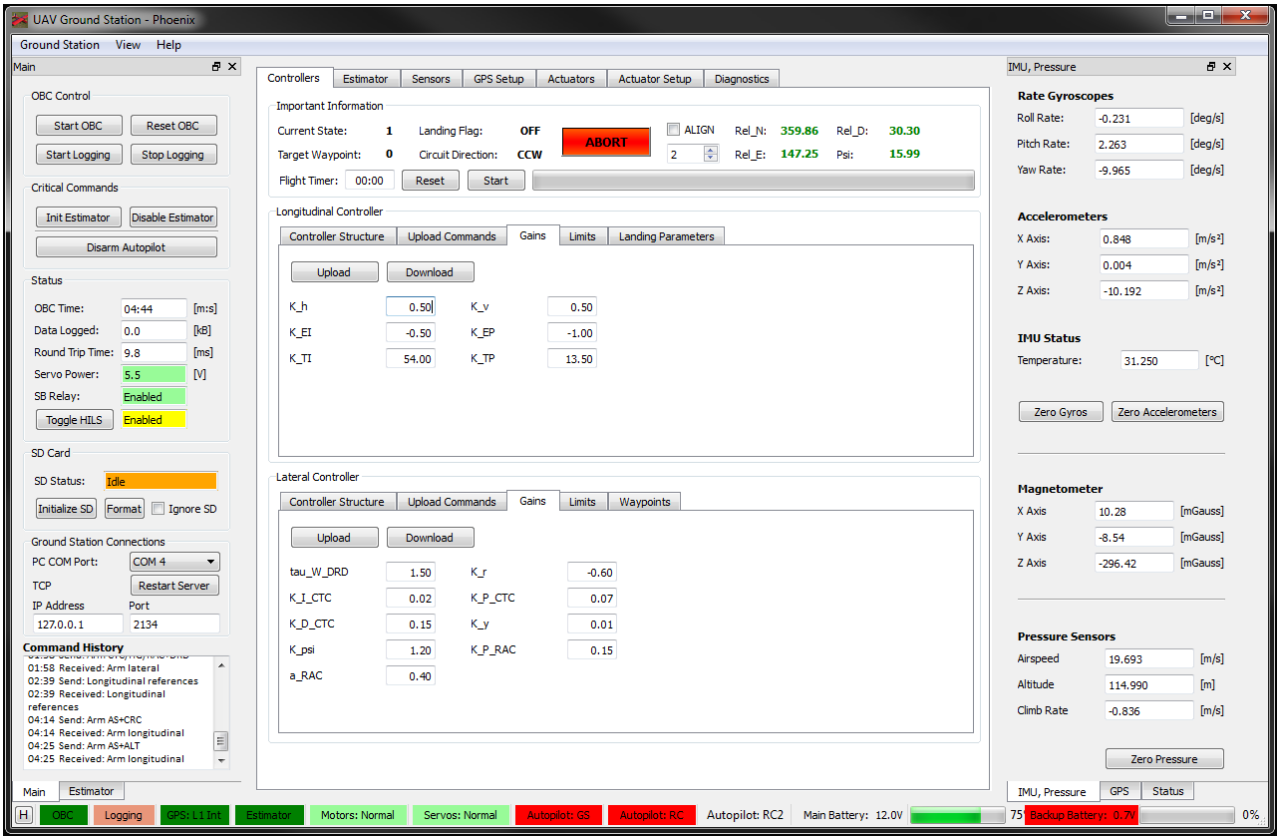

Figure B.4: *Gains* tab in the GCS.

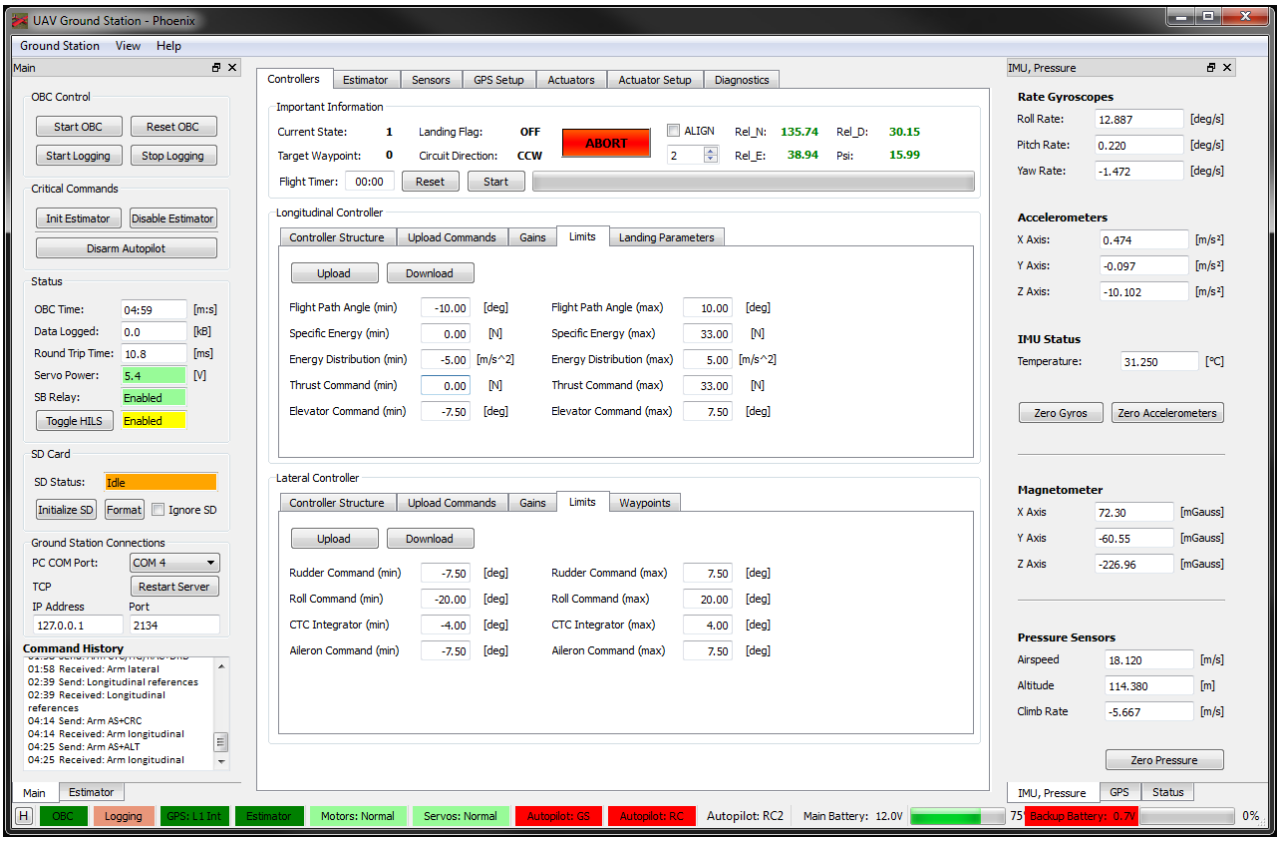

Figure B.5: *Limits* tab in the GCS.

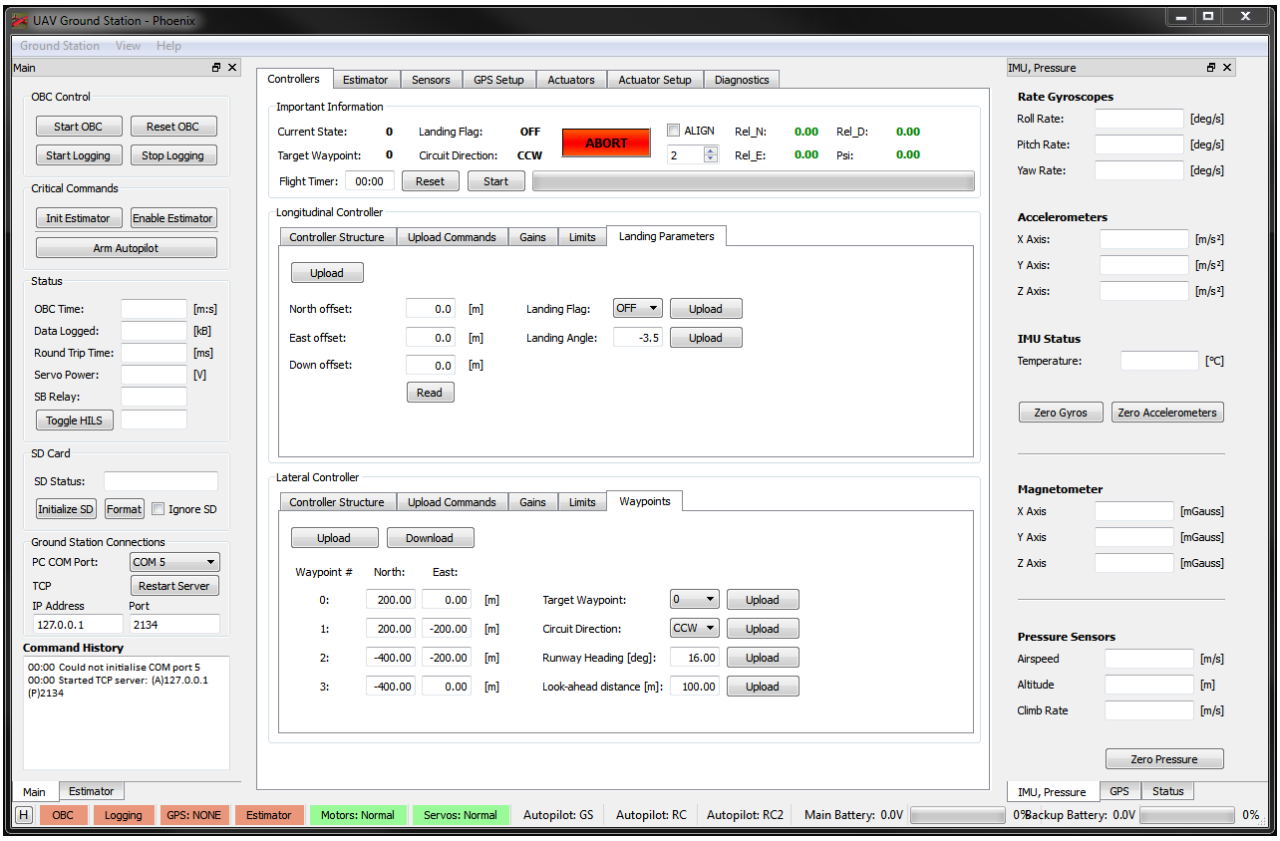

Figure B.6: *Landing Parameters* and *Waypoints* tabs in the GCS.

Above all the tabs, a special information section was added to indicate important state changes on the aircraft. This includes that state of the landing state machine, circuit direction and target waypoint. It also shows the relative offset and activation for the NovAtel ALIGN mode as well as an abort button which would immediately pull the aircraft out of the landing sequence when pressed.

Appendix C

System Parameters

This chapter lists all the physical parameters of the aircraft.

C.1 Aircraft Dimensions, Mass & Inertia

The following dimension-related coefficients were used:

$$\bar{c} = 0.37 \tag{C.1}$$

$$b = 1.918 \tag{C.2}$$

$$S = 0.677 \tag{C.3}$$

$$A = 5.184 \tag{C.4}$$

where $\bar{c}$ is the mean aerodynamic chord, b is the wingspan, S is the wing area, and A is the wing aspect ratio. The mass of the individual parts of the aircraft is given in Table C.1.

Table C.1: Mass of the individual parts of the aircraft.

Part	**Mass [g]**
Frame	3545 + 290 weights
Left wing	625 + 30 weights
Right wing	715
Motor battery	640
OBC battery	145
Backup battery	100
Strut	120
Total	6110

The total mass of the aircraft is thus given by

$$m = 6.11 \tag{C.5}$$

which is a 3.8% reduction from [16]. The inertia of the aircraft is given by

$$\boldsymbol{I} = \begin{bmatrix} I_{xx} & 0 & 0 \\ 0 & I_{yy} & 0 \\ 0 & 0 & I_{zz} \end{bmatrix} \tag{C.6}$$

where

$$I_{xx} = 0.722 \tag{C.7}$$
$$I_{yy} = 0.514 \tag{C.8}$$
$$I_{zz} = 0.925 \tag{C.9}$$

C.2 Thrust Coefficients

The following thrust-related coefficient was used:

$$\tau = 0.25 \tag{C.10}$$

where τ is the motor time-constant.

C.3 Natural Coefficients

The following natural coefficients were used:

$$g = 9.81 \tag{C.11}$$
$$\rho = 1.225 \tag{C.12}$$
$$e = 0.85 \tag{C.13}$$

where g is the gravitational constant, ρ is the air density, and e is the Oswald efficiency factor.

C.4 Aerodynamic Coefficients

The following aerodynamic coefficients were used:

$$C_{D_0} = 0.08 \tag{C.14}$$
$$C_{L_0} = 0.00 \tag{C.15}$$
$$C_{L_\alpha} = 4.808411 \tag{C.16}$$
$$C_{L_Q} = 7.812170 \tag{C.17}$$
$$C_{L_{\delta_E}} = 0.456085 \tag{C.18}$$
$$C_{m_0} = 0.00 \tag{C.19}$$

$$C_{m_\alpha} = -0.664939 \tag{C.20}$$
$$C_{m_Q} = -7.438796 \tag{C.21}$$
$$C_{m_{\delta_E}} = -0.957351 \tag{C.22}$$
$$C_{Y_\beta} = -0.167475 \tag{C.23}$$
$$C_{Y_P} = 0.137007 \tag{C.24}$$
$$C_{Y_R} = 0.113738 \tag{C.25}$$
$$C_{Y_{\delta_A}} = 0.003319 \tag{C.26}$$
$$C_{Y_{\delta_R}} = 0.093545 \tag{C.27}$$
$$C_{l_\beta} = -0.062813 \tag{C.28}$$
$$C_{l_P} = -0.429110 \tag{C.29}$$
$$C_{l_R} = 0.141714 \tag{C.30}$$
$$C_{l_{\delta_A}} = -0.264734 \tag{C.31}$$
$$C_{l_{\delta_R}} = 0.002171 \tag{C.32}$$
$$C_{n_\beta} = 0.058436 \tag{C.33}$$
$$C_{n_P} = -0.030226 \tag{C.34}$$
$$C_{n_R} = -0.063085 \tag{C.35}$$
$$C_{n_{\delta_A}} = 0.008785 \tag{C.36}$$
$$C_{n_{\delta_R}} = -0.041144 \tag{C.37}$$

These coefficients and their meanings are detailed in Appendix C.6.

C.5 State-Space Models

The final aircraft dynamics matrices are given by

$$\boldsymbol{A}_{lon} = \begin{bmatrix} -0.12136 & 13.49685 & 0.00000 & -9.76165 \\ -0.06056 & -5.87391 & 0.90192 & -0.05404 \\ 0.00000 & -64.30729 & -7.39401 & 0.00000 \\ 0.00000 & 0.00000 & 1.00000 & 0.00000 \end{bmatrix} \tag{C.38}$$

$$\boldsymbol{B}_{lon} = \begin{bmatrix} 0.00000 & 0.16367 \\ -0.55715 & 0.00000 \\ -92.58691 & 0.00000 \\ 0.00000 & 0.00000 \end{bmatrix} \tag{C.39}$$

$$\boldsymbol{A}_{lat} = \begin{bmatrix} -0.20459 & 0.00892 & -0.86106 & 0.54231 \\ -22.41820 & -8.15954 & 2.69470 & 0.00000 \\ 16.27898 & -0.44861 & -0.93631 & 0.00000 \\ 0.00000 & 1.00000 & 0.09965 & 0.00000 \end{bmatrix} \tag{C.40}$$

$$\boldsymbol{B}_{lat} = \begin{bmatrix} 0.00405 & 0.11427 \\ -94.48457 & 0.77484 \\ 2.44731 & -11.46181 \\ 0.00000 & 0.00000 \end{bmatrix} \tag{C.41}$$

C.6 Stability & Control Derivatives

The tables in this section provide background on the origins of the stability and control derivatives used in the aerodynamic forces and moments model of the aircraft. The majority of the information can be found in [2].

Table C.2: Drag Derivatives

C_{D_0}	Parasitic drag coefficient. Quantifies the aircraft's skin friction drag that is independent of the aircraft's angle of attack.
e	The Oswald efficiency factor. An empirically determined constant used in induced drag calculations. A typical value for this constant is 0.85.

Table C.3: Lift Derivatives

C_{L_0}	Static lift coefficient. Quantifies the lift produced by the aircraft as a whole at zero angle of attack. This lift is due primarily to camber on the main wing but is also influenced by factors such as body shape. This coefficient strongly influences the angle of attack required to trim the aircraft.
C_{L_α}	The aircraft's lift curve slope. It quantifies the increase in lift coefficient as a function of angle of attack. This derivative has a theoretical maximum of 2π. It is one of the fundamental aircraft modelling parameters and is can be quite accurately obtained using either empirical or numerical methods.
C_{L_q}	Quantifies the lift produced by the aircraft due to pitch rate motions. The lift produced is primarily as a result of the induced angle of incidence experienced by the tail-plane during pitch rate motions. The derivative can be quite accurately calculated using empirical or numerical methods. However, it typically has little to no significance on the aircraft dynamics.
$C_{L_{\delta_e}}$	Quantifies the lift force produced by elevator deflections. Few empirical methods exist to determine this control derivative and as such numerical methods are usually made use of. However, it is often has a negligible effect on the aircraft dynamics.

Table C.4: Side Force Derivatives

C_{y_β}	The side force due to sideslip derivative is contributed towards by the lateral lift of the fuselage and the angle of incidence on the fin during sideslip manoeuvres.
C_{y_p}	This derivative describes the side force produced due to roll rate perturbations. Due to the symmetry and streamlined nature of aircraft this derivative is most often negligibly small and thus has little influence on the aircraft dynamics.
C_{y_r}	Quantifies the side force produced by the aircraft due to yaw rate motions. The side force produced is primarily a result of the induced angle of incidence experienced by the fin during yaw rate motions. The derivative can be quite accurately calculated using empirical or numerical methods. However, it typically has very little significance on the aircraft dynamics.
$C_{y_{\delta_a}}$	Quantifies the side force produced by aileron deflections. Due to the orientation of the ailerons, this derivatives is usually very close to zero and has a negligible effect on the aircraft dynamics.
$C_{y_{\delta_r}}$	Quantifies the side force produced due to a rudder deflection. Few empirical methods exist to determine this control derivative and as such numerical methods are usually used to determine it. Its effect is usually quite small on the aircraft dynamics.

Table C.5: Roll Moment Derivatives

C_{l_β}	This important lateral derivative describes the tendency of the aircraft to return towards wings level flight during sideslip motions. A large number of factors contribute towards the sign and magnitude of the derivative. Wing dihedral provides a stabilising effect by inducing a net differential angle of incidence across the wings during sideslip. Wing sweepback also provides s stabilising effect through airflow velocity induced differential lift across the wings. A high fin also makes stabilising contributions through the side force produced during sideslip. Finally, a high wing tends to have a stabilising effect due to the airflow pattern around the fuselage during sideslip. Because of the many factors that contribute towards the derivative, it is often very difficult to obtain accurately.
C_{l_p}	Also, known as the roll damping coefficient, this important derivative quantifies the roll moment produced by the aircraft due to roll rate motions. The coefficient is dominated by the differentially induced angle of incidence across the wing during roll rate motions. The induced angle of incidence on the fin also contribute towards the derivative although its effect is typically negligible. The derivative can be quite accurately calculated using empirical or numerical methods and plays and important role in the aircraft dynamics.
C_{l_r}	Quantifies the roll moment produced through yaw rate perturbations. The derivative is dominated by the differential lift induced across the wings during yaw rate perturbations and the above roll axis force on the fin induced through yaw rate motions. The derivative is an important one in describing the coupling between the roll and directional dynamics.
$C_{l_{\delta_a}}$	Quantifies the roll moment produced by aileron deflections. The important control derivative is usually obtained using numerical methods.
$C_{l_{\delta_r}}$	Quantifies the roll moment produced by rudder deflections. A typical high fin will produce an adverse roll moment. Numerical methods are usually made use of to determine this derivative.

Table C.6: Pitch Moment Derivatives

C_{m_0}	Static pitching moment coefficient. Quantifies the pitching moment produced by the aircraft as a whole at zero angle of attack. This static pitching moment is due primarily to the camber of the main wing, the setting angle of the tail-plane and the shape of the aircraft's fuselage. This coefficient strongly influences the elevator required to trim the aircraft during straight and level flight.
C_{m_α}	This very important parameter, often referred to as the pitch stiffness coefficient quantifies the degree of static stability of the aircraft. This is the aircraft's tendency to return towards its trim condition when perturbed in angle of attack. A negative coefficient implies a statically stable aircraft, while a positive coefficient implies a statically unstable aircraft. This coefficient is dependent on the distance between the aircraft's centre of mass and its neutral point (the point where the total angle of attack based aerodynamic force acts). Although empirical and numerical methods exist for determining the location of the neutral point, the accuracy is often questionable. Thus, for aircraft that are designed to be stable, a measure of safety margin is usually included by shifting the centre of mass forwards by an appropriate amount.
C_{m_q}	Also, known as the pitch damping coefficient, quantifies the pitching moment produced by the aircraft due to pitch rate motions. This coefficient is related to the lift due to pitch rate coefficient through the normalised length to the tail-plane. The derivative can be quite accurately calculated using empirical or numerical methods and plays and important role in the aircraft dynamics.
$C_{m_{\delta_e}}$	Quantifies the pitching moment produced by elevator deflections. Few empirical methods exist to determine this important control derivative and as such numerical methods are usually made use of. The derivative directly influences eventual controller gains.

Table C.7: Yaw Moment Derivatives

C_{n_β}	This important lateral derivative describes the natural tendency of the aircraft to weathercock back into the airflow. It quantifies the degree of directional static stability of the aircraft, with a positive coefficient implying stability. The restoring moment is dominated by the angle of incidence induced force at the fin during sideslip manoeuvres. The derivative can be modelled well using both empirical and numerical methods.
C_{n_p}	Quantifies the yaw moment produced by roll rate perturbations. The major effect of roll rate is to induce differential lift across the wings. This differential lift is associated with a differential drag which in turn produces a yaw moment. This derivative couples the roll and directional modes of motion of the aircraft.
C_{n_r}	Also, known as the yaw damping coefficient, this important derivative quantifies the yaw moment produced by the aircraft due to yaw rate motions. This coefficient is contributed towards by induced angles of incidence on the fin and differential drag (due to local velocity perturbations) across the wings during yaw rate motions. The derivative can be quite accurately calculated using empirical or numerical methods and plays and important role in the aircraft dynamics.
$C_{n_{\delta_a}}$	Quantifies the adverse yaw moment produced as a result of an aileron deflection. Aileron deflections produce differential lift and thus differential drag across the wings. This differential drag produces a yaw moment that tends to yaw the nose of the aircraft into the opposite direction to that desired at the onset of a turn.
$C_{n_{\delta_r}}$	Quantifies the yaw moment due to rudder deflection. This control derivative is related to the side force due to rudder derivative through the normalised length to the fin. Numerical methods are usually made use of to determine this derivative.

References

[1] Google, "Google Maps." Accessed: September, 2013.

[2] M. V. Cook, *Flight Dynamics Principles*. Elsevier Ltd., 2nd ed., 2007.

[3] R. D. De Hart, "Advanced Take-off and Flight Control Algorithms for Fixed Wing Unmanned Aerial Vehicles," Master's thesis, Stellenbosch University, March 2010.

[4] I. K. Peddle, "Autonomous Flight of a Model Aircraft," Master's thesis, Stellenbosch University, April 2005.

[5] I. K. Peddle, *Acceleration Based Manoeuvre Flight Control System for Unmanned Aerial Vehicles*. PhD thesis, Stellenbosch University, December 2008.

[6] Mathworks, "Generate continuous wind turbulence with Dryden velocity spectra - Simulink." `http://www.mathworks.com/help/aeroblks/drydenwindturbulencemodelcontinuous.html`. Accessed: 03 April 2016.

[7] A. A. Lambregts, "Total Energy Based Flight Control System," May 1985.

[8] ESL, "ESL | World Class Research." `http://www.esl.sun.ac.za`. Accessed: 03 April 2013.

[9] M. Henderson, "Denel Dynamics Product Brochure," September 2012.

[10] "ATE Kiwit Brochure," April 2010.

[11] I. K. Peddle and G. W. Milne, "Development of a Low Cost Waypoint Navigation Autopilot for an Unmanned Aerial Vehicle." R & D Journal, 2007, of the South African Institution of Mechanical Engineering, 2007.

[12] T. Harris, "Landing on an Aircraft Carrier - How Aircraft Carriers Work | HowStuffWorks." `http://science.howstuffworks.com/aircraft-carrier4.htm`. Accessed: 17 February 2016.

[13] J.-C. Roos, "Autonomous Take-Off and Landing of a Fixed Wing Unmanned Aerial Vehicle," Master's thesis, Stellenbosch University, March 2007.

[14] B. J. Visser, "Precision Landing of an UAV," Master's thesis, Stellenbosch University, December 2008.

[15] S. J. A. Smit, "Autonomous Landing of a Fixed-Wing Unmanned Aerial Vehicle using Differential GPS," Master's thesis, Stellenbosch University, March 2013.

[16] F. N. Alberts, "Accurate Autonomous Landing of a Fixed-Wing Unmanned Aerial Vehicle," Master's thesis, Stellenbosch University, December 2012.

[17] A. Cho, J. Kim, S. Lee, S. Choi, B. Lee, B. Kim, N. Park, D. Kim, and C. Kee, "Fully Automatic Taxiing, Takeoff and Landing of a UAV Using a Single-Antenna GPS Receiver Only," in *Control, Automation and Systems, 2007. ICCAS '07. International Conference on*, pp. 821–825, October 2007.

[18] Z. Liu, Y. Wang, and X. Hao, "Coordinated Landing Control of Unmanned Aerial Vehicle," in *Electronics, Communications and Control (ICECC), 2011 International Conference on*, pp. 1965–1970, September 2011.

[19] J. Lopéz, R. Dormiro, and J. P. Gómez, "A Fully Autonomous UAV Landing Controller Synthesis - QFT and H_∞ Technique Comparison," in *Proceedings of the Institution of Mechanical Engineers, Part G: Journal of Aerospace Engineering 2012*, vol. 226, pp. 281–293, October 2011.

[20] K. Masuko, I. Takahashi, S. Ogawa, M.-H. Wu, A. Oosedo, T. Matsumoto, K. Go, F. Sugai, A. Konno, and M. Uchiyama, "Autonomous Takeoff and Landing of an Unmanned Aerial Vehicle," in *System Integration (SII), 2010 IEEE/SICE International Symposium on*, pp. 248–253, December 2010.

[21] R. Wang, Z. Zhou, and Y. Shen, "Robust Landing Control and Simulation for Flying Wing UAV," in *Control Conference, 2007. CCC 2007. Chinese*, June 2007.

[22] M. I. Salfi, U. Ahsun, and H. A. Bhatti, "Lateral and Longitudinal Guidance and Control Design of a UAV in Auto Landing Phase," in *Applied Sciences and Technology (IBCAST), 2009 6th International Bhurban Conference on*, January 2009.

[23] S. Singh and R. Padhi, "Automatic Path Planning and Control Design for Autonomous Landing of UAVs Using Dynamic Inversion," in *American Control Conference, 2009. ACC '09*, pp. 2409–2414, June 2009.

[24] S. Park, J. Deyst, and J. P. How, "A New Nonlinear Guidance Logic for Trajectory Tracking," in *AIAA Guidance, Navigation, and Control Conference (GNC)*, (Providence, RI), August 2004.

[25] K. R. Bruce, "NASA B737 Flight Test Results of the Total Energy Control System," Tech. Rep. NASA CR-178285, National Aeronautics and Space Administration, July 1987.

[26] M. A. Bruzzini, "Development of a TECS Control Law for the Lateral Directional Axis of the McDonell Douglas F-15 Eagle," Master's thesis, Air Force Inst. of Tech., Wright-Patterson AFB, OH, December 1994.

[27] P. Chudý and P. Rzucidlo, "Controller Design for a Digital Flight Control System DFCS," in *The 2nd International Multi-Conference on Engineering and Technological Innovation*, vol. 1 of *PROCEEDINGS*, (Orlando, Florida, US), pp. 259–264, The International Institute of Informatics and Systemics, 2009. ISBN: 978-1-934272-68-8.

[28] J. P. Dutton Jr, "Development of a Nonlinear Simulation for the MacDonnel Douglas F-15 Eagle with a Longitudinal TECS Control-Law," Master's thesis, Air Force Inst. of Tech., Wright-Patterson AFB, OH, September 1994.

[29] K. Ji, W. Wei, L. Ai-jun, and W. Chang-qing, "Lateral Directional Axis Control of Aircraft Based on TECS," in *Image and Signal Processing, 2009. CISP '09. 2nd International Congress on*, pp. 1–5, 2009.

[30] Z. Qingzhen, G. Chen, M. Wentao, and R. Zhang, "Decoupling Control for Airspeed and Flight Path Angle Using an Improved Total Energy Control Algorithm," in *Systems and Control in Aerospace and Astronautics, 2008. ISSCAA 2008. 2nd International Symposium on*, pp. 1–6, 2008.

[31] R. Akmeliawati and I. Mareels, "Nonlinear Energy-based Control Method for Aircraft Dynamics," in *Decision and Control, 2001. proceedings of the 40th IEEE Conference on*, vol. 1, pp. 658–663, 2001.

[32] R. Akmeliawati and I. M. Y. Mareels, "Nonlinear Energy-Based Control Method for Aircraft Automatic Landing Systems," *Control Systems Technology, IEEE Transactions on*, vol. 18, no. 4, pp. 871–884, 2010.

[33] G. Looye and H.-D. Joos, "Design of Autoland Controller Functions with Multi-Objective Optimization," in *AIAA Guidance, Navigation, and Control Conference and Exhibit*, August 2002.

[34] D. Lee, T. Ryan, and H. Kim, "Autonomous Landing of a VTOL UAV on a Moving Platform Using Image-based Visual Servoing," in *Robotics and Automation (ICRA), 2012 IEEE International Conference on*, pp. 971–976, 2012.

[35] G. Xu, X. Chen, B. Wang, K. Li, J. Wang, and X. Wei, "A Search Strategy of UAV's Automatic Landing on Ship in All Weathe," in *Electrical and Control Engineering (ICECE), 2011 International Conference on*, 2011.

[36] Matt Brown, "Hooked on RC Airplanes - Where flying radio control is more than just a hobby!." `http://www.hooked-on-rc-airplanes.com`. Accessed: February 20, 2016.

[37] Perkins and Hage, *Airplane Performance Stability and Control*. John Wiley & Sons, Inc., 1949.

[38] E. Chen and T. Yen, "Comparing SLC and MLC Flash Technologies and Structure," Technical White Paper Version 1.0, Advantech, September 2009.

[39] P. Novacek, "Flight Training." `http://flighttraining.aopa.org/students/presolo/special/antenna.html`. Accessed: 21 February 2016.

[40] NovAtel, *OEMV Family Installation and Operation User Manual*, 2008. OM-20000093 Rev 8.

[41] "The US Navy – Fact File: F/A-18 Hornet strike fighter." `http://www.navy.mil/navydata/fact_display.asp?cid=1100&tid=1200&ct=1`. Accessed: 22 February 2016.

[42] "The US Navy – Fact File: Aircraft Carriers - CVN." `http://www.navy.mil/navydata/fact_display.asp?cid=4200&tid=200&ct=4`. Accessed: 02 March 2016.

[43] Federal Aviation Administration, *Airplane Flying Handbook*. U.S. Department of Transportation, 2004.

[44] Etkin and Reid, *Dynamics of Flight Stability and Control*. John Wiley & Sons, Inc., 3rd ed., 1996.

[45] Federal Aviation Administration, *Pilot's Handbook of Aeronautical Knowledge FAA-H-8083-25A*. United States Department of Transportation, 2008.

[46] H. H. Hurt, *Aerodynamics for Naval Aviators*. Naval Air Systems Command, 1959.

[47] "MIL-F-8785C," November 1980.

[48] "MIL-HDBK-1797," December 1997.

[49] Mathworks, "Generate continuous wind turbulence with Von Kármán velocity spectra - Simulink." `http://www.mathworks.com/help/aeroblks/vonkarmanwindturbulencemodelcontinuous.html`. Accessed: 03 April 2016.

[50] D. Blaauw, "Flight Control for a Variable Stability Blended-Wing-Body Unmanned Aerial Vehicle," Master's thesis, Stellenbosch University, 2009.

[51] D. R. Gaum, "Aggressive Flight Control Technique for a Fixed-Wing Unmanned Aerial Vehicle," Master's thesis, Stellenbosch University, 2009.